UNIVERSITY OF BIRMINGHAM

Chemical Control of Thermal Expansion in Zeolites with the LTA Topology

by

Thomas Carey

Supervisors: Dr P. A. Anderson

Dr J. A. Hriljac

A thesis submitted to The University of Birmingham for the degree of Doctor of Philosophy

The School of Chemistry

College of Engineering and Physical Sciences

The University of Birmingham

April 2013

To Jess

Abstract

Zeolites are microporous materials that have been commonly shown to exhibit remarkable negative thermal expansion (NTE) behaviour in their purely siliceous forms, with reported thermal expansion coefficients ranging from -3×10^{-6} K^{-1} to -26.1×10^{-6} K^{-1}. In contrast, very little research has been reported on the aluminium-containing structures which are widely used for various commercial applications. Compounds exhibiting this property, which has only been observed in a small number of solids, are of considerable technological interest as their inclusion in devices or composite materials can counterbalance the more usual expansion on heating and contraction on cooling, thereby reducing the incidence of thermally induced failures. Here, we report an investigation into the effect that changing the chemical composition of the zeolite framework and intrapore species has on thermal expansion properties of zeolites with the LTA topology. Variable-temperature powder X–ray diffraction studies were used to determine the thermal expansion coefficients of the chemically modified zeolites over a sub-ambient temperature range and investigate the structural basis behind their thermal behaviour. Dramatic changes in the thermal expansion behaviour (from strong negative to weak positive) of the zeolites were observed as the structures were modified through ion-exchange, dehydration, varying the Al content in the framework and loading the pores with silver nitrate. The zeolitic pores contents have been shown to play a key role in the manner in which LTA-zeolites react to temperature variation, especially in the case of intra-porous water molecules. Detailed atomistic structural mechanisms behind the observed NTE behaviour have been produced for the more simplistic systems. Several key breakthroughs have also been achieved in understanding the formation of the superlattice when silver nitrate is incorporated into the zeolite pores and with regards to solving the unit cell structure.

Quote

“If I have seen a little further, it is by standing on the shoulders of giants.”

Sir Isaac Newton, 1676.

Acknowledgements

There are many people who have helped and supported me during this work and to whom I owe a great deal of thanks. Firstly, I would like to express my sincere gratitude to my supervisors, Paul Anderson, Joe Hriljac and Chiu Tang, for giving me the opportunity to undertake a PhD and for their outstanding help and guidance. I would also like to express my thanks to Jackie Deans, Louise Male, Phil Chater, Julia Parker, Jonathon Potter, Anna Warren and Dan Reed for providing their continuous technical support and expertise which enabled me to conduct my research. I am also grateful to my financial sponsors (University of Birmingham and Diamond Light Source) and to my collaborators Alvaro Mayoral, Avelino Corma and Fernando Rey for their contributions to my work.

Further thanks should go to the staff and students on the fifth floor (past and present) for their help and making it a pleasant place to work, especially Dave, Ian, Marianna, Julie, Annabelle and Tom for the interesting lunchtime conversations, Evin for all the eastern cooking and culture lessons and Tim for providing much entertainment (and frustration) along the way. I would also like to thank my close friends Dan H, Rich, Jimmy, Heather, Bert, Sarah, April, Dan M, Phil, Charl, Dave and Payam for providing a welcome distraction from my studies, particularly over the write up period.

Finally, and most importantly, thank you to my parents, brother and girlfriend Jess, without their continuous love and support this would not have been possible.

Contents

Chapter 7 – Summary and Further Work

Appendices (Included in attached CD)

Chapter 1 – Introduction

Zeolites are a type of mineral, the first of which was discovered in 1756 by Swedish mineralogist Axel Fredrik Cronstedt.[1] The name zeolite is derived from the two Greek words *zeos* (to boil) and *lithos* (a stone) and refers to the steam that evolved from the mineral when it was heated in a blow-pipe flame. Around 40 natural zeolites have been discovered to date and are found all over the world in volcanic rocks, ocean sediments and arid alkaline soils.[2] Mordenite was the first synthetic zeolite synthesised in 1948 by Barrer [3] and since then over 200 different structures have been synthetically produced.

1.1 Zeolite Structures and Nomenclature

Zeolites are crystalline aluminosilicate species that are made up of $[SiO_4]$ and $[AlO_4]$ tetrahedra, which are linked together through shared oxygen atoms (figure 1.1) to form regular three-dimensional frameworks. Löwenstein's rule states, however, that Al–O–Al

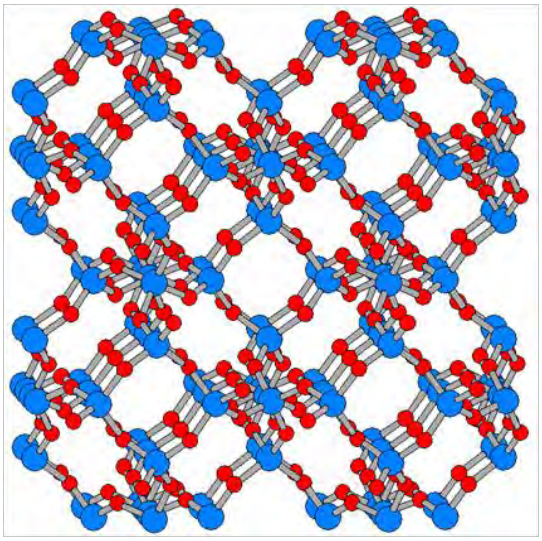

Figure 1.1 *– Zeolite lattices are constructed of corner sharing tetrahedra (Si or Al atoms [blue] in the centre and oxygen atoms [red] in the corners).*

linkages are not normally observed in zeolites structures due to increased charge repulsion, therefore the molar Si/Al ratio can never be smaller than one.[4] These frameworks are described as being microporous as they contain pores, channels and cages of molecular dimensions.[5]

The presence of $[AlO_4]$ tetrahedra in the zeolite structures causes the overall framework to have a net negative charge. This negative charge is then neutralised by the presence of non–framework cations (normally alkali and alkaline metals) that are located in the pores and channels of the zeolite. These charge balancing cations are weakly bound to the framework oxygen atoms and usually can be readily exchanged with other similar cations. Water molecules also reside within the zeolitic cavities and can be reversibly removed causing little or no change to the lattice structure. The general formula for a zeolite can be stated as:

$$M_{x/n}[(AlO_2)_x(SiO_2)_y].wH_2O \qquad (1.1)$$

where cation M has a charge of n.

$[SiO_4]$ and $[AlO_4]$ tetrahedra can be linked together in a number of different ways to form a large variety of different zeolite structure types (206 unique structures known to date). In order to clarify and describe these different structure types, a set of guidelines were published in 1979 by the International Union of Pure and Applied Chemistry (IUPAC) which set a standard for zeolite nomenclature.[6] Since this publication, all zeolites with the same structure type have been assigned a three-letter code. For example zeolites X and Y have a different Si/Al ratio but both of them have the same structure which is analogous to the natural mineral faujasite; therefore both are assigned the three-letter code FAU (figure 1.2).

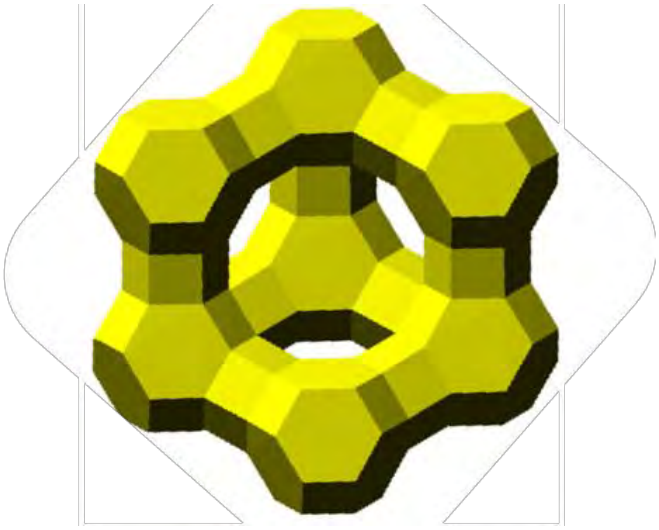

Figure 1.2 *– Representation of the FAU structure (Si or Al atoms occupy each corner with oxygen atoms in between).*

An up-to-date database of all the zeolite structures types and their three-letter codes can be found on the International Zeolite Association (IZA) website.[7]

1.2 Zeolite Modification and Applications

A simple method of modifying a zeolite can be achieved by replacing the charge balancing cations through an ion-exchange reaction. The possibilities of this modification are so large that the majority of the elements in the periodic table have been introduced into a zeolite framework.[5] The available space within a zeolitic pore is highly affected by the cations which are present; therefore substituting the non-framework cations can cause a significant change to the properties of a zeolite.

As mentioned previously, water molecules can be removed from a zeolite without structure collapse. When this occurs, cations which were coordinated to the water molecules have lower coordination and can move to more unfavourable intra-porous positions. As a result

of this property, dehydrated zeolites have a very high affinity for water molecules and are commonly used as drying agents. It is also possible to replace the zeolitic water molecules with salts (such as $AgNO_3$) by salt-inclusion (commonly called occlusion in this context) reactions.[8] Water is initially removed by heating in these reactions and then salt cations and anions are introduced to the pore space. Salts can also be incorporated into zeolite structures during synthesis.

Another way of modifying a zeolite is by altering the Si/Al ratio of the framework. The Si/Al ratio can be specified upon synthesis and dictates how negatively charged a lattice will be. This in turn affects the amount and positions of the non-framework cations within the structure.

Other microporous materials commonly referred to as zeotypes, have also been produced by modifying zeolite structures. These are made by substituting other similar elements for framework aluminium and silicon atoms. The first material of this type was an aluminophosphate, which was discovered in 1982 by Flanigen *et.* al.[9] In this structure all the SiO_4 tetrahedra are replaced by PO_4 tetrahedra, which are of a similar size to SiO_4. Other open-framework materials such as ferrophosphates, colbaltophosphates, titanophosphates, germanates and borosilicates have also since been produced.[10]

The unique properties of zeolites and their ability to be modified have lead to their application in numerous commercial processes in the past century. The dimensions of the cavities within a zeolite can dictate the size of the molecules that can be absorbed or released and lead to use as molecular sieves. This porous nature has also been utilised by the agricultural industry by using zeolites in slow release fertilisers.[11-12] Chemical fertilisers

have a detrimental effect on the environment as they are only partially absorbed by the soil. Excess fertiliser is then washed away into rivers and groundwater causing eutrophication (the pollution or rivers and lakes). Several slow release fertilisers have been produced which absorb nutrients (such as nitrates and phosphates) and gradually release them into the soil over time.

Other zeolitic properties, such as having a large internal surface area, strong acid sites in hydrogen forms, high thermal stability and size selectivity, has resulted in zeolites being widely used as heterogeneous catalysts. Unlike other catalysts, zeolites are able to absorb reactants into their pores. Once inside, the possible reaction pathways are limited as certain transition state geometries cannot be formed within the confined pores. Catalytic studies of zeolites were first carried out in the 1950s by Rabo[13] *et. al*, and in 1962 the first catalytic reaction using a zeolite was reported by Weisz and Frielette.[14] Since then zeolites have been engineered in numerous ways to catalyse specific reactions, especially those used in the petroleum and petrochemicals industry. One of oldest and most important processes used in this industry is fluid catalytic cracking.[15] Since the 1960s, zeolite Y (FAU) containing rare earth cations has been widely applied in this process as it had significantly greater activity and stability than the previously used catalysts. The isomerisation of paraffin is another important process that utilise zeolites in the petrochemical industry. Mordenite (MOR) containing Pt metal was the first zeolite to catalyse this process, but was later replaced by a catalyst based on zeolite ZSM–5 (MFI) which was much more effective.

Many more zeolite applications exist today. These include their uses in washing detergents, gas separation, nuclear waste management, water purification and medical treatments.

1.3 LTA Topology

The LTA topology is a synthetic zeolite structure type which was first characterised by Breck *et. al* in 1956.[16] Depending upon the Si/Al ratio, zeolites with the LTA topology can be referred to by different names. Zeolite A has a Si/Al ratio of 1, ZK4[17] has a Si/Al ratio of >1 and ITQ–29[18] is the purely siliceous form. The main building block in the LTA structure type is the sodalite cage (or β-cage), which consists of sub-unit 6-rings and 4-rings (figure 1.3). These β-cages are then joined together by four bridging oxygens at the sub-unit double 4-rings to form larger α-cages in between (figure 1.4). The β-cage has a internal diameter of ~6.5 Å and its largest pore opening is through the 6-ring with a diameter of ~2.2 Å. The α-cage has a larger pore size through the 8-ring at ~4.2 Å wide and an internal diameter of ~11.5 Å.

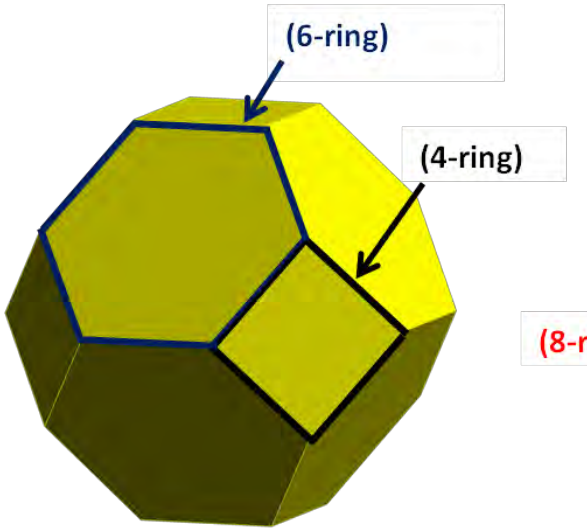

Figure 1.3 – *β-cage structure.*

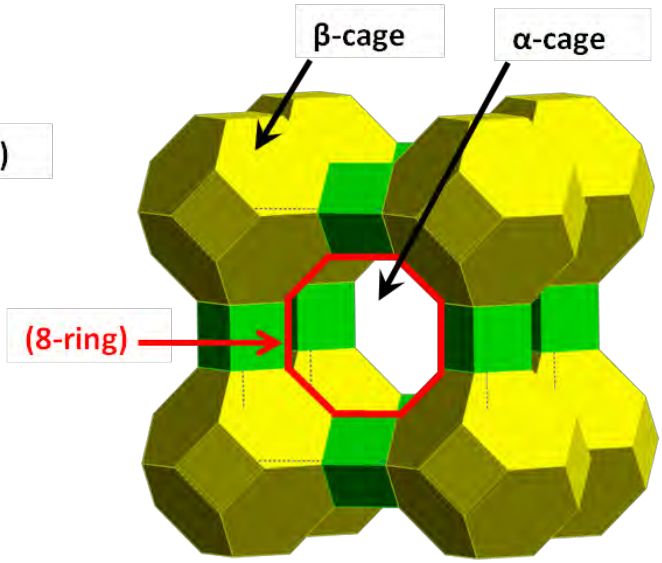

Figure 1.4 – *LTA structure.*

1.4 Negative Thermal Expansion in Zeolites

Negative thermal expansion (NTE) is an unusual phenomenon where materials contract in volume on heating (or expand on cooling). This property has only been observed in a small number of solids including some metal oxides,[19] metal cyanides,[20] polymers[21] and zeolites.[22-28] Materials exhibiting NTE have attracted some considerable interest in recent times as they have a variety of potential applications in electronic components, astro-materials, composites used in dental fillings and high-precision optical equipment.[29] One material that has attracted extensive research is ZrW_2O_8. This material has been shown to exhibit a isotropic NTE ($\alpha = -8.7 \times 10^{-6}$) over a very broad temperature range (0.3–693 K)[19] and when part of a Cu/ZrW_2O_8 composite, can be made to show a thermal expansion coefficient similar to that of silicon.[30] This is important as thermally induced failures can be a problem in silicon based electronic components.

There are several different types of NTE. Intrinsic NTE is based upon the unit cell (section 2.2.1) dimensions of a crystalline material and can be either isotropic or anisotropic. Isotropic NTE is when the unit cell contracts in all three dimensions upon thermal excitation and is only observed in cubic materials. Anisotropic NTE is when the unit cell contracts in only one or two dimensions. The mean volumetric coefficient of intrinsic thermal expansion ($\overline{\alpha_V}$) is defined as:

$$\overline{\alpha_V} = \frac{(V_{T2} - V_{T1})}{V_{T1}(T2 - T1)} \qquad (1.2)$$

where V is the unit cell volume and T1/T2 is the lowest/highest temperature, respectively.

Extrinsic NTE is also been shown in some materials where the unit cell volume actually increases during heating.[29] In certain ceramic materials, consolidated anisotropic NTE can cause microcracks to develop on cooling after formation. On reheating, these microcracks then reclose resulting in extrinsic NTE behaviour.

An accepted mechanism for NTE in zeolite structures can be understood by focusing on the longitudinal and transverse vibrations in the T–O–T linkages (where T = Si or Al) (figure 1.5). In the majority of materials, longitudinal vibrations are amplified on heating causing the interatomic bonds to lengthen. T–O bonds however are strong enough not to increase significantly upon thermal excitation resulting in little or no change to the structural volume; therefore the TO_4 tetrahedra can be thought of as rigid units. These rigid TO_4 tetrahedra are then able to rotate about the floppy T–O–T linkages due to correlated transverse vibrations which in turn cause a decrease in the T···T interatomic distances and a reduction in the overall unit cell volume (figure 1.6). This mechanism for NTE is known as the rigid unit

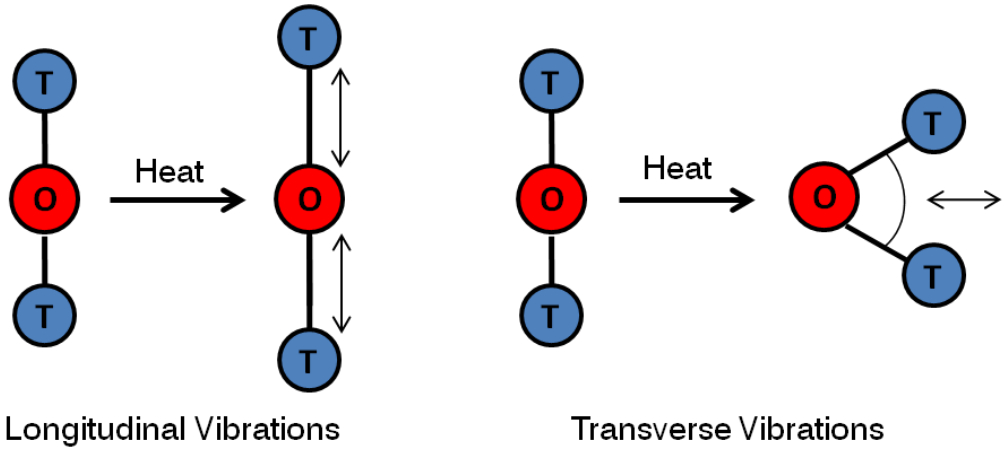

Figure 1.5 *– Longitudinal and transverse vibrations in zeolite frameworks.*

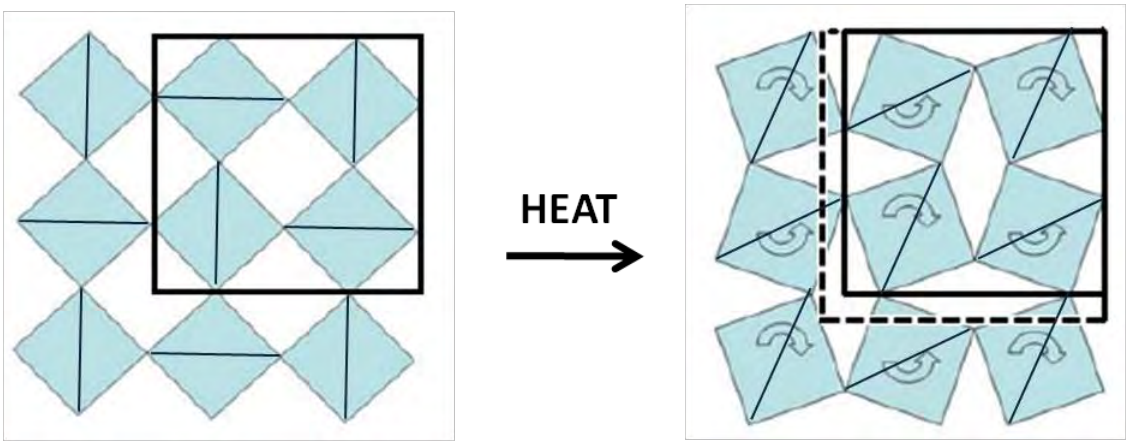

Figure 1.6 *– Diagram illustrating the contraction in unit cell volume caused by the rotation of the rigid units in tetrahedral structures.*

mode (RUM) model. Dove and co-workers were the first to apply the RUM model to silicate structures using the computational software CRUSH.[31-32] The RUM model cannot be applied to all structures that display NTE but it has been applied to some zeolite frameworks[33] and all crystalline forms of SiO_2.[34-35]

1.5 Research Aims

The primary aim of this thesis was to investigate the effect that changing the chemical composition of zeolite frameworks and intrapore species had on their thermal expansion behaviour. Extensive research on purely siliceous zeolite structures has been carried out in recent years,[22-28, 33] which has shown that NTE is the commonly observed thermal behaviour rather than the unexpected. In contrast, relatively little[36-40] attention has been paid to aluminium-containing zeolites where the structures and properties are known to be particularly sensitive to the extra-framework charge-balancing cations and guest molecules in the pores. For this reason, it is important to understand what effect changing the chemical contents of a zeolite framework and pores has on its thermal expansion properties. Zeolites with the LTA topology were exclusively chosen to be studied in this project due to

their relatively simple structure and large choice of compositional variations. Variable temperature XRD was used to determine the thermal expansion behaviour of zeolites which had been modified through ion-exchange, dehydration, varying the Al content in the framework and loading the pores with $AgNO_3$. A long-term objective of this work is to determine a structural mechanism behind the complex thermal expansion behaviour and to establish whether it is possible to tune chemically zeolite materials to produce a desired coefficient of thermal expansion (such as zero) for potential applications.

1.6 References

1. A. F. Cronstedt, *Kongl. Svenska Vetenskaps Academiens Handlingar*, 1756, **17**, 120.
2. R. M. Barrer, *Zeolites and Clay Minerals as Sorbents and Molecular Sieves*, Academic Press, London, 1978.
3. R. M. Barrer, *J. Chem. Soc*, 1948.
4. W. Lowenstein, *Am. Mineral*, 1954, **92**.
5. A. Dyer, *An Introduction to Molecular Sieves*, John Wiley and Sons Inc., 1988.
6. R. M. Barrer, *Pure Appl. Chem.*, 1979, **51**, 1091.
7. http://www.iza-online.org.
8. W. E. Meier and R. M. Barrer, *J. Chem. Soc.*, 1958, 299-304.
9. S. T. Wilson, B. M. Lok, C. A. Messina, T. R. Cannan and E. M. Flanigen, *J. Am. Chem. Soc.*, 1982, **104**, 1146-1147.
10. S. Mandal and S. Natarajan, *Angrew. Chem. Int. Ed.*, 2008, **47**, 4798.
11. A. K. Bansiwal, S. S. Rayalu, N. K. Labhasetwar, A. A. Juwarkar and S. Devotta, *J. Agric. Food Chem.*, 2006, **54**, 4773-4779.
12. A. Carvalho, J. Pires, P. Veloso, M. Machado, M. B. d. Carvalho and J. Rocha, *Micropor. Mesopor. Mater.*, 2003, **58**, 163-173.

13. J. A. Rabo, P. E. Pickett, D. N. Stamires and J. E. Boyle, *2nd Int. Congr. Catal.*, 1960, 2055.

14. V. Frielette and P. B. Weisz, *J. Phys. Chem.*, 1960, **64**.

15. C. Marcilly, *J. Catal.*, 2006, **216**, 47-62.

16. T. B. Reed and D. W. Breck, *J. Am. Chem. Soc.*, 1956, **78**, 5972-5977.

17. G. T. Kerr, *Inorg. Chem.*, 1966, **5**, 1537-1539.

18. A. Corma, F. Rey, J. Rius, M. J. Sabater and S. Valencia, *Nature*, 2004, **431**, 287-290.

19. T. A. Mary, J. S. O. Evans, T. Vogt and A. W. Sleight, *Science*, 1996, **272**, 90-92.

20. A. L. Goodwin, K. W. Chapman and C. J. Kepert, *J. Am. Chem. Soc.*, 2005, **127**, 17980-17981.

21. Y. Maniwa, R. Fujiwara, H. Kira, H. Tou, H. Kataura, S. Suzuki, Y. Achiba, E. Nishibori, M. Takata, M. Sakata, M. Fujiwara and H. Suematsu, *Phys. Rev. B*, 2001, **64**, 241402.

22. D. A. Woodcock, P. Lightfoot, L. A. Villaescusa, M. Díaz-Cabañas, M. A. Camblor and D. Engberg, *Chem. Mater.*, 1999, **11**, 2508-2514.

23. S. H. Park, R. W. G. Kunstleve, H. Graetsch and H. Gies, *Stud. Surf. Science Catal.* , 1997, **105**, 1989-1994.

24. M. P. Attfield and A. W. Sleight, *Chem. Commun.*, 1998, 601-602.

25. D. A. Woodcock, P. Lightfoot, P. A. Wright, L. A. Villaescusa, M. Díaz-Cabañas and M. A. Camblor, *J. Mater. Chem.*, 1999, **9**, 349-351.

26. L. A. Villaescusa, P. Lightfoot, S. J. Teat and R. E. Morris, *J. Am. Chem. Soc.*, 2001, **123**, 5453-5459.

27. P. Lightfoot, D. A. Woodcock, M. J. Maple, L. A. Villaescusa and P. A. Wright, *J. Mater. Chem.*, 2001, **11**, 212-216.

28. I. Bull, P.Lightfoot, L. A. Villaescusa, L. M. Bull, R. K. B. Gover, J. S. O. Evans and R. E. Morris, *J. Am. Chem. Soc.*, 2003, **125**, 4342-4349.

29. A. W. Sleight, *Current opinion in solid state & materials science*, 1998, **3**, 128-131.

30. H. Holzer and D. Dunand, *J. Mater. Res.*, 1999, **14**, 780-789.

31. A. P. Giddy, M. T. Dove, G. S. Pawley and V. Heine, *Acta Crystallogr.*, 1993, **A49**.

32. K. D. Hammonds, M. T. Dove, A. P. Giddy and V. Heine, *Am. Mineral.*, 1994, **79**.

33. K. D. Hammonds, V. Heine and M. Dove, *J. Phys. Chem. B*, 1998, **102**, 1759-1767.

34. K. D. Hammonds, M. T. Dove, A. P. Giddy, V. Heine and B. Winkler, *Am. Mineral*, 1996, **81**, 1057-1079.

35. I. P. Swainson and M. T. Dove, *J. Phys. Condens. Matter.*, 1995, 1771-1788.

36. X. Wang, J. C. Hanson, J. Szanyi and J. A. Rodriguez, *J. Phys. Chem. B*, 2004, **108**, 16613-16616.

37. R. M. Reisner, Y. Lee, J. C. Hanson, G. A. Jones, J. B. Parise, D. R. Corbin, B. H. Toby, A. Freitag, J. Z. Larese and V. Kahlenberg, *Chem. Commun.*, 2000, 2221-2222.

38. P. M. Jardim, B. A. Marinkovic, A. Saavedra, L. Y. Lau, C. Baehtz and F. Rizzo, *Micropor. Mesopor. Mater.*, 2004, **76**, 23-28.

39. J. W. Couves, R. H. Jones, S. C. Parker, P. Tschaufeser and C. R. A. Catlow, *J. Phys.: Condens. Matter*, 1993, **5**, 329-332.

40. P. G. Krokidas, E. D. Skouras, V. Nikolakis and V. N. Burganos, *J. Phys. Chem. C*, 2010, **114**, 22441-22448.

Chapter 2 – Experimental

2.1 Introduction

The experimental techniques performed in this research fall into one of two areas: (i) the preparation of the zeolite materials and (ii) their subsequent characterisation. The synthesis and modification of the zeolites will be discussed in the relevant sections of this thesis. Characterisation of the zeolite materials were performed using the techniques discussed in this chapter.

2.2 Crystallography and X–ray Diffraction

Crystallography and X–ray diffraction (XRD) are two of the most powerful tools used in solid state chemistry. Crystallography provides the means to describe how atoms are arranged in solids and XRD is one technique used to discover the atomic structure.

2.2.1 Fundamentals of Crystallography

In a crystalline solid, the atoms adopt a periodic arrangement in a three dimensional lattice.[1] This arrangement can be represented by an individual repeat unit known as the unit cell. The unit cell is defined as the smallest repeating parallel sided unit which shows the full symmetry of a crystal structure. Using only translational symmetry, the entire crystal lattice can be produced from the unit cell. The three axes (*a*, *b* and *c*) and three angles (α, β and γ) that are used to define a unit cell are known as the lattice parameters (figure 2.1). A unit cell can be one of seven different crystal systems (table 2.1). Combination of these crystal systems with the four types of lattice centring (*P*, *I*, *F* and *C*) gives a total of 14

Table 2.1 *– The seven crystal systems.*

Crystal system	Unit cell dimensions		Allowed lattices
Cubic	$a = b = c$	$\alpha = \beta = \gamma = 90°$	*P, I, F*
Tetragonal	$a = b \neq c$	$\alpha = \beta = \gamma = 90°$	*P, I*
Orthorhombic	$a \neq b \neq c$	$\alpha = \beta = \gamma = 90°$	*P, I, F, C (or B)*
Monoclinic	$a \neq b \neq c$	$\alpha = \gamma = 90°, \beta \neq 90°$	*P, C*
Triclinic	$a \neq b \neq c$	$\alpha \neq \beta \neq \gamma \neq 90°$	*P*
Hexagonal	$a = b \neq c$	$\alpha = \beta = 90°, \gamma = 120°$	*P*
Trigonal / Rhombohedral	$a = b = c$	$\alpha = \beta = \gamma \neq 90°$	*P (R)**

* the primitive description of a rhombohedral lattice is normally given the symbol *R*.

different lattice types, known as the Bravais lattices. Bravais lattices show the intrinsic symmetry of a unit cell by identifying the equivalent symmetry positions which are known as lattice points. Any atom, ion or molecule located on one of the lattice points is identical to that placed any other lattice point.

Atomic positions within a unit cell are expressed as fractional coordinates with respect to the unit cell axis. Upon inclusion of atoms into a unit cell, additional symmetry operations are introduced (glide and screw planes) which must be considered. Combination of the 14 Bravais lattices with the 32 crystallographic point groups produces 230 space groups in which any crystal structure can be characterised.

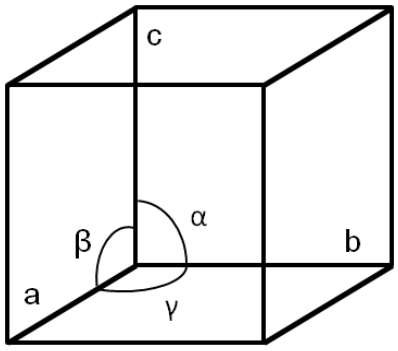

Figure 2.1 - *Representation of a three dimensional unit cell*.

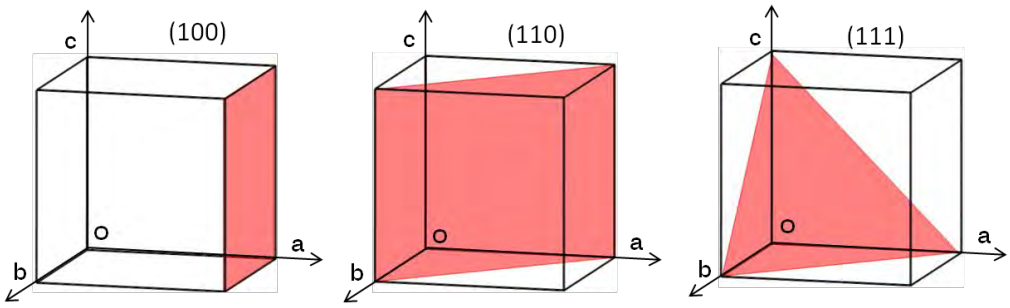

Figure 2.2 *– Representation of lattice planes with their corresponding Miller indices. O indicates the unit cell origin.*

2.2.2 Lattice planes and Miller indices

For the purpose of diffraction, imaginary planes can be used to divide up a unit cell and provide a reference grid to which the atoms in the crystal structure may be referred. These imaginary planes are called lattice planes and are characterised using three integers known as Miller indices, denoted (*hkl*). The values *h*, *k* and *l* are defined by the inverse of the fractional intercept of the first plane in the set not to pass through the origin with each of the axes a, b and c, respectively (figure 2.2). Depending upon the symmetry of a crystal, some lattice planes can be equivalent, such as the (100), (010) and (001) planes in a cubic system. Parallel planes have the same Miller indices and are separated by a perpendicular distance known as the *d*–spacing, d_{hkl}.

2.2.3 Reciprocal lattice

The reciprocal lattice is an important concept used for understanding both the geometry and mathematical relationships in diffraction. Thus far the idea of lattice planes in a three dimensional unit cell has been discussed. In a reciprocal lattice, lattice planes are represented by their perpendicular vectors from the origin. At the end of each vector, reciprocal lattice points are positioned to which *hkl* values can be assigned. The distance,

d_{hkl}^* from the origin to a reciprocal lattice point is inversely proportional to the *d*-spacing, d_{hkl} in a real lattice:

$$d_{hkl}^* = \frac{\lambda}{d_{hkl}} \qquad (2.1)$$

where λ is the wavelength of the diffracted radiation. Figure 2.3 illustrates the relationship between the real lattice and the reciprocal lattice.

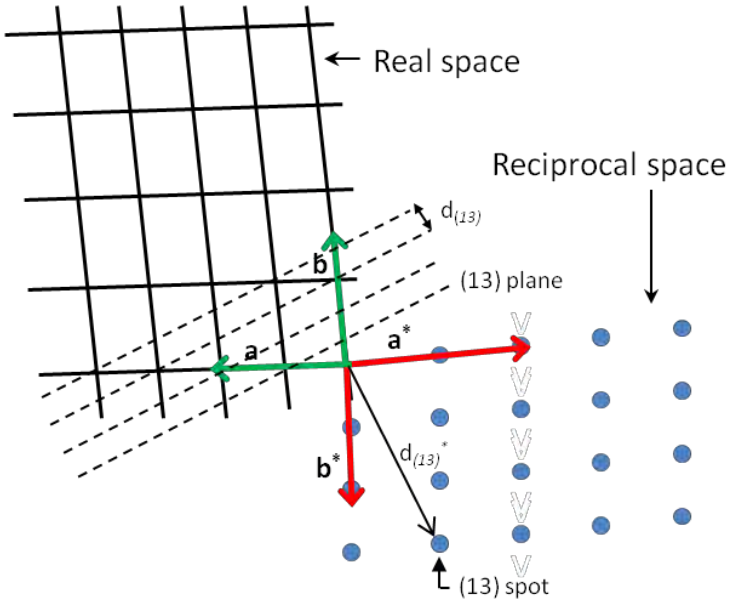

Figure 2.3 *– Diagram illustrating the relationship between real and reciprocal space in two-dimensions (adapted from reference[2]).*

2.2.4 Fundamentals of X-ray Diffraction

XRD is one of the most powerful and commonly used techniques for characterising crystalline solids.[3] In this technique, X–rays focused onto a crystal are scattered by the atomic electrons and the direction and intensity of the scattered waves are detected. X–rays have an approximate wavelength of around 1×10^{-10} m (1 Å), which is comparable to the distances between atoms in a crystalline lattice. As the X–ray wavelength and interatomic

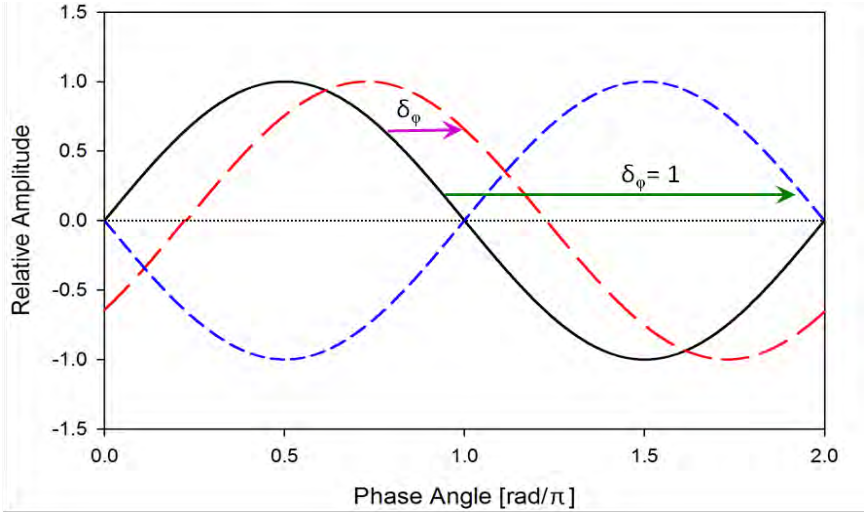

Figure 2.4 *– X–rays modelled as sine waves.*

distances are similar, interference between the scattered X–rays can occur, resulting in interference maxima and minima. If two identical waves travelling in the same direction and are not in–phase with one another, they are said to have a phase shift, δ_φ (figure 2.4). The phase shift determines the resulting amplitude of the combined waves. For example if two identical waves are completely in phase with each another (i.e. $\delta_\varphi = 0$), constructive interference will occur causing the resulting wave to have an increased intensity. However if two identical waves become completely out of phase with one another (i.e. $\delta_\varphi = 1$), destructive interference takes place causing the resulting wave to have zero intensity. X–rays that are scattered by atoms at different positions in the unit cell arrive at the detector with a relative phase shift. Therefore, information about the relative atomic positions can be calculated from the measured intensities.

2.2.5 Bragg Equation

Bragg's law[4] is derived by assuming that X–rays behave like visible light and are reflected by the planes in a lattice. However, in contrast to visible light, X–rays are able to partially

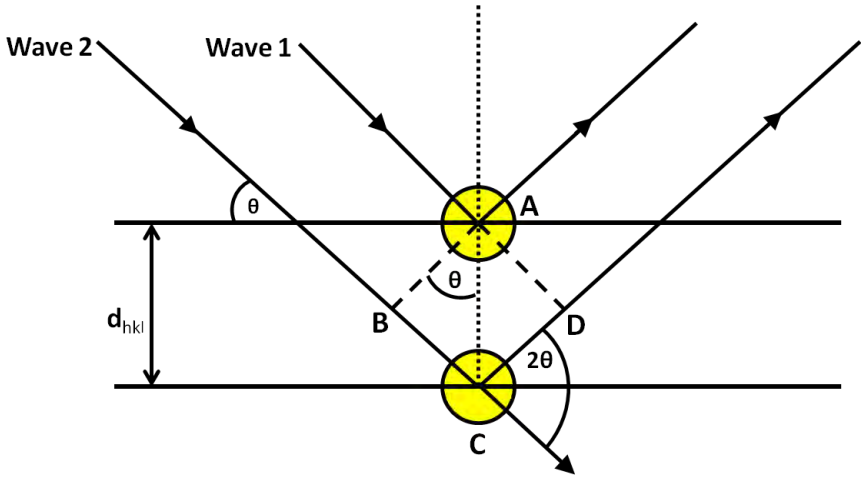

Figure 2.5 *– Reflection of X–rays from lattice planes (adapted from reference [3])*

penetrate the surface of crystalline solids and are reflected by the parallel planes within a material. This in turn means that not all reflected waves will travel the same distance before reaching the detector. As shown in figure 2.5, wave 2 has to travel a longer distance (BC+CD) before and after reflection occurs when compared to wave 1. Therefore, the waves scattered by parallel planes will arrive at the detector with a relative phase shift. If the additional distance (BC +CD) travelled by wave 2 is a multiple (*n*) of the X–ray wavelength (λ), then wave 1 and 2 will be in phase, resulting in constructive interference. For an integral wavelength pathlength difference the following relationship can be calculated:

If

$$(BC+CD) = (d_{hkl}\sin\theta + d_{hkl}\sin\theta) = 2d_{hkl}\sin\theta \qquad (2.2)$$

and

$$n\lambda = (BC+CD) \qquad (2.3)$$

then

$$\text{Bragg's equation:} \quad n\lambda = 2d_{hkl}\sin\theta \qquad (2.4)$$

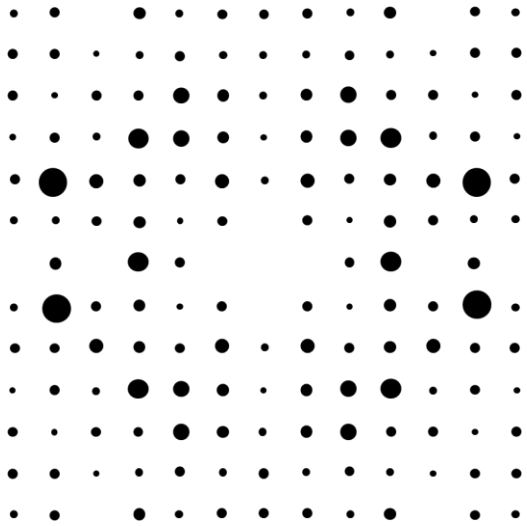

Figure 2.6 *– A simulated single crystal XRD pattern.*

For all non-integer values of n, complete destructive interference results since reflected beams from deeper planes will always be perfectly out of phase. As a result of this, sharp intensity maxima will only arise from a crystal at specific angles of 2θ, with no intensity in between. By focusing X–rays onto a crystalline sample and detecting the scattering over a 2θ range, the sharp intensity maxima can be identified thus structural information about the sample can be gained. This is the basis of an XRD experiment.

2.2.6 Single Crystal X–ray Diffraction

Large crystals (>1μm) of extremely high purity are required for single crystal XRD. Figure 2.6 shows a simulation of a recorded XRD pattern as a single crystal in rotated in an X–ray beam. Numerous XRD patterns are collected in an experiment at specified step intervals. In each pattern, diffraction spots of varied intensity are observed in a reciprocal lattice to which *hkl* values can be assigned. Using this information the geometry, symmetry and atomic structure of a crystal can be determined.

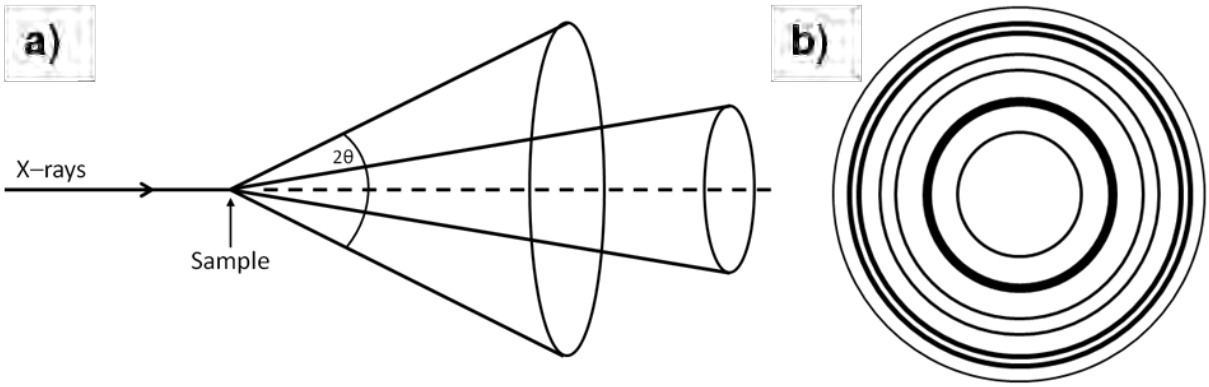

Figure 2.7 *– Diagram illustrating a) the diffraction cones produced from a polycrystalline sample and b) the detected diffraction rings (adapted from reference [5]).*

2.2.7 Powder X-ray Diffraction

Powder (or polycrystalline) samples effectively contain an infinite number of crystallites arranged in all possible orientations. X–rays focussed onto a powder sample will, therefore, be diffracted in all possible directions, resulting in a cone of diffraction spots as illustrated in figure 2.7. The outcome of this effect leads to the systematic overlap of diffraction peaks and a considerable loss in the direct structural data when compared to single crystal diffraction data. However, despite this powder XRD data still contains a wealth of information which can be used in understanding the structure of a crystal. Every crystalline material has its own characteristic powder XRD pattern which can be used to identify the phases present in a sample. Figure 2.8 shows the main components of a powder XRD pattern. The background of a powder XRD pattern is caused by sample effects such as amorphous phases, Compton scattering and X–ray absorbance and florescence. Instrumental factors such as the detector noise and experimental factors such as the sample container used can also contribute to the background. Peak positions are determined by the size, shape and symmetry of the unit cell, as well as the wavelength of X-rays used in the diffraction experiment. The peak positions are directly linked to the distances between the parallel lattice planes in the unit cell by Bragg's law. Instrumental contributions such as zero

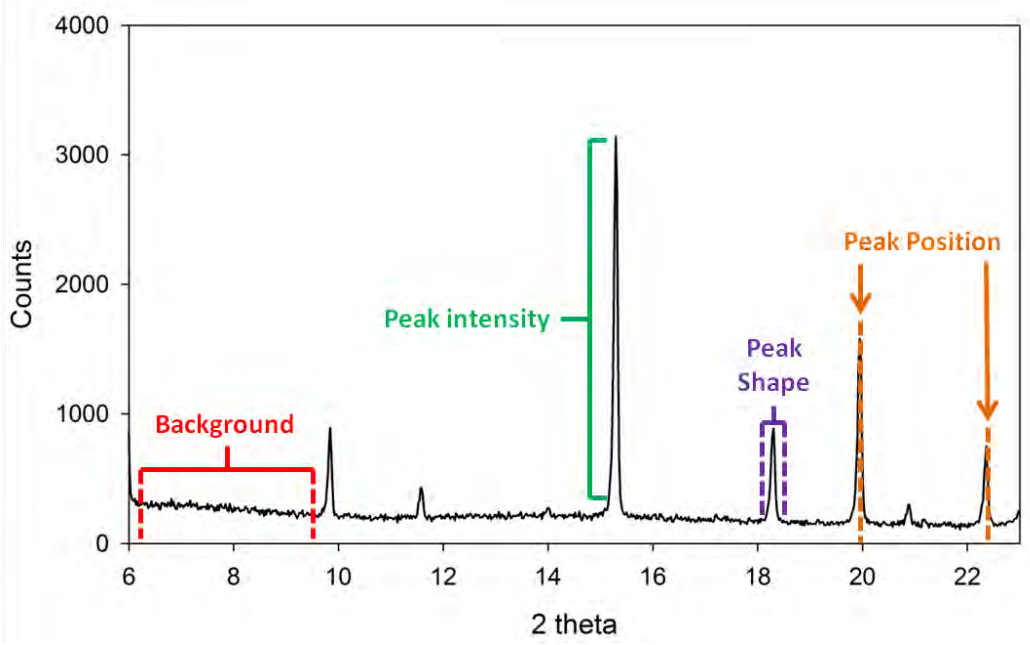

Figure 2.8 – *Components of a typical powder XRD pattern.*

point error and the sample height can cause a shift in the peak positions. Peak intensities are predominantly determined by the type, position and thermal motion of the atoms in a unit cell. However, numerous other factors can also have an effect on the overall intensities. These include instrumental factors such as the intensity of the X-ray source and properties of the detector and experimental factors such as sample scattering ability and data collection time. The size and shape of crystallites can also have a significant effect on the intensity and shape of the diffraction peaks. For certain crystallite morphologies (e.g. needles and plates) preferred orientation can occur where by the crystals align with each other, removing the random orientation and causing distortions of the scattered intensity from the lattice planes in the aligned crystallographic planes. Small crystallites can lead to broadening of the observed diffraction peaks. The relationship between crystallite size and peak width can be calculated using the Scherrer equation.[6-7]

2.2.8 X–ray Diffraction methods

When broken down into its basic essentials, an angular dependent X–ray diffraction experiment requires a monochromatic X–ray source, the sample under investigation and a detector to measure the scattered X–rays. The various aspects of an X–ray diffraction experiment will now be discussed in turn.

2.2.8.1 X–ray Generation

2.2.8.1.1 Laboratory X–ray Sources

In laboratory diffractometers, X–rays are produced by bombarding a metal anode target typically copper (used exclusively in this project), with a high-energy beam of electrons. This high-energy beam causes electrons to be ejected from the core atomic orbitals of the atoms in the metal target. For copper, electrons from both the L (2p) and M (3p) orbitals drop down into the vacant K (1s) orbital causing X–rays to be emitted (figure 2.9a). At high resolution, doublet splitting is observed in the L orbital of copper due to spin multiplicity; therefore in K_α radiation two transitions from the L orbital are observed termed $K_{\alpha1}$ and $K_{\alpha2}$. Background (or bremsstrahlung) X-rays are also produced in the process when the beam of electrons are rapidly slowed upon collision with the copper target (figure 2.9b).

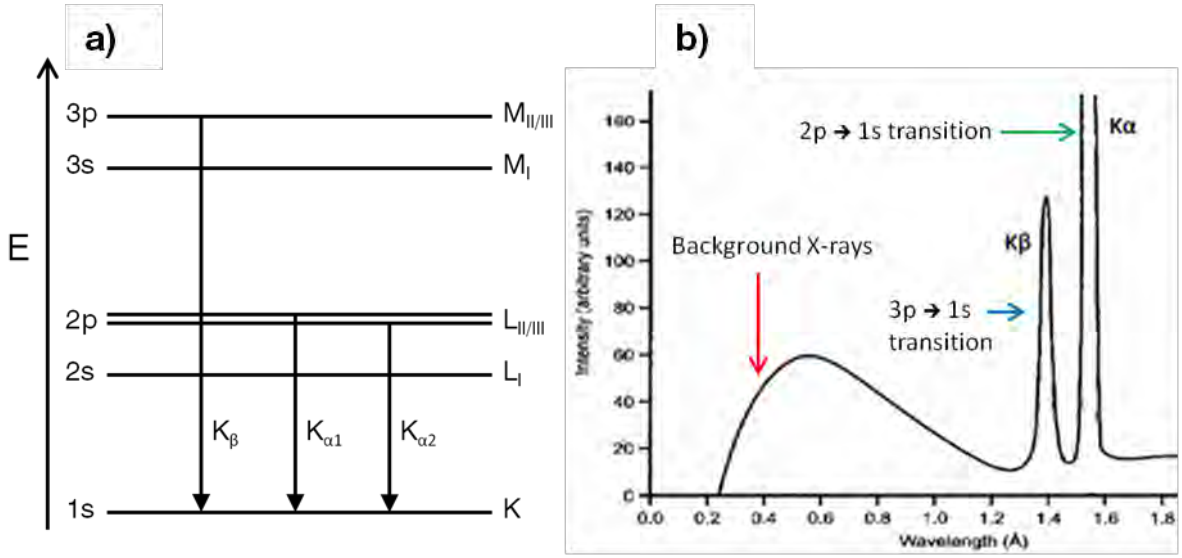

Figure 2.9 *– a) Energy level diagram for a copper atom and b) an X-ray spectrum for a copper target (adapted from reference [3]).*

2.2.8.1.2 Synchrotron X–ray Sources

Synchrotron sources can be used to produce diffraction data of far superior quality (in terms of resolution, signal-to-noise and peak-to-background ratio) when compared to that produced from a laboratory diffractometer. Synchrotron radiation is produced by a process where electrons, generated from an electron gun, are accelerated to near the speed of light using a series of particles accelerators (linear accelerator and booster synchrotron) and injected into a storage ring (figure 2.10). Electrons are then guided around the storage ring by strong magnetic fields. A storage ring is made up of several straight segments which are joined together with bending magnets. As the electrons move through the bending magnets, energy is emitted in the form of light. This light is then channelled out through tangential beamlines and optimised for specific experiments. In modern synchrotron sources, magnetic devices called insertion devices are placed in the straight sections of the storage beam to give the synchrotron radiation specific enhanced properties. One example of such a device is an undulator. These sections use alternating magnetic fields that cause

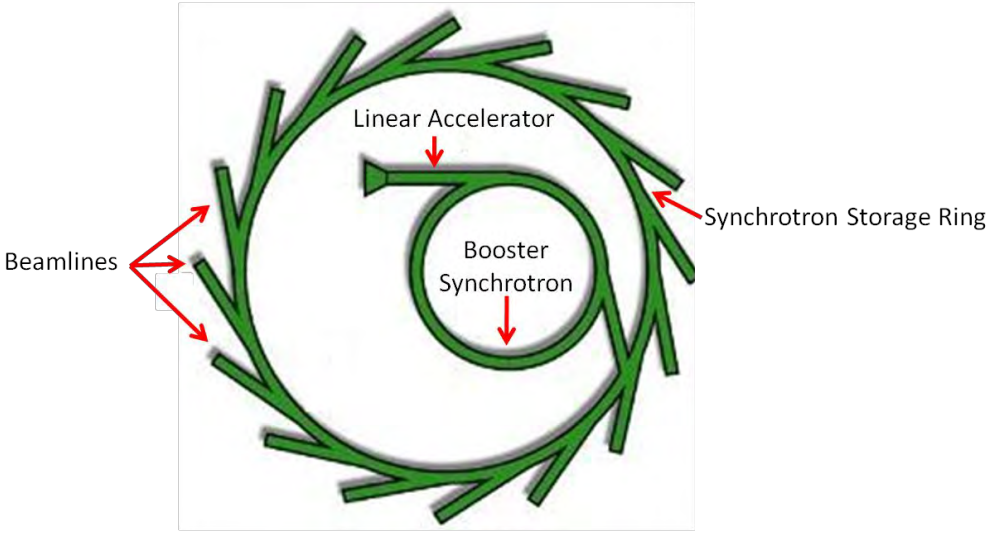

Figure 2.10 *– A schematic diagram of a synchrotron source (adapted from reference [8]).*

the path of electrons to oscillate. This oscillating motion leads to a narrow beam of very intense X–rays, perfect for diffraction measurements. In this project two different synchrotron beamlines were used at the Diamond Light Source in Oxfordshire, UK. Beamlines I11 ($\lambda \approx 0.82$ Å) and I19 ($\lambda = 0.68890$ Å) were used to collect high resolution powder and single crystal XRD data, respectfully (see sections 2.2.8.4.2 and 2.2.8.4.3).

2.2.8.2 Monochromation

2.2.8.2.1 Monochromation of Laboratory X–rays

Monochromation is required for XRD in order to produce a single wavelength of focused radiation. Radiation produced from a metal anode source contains a continuous spectrum of X–rays due to the many different electronic transitions into the metal target's atomic core. Monochromators are used to isolate the most intense part of the X–ray spectrum, $K_{\alpha 1}$ ($\lambda = 1.5406$ Å) in the case of copper. Two different types of monochromators are commonly used in laboratory diffractometers. Crystal monochromators typically use single crystals of either silicon or germanium to set a particular orientation, θ_m in the beam so that the desired

X–ray wavelength satisfies the Bragg equation. Göbel Mirror monochromators use multilayer crystals manufactured in a parabolic shape to cause divergent beam intercepting the mirror at different points into a parallel beam.

2.2.8.2.2 Monochromation of Synchrotron X–rays

At a synchrotron source, monochromators are used to select a specific wavelength from a polychromatic beam. As shown in figure 2.11, double-crystal arrangements are used in order to preserve the direction of the incident beam. Single crystal silicon is usually used in synchrotron monochromators due its smaller Darwin width, high crystal purity and excellent thermal properties in the intense beam.

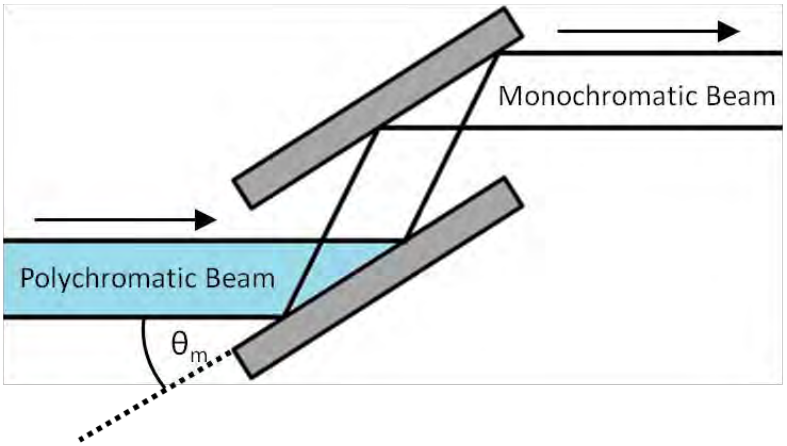

Figure 2.11 *- Double-crystal arrangement used in synchrotron monochromators (adapted from reference [3]).*

2.2.8.3 Detectors

Four different types of detectors where used in this project to detect scattered X–rays. The Braun position sensitive detector (PSD) is a gas proportional device that measures the induced electrical current when the gas molecules are ionised by scattered X–rays inside the charged ionisation chamber. This type of detector was exclusively used for collecting diffraction data in laboratory experiments. The multi-analysing crystal (MAC) detector

consists of a series of individual scintillation counters that generate photons of light in response to the scattered X-rays. Photomultiplier tubes then convert the emitted light into an electronic signal which is measured. Semiconductor PSD's are analogue devices that detect changes in the photosensitive PIN diode surface resistance to calculate the position of the scattered X-rays. Charged-coupled device (CCD) or 'area' detectors are digital devices that consist of an array of closely spaced photosensitive metal-oxide semiconductor (MOS) diodes. Individual MOS diodes are excited by scattered X-rays which can store and transfer positional information using packets of charge.

2.2.8.4 Instrumental Equipment and Configurations

2.2.8.4.1 Siemens D5000 Laboratory Diffractometer

All laboratory powder XRD data collected in this research was done using a Siemens D5000 diffractometer (figure 2.12) operating in capillary transmission (Debye-Scherrer) mode. Copper $K_{\alpha 1}$ radiation ($\lambda = 1.5406$ Å) was isolated and focused into a convergent beam using a germanium crystal monochromator. Samples were loaded into sealed borosilicate capillaries, mounted and aligned using the goniometer and rotated in the plane perpendicular to the X–ray beam. X–ray scattering was detected by a Braun PSD which rotated through 2θ with a step size of $\sim 0.02°$. An Oxford cryostream was mounted over the sample for variable-temperature experiments.

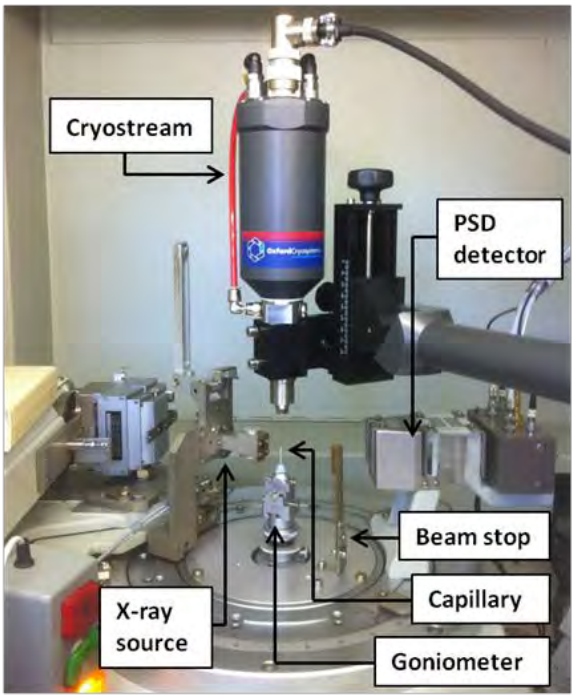

Figure 2.12 *– Siemens D5000 X-ray diffractometer*

2.2.8.4.2 Synchrotron Beamline I11 – High Resolution Powder Diffraction

Beamline I11 at the Diamond synchrotron light source was used in this project to collect high resolution powder diffraction data ($\lambda \approx 0.82$ Å). Samples were loaded into sealed borosilicate capillaries, mounted and aligned in brass capillary holders and rotated in the plane perpendicular to the X–ray beam. Two different detectors were used on this beamline to detect X–ray scattering. For monitoring fast chemical processes, the PSD detector was used which could collect powder XRD patterns every 2 seconds (figure 2.13). For longer data collection scans of better quality, the MAC detector was used with a step size of ~0.001°.[9] An Oxford cryostream was mounted over the sample capillaries for variable-temperature experiments.

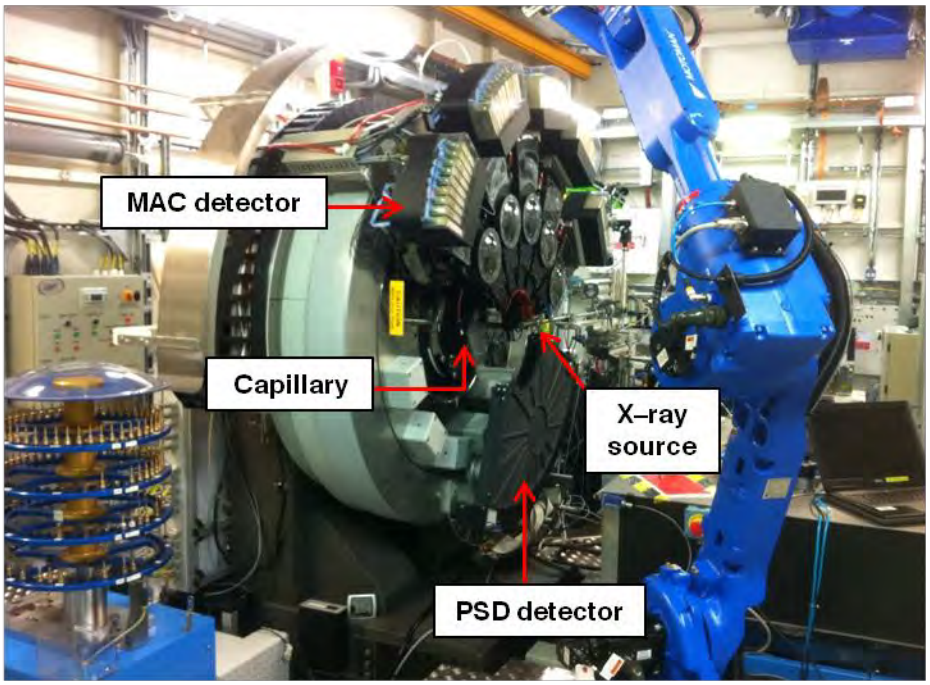

Figure 2.13 *– Experimental hutch of the high resolution powder diffraction beamline (I11) at the Diamond synchrotron light source.*

2.2.8.4.3 Synchrotron Beamline I19 –Single Crystal Diffraction

Beamline I19 at the Diamond synchrotron light source was used in this project to collect high resolution single crystal diffraction data (Rigaku Saturn724+ diffractometer, $\lambda = 0.6889$ Å). Large single crystals were mounted in a loop on a goniometer and rotated in the X–ray beam. X-ray scattering was detected by a CCD area detector (figure 2.14). All data collected at beamline I19 was done so through rapid access beamtime by Anna Warren.

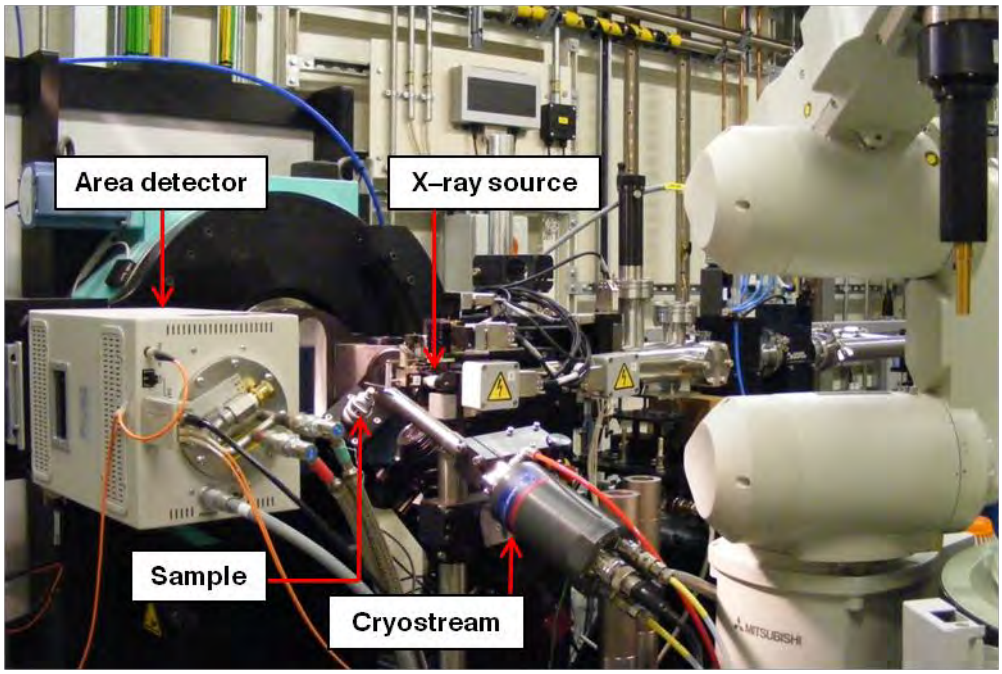

Figure 2.14 *– Experimental hutch of the small molecule single crystal diffraction beamline (I19) at the Diamond synchrotron light source.*

2.2.9 Analysis of Diffraction Data

As mentioned in sections 2.2.4 and 2.2.5, structural information of a crystalline material can be gained from analysing the diffraction peaks detected in a XRD experiment. Using a mathematical process known as Fourier transformation, an atomic structural image can be produced from a scattering pattern. Although individual wave amplitudes are measured (relative peak intensities are proportional to the square of the amplitude) in an X-ray scattering pattern, the relative wave phases are lost. This is known as the phase problem and without knowing the phases of the scattered X-rays a direct Fourier transformation cannot be made.

2.2.9.1 Rietveld Method

One way of analysing Bragg peaks in a powder XRD pattern is through the Rietveld method. In the 1960s, H. M. Rietveld [10-11] showed that it was possible to characterise and refine crystal structures using an approximate structural model, which is then modified in an iterative process so that the calculated diffraction pattern from the model structure closely resembles that of the observed diffraction pattern. A model structure is constructed from parameters that describe i) the unit cell size, shape and symmetry, ii) the atomic positions, occupancy and thermal motion and iii) experimental parameters that define the peak profile and background shape. These parameters (except the unit cell symmetry; the space group is fixed) are then modified using the least-squares method until the difference between the calculated and observed diffraction patterns is minimised.

The residual S_y, the function optimised during the least-squares method, may be expressed as:

$$S_y = \sum_i \omega_i \left(y_i(obs) - y_i(calc)\right)^2 \qquad (2.5)$$

where $\omega_i = 1/\, y_i(obs)$

$y_i(obs) =$ observed intensity at the ith step

$y_i(calc) =$ calculated intensity at the ith step

Determination of whether a refinement has been successful is an important part of Rietveld method. One way of doing this is by visual inspection of the Rietveld plot (figure 2.15). For a perfect fit, the difference line would be completely flat. Another way of doing this is by considering the numerical values known as *R*-factors. The weighted-profile *R*-factor, R_{wp}, is a statistical value based on the process of convergence between the calculated and

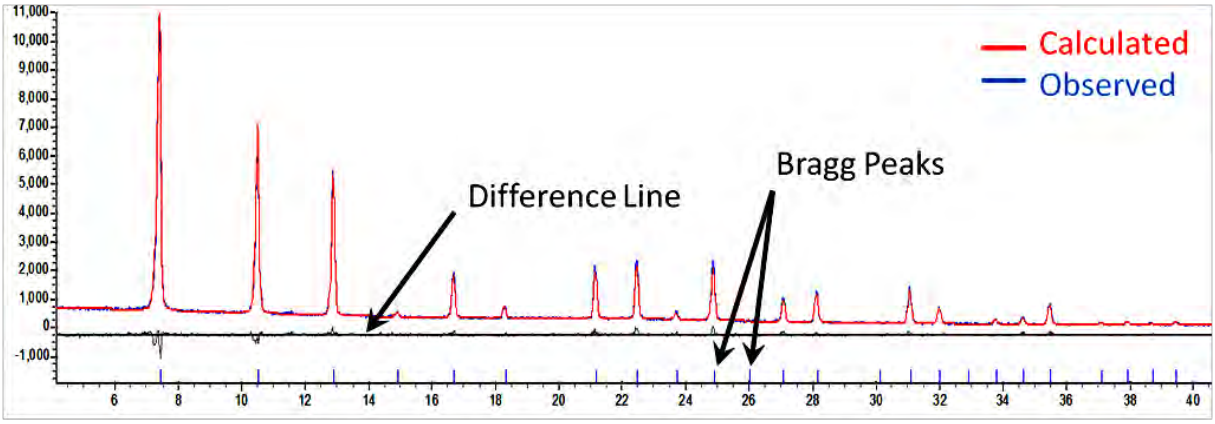

Figure 2.15 *– An example of a Rietveld refinement plot*

observed diffraction patterns:

$$R_{wp} = 100\left[\frac{\sum w_i[y_i(obs)-y_i(calc)]^2}{\sum w_i[y_i(obs)]^2}\right]^{\frac{1}{2}} \quad (2.6)$$

As the refinement progresses, the R_{wp} value should get closer to the expected *R*-factor, R_{exp}, which is the best possible *R*-value for a data set based on the data quality:

$$R_{exp} = 100\left[\frac{N-P-C}{\sum w_i[y_i(obs)]^2}\right]^{\frac{1}{2}} \quad (2.7)$$

where N = number of observations

P = number of refined parameters

C = number of constraints used

χ^2 is another useful the value that gives an indication of the 'goodness if fit' for a refinement:

$$\chi^2 = \left(\frac{R_{wp}}{R_{exp}}\right)^2 \quad (2.8)$$

Acceptable refinements will have a χ^2 value of close to 1. However, small values of χ^2 can also be produced when the errors associated with the structural model are outweighed by

the errors in poor quality data and for data sets with high backgrounds. It is worth noting that application of good chemical knowledge is essential in the refinement process. When carrying out structural analysis, a refinement can fall into a 'false minima' where by the difference between the calculated and observed diffraction pattern is reduced but the calculated structural model becomes chemically unrealistic.

2.2.9.2 Pawley Method

Derived from the Rietveld method in the 1980s, the Pawley method is a technique that is used for calculating the unit cell parameters of a crystalline material.[12] Other useful information such as the peak shape and integrated peak intensities can also be gained from this method but not the unit cell structure. As in the Rietveld method, the difference between the observed and calculated diffraction profiles is minimised using the least squares procedure. However, in the Pawley method the calculated peak intensity of each peak is refined until it closely matches that of the observed intensity, rather than being calculated from a structural model. A calculated diffraction pattern is generated using non-refineable parameters such as the radiation wavelength and the unit cell symmetry and refineable parameters such as the unit cell parameters, instrumental zero point error, peak shape and background. All analysis of the powder diffraction data was done so using the computer software Topas.[13]

2.2.9.3 Direct Methods

Single crystal data was analysed using direct methods in this thesis. In this method, an approximate structural model is produced by analysing the position, symmetry and intensity of the observed diffraction spots. Difference Fourier maps are then used to locate areas of

unassigned electron density and improve the calculated structural model. Least squares refinement is then used to minimise the difference between the calculated and observed diffraction patterns. At the end of a successful refinement, no significant features should remain in the Fourier difference map. All analysis of the single crystal data was done so using the computer software CrystalClear-SM Expert 2.0 r13 [14] and ShelXS-97. [15]

2.2.10 Humidity Cell

As part of the funding arrangement for this PhD studentship, a custom humidity cell was developed for beamline I11 at the Diamond Light Source. This enabled synchrotron powder XRD data to be collected for zeolites samples which were exposed to various humidified environments. In order to control the amount of moisture in the carrier gas, a humidity gas board was produced so that the desired humidity could be established before it reached the sample (figure 2.16). For humidities of greater than 5%, the Ansyco Sycos H-Hot temperature controller was utilised which used a heated water reservoir to determine the amount of moisture in the synthetic air (21% O_2 /79% N_2) carrier gas. For humidities of less than 5%, wet nitrogen and dry synthetic air was mixed manually. All pipelines were purged with the humidified carrier gas to avoid sample contamination from atmospheric moisture. After a desired humidity was established, the carrier gas was directed to the humidity cell (figure 2.17). The humidity cell was loaded with sample inside a dry glove box, sealed using two gas taps and transported to the beamline. The cell was mounted and aligned using the goniometer in the synchrotron beam. Samples were exposed to the various humidified gas environments and powder synchrotron XRD data were collected.

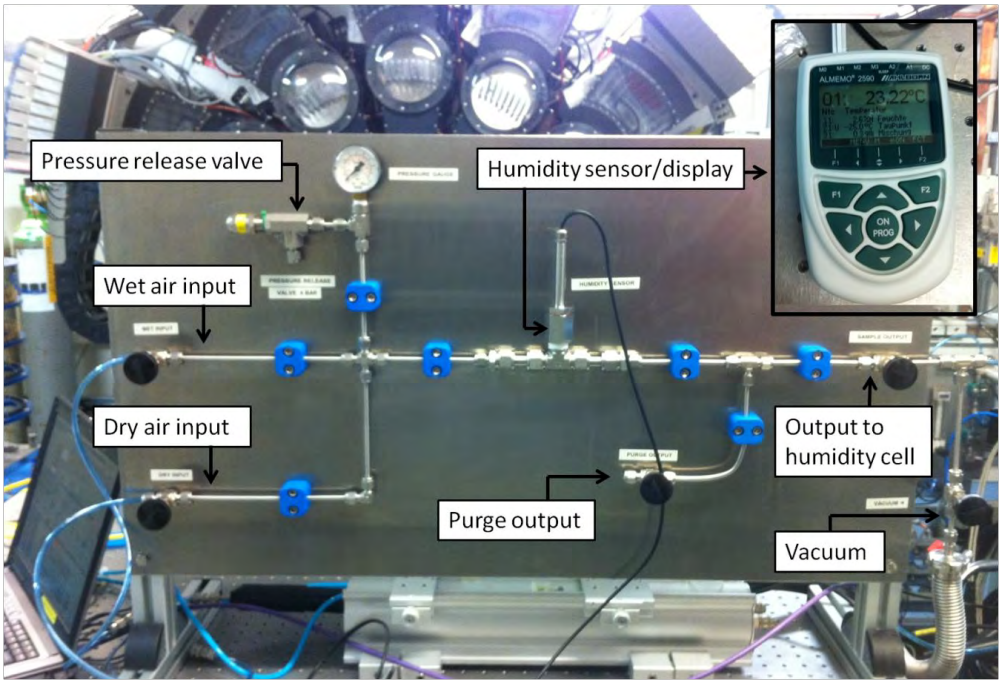

Figure 2.16 *– Image of the humidity gas board.*

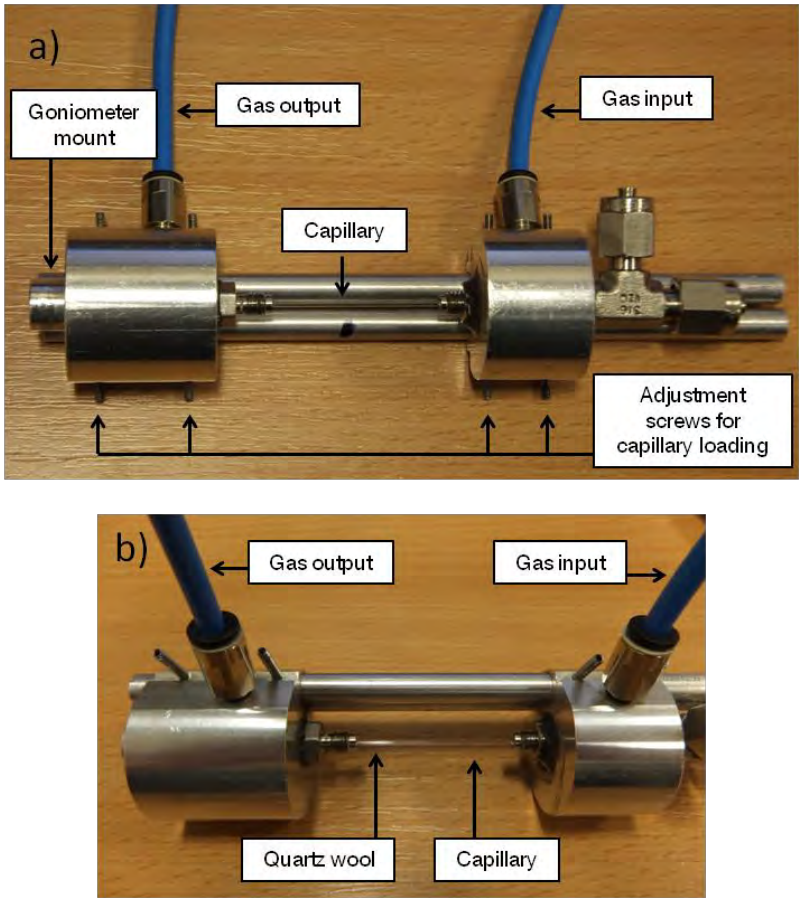

Figure 2.17 *– Images of the humidity cell from a a) top down and b) side on view.*

2.2.3 X–ray Florescence Spectroscopy

X–ray florescence (XRF) spectroscopy is an analytical technique used to determine the elemental composition of a material. In this technique, core electrons are removed from atoms by bombarding a sample with beam of incident X–rays. Electrons from higher energy levels then drop down into lower energy levels and a photon is emitted. The energy released during this process can either be emitted in the form of X–rays or transferred to another atomic shell known as the Auger effect. All elements have a unique set of energy levels that can be used to characterise the emitted photons. By recording the energy and intensity of the emitted energy during the process above, an X–ray spectrum is acquired that contains set of characteristic peaks. The energy of these peaks leads to the identification of the elements present in a material, while the peak intensities are relevant to the elemental concentration. All XRF data presented in this research was collected on a Bruker S8 Tiger spectrometer.

2.4 Infrared Spectroscopy

Infrared (IR) spectroscopy is a common technique used for identifying chemical functional groups and therefore chemical compounds in materials. IR radiation is of the appropriate order to cause vibrational transitions in certain molecules.[16] If a photon of energy is equal to that of the energy gap between two vibrational states, the photon may be absorbed causing the molecule to vibrate. Vibrational motions are only IR active if a change in the molecular dipole moment is observed. As a result, certain vibrations can be deemed completely forbidden by molecular symmetry.

An IR spectrum is produced by focusing an incident beam of radiation through a sample cell and measuring its resulting absorbance over a range of wavelengths. Absorbance from the sample cell is then compared to the absorbance from blank cell and plotted as a function of wavelength:

$$A_\lambda = -\log_{10}\left(\frac{I}{I_0}\right) \quad (2.9)$$

where A_λ = absorbance at a specific wavelength

I = intensity of beam after passing through the sample

I_o = intensity of beam after passing through the blank cell

In Fourier transform infrared (FTIR) spectroscopy the sample is exposed to all wavelengths of IR radiation simultaneously. Fourier transformation is then used to mathematically separate the resulting waveform into its component wavelengths. FTIR data was collected in this project using a Thermo Nicolet 8600 Fourier Transform Infrared (FTIR) spectrometer. Inert gas measurements were performed in an Specac Golden gate ATR sample cell which allowed inert loading and atmospheric control during measurements under argon.

2.5 Raman Spectroscopy

Raman spectroscopy is a spectroscopic technique based upon the inelastic scattering of light.[17] In Raman spectroscopy, the sample is irradiated with a monochromic beam, usually generated from a laser. Upon interaction with the beam, photons are absorbed by the molecules in the sample causing their electrons to be excited into a virtual state. However, this virtual state is short lived and the photons are quickly emitted. In the majority of cases elastic scattering takes place where by the energy of the absorbed and emitted photon is equal (figure 2.18). This scattering process is known as Rayleigh scattering. Inelastic

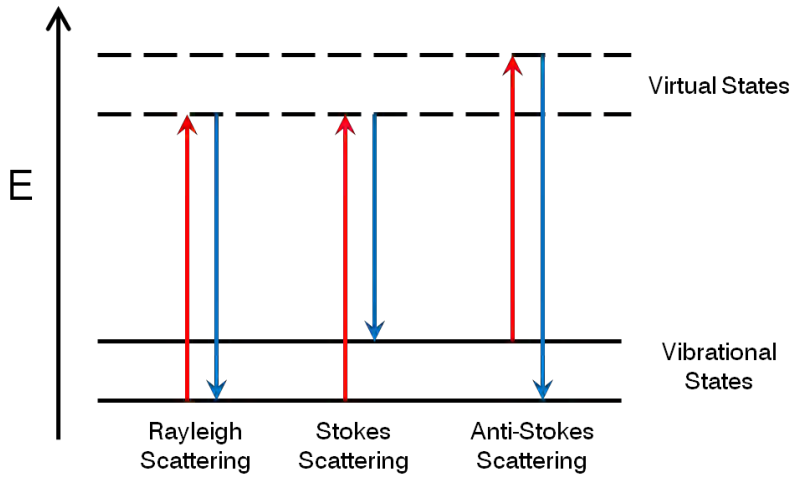

Figure 2.18 *– Diagram illustrating the Rayleigh, Stokes and Anti–Stokes scattering processes.*

scattering can also take place where by energy is transferred between the photon and molecule, resulting in nuclear motion in some cases. If the energy of the absorbed photon is greater than that of the emitted photon, the molecule is promoted to a higher vibrational state ($\Delta v = +1$). This scattering process is known as Stokes scattering. If the energy of absorbed photon is less than that of the emitted photon, the molecule is demoted to a lower vibrational level ($\Delta v = -1$). This scattering process is known as Anti-Stokes scattering. It is this shift in vibrational energy that is detected in Raman spectroscopy. A Raman spectrum consists of the intensity of the scattered radiation plotted as a function of wavenumber. Molecular vibrations induced by inelastic scattering can only be Raman active if there is a change in the polarisability of the molecule. The symmetry of a molecule determines which vibrations are Raman active. Symmetric vibrations are much more intense when compared to anti-symmetric vibrations in Raman spectroscopy.

Raman spectra were collected using a Renishaw Invia reflex Raman microscope. 488 and 633 nm lasers were focused through a long working distance 20x objective to give a spot

size of around 50 μm with a beam power of 20 mW. Inert gas measurements were performed in an Instec HCS621C sample cell with a fused quartz; the cell allowed inert loading and atmospheric control during measurements under argon.

2.6 Thermogravimetric Analysis and Mass Spectrometry

Thermogravimetric analysis (TGA) and mass spectrometry was used in combination in this research to aid in determining the contents of the zeolite frameworks.

2.6.1 TGA

TGA is technique used for the monitoring the mass changes in a material as the temperature is varied. A TGA analyser consists of an extremely accurate balance (±0.0005g) mounted inside a furnace which continually records the mass of a sample during the experiment. All TGA data was collected using a Netzsch STA F1 Jupiter analyser in this project. Small quantities of sample (~ 30 mg) was placed in an alumina crucible and mounted on a fine platinum balance inside the TGA analyser. Samples were then heated and cooled at 5 K/min in the desired temperature range.

2.6.2 Mass Spectrometry

Mass spectroscopy is an analytical technique that is used to determine the elemental composition of a sample. When an electromagnetic field is applied to a charged particle in flight, the trajectory of the ion is distorted.[18] The amount of distortion away from the original trajectory depends upon the mass of the ion and its relative charge. These combined factors are known as the mass/charge ratio (m/z). If the strength of the applied magnetic field is varied, the trajectory of the deflected ion(s) can also be manipulated. This is the

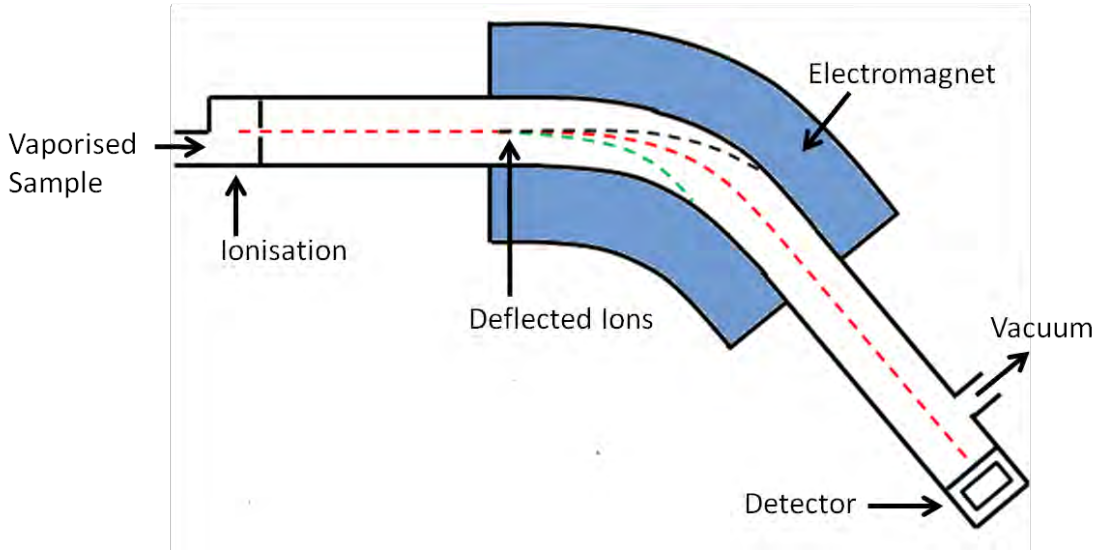

Figure 2.19 *– Schematic diagram of a mass spectrometer illustrating the separation of cations with different m/z values.*

basis of mass spectroscopy which consists of three main processes: ionisation, separation and detection. These three processes will now be discussed.

Vaporised sample is passed into an ionisation chamber to convert the atoms/molecules into ionic species. Electron ionisation is achieved by bombarding the analyte atoms/molecules with an electron beam to remove electrons and produce singly charged cations. Exclusively single charge species are preferable in mass spectroscopy as the relative abundance of ions with a specific *m*/*z* ratio is detected. Multiple ionisation is usually avoided by tuning the energy of the electron beam. Ionised species are accelerated out of the ionisation chamber using a voltage and focused toward the electromagnet under vacuum. A high vacuum is essential during the mass selection process so that the sample cations do not collide with other species. Various cations are deflected by different amounts in the magnetic field depending upon their *m*/*z* ratio. As illustrated in figure 2.19 lighter cations will be deflected by a greater amount when compared to heavier cations with the same charge in a constant

magnetic field. By varying the strength of the magnetic field, the trajectory of the different cations with a specific *m*/*z* values are brought into line with the detector. Cations are detected by measuring the electric current generated when ions collide with the detector and comparing it to the strength of the applied magnetic field. The current is proportional to the number ions arriving at the detector and used to calculate the relative abundance at each *m*/*z* value. Mass spectrometry data was collected in this project using the Netzsch QMS 403 C Aëolos. All exhaust gases emitted from the TGA analyser where vented into the mass spectrometer to analyse the sample contents.

2.7 SEM and STEM Imaging

Scanning electron microscopy (SEM)[19] and scanning transmission electron microscopy (STEM)[20] are two similar techniques used to produce high resolution images on a very small scale (100 μm – 1 nm). In both techniques, a beam of incident electrons is scanned across a segment of a thin sample and the scattered electrons are detected. One way of producing a SEM image is by detecting the low energy secondary electrons emitted from the surface of the sample. Secondary electrons are produced when electrons in the sample are excited by the incident beam. These excited electrons then moves to the surface of the sample and are emitted if they have sufficient energy. Local variations in the detected secondary electron density produce the contrast in the SEM image.

In STEM, the scattered and un-scattered electrons transmitted through the thin sample are detected. Depending on what type of image is required from the sample, different types of the transmitted electrons are detected. Incoherently scattered electrons are used in high-angle annular dark field (HAADF) STEM to produce images where contrast in related to atomic number (Z^2). In these images atoms with higher atomic numbers appear lighter

when compared to atoms with lower atomic number or areas of no electron density which will appear darker.

All SEM images presented in this thesis were collected using a Philips XL30 ESEM–FEG operating at 10 KeV. All HAADF–STEM images were collected by Alvaro Mayoral at the Laboratorio de Microscopias Avanzadas in the Institute of Nanoscience of Aragon, Spain using a XFEG FEI TITAN operating at 60–300 KV.

2.8 References

1. C. Giacovazzo, H. L. Monaco, D. Viterbo, F. Scordari, G. Gilli, G. Zanotti and M. Catti, *Fundamentals of Crystallography*, Oxford Science Publications, 1998.
2. V. K. Pecharsky and P. Y. Zavali, *Fundamentals of Powder Diffraction and Structural Characterization of Materials*, 2 edn., Springer, 2009.
3. R. E. Dinnebier and S. J. L. Billinge, *Powder diffraction - Theory and Practise*, RSC Publishing, 2008.
4. W. L. Bragg, Proceedings of the Royal Society of London. Series A, 89, 248- 277, 1913.
5. M. T. Weller, *Inorganic Materials Chemistry*, Oxford University Press Inc., 1994.
6. P. Scherrer, *Nachr. Ges. Wiss. Gottingen*, 1918, **26**, 98-100.
7. J. I. Langford and A. J. C. Wilson, *J. Appl. Cryst.*, 1978, **11**, 102-113.
8. www.diamond.ac.uk.
9. S. P. Thompson, J. E. Parker, J. Potter, T. P. Hill, A. Birt, T. M. Cobb, F. Yuan and C. C. Tang, *Rev. Sci. Instrum.*, 2009, **80**, 075107.
10. H. M. Rietveld, *J. Applied Crystallography*, 1969, **65**.
11. R. A. Young, *The Rietveld Method*, Oxford University Press, 1993.

12. G. S. Pawley, *J. Appl. Cryst.*, 1980, **13**, 630-633.

13. A. Coelho, Topas Academic Version 4.1., 2007

14. Sendagaya and Shibuya-Ku, CrystalClear-SM Expert 2.0 r13, Rigaku Corporation, 4-14-4, 2011

15. G. M. Sheldrick, *Acta Cryst.*, 2008, 112-122.

16. W. Brugel, *An Introduction to Infrared Spectroscopy*, Methuen & Co. Ltd, 1962.

17. T. R. Gilson and P. J. Hendra, *Laser Raman Spectroscopy*, Wiley-Interscience, 1971.

18. I. Howe, H. Williams and R. D. Bowen, *Mass Spectrometry Principles and Application*, 2nd edn., McGrow-Hill Int. Book Company, 1981.

19. A. J. Bond and M. V. Mirkin, *Scanning Electron Microscopy*, Marcel Dekker, 2001.

20. D. B. Williams and C. B. Carter, *Transmission Electron Microscopy - A Textbook for Materials Science*, Springer, 2009.

Chapter 3 – Cation Modification

3.1 Introduction

As discussed in chapter 1, considerable research on NTE in purely siliceous zeolite structures has been carried out in recent years but relatively little attention has been focused on aluminium-containing structures. Using powder synchrotron XRD, Couves *et al*.[1] reported that zeolite Na-X showed NTE behaviour over a sub-ambient temperature range, but no structural details were provided. Other studies on zeolites Ba-Y,[2] HZSM-5,[3] and Pb- and Cd-RHO[4] have shown that varying the water content in the zeolitic pores can have a significant effect on the thermal expansion behaviour. In this chapter the effect of modifying the zeolite pore contents on the thermal expansion behaviour will be discussed. The hydrated and dehydrated forms of lithium- (Li-), sodium- (Na-), silver- (Ag-), potassium- (K-), rubidium- ($Rb_{0.79}Na_{0.21}$-) and caesium- ($Cs_{0.58}Na_{0.42}$-) exchanged zeolite A were investigated as well as the purely siliceous analogue ITQ-29. Data were collected in the sub-ambient temperature range of 100–300 K to avoid compositional changes from dehydration.

3.1.1 ITQ-29

Zeolites with the LTA topology have been widely applied over the past few decades in various commercial processes including in detergents and molecular sieving, but not in the petrochemicals industry. Poor catalytic activity, hydrothermal stability and low hydrophobicity are common properties of zeolites with a low Si/Al ratio. Before 2004, various research groups tried to prepare highly siliceous LTA-zeolites but only managed to produce structures with a maximum Si/Al ratio of three.[5-8] Later work by Corma and co-workers[9] reported that the purely siliceous LTA structure, named ITQ-29, could be

synthesised using a supramolecular organic structure directing agent. Since this publication, significant research[10-16] has focused on the diffusion and adsorption properties of ITQ-29 for its use as a petroleum-refinement material. Zeolites that control diffusional access through an 8-ring are of particular interest to this industry as they are useful for the separation of gases and small hydrocarbons. Contrary to expectation, lower diffusion rates were reported for ITQ-29 when compared to Na/Ca zeolite A due to large a contraction in the 8-ring diameter.[10-11] However, this small 8-ring has been shown to be useful for separating hydrogen from other small molecules.[12]

Despite the vast amount of literature on siliceous zeolites, the thermal expansion behaviour of ITQ-29 has not previously been reported. ITQ-29 was studied in this project as a comparison to the various cation-exchanged forms of zeolite A. No cations or water molecules occupy the pores of ITQ-29 as its framework bears no charge. This allowed the thermal expansion behaviour of the LTA structure to be investigated when the pores were vacant.

3.1.2 Silver-Exchanged Zeolite A

Silver-containing zeolites have attracted a considerable amount of interest in recent times due to their ease of synthesis and interesting properties. In 1962 Rálek *et al.*[17] reported that Ag-A underwent several colour changes upon dehydration from white, to yellow, to orange and finally to brick red. This unusual physical property was further investigated by a number of research groups[18-20] and lead to the suggestion that dehydrated Ag-A could have a potential application in moisture sensing.[21] Seifert *et al.*[19-20] attributed the yellow colour in dehydrated Ag-A to a charge transfer between the lone pair of the framework oxygens to the empty 5s orbital of the Ag^{+} cations located in the 4-ring position. The red colour was

assigned to the coordination of Ag^+ cations at the 4-ring site to other Ag^+ cations in close proximity.[20]

Zeolite A is not the only silver-exchanged zeolite that has attracted a vast amount of interest. Other silver-exchanged zeolite structures types, such as FAU,[22] have been studied due to their antimicrobial properties. Increasing public awareness and concern over sanitation in hospitals and kitchens has lead to the development of new safe and cost-effective antimicrobial materials. The ability of silver to kill and prevent the growth of microorganisms has been known for centuries and has recently been incorporated into zeolite structures for their application in food packaging,[23] culinary equipment,[24] medical implants[25] and dental treatments.[26]

The presence of silver clusters within silver zeolites has received significant interest in recent times due to their potential application in a range of modern day contexts. Silver clusters within zeolites have been shown to have a catalytic ability to photochemically split water molecules[27-29] and used to artificially mimic photosynthesis.[30-31] Calzaferri[29] reported that silver zeolite L (LTL) containing silver chloride clusters can be deposited on a conducting support and used to photo-catalyse the oxidation of water to O_2. Other silver halide clusters have been shown to have photo-stimulated luminescence properties which could one day be used in media for erasable optical memory. [32-33]

The formation of silver clusters in silver-exchanged zeolites has been reported to occur in a number of different ways including through dehydration,[18-20, 34-38] interaction with hydrogen gas[39-41] and organic solvents,[42] and exposure to high energy radiation.[43-46] The mechanism of reduction through dehydration has been proposed to occur in two different ways: [36-37] first

the reduction by water upon dehydration (equation 3.1) and secondly through a reaction with the zeolitic framework oxygens (equation 3.2).

$$4\ Ag^{+} + 2H_2O \rightarrow 4\ Ag^{0} + 4\ H^{+} + O_2 \qquad (3.1)$$

$$2\ Ag^{+} + ZO^{2-} \rightarrow 2\ Ag^{0} + \frac{1}{2}O_2 + Z[\ ] \qquad (3.2)$$

where ZO^{2-} is the zeolitic oxygen and Z[ ] is a zeolitic oxygen vacancy.

In 1977, Kim and Seff[35] were the first to suggest that colour changes in dehydrated Ag-A were caused by the formation of uncharged octahedral silver clusters (Ag_6^0) in the β-cages (3.1a). Based on single crystal XRD data, clusters were determined to be in two-thirds of the β-cages and were coordinated by up to eight Ag^+ cations located in the 6-ring.[34-35, 47] Analysis was performed in the cubic space group $Pm\bar{3}m$ (~12 Å unit cell) which ignores Si/Al ordering.

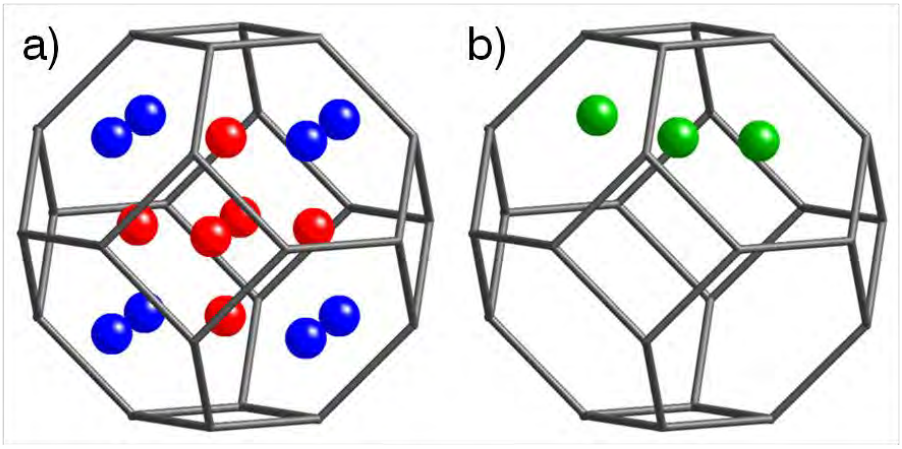

Figure 3.1 *– Proposed silver clusters located in the β-cage of zeolite Ag-A. a) Octahedral Ag^0 cluster (red) co-ordinated to Ag^+ cations in the 6-ring positions (blue). b) Linear Ag_3^{2+} cluster (green).*

Further work by Jacobs *et al.*[37] investigated the reduction of Ag^+ ions within Ag-A and proposed that linear Ag_3^{2+} ($Ag^+ - Ag^0 - Ag^+$) clusters were responsible for the colour changes upon dehydration as the Ag_6^0 clusters proposed by Kim and Seff were improbable. These linear Ag_3^{2+} clusters were understood to consist of two Ag^+ cations that were located in opposing 6-ring sites with one Ag^0 atom positioned in between (figure 3.1b). Using powder XRD, Gellens and co-workers later interpreted the two silver sites from Kim and Seff's model in terms of Ag_3^{2+} clusters and suggested these linear clusters were responsible for the yellow colour. A colour shift from yellow to brick red was then attributed to 2–4 interacting Ag_3^{2+} clusters. ESR spectroscopy finally confirmed the existence of hexasilver clusters by exposing dehydrated Ag-A to hydrogen gas at low temperature.[39-40, 43] The resultant seven-line ESR spectra could only have been caused by the formation of charged highly symmetric hexasilver clusters inside the β-cage and thus confirmed Kim and Seff's model.

3.1.3 Alkali-Metal-Exchanged Zeolite A

Introducing and exchanging various alkali metal cations into LTA zeolites has been shown to have a considerable effect on the framework structure, especially on the diameter of the pores. For example, Na-exchanged zeolite A has an effective 8-ring diameter of ~4 Å and is denoted zeolite 4A. However, K-exchanged zeolite A has a smaller effective diameter of ~3 Å and is denoted zeolite 3A. Due to their ease of synthesis and desirable pore dimensions zeolites with the LTA topology have been widely applied in the separation and purification of gas mixtures. Zeolite 3A is used in the separation of small gas molecules such as ammonia and helium whereas zeolite 4A is used to separate larger molecules including methanol and ethane. Interesting electronic and magnetic properties have also been shown in dehydrated alkali-metal-loaded LTA zeolites due to cluster formation, however, this will not be discussed further in this work.[48] Crystal structures of the hydrated

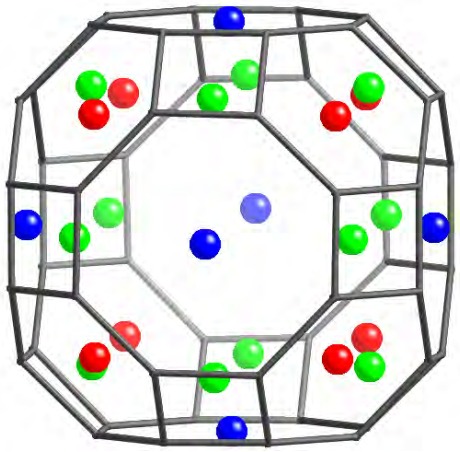

Figure 3.2 *– Diagram illustrating the location of the cations in the α-cage of zeolite A (red = 6R cation, blue = 8R cation and green = 4R cation).*

and dehydrated forms of Li-,[49-50] Na-,[51-52] K-,[53] Rb-[54] and Cs-exchanged[55] zeolite A have all been reported by various research groups since the 1950's. Three common cationic positions have been identified in all the alkali-metal-exchanged systems. Each α-cage contains approximately eight cations in the 6-ring, three cations in the 8-ring and one inside the α-cage near the 4-ring (figure 3.2). Slight variations in the cationic positions were reported upon hydration but the same number of cations remained associated with their respective zeolite rings. Considerable debate on the position of the 4-ring cation has been held in literature with some research groups reporting that the cation is located inside the α-cage with "zero-coordination". Low occupancy of this 4-ring site made assignment of the cation position extremely difficult using Fourier difference mapping, especially in the hydrated systems. Later work by Pluth *et al.* contested the zero-coordinated cation describing the evidence of its existence as 'false'. Using more advanced crystallographic techniques, cations were found to be coordinated to 4-ring oxygens with realistic bond distances.

3.2 Synthesis

3.2.1 Synthesis of ITQ-29

The ITQ-29 sample used in this research was provided by the Corma group in Valencia, Spain.[9]

3.2.2 Synthesis of Zeolite A

Sodium zeolite A (Na-A) was prepared by dissolving 1.44 g of sodium hydroxide in 160 ml of deionised water and dividing the resulting solution into two equal portions.[56] To the first portion, 16.52 g of sodium aluminate was added and the solution was stirred. To the second portion, 30.96 g of sodium metasilicate pentahydrate was added and the solution was stirred under gentle heating. The two resulting solutions were then mixed together in a seeded polymethylpentene container and shaken until homogeneous. This mixture was then heated in a furnace for 5 hours at 372 K (for the first 30 minutes the container was inverted and shaken at 5 minute intervals to ensure good mixing). The resulting zeolite was then washed and filtered before being dried in a furnace at 333 K overnight.

3.2.3 Ion Exchange

Ion exchange reactions with zeolite Na-A were used to prepare the lithium, silver, potassium, rubidium and caesium forms of zeolite A. 4 g of zeolite Na-A was added to 400 ml of the appropriate 0.1 mol dm^{-3} nitrate solution (table 3.1) and stirred under gentle heat (35–45°C) for 24 hours. The resulting zeolite was then filtered and dried overnight. Powder XRD was used to check the crystallinity of the ion-exchanged zeolite and XRF analysis was used to confirm its elemental composition. This whole process was then repeated a number of times to ensure good ion exchange (>95%). Due to silver nitrate being sensitive to light, the

Table 3.1 – *Ion exchange details for the preparation of Li-, Ag-, K-, ($Rb_{0.79}Na_{0.21}$)- and ($Cs_{0.58}Na_{0.42}$)-A.*

Sample	Mass of nitrate (MNO_3)* weighed out (g) / 400 ml of deionised water	No. of ion exchanges	Calculated unit cell formula from XRF results
Li-A	2.76	8	$Li_{92}Na_4(Al_{96}Si_{96}O_{384})$
Ag-A	6.80	2	$Ag_{92}Na_4(Al_{96}Si_{96}O_{384})$
K-A	4.04	8	$K_{93}Na_3(Al_{96}Si_{96}O_{384})$
$Rb_{0.79}Na_{0.21}$-A	5.90	10	$Rb_{76}Na_{20}(Al_{96}Si_{96}O_{384})$
$Cs_{0.58}Na_{0.42}$-A	7.80	10	$Cs_{56}Na_{40}(Al_{96}Si_{96}O_{384})$

* *where M = Li, Ag, K, Rb or Cs*

flask was wrapped in aluminium foil to prevent light affecting the ion-exchange reaction. The high selectivity of zeolite A for silver cations also meant that this reaction was virtually stoichiometric.[57] For the other monovalent cation zeolites, further ion-exchange reactions were required. Full cation exchange was not achieved for $Rb_{0.79}Na_{0.21}$-A and $Cs_{0.58}Na_{0.42}$-A, as the crystallinity of the zeolites greatly deteriorated after more than 10 ion exchanges.

3.2.4 Dehydration

Dehydration of all the zeolites was done by placing a small amount of sample (~2 g) in a quartz tube with a Young's tap attached. The Young's tap was then attached to a vacuum line and the quartz tube placed in a furnace (figure 3.3). Samples were heated at 1 K/min to 423 K, before heating further at 2 K/min to 673 K under standard vacuum (~4×10^{-6} bar). After reaching temperature, samples were kept at 673 K for 12 hours under high vacuum (~5×10^{-9} bar). Dehydrated zeolites were sealed in the evacuated quartz tubes by closing the Young's tap and transported into a dry glove box to be prepared for analysis.

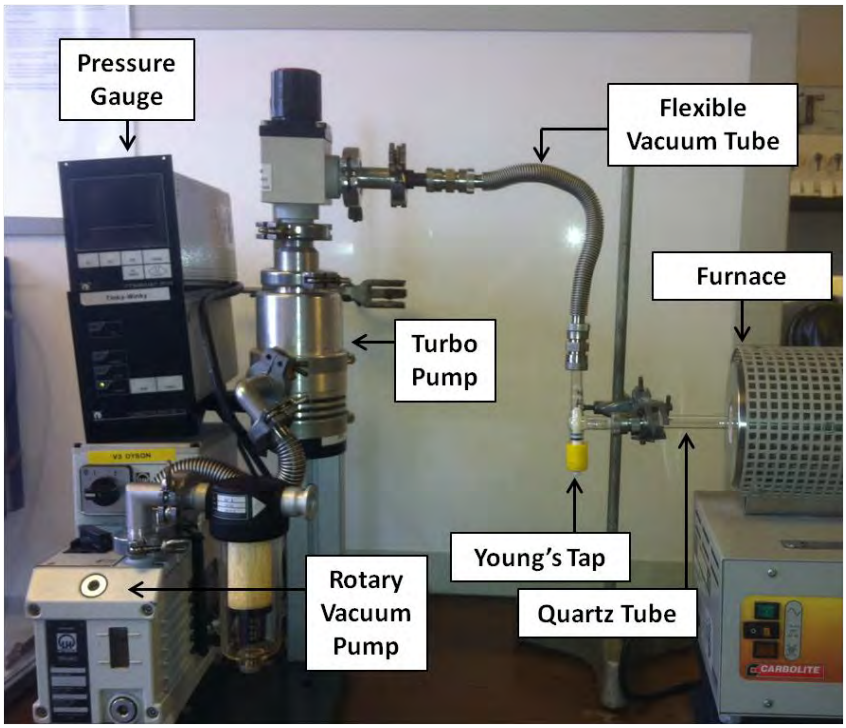

Figure 3.3 *– Apparatus for zeolite dehydration procedure.*

3.3 Results and Discussion

3.3.1 Anhydrous Zeolite LTA Systems

3.3.1.1 Structural and Compositional Analysis of ITQ-29 at 300 K

The crystal structure of ITQ-29 was refined from powder diffraction data collected on the Siemens D5000 laboratory diffractometer using the computer program Topas.[58] Successful Rietveld analysis was performed in the cubic space group $Pm\bar{3}m$ ($\chi^2 = 1.59$, $R_{wp} = 7.29$ %) with a calculated unit cell parameter of $a = 11.853(2)$ Å at 300 K. Figures 3.4 and 3.5 show the refinement fit and crystal structure of ITQ-29 at 300 K, respectively. Table 3.2 shows the refined atomic coordinates and table 3.3 shows selected bond lengths and angles.

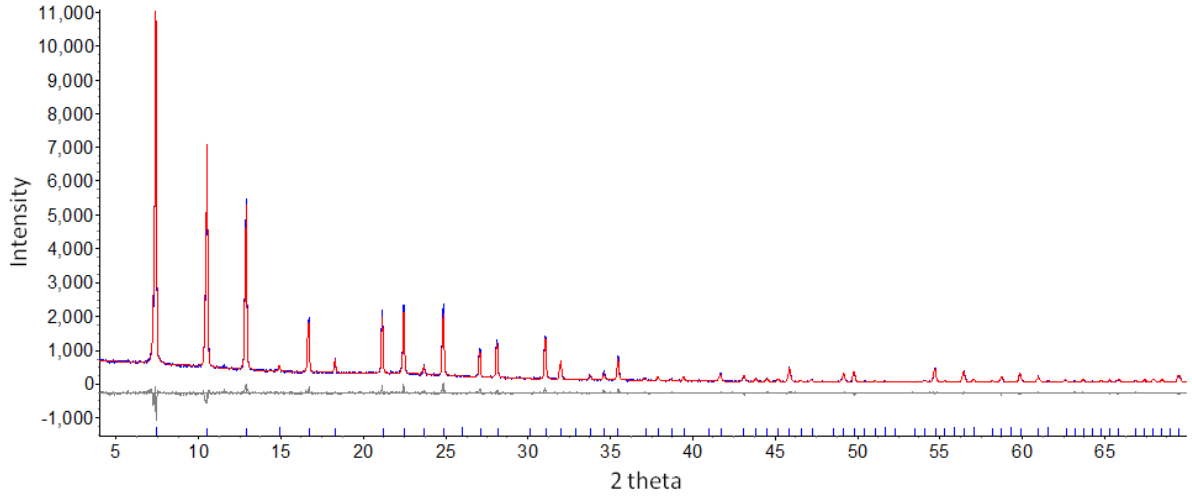

Figure 3.4 *– Rietveld refinement plot of ITQ-29 at 300 K.*

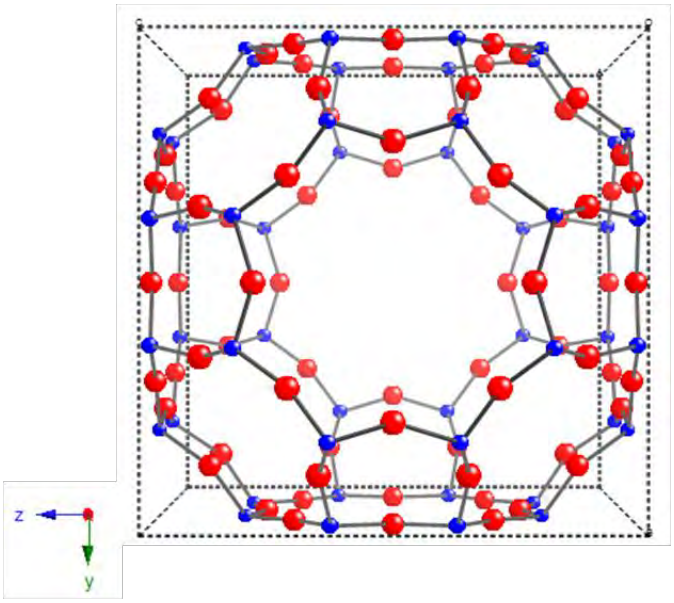

Figure 3.5 *– Crystal structure of ITQ-29 at 300 K. (Si = blue and O = red).*

Table 3.2 – *Refined atomic parameters of ITQ-29 at 300 K.*[a]

Atom	Wyckoff position	*x*	*y*	*z*	Occupancy	B
Si(1)	24k	0	0.3701(3)	0.1840(3)	1	1.4(1)
O(1)	12h	0	0.5	0.2235(7)	1	1.7(1)
O(2)	12i	0	0.2913(4)	0.2913(4)	1	1.7(1)
O(3)	24m	0.1086(3)	0.1086(3)	0.3481(4)	1	1.7(1)

[a] *a = 11.8532(1) Å, space group = $Pm\bar{3}m$, χ^2=1.59, R_{wp} = 7.29 %, R_p = 5.80 %*

Table 3.3 - *Selected bond lengths and angles of ITQ-29 at 300 K [errors at 1σ level].*

Bond Lengths		Bond Angles	
Si – O(1)	1.609(4)	O(1) – Si – O(2)	109.4(4)
Si – O(2)	1.578(4)	O(1) – Si – O(3)	108.7(3)
Si – O(3)	1.589(3)	O(2) – Si – O(3)	110.9(3)
		O(3) – Si – O(3)	108.2(4)

As shown in table 3.3, only small (<5σ) distortions away from the ideal SiO_4 tetrahedra where determined from Rietveld analysis. This meant that tetrahedra in ITQ-29 could be classed as uniform structural units. TGA and mass spectrometry were carried out on ITQ-29 in order to confirm that its pores did not contain any water molecules (figure 3.6). A small mass change due to the release of water was observed over this temperature range. However, as no change in mass was observed above 330 K (57 °C), this initial mass change was attributed to residual water on the surface of the powder, thus confirming that no water molecules resided within the pores.

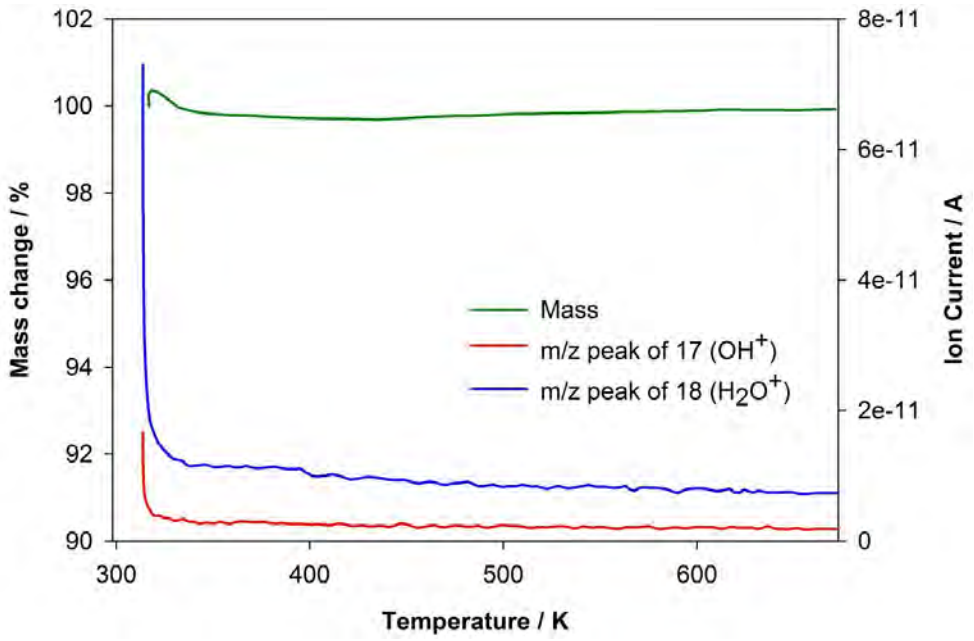

Figure 3.6 *– Combined TGA and mass spectrometry plot of ITQ-29 from 298–673 K.*

.

3.3.1.2 Structural Analysis of Dehydrated Ag-A at 300 K

The crystal structure of dehydrated Ag-A was refined against powder synchrotron XRD data (λ = 0.825035 Å) through Rietveld analysis using the computer program Topas.[58] Synchrotron data were required for this study as laboratory diffraction data was found to be inadequate to monitor the small structural changes that occurred upon thermal excitation in the Al-containing systems. Figure 3.7 illustrates the difference in signal-to-noise between an XRD pattern collected using a laboratory and synchrotron source. Successful Rietveld analysis was performed in the cubic space group $Fm\bar{3}c$ (χ^2 = 1.30, R_{wp} = 8.89 %) with a calculated unit cell parameter of a = 24.66358(7) Å at 300 K. Previous structural studies of zeolite A systems have been carried out in the cubic space group $Pm\bar{3}m$ (a ≈ 12 Å), which does not allow for Si/Al ordering. The observation of the (531) reflection in the powder

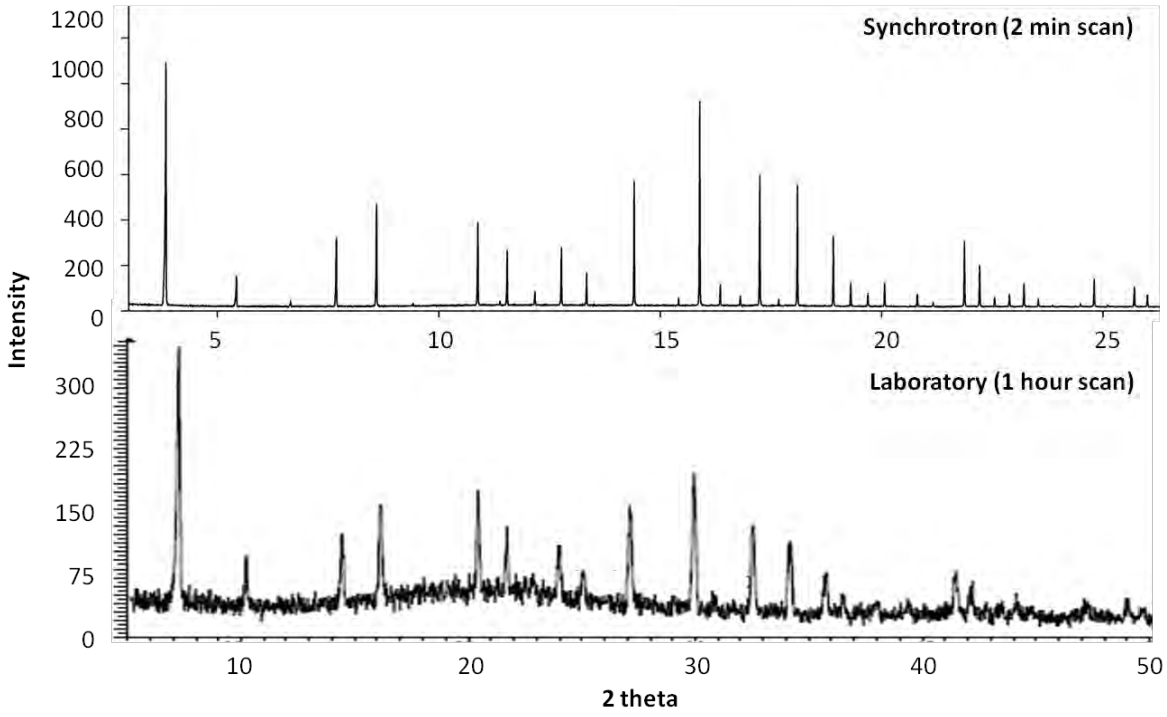

Figure 3.7 – *Comparison of a synchrotron and laboratory powder XRD pattern of hydrated Ag-A.*

synchrotron XRD pattern confirmed the ordering and need to use $Fm\bar{3}c$. Figures 3.8 and 3.9 show the refinement fit and crystal structure of dehydrated Ag-A at 300 K, respectively, and table 3.4 shows the refined atomic coordinates. Despite the difference in unit cell symmetry, $Fm\bar{3}c$ had the same number of crystallographic sites as $Pm\bar{3}m$ for the zeolite framework oxygen atoms but double the amount for the T sites (where T = Si or Al). Three different crystallographic silver positions were identified in dehydrated Ag-A: Ag(1) located in the centre of the 6-ring, Ag(2) located off-centre in the middle of the 8-ring and Ag(3) located in the β-cage as described by Seff *et al.*[34-35, 47] Cations near the 4-ring position were not accepted due to their very low occupancy. This structural refinement was strongly supported by HAADF–STEM images recorded of dehydrated Na-A and Ag-A (figures 3.10 and 3.11).[59] Images of both dehydrated Na-A and Ag-A were record for comparison. As shown in figure 3.10, the larger α-cages appeared as dark spots in the HAADF–STEM image of Na-A, as these correspond to the areas with no mass. The α-cages were then linked together by the lighter appearing β-cages in which the 4-rings were clearly visible. This assignment of the light and dark regions to the zeolite framework becomes even clearer when the recorded and simulated HAADF–STEM images are compared. In the HAADF–STEM image of dehydrated Ag-A the zeolite framework atoms were effectively virtually invisible due to their large difference in atomic number to silver (figure 3.11). Nine different light spots forming a square shape were identified in this image, which were attributed to columns of Ag atoms. Atoms located in the corner of the squares were assigned to silver in the 6-ring position by measuring an internal distance of 4.72 Å between them and a distance to an adjacent β-cage of 7.41 Å. These distances were comparable to the values determined through Rietveld analysis of 4.76 Å and 7.57 Å, respectively. In between the corner spots, five less bright spots were observed which perfectly match the Ag

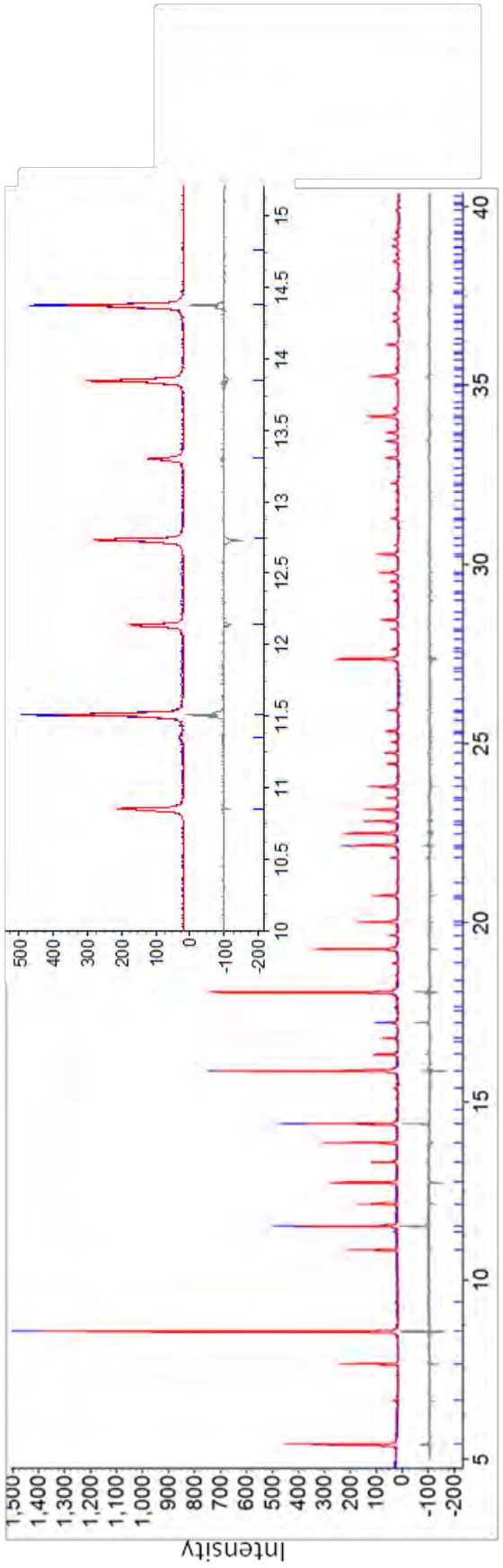

***Figure 3.8** – Rietveld refinement plot of dehydrated Ag-A at 300 K.*

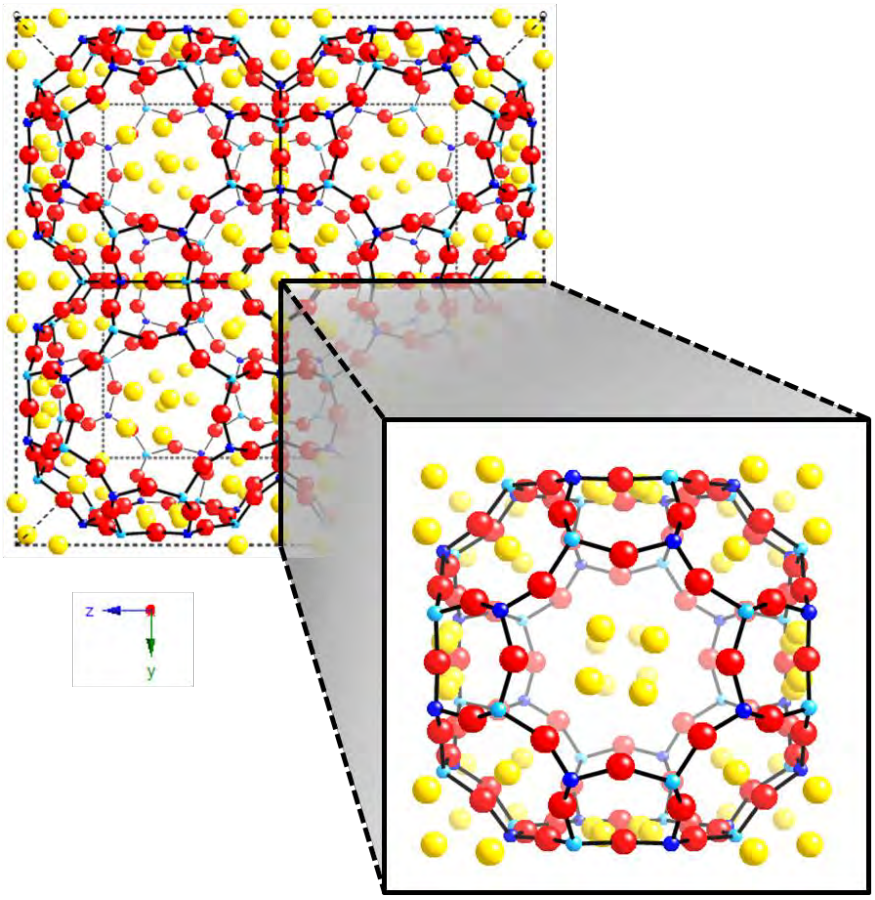

Figure 3.9 *– Crystal structure of dehydrated Ag-A at 300 K (dark blue = Si, light blue = Al, red = O and yellow = Ag). A single α-cage has been highlighted for clarity.*

Table 3.4 *– Refined atomic parameters of dehydrated Ag-A at 300 K.*[a]

Atom	Wyckoff Position	*x*	*y*	*z*	Occupancy	B
Si(1)	96i	0	0.0939(3)	0.1841(3)	1	0.70(4)
Al(1)	96i	0	0.1853(3)	0.0914(3)	1	0.70(4)
O(1)	96i	0	0.1109(2)	0.2479(7)	1	1.38(9)
O(2)	96i	0	0.1476(6)	0.1515(6)	1	1.38(9)
O(3)	192j	0.0529(3)	0.0568(3)	0.1714(2)	1	1.38(9)
Ag(1)	64g	0.0964(3)	0.0964(3)	0.0964(3)	0.97(3)	2.90(4)
Ag(2)	96i	0	0.2227(2)	0.2089(3)	0.19(1)	2.90(4)
Ag(3)	48e	0	0	0.0806(3)	0.17(2)	2.90(4)

[a] *$a = 24.66358(7)$ Å, space group = $Fm\bar{3}c$, $\chi^2 = 1.30$, $R_{wp} = 8.89$ %, $R_p = 7.80$ %*

octahedron positions, Ag_6^0, as described by Seff *et al.*[34-35, 47] The intensity of the central spots were weaker than those in the corners as there are a higher number atoms in the 6-ring position. An interatomic distance of 2.70 Å was measured between the silver atoms in the cluster which is comparable to a distance of 2.81 Å determined from the Rietveld model.

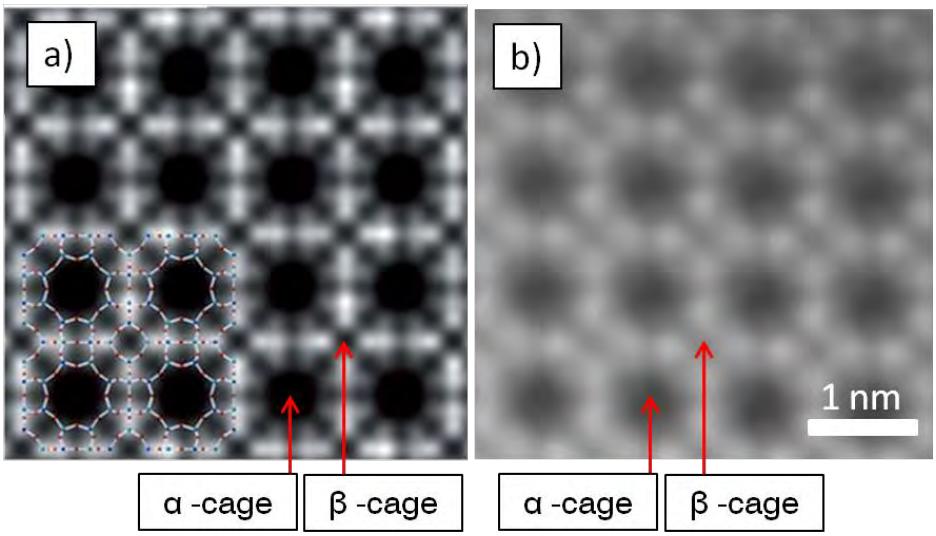

Figure 3.10 *– a) Simulated and b) recorded HAADF–STEM image of Na-A along the [100] direction.*

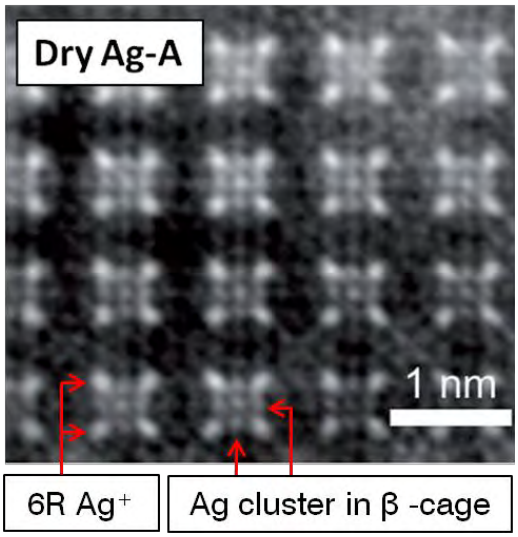

Figure 3.11 *– HAADF–STEM image of Ag-A along the [100] direction.*

3.3.1.3 Structural Analysis of the Dehydrated Alkali-Metal-Exchanged Zeolite A Systems at 300 K

All crystal structures of the dehydrated alkali-metal-exchanged zeolite A systems were refined from powder synchrotron XRD data (λ = 0.827412(4) Å) in the cubic space group $Fm\bar{3}c$. Rietveld refinement plots and refined atomic coordinates of all the dehydrated systems can be found in figures 3.12–3.16 and tables 3.5–3.9, respectively.

Table 3.5 – *Refined atomic parameters of dehydrated Li-A at 300K*[a]

	Atom	Wyckoff position	*x*	*y*	*z*	Occupancy	B
Framework	Si(1)	96i	0	0.0932(2)	0.1806(2)	1	0.90(4)
	Al(1)	96i	0	0.1818(2)	0.0896(2)	1	0.90(4)
	O(1)	96i	0	0.0970(2)	0.2436(3)	1	0.69(6)
	O(2)	96i	0	0.1552(3)	0.1566(3)	1	0.69(6)
	O(3)	192j	0.0548(2)	0.0608(2)	0.1581(1)	1	0.69(6)
6R	Li(1)	64g	0.0980(4)	0.0980(4)	0.0980(4)	0.84(3)	0.3(5)
8R	Li(2)	96i	0	0.232(9)	0.234(9)	0.25(1)	0.3(5)

[a] *a = 23.88056(8) Å, space group: $Fm\bar{3}c$, $\chi^2 = 2.52$, $R_{wp} = 19.58$ %, $R_p = 12.32$ %.*

Figure 3.6 – *Refined atomic parameters of dehydrated Na-A at 300K*[a]

	Atom	Wyckoff position	*x*	*y*	*z*	Occupancy	B
Framework	Si(1)	96i	0	0.0920(2)	0.1849(1)	1	1.34(2)
	Al(1)	96i	0	0.1867(2)	0.0916(2)	1	1.34(2)
	O(1)	96i	0	0.1131(1)	0.2424(2)	1	1.79(4)
	O(2)	96i	0	0.1460(2)	0.1450(2)	1	1.79(4)
	O(3)	192j	0.0531(2)	0.0579(2)	0.1713(1)	1	1.79(4)
6R	Na(1)	64g	0.5992(1)	0.5992(1)	0.5992(1)	0.965(5)	2.0(1)
8R	Na(2)	96i	0	0.2779(6)	0.2119(6)	0.189(2)	2.0(1)

[a] *a = 24.55930(8) Å, space group: $Fm\bar{3}c$, $\chi^2 = 1.40$, $R_{wp} = 14.17$ %, $R_p = 11.96$ %.*

Figure 3.7 – Refined atomic parameters of dehydrated K-A at 300K[a]

	Atom	Wyckoff position	x	y	z	Occupancy	B
Framework	Si(1)	96i	0	0.0944(4)	0.1881(3)	1	0.49(4)
	Al(1)	96i	0	0.1889(3)	0.0928(4)	1	0.49(4)
	O(1)	96i	0	0.1195(2)	0.2448(5)	1	1.35(7)
	O(2)	96i	0	0.1411(5)	0.1447(4)	1	1.35(7)
	O(3)	192j	0.0525(3)	0.0584(3)	0.1777(1)	1	1.35(7)
6R	K(1)	64g	0.1158(1)	0.1158(1)	0.1158(1)	0.868(5)	3.4(1)
	K(2)	64g	0.0716(4)	0.0716(4)	0.0716(4)	0.152(3)	3.4(1)
8R	K(3)	96i	0	0.240(4)	0.236(2)	0.236(2)	3.4(1)

[a] *$a = 24.55825(15)$ Å, space group: $Fm\bar{3}c$, $\chi^2 = 2.67$, $R_{wp} = 21.90$ %, $R_p = 13.40$ %.*

Table 3.8 – *Refined atomic parameters of dehydrated $Rb_{0.79}Na_{0.21}$-A at 300K*[a]

	Atom	Wyckoff position	x	y	z	Occupancy	B
Framework	Si(1)	96i	0	0.0936(2)	0.1858(2)	1	1.15(3)
	Al(1)	96i	0	0.1876(2)	0.0910(2)	1	1.15(3)
	O(1)	96i	0	0.1153(1)	0.2441(3)	1	1.87(5)
	O(2)	96i	0	0.1445(3)	0.1455(3)	1	1.87(5)
	O(3)	192j	0.0532(2)	0.0590(2)	0.1739(1)	1	1.87(5)
6R	Na(1)	64g	0.1011(2)	0.1011(2)	0.1011(2)	0.527(2)	0.4(2)
	Rb(1)	64g	0.1274(1)	0.1274(1)	0.1274(1)	0.447(7)	3.52(6)
	Rb(2)	64g	0.0489(2)	0.0489(2)	0.0489(2)	0.118(8)	3.52(6)
8R	Rb(3)	96i	0	0.250(4)	0.234(2)	0.248(5)	3.52(6)

[a] *$a = 24.55332(4)$ Å, space group: $Fm\bar{3}c$, $\chi^2 = 1.74$, $R_{wp} = 13.06$ %, $R_p = 9.91$ %.*

Table 3.9 – *Refined atomic parameters of dehydrated $Cs_{0.58}Na_{0.42}$-A at 300K*[a]

	Atom	Wyckoff position	x	y	z	Occupancy	B
Framework	Si(1)	96i	0	0.0917(3)	0.1842(2)	1	1.03(4)
	Al(1)	96i	0	0.1861(3)	0.0905(3)	1	1.03(4)
	O(1)	96i	0	0.1092(2)	0.2413(4)	1	1.65(7)
	O(2)	96i	0	0.1459(4)	0.1478(4)	1	1.65(7)
	O(3)	192j	0.0543(3)	0.0580(3)	0.1682(1)	1	1.65(7)
6R	Na(1)	64g	0.1009(1)	0.1009(1)	0.1009(1)	0.679(8)	0.9(8)
	Cs(1)	64g	0.0406(2)	0.0406(2)	0.0406(2)	0.107(6)	5.8(8)
	Cs(2)	64g	0.1385(1)	0.1385(1)	0.1385(1)	0.171(2)	5.8(8)
8R	Cs(3)	96i	0	0.2600(5)	0.2502(1)	0.253(5)	5.8(8)

[a] *$a = 24.49934(7)$ Å, space group: $Fm\bar{3}c$, $\chi^2 = 2.63$, $R_{wp} = 16.48$%, $R_p = 10.15$%.*

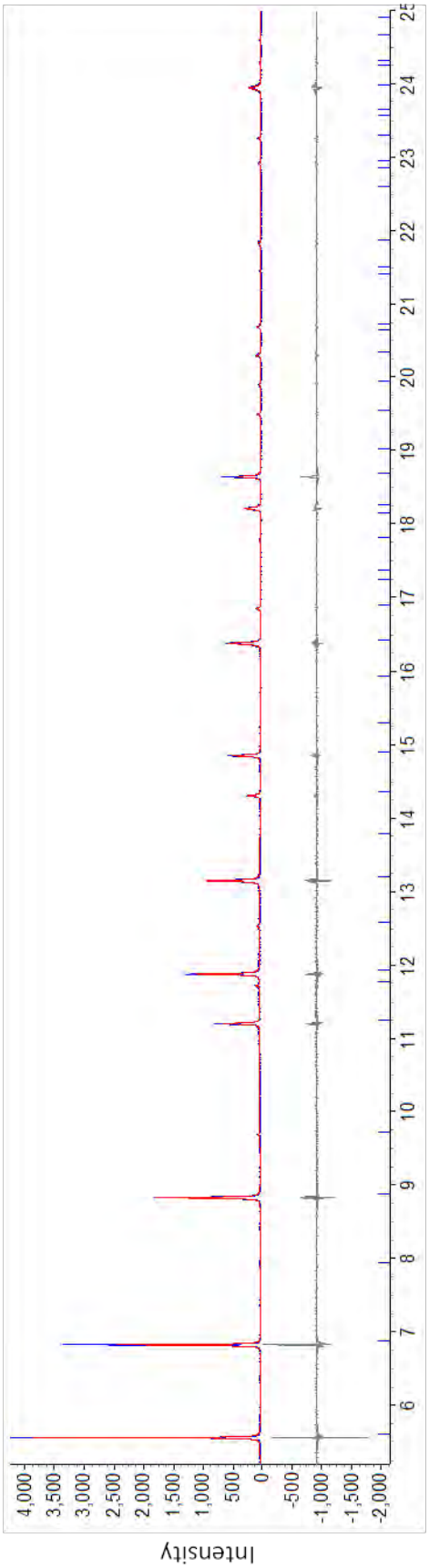

***Figure 3.12** - Rietveld refinement plot of dehydrated Li-A at 300 K.*

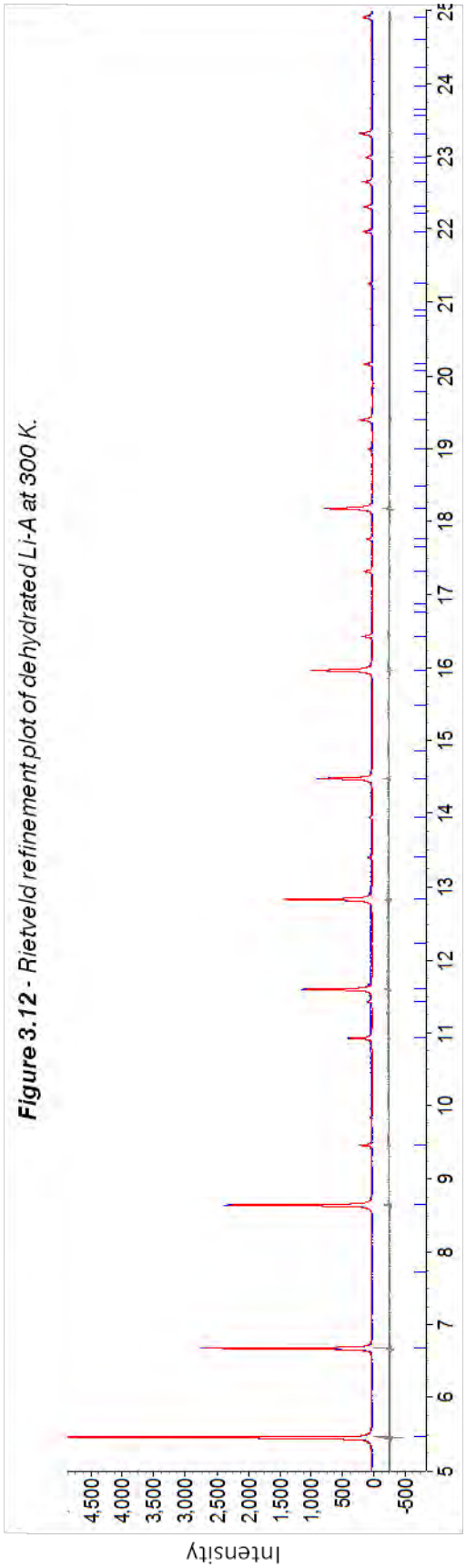

***Figure 3.13** - Rietveld refinement plot of dehydrated Na-A at 300 K.*

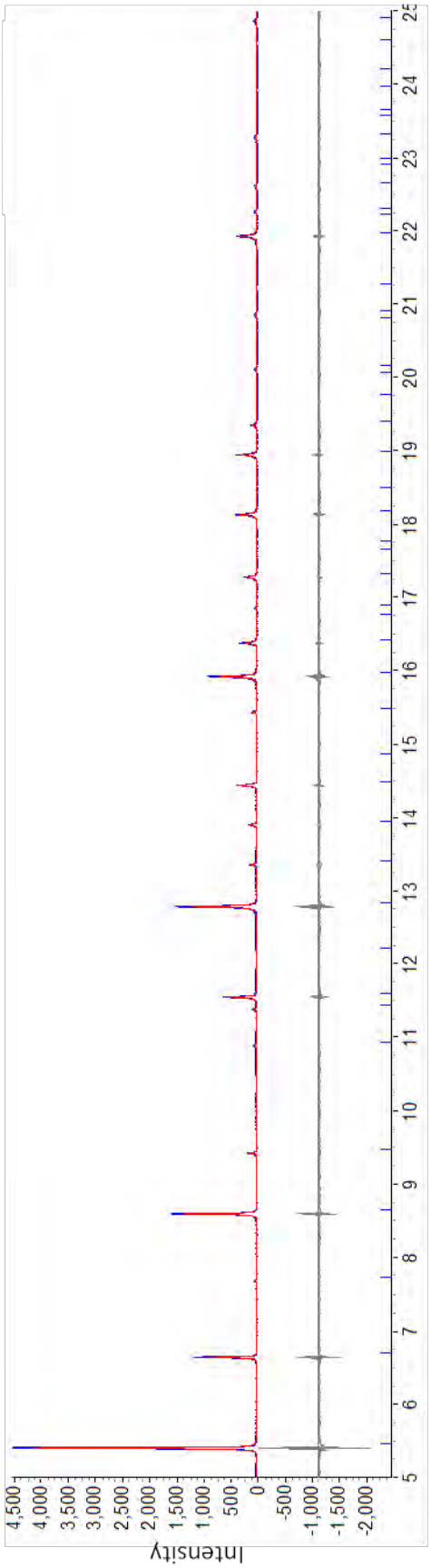

Figure 3.14 *- Rietveld refinement plot of dehydrated K-A at 300 K.*

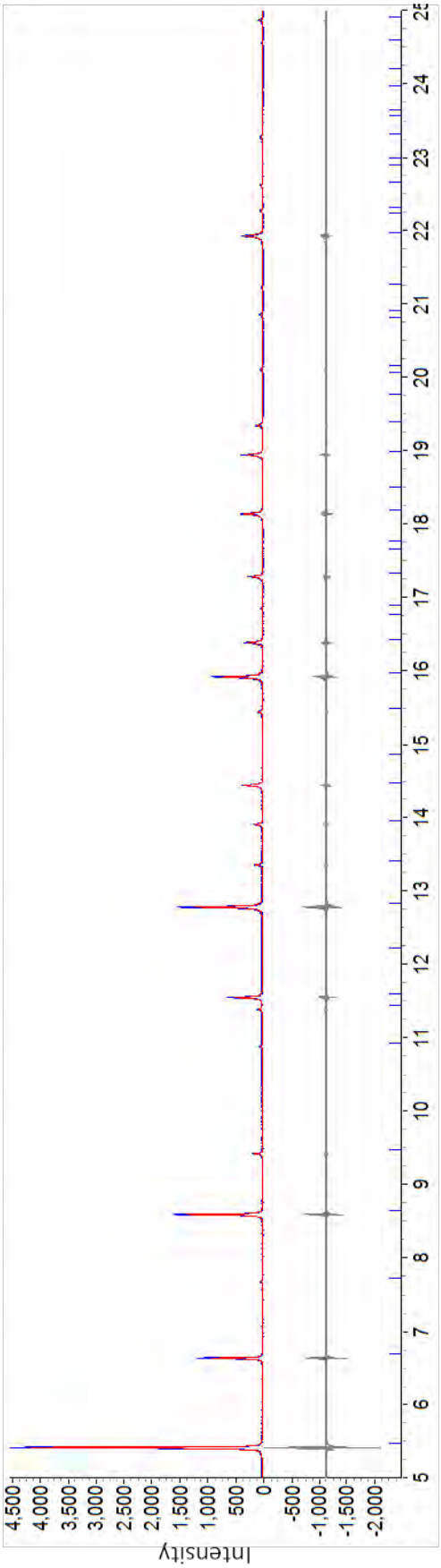

Figure 3.15 *- Rietveld refinement plot of dehydrated $Rb_{0.79}Na_{0.21}$-A at 300 K.*

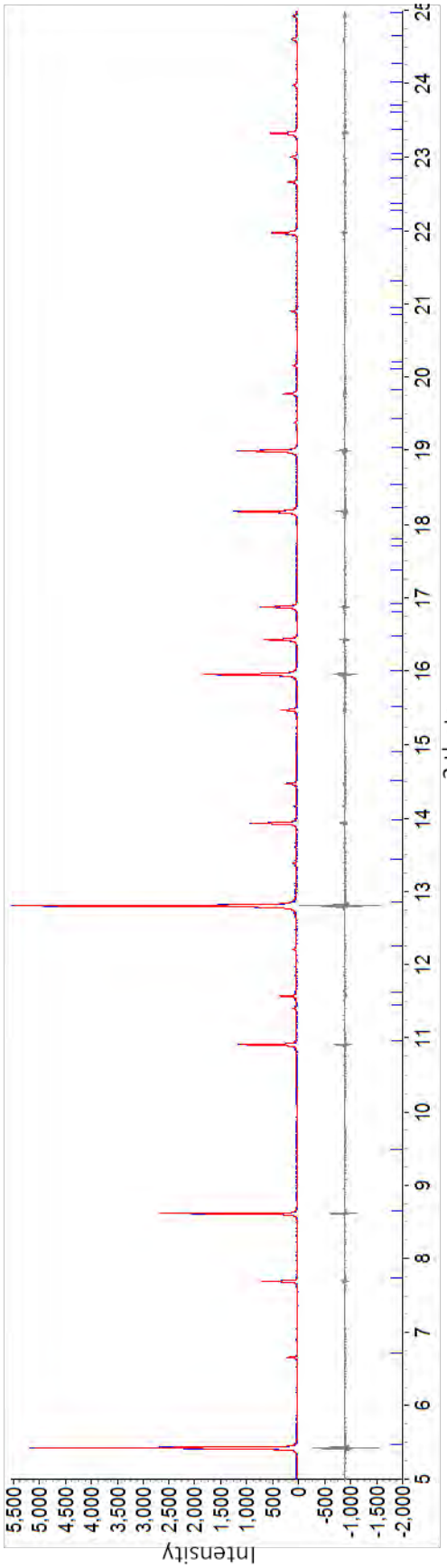

Figure 3.16 *- Rietveld refinement plot of dehydrated* $Cs_{0,58}NaO_{0,42}$*-A at 300 K.*

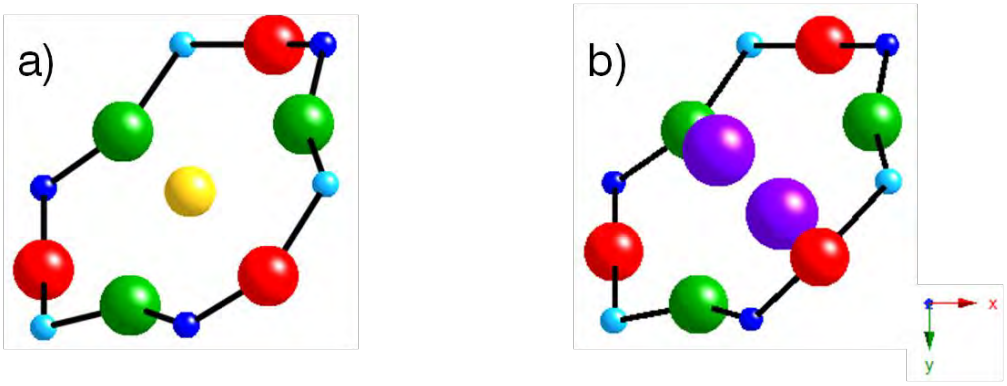

Figure 3.17 *– Diagram illustrating the position of a) small cations (i.e. $Li^+$and Na^+) and b) large cations (i.e. K^+, Rb^+ and $Cs^{+)}$ in the 6-ring of zeolite A (light blue = Al, dark blue = Si, red = O(2), green = O(3), yellow = small cation and purple = large cation).*

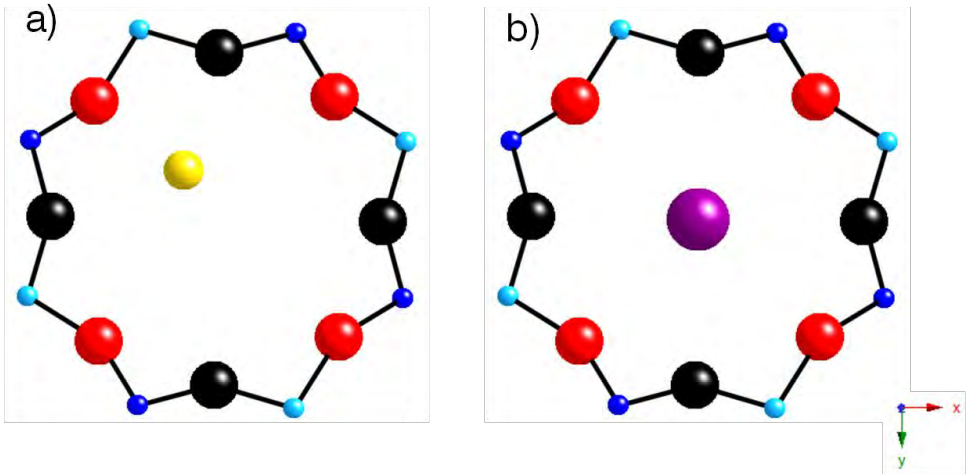

Figure 3.18 *– Diagram illustrating the position of a) small cations (i.e. $Li^+$and Na^+) and b) large cations(i.e. K^+, Rb^+ and $Cs^{+)}$ in the 8-ring of zeolite A (light blue = Al, dark blue = Si, black = O(1), red = O(2), yellow = small cation and purple = large cation).*

Two common cation positions were identified in the dehydrated systems: the 6-ring and 8-ring. Depending upon their ionic radii, cations were determined to occupy slightly different positions within the zeolite rings. Small cations, such as Li^+ and Na^+, were able to fit in the centre of the 6-ring and coordinate to the framework O(2) and O(3) atoms (figure 3.17a). In the 8-ring, however, these small cations were unable to coordinate to all framework O(1) and O(2) atoms and as a result were positioned just off-centre in the ring (figure 3.18a). In

the case of dehydrated Li-A, the small cationic size caused a large contraction in the 6-ring and consequently the unit cell. This contraction of the 6-ring was reflected in the Si–O–Al bond angles through small Si–O(2)–Al and Si–O(3)–Al bond angles and a large Si–O(1)–Al bond angle (table 3.10). Larger cations, such as K^+, Rb^+ and Cs^+, were not able to fit into the 6-ring and were identified in sites either side of the 6-ring in the α-cage (6Rα) or β-cage (6Rβ) (figure 3.17b). In the majority of cases, large 6-ring cations preferred to sit in the 6Rα position as 6Rβ cations had weaker coordination with O(2) when the 6-ring was puckered. In the partially exchanged $Rb_{0.79}Na_{0.21}$-A and $Cs_{0.58}Na_{0.42}$-A systems, all residual Na^+ cations were found to be located in the middle of the 6-ring. The remaining Rb^+ and Cs^+ cations were then determined to occupy either the 6Rα, 6Rβ or 8-ring positions. Larger cations occupied a more centralised site in the 8-ring, when compared to the smaller cations, as illustrated in figure 3.18b. Clear trends in the Si–O–Al bond angles were evident as the cationic size was modified. Focusing on the fully exchanged systems, considerable increases in the Si–O(2)–Al and Si–O(3)–Al angles were observed as the cation size was increased causing a significant increase in the 6-ring diameter. In contrast, a large decrease in the Si–O(1)–Al was observed leading to decrease in the 8-ring diameter.

Table 3.10 *– Calculated Si–O–Al bond angles for all of the dehydrated alkali-metal-exchanged zeolite A systems at 300 K [error at 1σ level].*

Dehydrated System	Si–O(1)–Al	Si–O(2)–Al	Si–O(3)–Al
Li-A	170.85(34)	132.98(48)	132.08(30)
Na-A	141.28(30)	162.21(50)	146.39(29)
K-A	134.21(52)	175.60(86)	152.35(53)
$Rb_{0.79}Na_{0.21}$-A	140.00(31)	166.75(48)	147.42(31)
$Cs_{0.58}Na_{0.42}$-A	148.54(53)	158.89(77)	141.25(47)

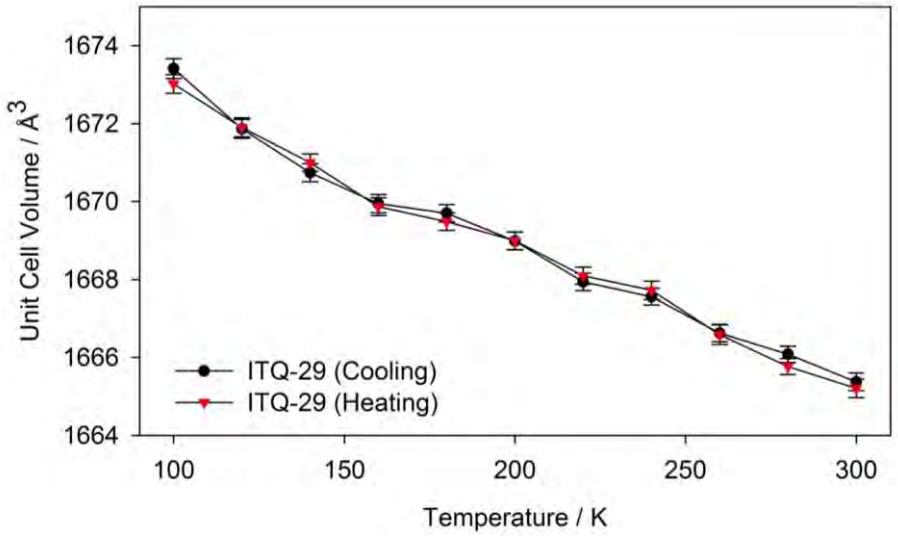

Figure 3.19 *- Calculated unit cell volumes of ITQ-29 from 100–300 K [errors at 3σ level].*

3.3.1.4 Thermal Expansion Studies of ITQ-29

Variable temperature powder XRD studies were used to determine the thermal expansion behaviour of ITQ-29 from 100–300 K. XRD patterns were collected at 20 K intervals and Rietveld analysis was performed at each interval to monitor any thermally induced structural changes. As shown in figure 3.19, strong NTE behaviour was observed over this temperature range with a mean volume thermal expansion coefficient, $\overline{\alpha_v}_{(100\text{–}300\ K)}$, of –22.1 x 10^{-6} K^{-1}. This equated to a unit cell volume change of 0.46 % upon thermal excitation and is comparable to that of siliceous chabazite, which has the largest known NTE coefficient for zeolites ($\overline{\alpha_v}_{(293\text{-}873\ K)} = -26.1 \times 10^{-6}\ K^{-1}$).[60] Significant changes in the relative Bragg peak intensities suggested that the contraction in the unit cell upon heating was caused by a structural change. As shown in figure 3.20 the intensity of (100), (110), (111), (210) and (211) peaks all increased upon heating where as both the (311) and (320) peaks decreased. Table 3.11 details selected bond lengths and angles calculated from Rietveld analysis over the whole temperature range. Rietveld refinement plots and refined atomic coordinates of ITQ-29 at regular temperature intervals can be found in appendix 1 and 2.

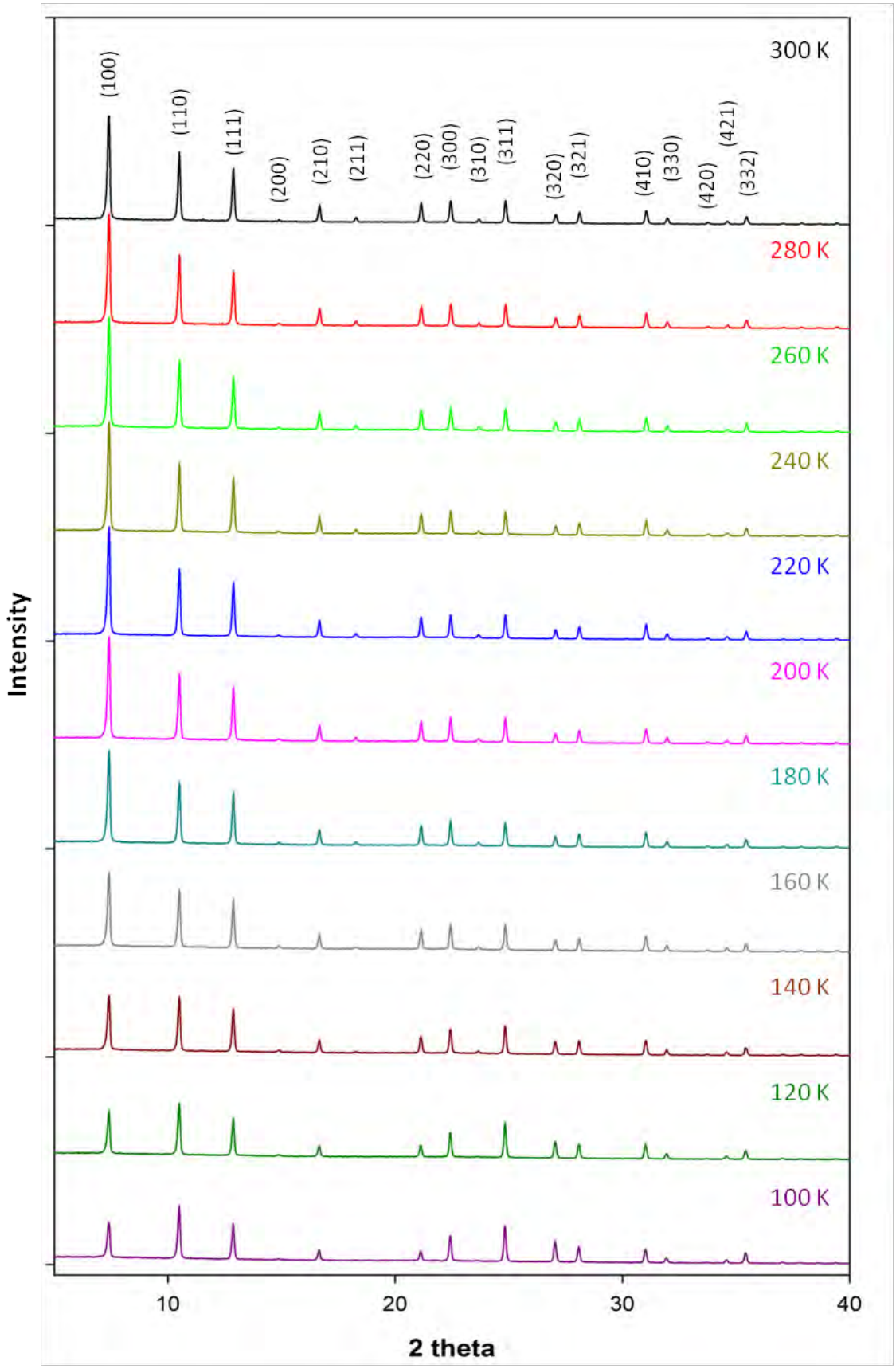

Figure 3.20 *– Powder XRD patterns of ITQ-29 from 100–300 K.*

Table 3.11 *– Bond Distances (Å) and Angles (deg) in ITQ-29 from 100–300 K (errors at 1σ level).*

Bond Length/Angle	Temperature										
	300K	280K	260K	240K	220K	200K	180K	160K	140K	120K	100K
Si – O1	1.609(4)	1.615(4)	1.615(4)	1.615(4)	1.614(4)	1.613(4)	1.613(5)	1.609(4)	1.605(5)	1.59(1)	1.59(1)
Si – O2	1.578(4)	1.578(4)	1.578(4)	1.579(4)	1.579(4)	1.580(4)	1.580(5)	1.579(4)	1.577(5)	1.59(1)	1.58(1)
Si – O3	1.589(3)	1.585(3)	1.586(3)	1.587(3)	1.587(3)	1.588(3)	1.588(3)	1.592(3)	1.599(3)	1.613(7)	1.616(9)
Si – O1 – Si	146.2(6)	144.1(6)	144.6(6)	145.2(6)	145.7(6)	146.5(6)	146.2(8)	150.1(7)	152.0(8)	152.6(2)	155.7(2)
Si – O2 – Si	162.6(5)	164.3(5)	163.7(5)	163.0(5)	162.3(5)	161.4(5)	161.8(7)	158.2(5)	157.2(7)	155.6(2)	158.4(2)
Si – O3 – Si	152.3(4)	153.0(5)	153.8(5)	152.6(4)	152.5(4)	152.4(5)	152.4(6)	151.8(5)	151.2(6)	148.7(1)	146.9(2)
O1 – Si – O2	109.4(4)	109.2(4)	109.1(4)	109.1(4)	109.0(4)	109.0(4)	109.0(5)	109.2(4)	109.6(6)	109.1(1)	112.1(2)
O1 – Si – O3	108.7(3)	109.0(3)	108.3(3)	108.9(3)	108.8(3)	108.7(3)	108.7(3)	108.1(3)	107.6(4)	105.12(7)	105.7(9)
O2 – Si – O3	110.9(3)	110.8(3)	110.9(3)	111.0(3)	111.1(3)	111.2(3)	111.2(3)	111.8(3)	111.7(3)	111.05(7)	109.4(9)
O3 – Si – O3	108.2(4)	107.9(3)	107.9(5)	108.0(5)	108.0(5)	108.0(5)	108.0(6)	107.8(5)	108.(6)	114.9(1)	114.6(2)
Lattice Parameter (Å)	11.8532(1)	11.8535(1)	11.8550(1)	11.8572(1)	11.8580(1)	11.8603(1)	11.8602(2)	11.8635(1)	11.8661(2)	11.870(3)	11.872(4)
Unit Cell Volume (Å)	1665.34(5)	1665.49(5)	1666.12(5)	1667.05(5)	1667.38(5)	1668.34(5)	1668.30(6)	1669.68(6)	1670.79(7)	1672.3(1)	1673.4(2)

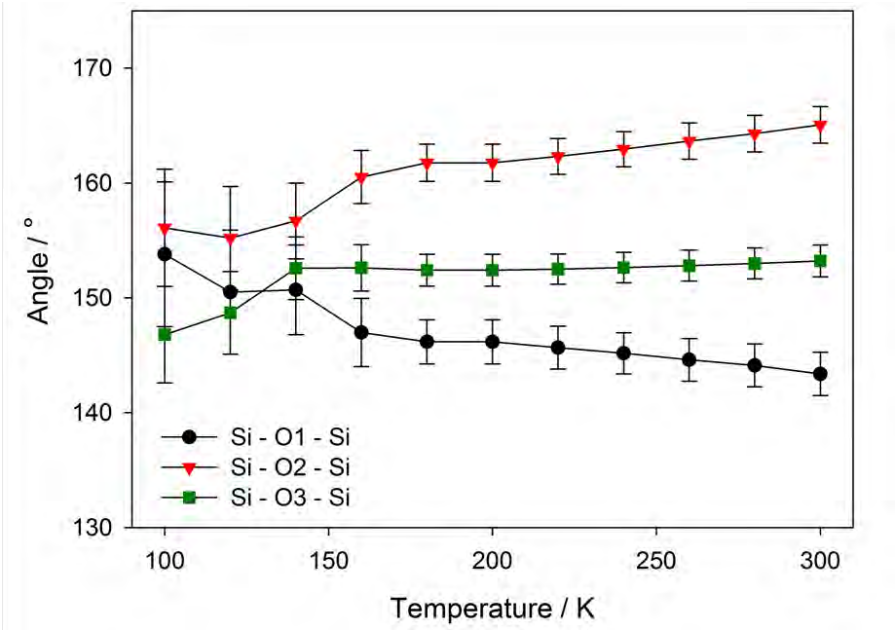

Figure 3.21 *– Calculated Si–O–Si bond angles for ITQ-29 from 100–300 K.*

As shown in table 3.11 the rigid SiO_4 tetrahedra were not distorted upon thermal excitation as the Si–O bond length and O-Si–O bond angles remained constant. However, significant changes were observed in the Si–O–Si bond angles as shown in figure 3.21. As illustrated in figures 3.21 and 3.22, the Si–O(1)–Si bond angle decreased by 6.39 % on heating causing the O(1) to move towards the centre of the 8-ring. In contrast, the Si–O(2)–Si and Si–O(3)–Si bond angles both increased by 6.29 % and 1.62 % on heating, respectively, causing O(2) to move away from the centre of the 8-ring towards the plane of the 6-ring and O(3) to move towards the centre of the double 4-ring. The three different crystallographic oxygens have been colour coded in figures 3.21 and 3.22 for clarity. These changes in the Si–O–Si bond angles indicated a rotation of the rigid tetrahedra upon heating as illustrated in figure 3.22 causing the unit cell to contract in volume. This thermally induced motion of the tetrahedra in the LTA structure type is essentially the behaviour predicted by Hammonds *et al*.[61] Using computational modelling, Hammonds and co-workers described the motion as a 'local RUM' that could only occur if all eight SiO_4 tetrahedra in a single double 4-ring

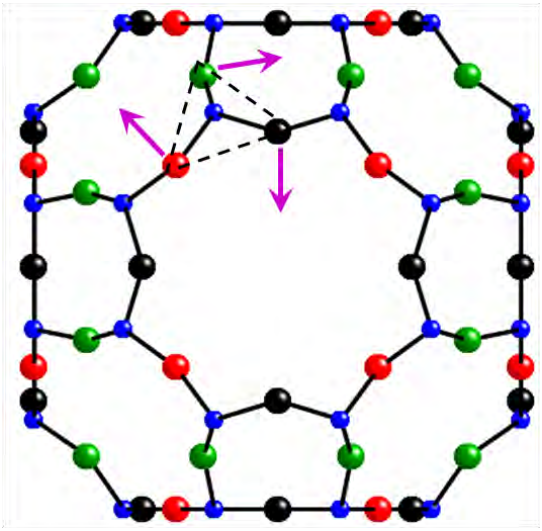

Figure 3.22 *– Diagram of the α-cage in ITQ-29 down [100] plane illustrating the changes in Si–O–Si bond angles and the rotation of the rigid tetrahedra on heating (blue=Si, black=O1, red=O2, green=O3).*

moved in a concerted fashion, but did not require the cooperative movement of the rest of the structure. From the experimental data presented in this thesis, the Si–O(1)–Si bond angle has been shown to play a key role in the thermal expansion behaviour of ITQ-29 as it was the only bond angle to decrease in value upon unit cell contraction. As this bond angle bridges the double 4-ring (connecting the β-cages) in ITQ-29, any change in its value will have a huge effect on the unit cell volume. The Si–O(1)–Si distance was shown to contract by 1.04 % of heating.

3.3.1.5 Thermal Expansion Studies of Dehydrated Ag-A

Variable temperature powder synchrotron XRD studies were used to determine the thermal expansion behaviour of dehydrated Ag-A from 100–300 K. XRD patterns were collected at 20 K intervals and Rietveld analysis was performed at each interval to monitor any thermally induced structural changes. As shown in figure 3.23 weak NTE behaviour was observed over this temperature change with a mean volume thermal expansion coefficient, $\overline{\alpha_v}_{(100\text{–}300\ K)}$, of –7.68 x 10^{-6} K^{-1}. This equated to a unit cell volume contraction of 0.17 % upon heating, much smaller than that observed in ITQ-29. As shown in figure 3.24 considerably fewer changes in the relative XRD peak intensities were observed upon thermal excitation in dehydrated Ag-A when compared to ITQ-29. A significant decrease in the (200) peak was observed upon heating, but the other relative peak intensities remained roughly the same.

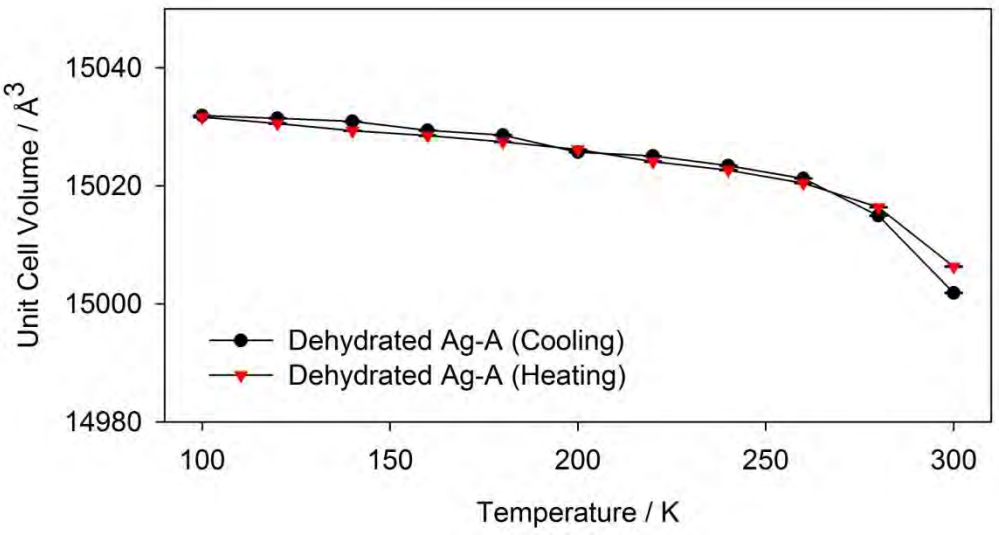

Figure 3.23 *– Calculated unit cell volumes of dehydrated Ag-A from 100–300 K [small error bars at 3σ level, not visible on this scale].*

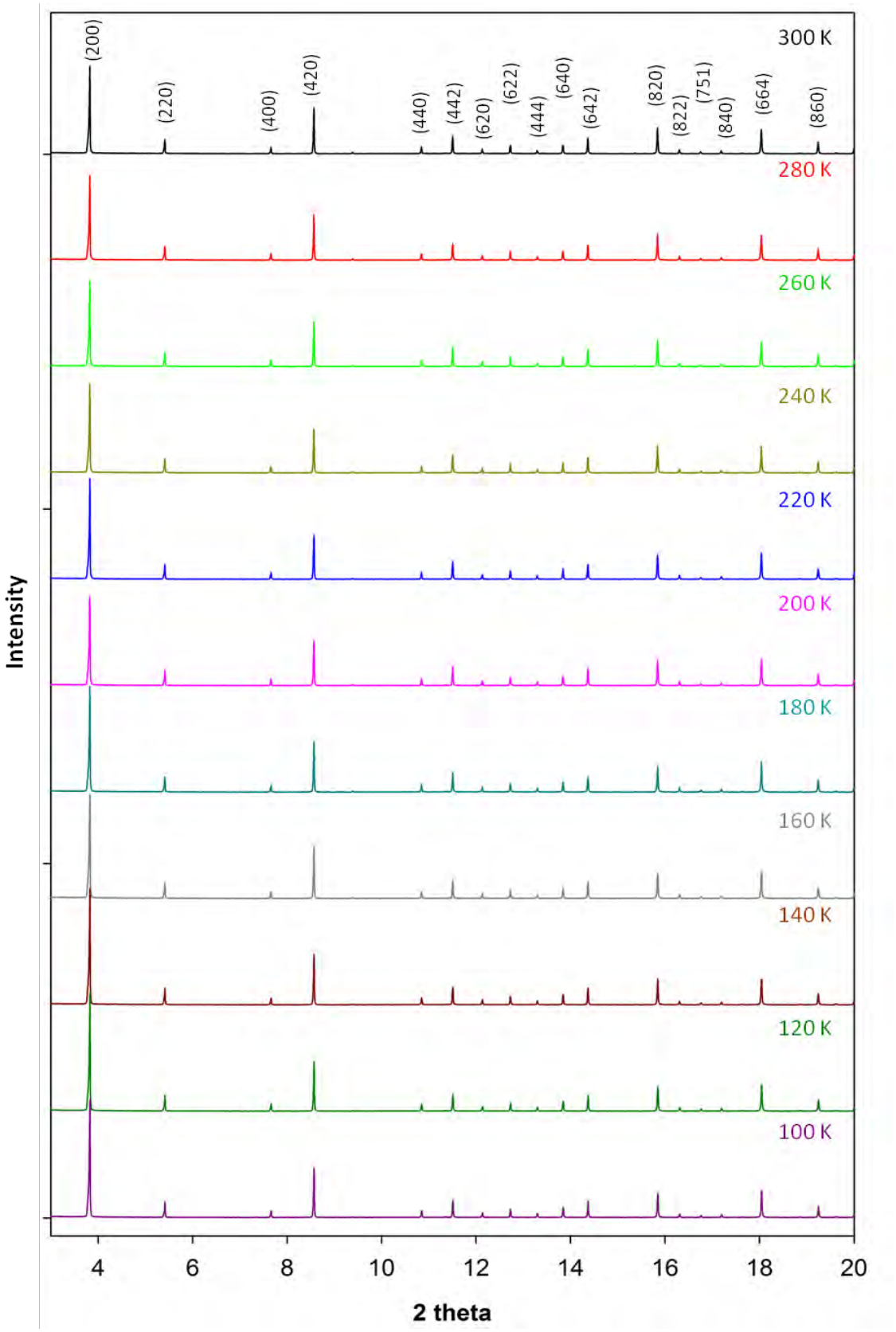

Figure 3.24 *– Powder synchrotron XRD patterns of dehydrated Ag-A between 300–100 K.*

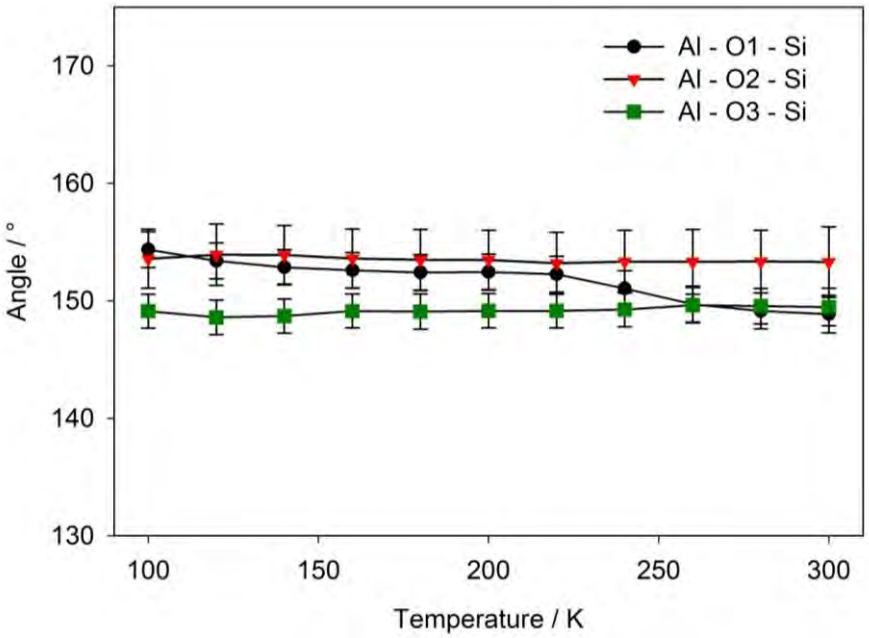

Figure 3.25 *– Calculated Si–O–Al bond angles for dehydrated Ag-A from 100–300 K [errors at 3σ level].*

Through examination of the calculated Si–O–Al and O–T–O bond angles in dehydrated Ag-A, table 3.12, the mechanism behind the weaker thermal expansion behaviour can be explained. Rietveld refinement plots and refined atomic coordinates of dehydrated Ag-A at regular temperature intervals can be found in appendix 1 and 2. As illustrated in figures 3.25 and 3.26, the Si–O(1)-Al bond angle decreased on heating as it did in ITQ-29 but by a smaller amount of 3.49 %. However, the Si–O(2)–Al and Si–O(3)–Al angles did not increase, but remained roughly constant over the whole temperature range. Significant distortions in the TO_4 tetrahedra were also observed upon heating. The O(1)–T–O(2) angle decreased by ~2.5° upon heating from the ideal value and O(1)–T–O(3) angle increased by ~2°. Taken together, these results suggested that the Ag^+ cations had an anchoring effect on the framework O(2) and O(3) atoms, which restricted the rotation of the TO_4 tetrahedra on heating. This resulted in a distortion of the tetrahedra and a much smaller reduction in the Si–O(1)–Al angle and distance (0.22 %), mirrored by a considerably reduced overall unit cell contraction compared to ITQ-29.

Table 3.12 *– Bond Distances (Å) and Angles (deg) in Dehydrated Ag-A from 100–300 K (errors at 1σ level).*

Bond Length/Angle	Temperature										
	300K	280K	260K	240K	220K	200K	180K	160K	140K	120K	100K
Si – O1	1.63(3)	1.63(2)	1.63(2)	1.62(2)	1.62(2)	1.62(2)	1.62(2)	1.62(2)	1.62 (2)	1.64(2)	1.61 (2)
Si – O2	1.55(3)	1.53(1)	1.54(1)	1.53(1)	1.53(1)	1.52(1)	1.52(1)	1.52(1)	1.52(1)	1.52(1)	1.51 (1)
Si – O3	1.62(1)	1.614(8)	1.620(9)	1.626(8)	1.619(8)	1.628(8)	1.628(8)	1.629(8)	1.630(8)	1.633(8)	1.639(8)
Al – O1	1.72(3)	1.72(2)	1.71 (2)	1.71 (2)	1.70(2)	1.70(2)	1.70(2)	1.70(2)	1.69(2)	1.68(2)	1.70(2)
Al – O2	1.75(3)	1.77(1)	1.76(1)	1.76(1)	1.75(1)	1.77(1)	1.77(1)	1.77(1)	1.77(1)	1.77(1)	1.78(1)
Al – O3	1.73(1)	1.736(8)	1.730(9)	1.735(8)	1.747(8)	1.737(8)	1.737(9)	1.738(8)	1.739(8)	1.733(8)	1.726(8)
Si – O1 – Al	148.8(9)	149.1(5)	149.7(5)	151.0(5)	152.3(5)	152.5(5)	152.4(5)	152.6(5)	152.9(5)	153.4(5)	154.4(5)
Si – O2 – Al	153.4(2)	153.3(9)	153.3(9)	153.3(9)	153.2(9)	153.5(8)	153.5(9)	153.6(8)	153.9(8)	153.9(9)	153.6(8)
Si – O3 – Al	149.6(9)	149.5(5)	149.6(5)	149.3(5)	149.1(5)	149.2(5)	149.1(5)	149.1(5)	148.7(5)	148.6(5)	149.1(5)
O1 – Si – O2	106(1)	106.1(7)	106.3(7)	106.7(7)	107.1(7)	107.8(6)	107.5(6)	107.8(6)	108.1(6)	108.6(6)	109.0(6)
O1 – Si – O3	109.5(6)	109.7(3)	109.3(3)	109.3(3)	109.0(3)	108.9(3)	108.9(3)	108.9(3)	108.7(3)	108.4(3)	107.8(3)
O2 – Si – O3	112.5(7)	112.5(4)	112.6(4)	112.5(4)	112.3(4)	112.4(4)	112.4(4)	112.4(4)	112.2(4)	112.3(4)	113.0(4)
O3 – Si – O3	106(1)	106.6(6)	106.6(6)	106.6(6)	107.1(6)	106.5(6)	106.6(6)	106.5(6)	106.7(6)	106.7(6)	106.0(6)
O1 – Al – O2	106(1)	106.4(6)	106.7(6)	107.6(6)	108.4(6)	108.4(6)	108.4(6)	108.4(6)	108.7(6)	108.7(6)	109.0(6)
O1 – Al – O3	110.2(6)	110.1(3)	110.1(3)	110.0(3)	109.5(3)	109.7(3)	109.7(3)	109.7(3)	109.8(3)	109.9(3)	109.8(3)
O2 – Al – O3	111.3(7)	111.3(4)	111.3(4)	111.1(4)	111.2(4)	111.0(4)	110.9(4)	110.9(4)	110.5(4)	110.3(4)	110.3(4)
O3 – Al – O3	108(1)	107.5(6)	107.5(6)	107.2(6)	107.1(6)	107.2(6)	107.3(6)	107.3(6)	107.5(6)	107.7(6)	107.7(6)
Lattice Parameter (Å)	24.66358(9)	24.67046(6)	24.67394(6)	24.67524(6)	24.67623(6)	24.67687(6)	24.67781(6)	24.67885(6)	24.67956(6)	24.67992(6)	24.68011(6)
Unit Cell Volume (Å)	15002.7(2)	15015.2(1)	15021.6(1)	15024.0(1)	15025.8(1)	15026.9(1)	15028.7(1)	15030.5(1)	15031.8(1)	15032.5(1)	15032.8(1)

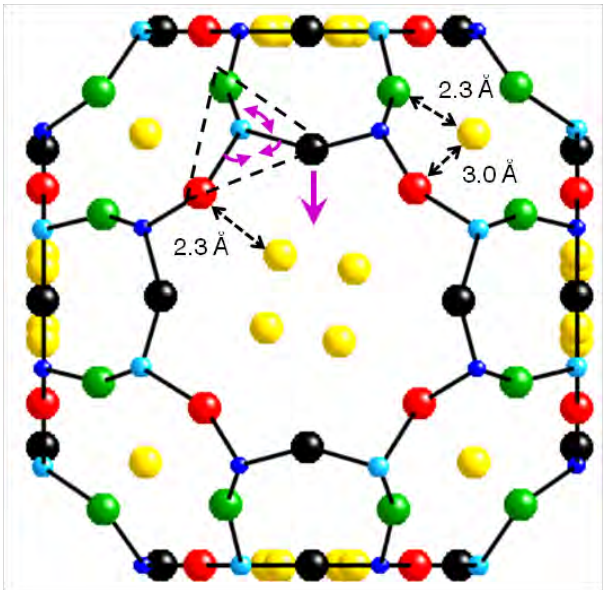

Figure 3.26 - *Diagram of a single α-cage in dehydrated Ag-A down [100] plane illustrating the changes in Si–O–Al and O–T–O bond angles on heating (dark blue = Si, light blue = Al, black = O(1), red = O(2), green = O(3), yellow = Ag). Ag(3) is not included.*

Due to the off centre position and relatively small quantity of the Ag^+ cations in the 8-ring position (~2.2 per α-cage), cations in the 6-ring site were deemed the most likely cause of the anchoring effect in dehydrated Ag-A with bond distances of 2.3 Å and 3.0 Å to O(2) and O(3), respectively. As with ITQ-29, experimental data showed that the Si-O(1)-Al bond angle plays a key role in the unit cell volume of dehydrated Ag-A.

3.3.1.6 Thermal Expansion Studies of the Dehydrated Alkali-Metal-Exchanged Zeolite A Systems

Variable temperature powder synchrotron XRD studies were used to determine the thermal expansion behaviour of all the dehydrated alkali-metal-exchanged zeolite A systems from 100–300 K. XRD patterns were collected at 20 K intervals and Rietveld analysis was performed at each interval to monitor any thermally induced structural changes. As shown in table 3.13 weak NTE behaviour was observed for dehydrated Na-A with a mean volume thermal expansion coefficient similar to of dehydrated Ag-A. This was not unexpected as the ionic radii of Na^+ (1.02 Å) and Ag^+ (1.15 Å) are comparable. More surprisingly, however, weak positive thermal expansion (PTE) was observed for dehydrated Li-A and K-A, and extremely weak NTE behaviour was observed for the dehydrated $Rb_{0.79}Na_{0.21}$-A and $Cs_{0.58}Na_{0.42}$-A systems.

Table 3.13 – *Calculated mean volume thermal expansion coefficients of the anhydrous LTA systems.*

Anhydrous LTA System	Mean Volume Thermal Expansion Coefficient / x 10^{-6} K^{-1}
ITQ-29	–22.1
Li-A	0.79
Na-A	–6.34
Ag-A	–7.68
K-A	2.03
Rb-A	–0.78
Cs-A	–1.76

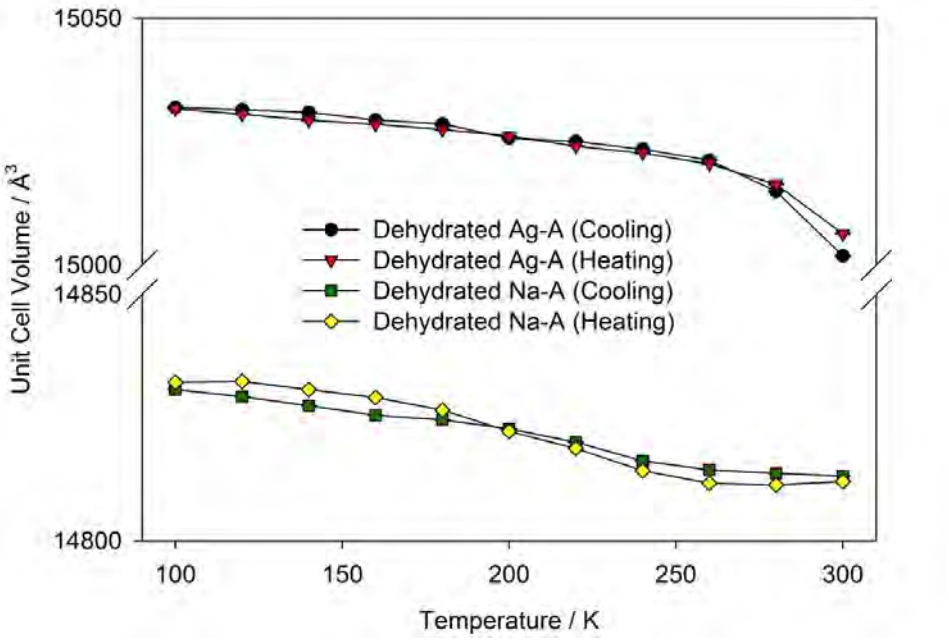

Figure 3.27 *- Calculated unit cell volumes of dehydrated Na-A and Ag-A from 100–300 K [small error bars at 3σ level, not visible on this scale].*

Despite the similarities in thermal expansion behaviour (figure 3.27), significant differences in the structural mechanism behind the NTE were determined for dehydrated Na-A and Ag-A. In dehydrated Na-A, the Si–O(1)–Al and Si–O(2)–Al bond angles increased on heating by 2.04% and 1.36%, respectively (figure 3.28). In contrast, the Si–O(3)–Al bond angle decreased upon heating by 0.44%. These trends in the Si–O–Al bond angle were completely different to those observed in dehydrated Ag-A and from previous observations, an increase in the Si–O(1)–Al should have resulted in a thermal expansion of the unit cell not a contraction. However, through a closer examination of the O–T–O bond angles, the thermal contraction can be explained. As shown in figure 3.29 and table 3.14, considerable distortions away from the ideal TO_4 tetrahedra were observed at low temperature in dehydrated Na-A.

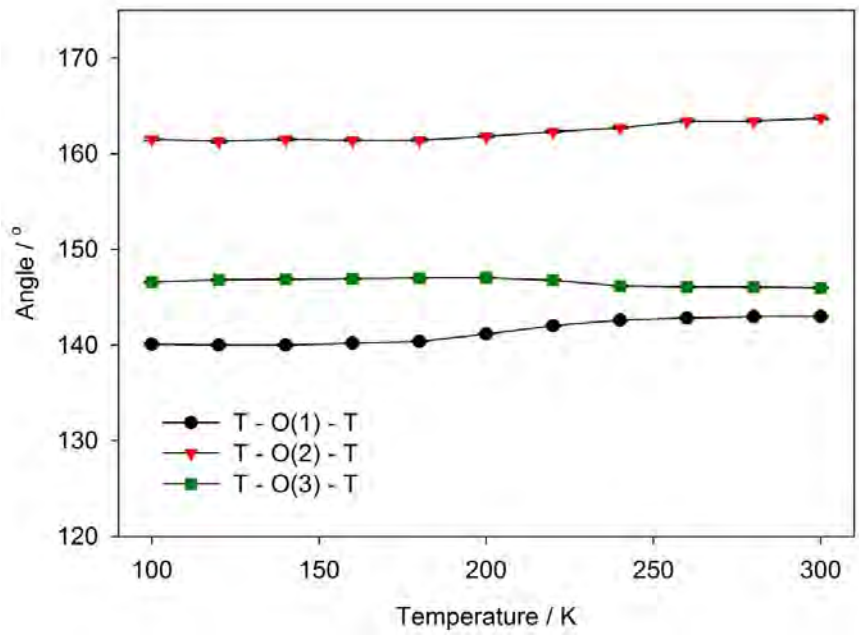

Figure 3.28 *– Calculated Si–O–Al bond angles for dehydrated Na-A from 100–300 K.*

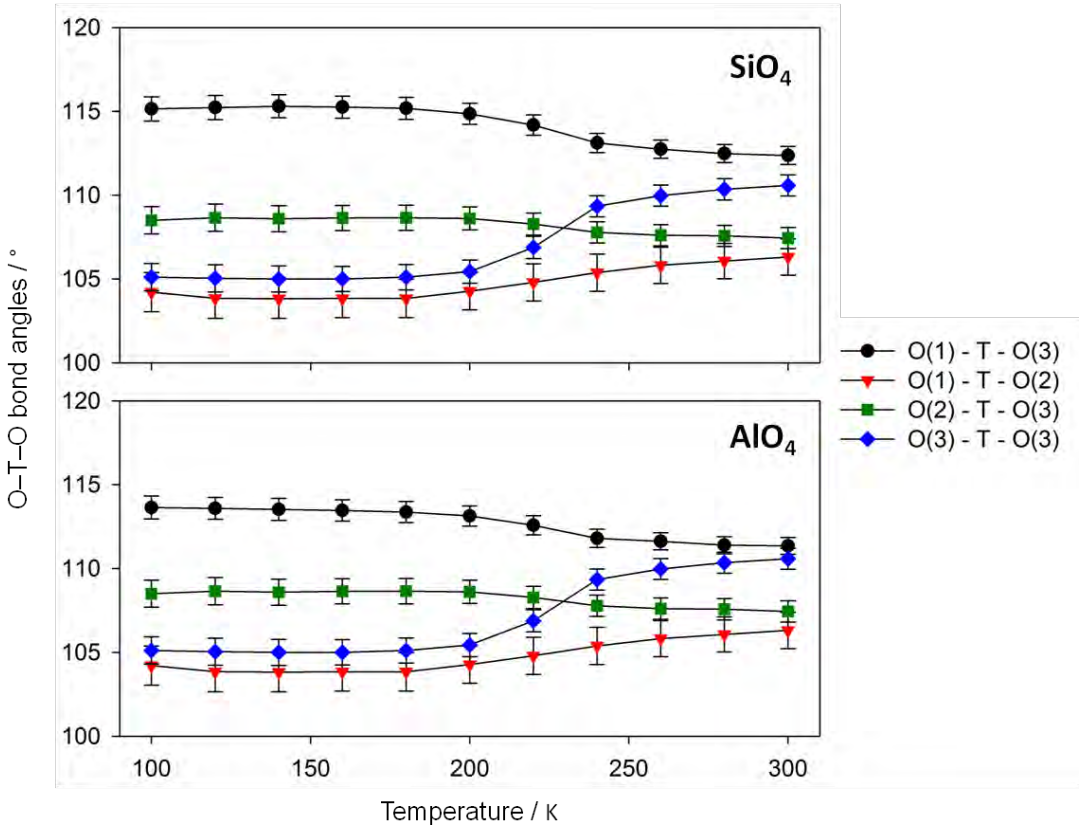

Figure 3.29 *– Calculated O–T–O bond angles for dehydrated Na-A from 100–300 K.*

Table 3.14 *– Bond Distances (Å) and Angles (deg) in Dehydrated Na–A from 100–300 K (errors at 1σ level).*

Bond Length/Angle	Temperature										
	300K	280K	260K	240K	220K	200K	180K	160K	140K	120K	100K
Si – O1	1.503(7)	1.501(6)	1.499(6)	1.497(7)	1.493(7)	1.495(7)	1.498(7)	1.500(7)	1.502(8)	1.509(8)	1.511(8)
Si – O2	1.650(7)	1.652(7)	1.655(7)	1.661(7)	1.655(7)	1.657(7)	1.656(7)	1.652(7)	1.651(8)	1.646(8)	1.640(8)
Si – O3	1.587(5)	1.585(5)	1.583(5)	1.581(5)	1.576(5)	1.569(5)	1.565(5)	1.565(5)	1.565(5)	1.567(5)	1.571(5)
Al – O1	1.820(7)	1.825(7)	1.830(7)	1.838(7)	1.848(7)	1.858(7)	1.862(8)	1.860(8)	1.860(8)	1.854(8)	1.847(8)
Al – O2	1.649(7)	1.647(7)	1.646(7)	1.644(7)	1.649(7)	1.659(7)	1.669(8)	1.675(7)	1.679(8)	1.684(8)	1.687(8)
Al – O3	1.748(5)	1.749(5)	1.747(5)	1.745(5)	1.747(5)	1.740(5)	1.738(5)	1.738(5)	1.736(5)	1.737(5)	1.738(5)
Si – O1 – Al	143.0(3)	142.8(3)	142.8(3)	142.6(3)	142.0(3)	141.2(3)	140.4(3)	140.2(3)	140.0(4)	140.0(4)	140.1(4)
Si – O2 – Al	163.7(4)	163.4(4)	163.4(4)	162.7(4)	162.3(4)	161.8(4)	161.5(5)	161.4(4)	161.5(5)	161.3(5)	161.6(5)
Si – O3 – Al	146.0(3)	146.1(3)	146.1(3)	146.2(3)	146.8(3)	147.0(3)	147.0(3)	146.9(3)	146.9(3)	146.8(3)	146.6(3)
O1 – Si – O2	106.3(4)	106.1(4)	105.8(4)	105.4(4)	104.8(4)	104.3(4)	103.8(4)	108.6(3)	103.8(4)	103.9(4)	104.2(4)
O1 – Si – O3	112.4(3)	112.5(3)	112.7(3)	113.1(3)	114.2(3)	114.9(2)	115.2(2)	115.3(2)	115.3(2)	115.2(2)	115.1(2)
O2 – Si – O3	107.4(2)	107.6(21)	107.6(2)	107.8(2)	108.3(2)	108.6(2)	108.7(3)	103.8(4)	105.0(4)	108.7(2)	108.5(3)
O3 – Si – O3	110.6(2)	110.4(2)	110.0(2)	109.3(2)	106.9(2)	105.4(4)	105.1(4)	104.4(4)	108.6(3)	105.0(4)	105.1(4)
O1 – Al – O2	110.4(3)	110.3(3)	110.4(4)	109.9(4)	109.5(4)	108.7(4)	108.0(4)	107.8(4)	107.7(4)	107.4(4)	107.4(4)
O1 – Al – O3	111.4(2)	111.4(2)	111.6(2)	111.8(2)	112.6(2)	113.1(2)	113.4(2)	113.5(2)	113.5(2)	113.6(2)	113.6(2)
O2 – Al – O3	107.4(2)	107.6(2)	107.6(2)	107.9(2)	108.4(2)	108.7(2)	108.8(2)	108.8(2)	108.7(3)	108.7(3)	108.5(3)
O3 – Al – O3	108.8(4)	108.5(4)	107.9(4)	107.4(4)	105.3(4)	104.3(4)	104.3(4)	104.4(4)	104.5(4)	104.7(4)	105.0(4)
Lattice Parameter (Å)	24.55930(8)	24.55958(8)	24.55995(8)	24.56104(9)	24.56310(9)	24.56459(9)	24.56557(9)	24.56605(9)	24.56723(9)	24.56818(9)	24.56898(9)
Unit Cell Volume (Å)	14813.2(2)	14813.7(2)	14814.3(2)	14816.3(2)	14820.0(2)	14822.7(2)	14824.5(2)	14825.4(2)	14827.5 (2)	14829.2(2)	14830.7(2)

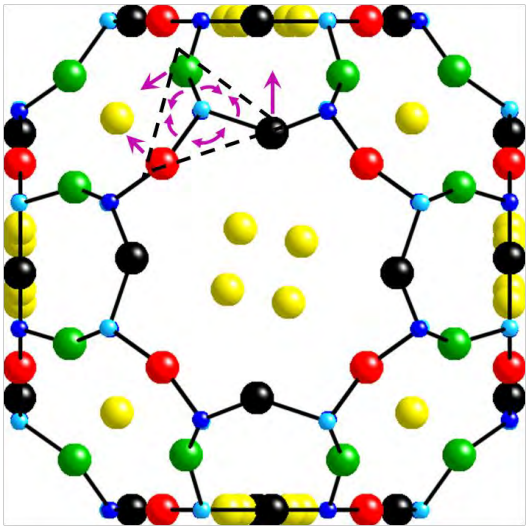

Figure 3.30 – *Diagram of a single α-cage in dehydrated Na–A down [100] plane illustrating the changes in T–O–T and O–T–O bond angles on heating (dark blue = Si, light blue = Al, black = O(1), red = O(2), green = O(3), yellow = Na).*

At 100 K, the O(3)–T–O(3) and O(1)–T–O(2) bond angles decreased by ~4.4% and ~2.3%, respectively, from their values at 300 K whereas the O(2)–T–O(3) and O(1)–T–O(3) increased by 1% and 2.2%. Taken together the changes in the Si–O–Al angles and distortions in the TO_4 tetrahedra (illustrated in figure 3.30) resulted in a contraction in the Si–O(1)–Al distance on heating by 0.16% and an overall NTE over the whole temperature range.

The different thermally induced structural changes observed in dehydrated Ag-A and Na-A suggested that the thermal expansion mechanism in zeolite A structures was not solely affected by the ionic size of the monovalent cations inside the pores. Bond valence sums, atomic partial charges and M^+–O distances were calculated and compared to determine if an electronic contribution also had an effect on the thermal expansion mechanism (tables 3.15 and 3.16). Bond valence sums are a useful tool for measuring the interaction between cation and anion pairs and were calculated using the following equation:[62]

$$s = exp\left(\frac{R_0 - R}{0.37}\right) \quad (3.3)$$

where *s* is the bond valence, *R* is the bond length and R_0 is a value corresponding to the ions forming the bond.

Atomic partial charge calculations are a method of determining the level of covalency in atomic interactions and are based upon the principle of electronegativity equalization in a structure. The effective nuclear charge of the bonded atoms were calculated using the following equations:[63]

$$\text{geometric mean} = \left((S_{atom\,x})^n (S_{atom\,y})^m\right)^{\frac{1}{n+m}} \quad (3.4)$$

$$\delta_{(atom\,x)} = \frac{\left(\text{geometric mean} - S_{(atom\,x)}\right)}{2.08\sqrt{S_{(atom\,x)}}} \quad (3.5)$$

where *S* are Sanderson's electronegativity values for specific atoms, n and m are the relative number of specific atoms in the unit cell and δ is the atomic partial charge.

Small variations in the calculated M^+–O bond distances and bond valence sums were observed when dehydrated Na-A and Ag-A were compared (table 3.15 and 3.16), however, significant differences were determined in the calculated partial charge values (3.17). As shown in tables 3.16 and 3.17, slightly higher coordination of the cations was calculated for dehydrated Ag-A as well as a considerably smaller partial charge. This suggested that greater covalency in the Ag^+–O bonds was present in dehydrated Ag-A which may have contributed to the different thermal expansion mechanisms. However, this could not be

taken to be the sole contributing factor affecting the thermal expansion mechanism as cluster formation in dehydrated Ag-A may also have had a significant influence.

Table 3.15 *– Calculated M^+–O bond distances in dehydrated Na-A and Ag-A*

M^+– O Bond		**Bond Length / Å**			
		Ag-A		**NaA**	
		300 K	**100 K**	**300 K**	**100K**
6-ring	M – O(2)	3.016(9)	3.016(7)	2.936(4)	2.933(3)
	M – O(3)	2.356(6)	2.341(6)	2.349(3)	2.358(3)
8-ring	M – O(1)	2.52(1)	2.582(9)	2.43(1)	2.43(1)
	M – O(2)	2.33(2)	2.35(1)	2.49(1)	2.52(1)

Table 3.16 – *Calculated bond valence sums for cations in the 6-ring and 8-ring in dehydrated Ag-A and Na-A at 300 K and 100 K (R_0 = 1.842 for Ag–O and 1.904 for Na–O)*

M^+– O Bond		**Bond Valence Sums**			
		Ag-A		**Na-A**	
		300 K	**100 K**	**300 K**	**100 K**
6-ring	M – O(2)	0.249	0.260	0.229	0.224
	M – O(3)	0.042	0.042	0.047	0.047
Total		0.873	0.906	0.828	0.813
8-ring	M – O(1)	0.160	0.135	0.184	0.184
	M – O(2)	0.267	0.253	0.156	0.144
Total		0.427	0.388	0.340	0.328

Table 3.17 – *Calculated partial charge on selected atoms in dehydrated Ag-A and Na-A*

Atom	**Calculated Partial Charge**	
	Ag-A	**Na-A**
M^+	0.04	0.68

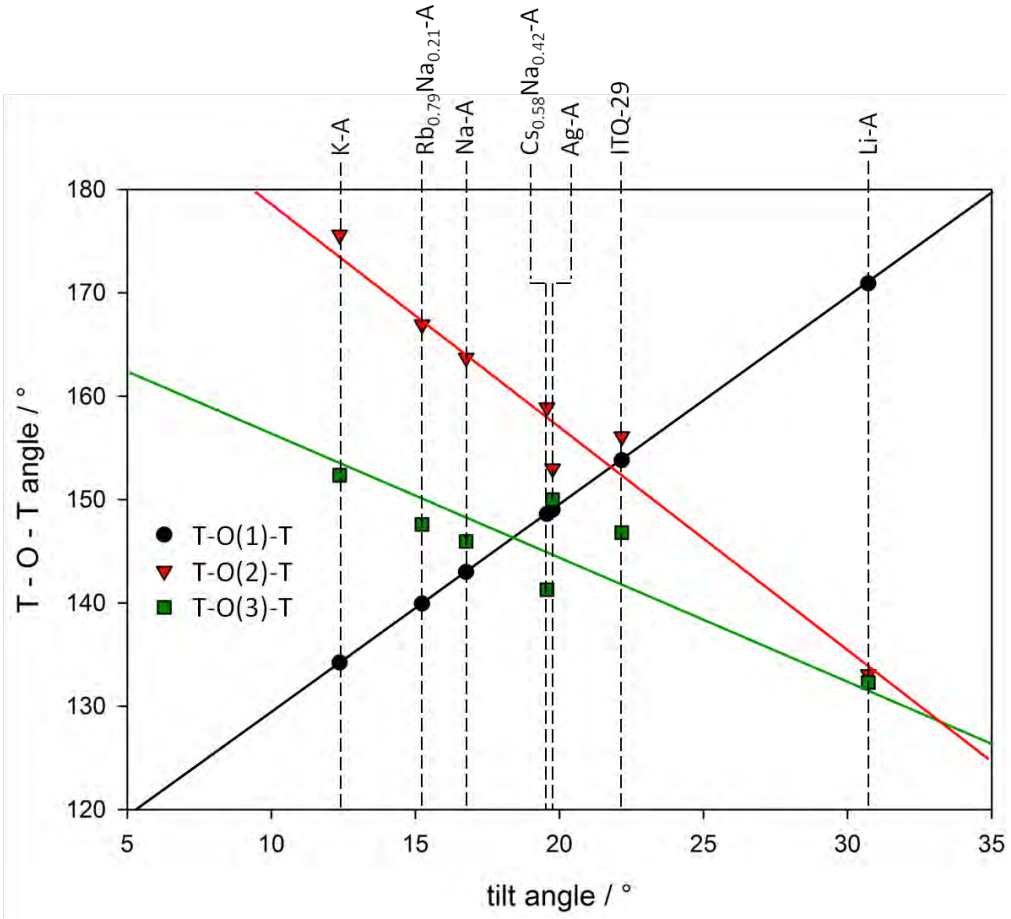

Figure 3.31 *– Graph illustrating the relationship between the Si–O–Al angles and tilt angles in all of the anhydrous LTA systems at 300 K.*

For the remaining anhydrous systems, the general trends in the thermal expansion behaviour can be explained by plotting the Si–O–Al bond angle vs tilt angle, φ (figure 3.31). Depmeier[64] first reported this relationship when investigating distortions in the zeolite A framework and defined the tilt angle as the angle between the T–O(1) bond and a plane parallel to the unit cell face:

$$\text{Tilt angle} = \tfrac{1}{2}([\text{Si–O(1)–Al}]^\circ - 109.47^\circ) \qquad (3.6)$$

As shown in figure 3.31, clear trends in the Si–O–Al bond angles were observed at 300 K as the size of the cations inside the zeolite framework (was) varied (ITQ-29 has also been included for comparison). A linear increase in the Si–O(1)–Al bond angle was observed as the size of the zeolitic cations (were) decreased, whereas a decrease was observed in the Si–O(2)–Al and Si–O(3)–Al bond angles. Through comparing figure 3.31 with the mean volume thermal expansion coefficients, it can be shown that NTE behaviour was only observed in zeolite A when the framework was least strained (i.e. when the Si–O–Al bond angles are similar and the cations are a good fit for the zeolite pores). In this region (φ = 15–25) the TO_4 tetrahedra are restricted by coordination to the cations and cannot rotate as they can in ITQ-29. This resulted in distortions to the TO_4 tetrahedra and weaker NTE coefficients. When larger or smaller cations were included in the pores, greater strain was introduced into the zeolite A framework causing the Si–O–Al bond angles to become more acute or obtuse. In these regions (φ = 5–15 and 25–35) any rotations of the TO_4 tetrahedra upon thermal excitation are restricted due the cation-induced high strain in the framework. This was well illustrated in the dehydrated Li-A and K-A systems where virtually no change in the Si–O–Al and O–T–O bond angles were observed over the whole temperature range (figures 3.32 and 3.33). Tables detailing all of the calculated bond lengths and angles for dehydrated Li-, K-, $Rb_{0.79}Na_{0.21}$- and $Cs_{0.58}Na_{0.42}$-A can be found in appendix 2. Cations occupying the 6-ring position seemed to have the most effect on the framework strain in zeolite A and consequently its thermal expansion behaviour. In dehydrated $Rb_{0.79}Na_{0.21}$-A, approximately 69% of the 6-ring positions were occupied by large Rb^+ cations and an extremely weak NTE coefficient was observed. In dehydrated $Cs_{0.58}Na_{0.42}$-A, only ~38% of the 6-ring positions were occupied by Cs^+ cations and a stronger NTE coefficient was observed. Interestingly the shift towards a positive thermal expansion coefficient correlated with amount of Na^+ cations in the 6-ring.

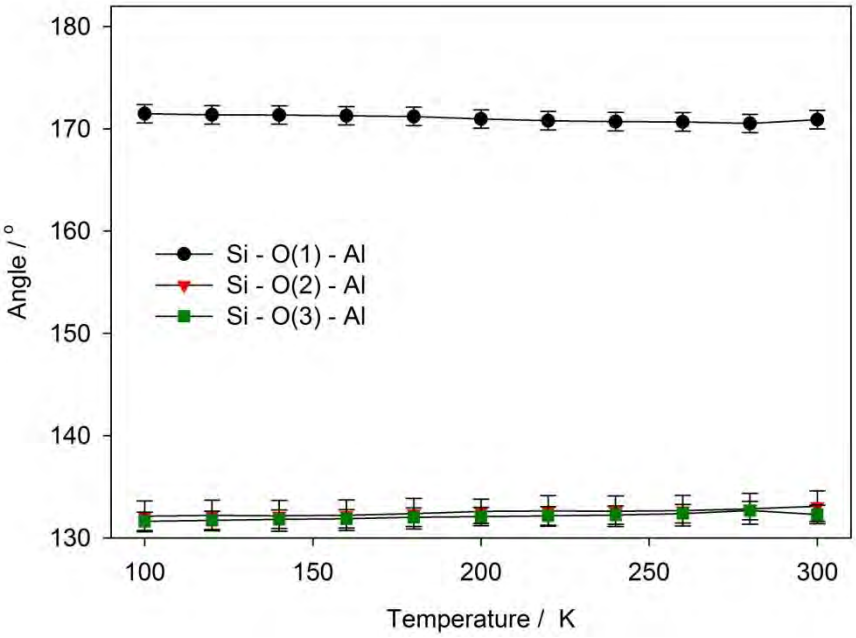

Figure 3.32 – *Calculated Si–O–Al bond angles for dehydrated Li-A from 100–300 K [errors at 3σ level].*

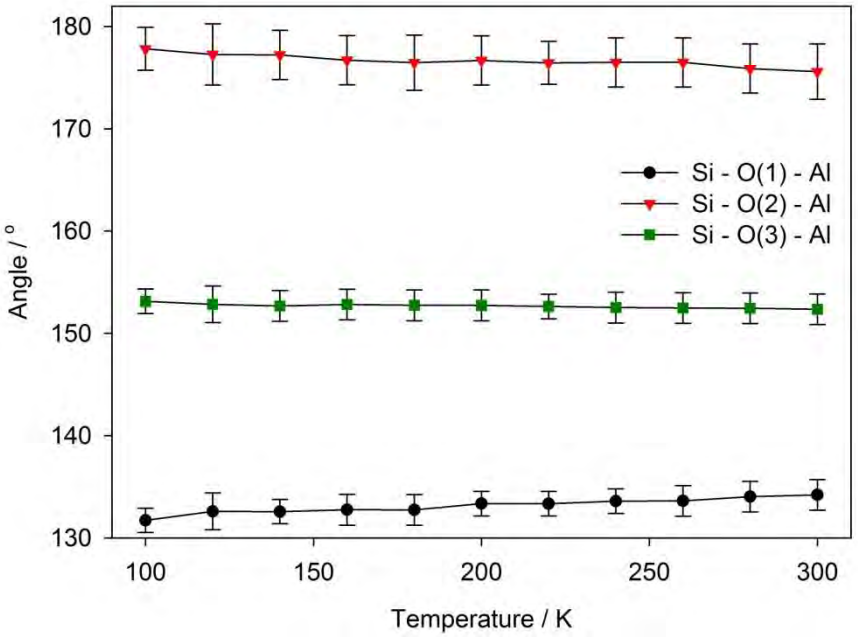

Figure 3.33 – *Calculated Si–O–Al bond angles for dehydrated K-A from 100–300 K. [errors at 3σ level].*

3.3.2 Hydrated Zeolite LTA Systems

3.3.2.1 Structural Analysis of Hydrated Ag-A at 300 K

The crystal structure of hydrated Ag-A was refined against powder synchrotron XRD data (λ = 0.825035 Å). Rietveld analysis was performed in the cubic space group $Fm\bar{3}c$ (χ^2 = 1.29, R_{wp} = 8.59%) with a calculated unit cell parameter of a = 24.5970(4) Å at 300 K (figure 3.34). The unit cell volume of hydrated Ag-A was 0.81% smaller than that of dehydrated Ag-A. This may have been due to the formation of silver clusters on dehydration causing an expansion in unit cell volume. Figure 3.35 and table 3.18 show the crystal structure and refined atomic coordinates, respectively. Five different crystallographic silver positions were identified in hydrated Ag-A. Ag(1)–Ag(4) were all located in the 6-ring position but occurred at different positions along the threefold axis. Ag(1) and Ag(2) were positioned on the β-cage side of the 6-ring with a combined occupancy of 0.34 whereas Ag(3) and Ag(4) were located on the α–cage side of the 6-ring with a combined occupancy of 0.59. This delocalisation of the 6-ring cations may have been caused by their coordination to water molecules either side of the 6-ring (O(5) and O(6)).

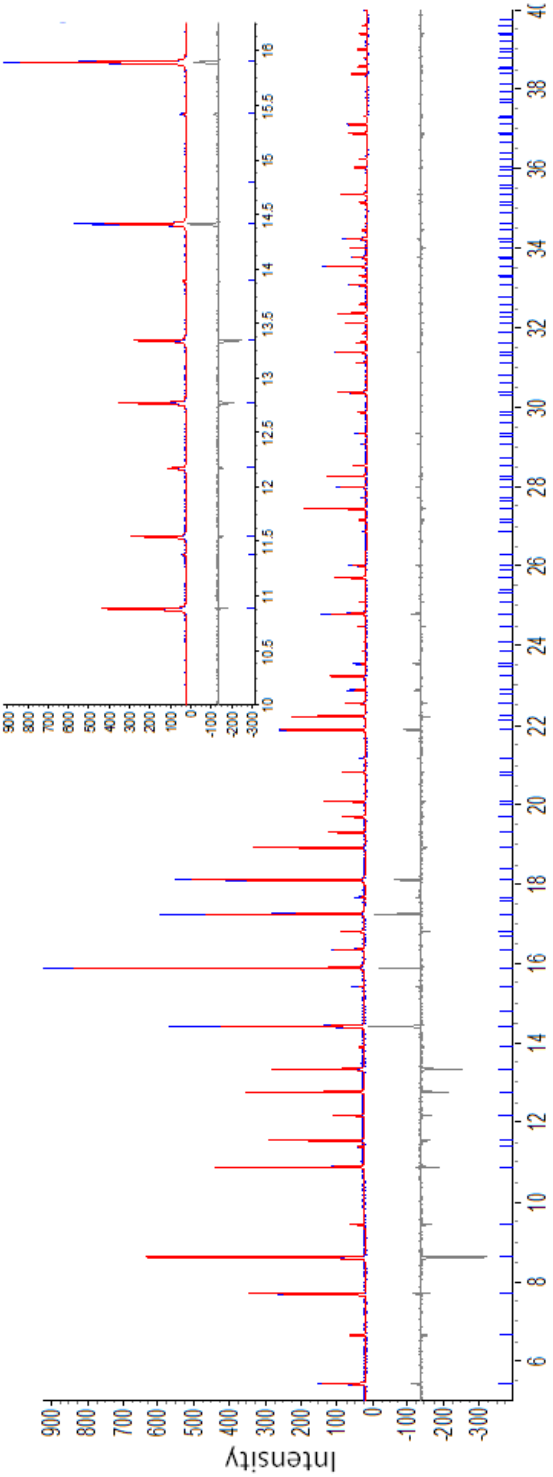

Figure 3.34 *– Rietveld refinement plot of hydrated Ag-A at 300 K.*

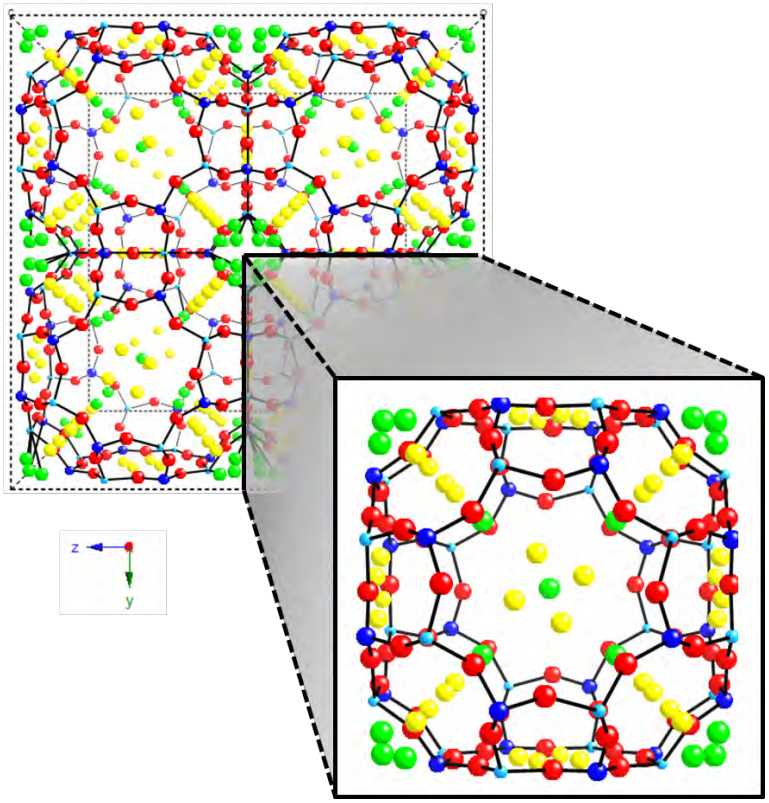

Figure 3.35 *– Crystal structure of hydrated Ag-A at 300 K (dark blue = Si, light blue = Al, red = O (zeolite framework), green = O (water) and yellow = Ag). A single α-cage highlighted for clarity.*

Table 3.18 *– Refined atomic parameters of hydrated Ag-A at 300 K.*[a]

Atom	Wyckoff position	x	y	z	Occupancy	B
Si(1)	96i	0	0.090(2)	0.184(2)	1	1.03(4)
Al(1)	96i	0	0.184(2)	0.089(2)	1	1.03(4)
O(1)	96i	0	0.109(2)	0.245(5)	1	2.26(8)
O(2)	96i	0	0.150(4)	0.151(5)	1	2.26(8)
O(3)	192j	0.051(3)	0.056(3)	0.171(2)	1	2.26(8)
Ag(1)	64g	0.069(2)	0.069(2)	0.069(2)	0.20(4)	2.06(5)
Ag(2)	64g	0.086(4)	0.086(4)	0.086(4)	0.14(4)	2.06(5)
Ag(3)	64g	0.107(3)	0.107(3)	0.107(3)	0.26(7)	2.06(5)
Ag(4)	64g	0.120(2)	0.120(2)	0.120(2)	0.33(8)	2.06(5)
Ag(5)	96i	0	0.234(3)	0.205(2)	0.13(1)	2.06(5)
O(4)	8a	0.25	0.25	0.25	0.23(2)	10(1)
O(5)	192j	0.941(5)	0.027(3)	0.025(3)	0.291(5)	10(1)
O(6)	64g	0.156(8)	0.156(8)	0.156(8)	0.39(2)	10(1)

[a] *a = 24.5970(4) Å, space group = $Fm\bar{3}c$, χ^2 = 1.29, R_{wp} = 8.59 %, R_p = 6.66 %*

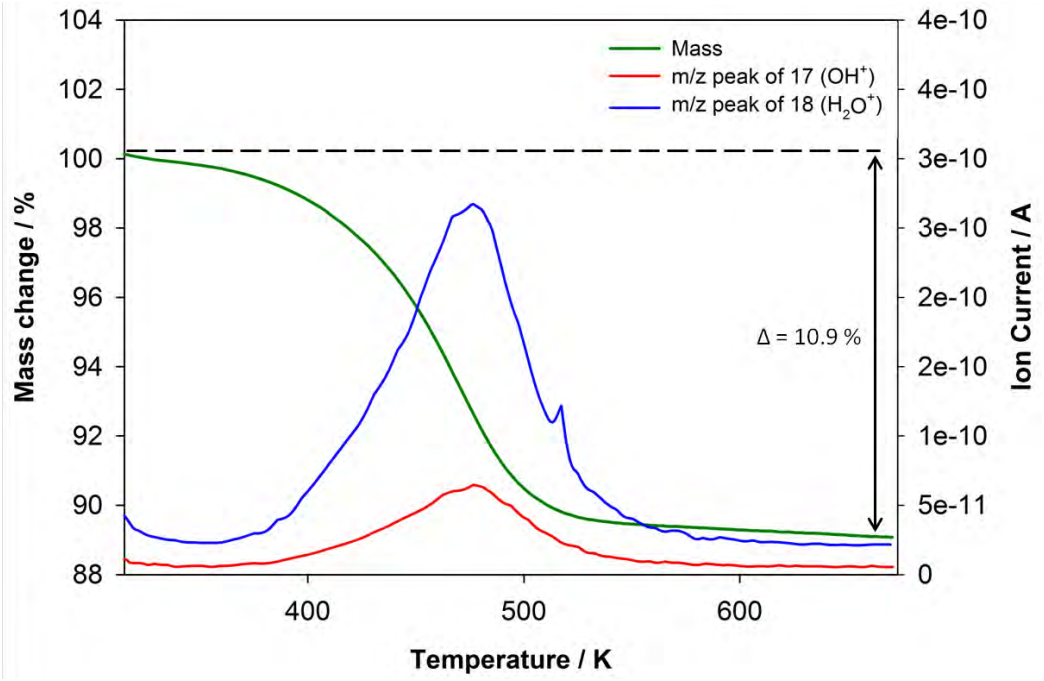

Figure 3.36 *– TGA and mass spectroscopy plot of hydrated Ag-A from 298–673 K.*

Due to the high disorder of water molecules in the zeolite framework not all water molecules were accounted for in the Rietveld model. TGA and mass spectrometry analysis showed that there was a 10.9% weight loss upon dehydration (figure 3.36), which equated to ~18.7 water molecules per 12 Å cell. Ag^+ cations in the 8-ring position (Ag(5)) were located just off-centre in the ring. Cations in the 4-ring position could not be identified through Fourier mapping.

Significant distortions in the TO_4 tetrahedra were observed in hydrated Ag-A at 300 K. As shown in table 3.19, large contractions away from the ideal tetrahedral angle were observed in the O(1)–T–O(2) bond angles whereas smaller expansions were observed in O(2)–T–O(3) bond angles. This distortion of the tetrahedra may have been caused by the high concentration of water molecules in the structure, which in turn had an effect on the position of the cations and the zeolite framework.

Table 3.19 *– Calculated bond lengths and angles of the TO_4 tetrahedra in hydrated Ag-A [errors at 1σ level].*

Bond Lengths		Bond Angles	
Si – O(1)	1.57(1)	O(1) – Si – O(2)	101.4(6)
Si – O(2)	1.68(1)	O(1) – Si – O(3)	110.4(3)
Si – O(3)	1.535(7)	O(2) – Si – O(3)	112.7(4)
Al – O(1)	1.83(1)	O(3) – Si – O(3)	109.0(6)
Al – O(2)	1.73(1)	O(1) – Al – O(2)	103.6(6)
Al – O(3)	1.700(8)	O(1) – Al – O(3)	108.6(3)
		O(2) – Al – O(3)	113.9(3)
		O(3) – Al – O(3)	108.1(6)

3.3.2.2 Structural Analysis of the Hydrated Alkali-Metal-Exchanged Zeolite A Systems at 300 K

All crystal structures of the hydrated alkali-metal-exchanged zeolite A systems were refined from powder synchrotron XRD data (λ = 0.827412 Å) in the cubic space group $Fm\bar{3}c$. It is worth noting that the refinement process proved a lot more difficult with the hydrated systems (especially for Li-A) due to the high quantity of disordered water molecules inside the pores. This resulted in the structural refinements for the hydrated systems being much poorer when compared with the dehydrated systems. In the case of hydrated Li-A, the occupancy and thermal parameter of the Li^+ cations had to be restrained and constrained, respectively because of the relatively poor scattering ability. Rietveld refinement plots and refined atomic coordinates of all the hydrated systems can be found in figures 3.37–3.41 and tables 3.20–3.24, respectively.

Table 3.20 *– Refined atomic parameters of hydrated Li-A at 300K*[a]

	Atom	Wyckoff position	*x*	*y*	*z*	Occupancy	B
Framework	Si(1)	96i	0	0.0931(2)	0.1819(3)	1	0.5(1)
	Al(1)	96i	0	0.1822(3)	0.0919(2)	1	0.5(1)
	O(1)	96i	0	0.1032(2)	0.2459(5)	1	1.2(2)
	O(2)	96i	0	0.1554(4)	0.1624(4)	1	1.2(2)
	O(3)	192j	0.0549(3)	0.0597(3)	0.1592(1)	1	1.2(2)
6R	Li(1)	64g	0.0774(7)	0.0774(7)	0.0774(7)	0.81(3)	0.3
	Li(2)	64g	0.101(2)	0.101(2)	0.101(2)	0.19(3)	0.3
8R	Li(3)	96i	0	0.185(3)	0.265(3)	0.25(2)	0.3
Water	O(4)	64g	0.1636(2)	0.1636(2)	0.1636(2)	1.00(9)	1.6(2)

[a] *$a = 23.88056(8)$ Å, space group: $Fm\bar{3}c$, $\chi^2 = 4.12$, $R_{wp} = 25.57\%$, $R_p = 12.59\%$.*

Table 3.21 *– Refined atomic parameters of hydrated Na-A at 300K*[a]

	Atom	Wyckoff position	*x*	*y*	*z*	Occupancy	B
Framework	Si(1)	96i	0	0.0940(1)	0.1850(2)	1	0.36(3)
	Al(1)	96i	0	0.1850(2)	0.0920(2)	1	0.36(3)
	O(1)	96i	0	0.1122(2)	0.2467(4)	1	0.50(5)
	O(2)	96i	0	0.1474(3)	0.1486(3)	1	0.50(5)
	O(3)	192j	0	0.0572(2)	0.1739(1)	1	0.50(5)
6R	Na(1)	64g	0.1081(2)	0.1081(2)	0.1081(2)	0.641(6)	1.2(1)
	Na(2)	64g	0.9147(3)	0.9147(3)	0.9147(3)	0.359(7)	1.2(1)
8R	Na(3)	96i	0	0.2682(6)	0.1889(6)	0.250(5)	1.2(1)
Water	O(4)	48f	0.9578(4)	0.25	0.25	0.654(8)	0.55(5)
	O(5)	64g	0.1828(3)	0.1828(3)	0.1828(3)	0.414(9)	0.55(5)
	O(6)	64g	0.1571(3)	0.1571(3)	0.1571(3)	0.598(9)	0.55(5)

[a] *$a = 24.59971(3)$ Å, space group: $Fm\bar{3}c$, $\chi^2 = 3.28$, $R_{wp} = 20.86$ %, $R_p = 12.72$ %.*

Table 3.22 *– Refined atomic parameters of hydrated K-A at 300K*[a]

	Atom	Wyckoff position	*x*	*y*	*z*	Occupancy	B
Framework	Si(1)	96i	0	0.0932(3)	0.1891(3)	1	2.0(1)
	Al(1)	96i	0	0.1883(3)	0.0918(3)	1	2.0(1)
	O(1)	96i	0	0.1245(3)	0.2492(6)	1	4.0(2)
	O(2)	96i	0	0.1525(5)	0.1518(5)	1	4.0(2)
	O(3)	192j	0	0.0579(2)	0.1750(2)	1	4.0(2))
6R	K(1)	64g	0.1337(1)	0.1337(1)	0.1337(1)	0.827(3)	0.66(2)
	K(2)	64g	0.0784(4)	0.0784(4)	0.0784(4)	0.173(3)	0.66(2)
8R	K(3)	96i	0	0.2503(3)	0.2240(3)	0.25(2)	0.66(2)
Water	O(4)	64g	0.0499(2)	0.0499(2)	0.0499(2)	0.746(9)	5.0(6)
	O(5)	64g	0.2190(9)	0.2190(9)	0.2190(9)	0.171(7)	5.0(6)
	O(6)	64g	0.1778(4)	0.1778(4)	0.1778(4)	0.61(1)	5.0(6)

[a] *$a = 24.59137(4)$ Å, space group: $Fm\bar{3}c$, $\chi^2 = 3.69$, $R_{wp} = 20.03$ %, $R_p = 10.45$ %.*

Table 3.23 *– Refined atomic parameters of hydrated* $Rb_{0.79}Na_{0.21}$*-A at 300K*[a]

	Atom	Wyckoff position	*x*	*y*	*z*	Occupancy	B
Framework	Si(1)	96i	0	0.0926(4)	0.1840(4)	1	0.57(4)
	Al(1)	96i	0	0.1844(5)	0.0913(5)	1	0.57(4)
	O(1)	96i	0	0.1190(3)	0.2480(9)	1	1.9(2)
	O(2)	96i	0	0.1478(8)	0.1481(8)	1	1.9(2)
	O(3)	192j	0.0486(4)	0.0593(3)	0.1747(2)	1	1.9(2)
6R	Rb(1)	64g	0.1346(9)	0.1346(9)	0.1346(9)	0.681(2)	3.75(6)
	Rb(2)	64g	0.0514(2)	0.0514(2)	0.0514(2)	0.319(2)	3.75(6)
8R	Rb(3)	96i	0	0.2255(6)	0.250(8)	0.20(2)	3.75(6)
Water	O(4)	48f	0.25	0.25	0.958(1)	0.97(4)	6.0(8)
	O(5)	64g	0.242(3)	0.242(3)	0.242(3)	0.132(4)	6.0(8)
	O(6)	64g	0.1715(7)	0.16972(4)	0.16972(4)	0.40(1)	6.0(8)

[a] *$a = 24.71682(18)$ Å, space group: $Fm\bar{3}c$, $\chi^2 = 3.90$, $R_{wp} = 19.16$ %, $R_p = 9.69$ %.*

Table 3.24 *– Refined atomic parameters of hydrated* $Cs_{0.58}Na_{0.42}$-A *at 300K*[a]

	Atom	Wyckoff position	*x*	*y*	*z*	Occupancy	B
Framework	Si(1)	96i	0	0.0916(3)	0.1855(3)	1	0.77(3)
	Al(1)	96i	0	0.1868(3)	0.0907(3)	1	0.77(3)
	O(1)	96i	0	0.1111(2)	0.2445(5)	1	2.61(7)
	O(2)	96i	0	0.1460(4)	0.1495(4)	1	2.61(7)
	O(3)	192j	0	0.0577(3)	0.1714(1)	1	2.61(7)
6R	Na(1)	64g	0.0872(9)	0.0872(9)	0.0872(9)	0.13(8)	0.8(4)
	Na(2)	64g	0.1068(4)	0.1068(4)	0.1068(4)	0.279(9)	0.8(4)
	Cs(1)	64g	0.0463(3)	0.0463(3)	0.0463(3)	0.074(1)	6.1(2)
	Cs(2)	64g	0.1425(2)	0.1425(2)	0.1425(2)	0.232(3)	6.1(2)
8R	Cs(3)	96i	0	0.250(5)	0.246(4)	0.130(9)	6.1(2)
Water	O(4)	48f	0.9682(7)	0.25	0.25	0.95(9)	6.0(3)
	O(5)	64g	0.2213(2)	0.2213(2)	0.2213(2)	0.381(4)	6.0(3)
	O(6)	64g	0.169(1)	0.169(1)	0.169(1)	0.26(2)	6.0(3)

[a] *$a = 24.57754(4)$ Å, space group: $Fm\bar{3}c$, $\chi^2 = 1.86$, $R_{wp} = 14.16$ %, $R_p = 10.38$ %.*

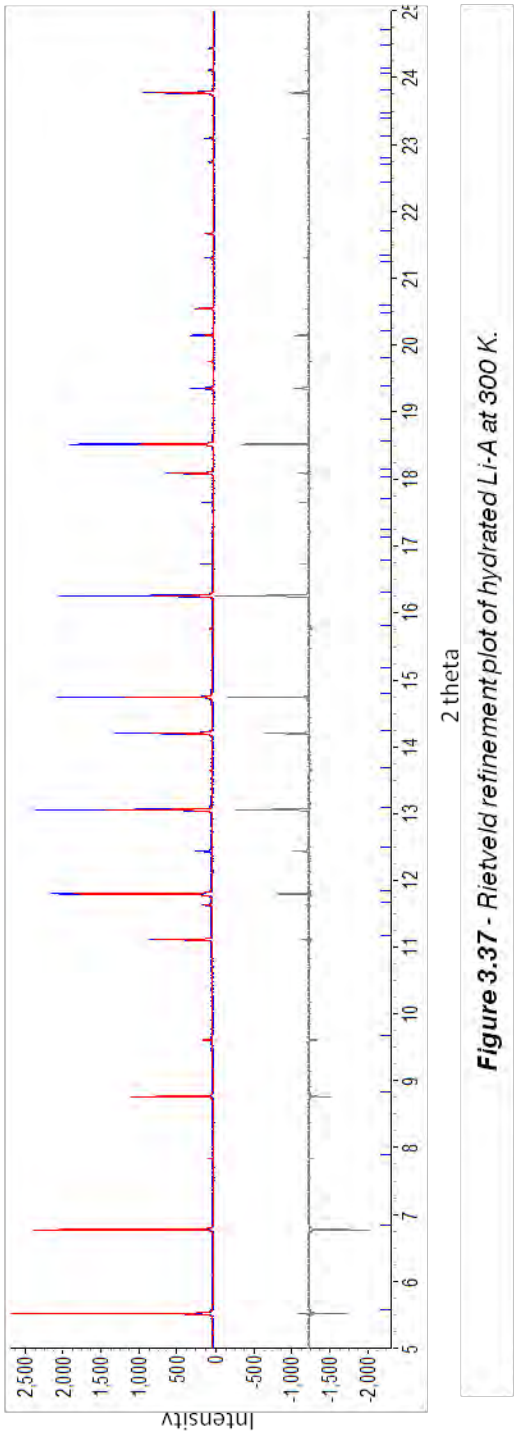

Figure 3.37 *- Rietveld refinement plot of hydrated Li-A at 300 K.*

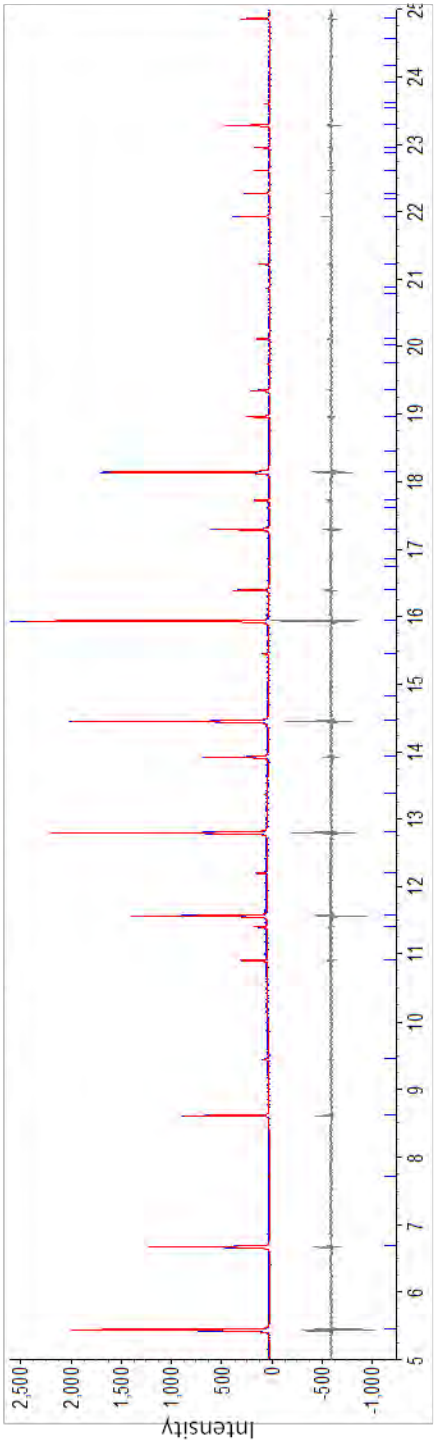

Figure 3.38 *- Rietveld refinement plot of hydrated Na-A at 300 K.*

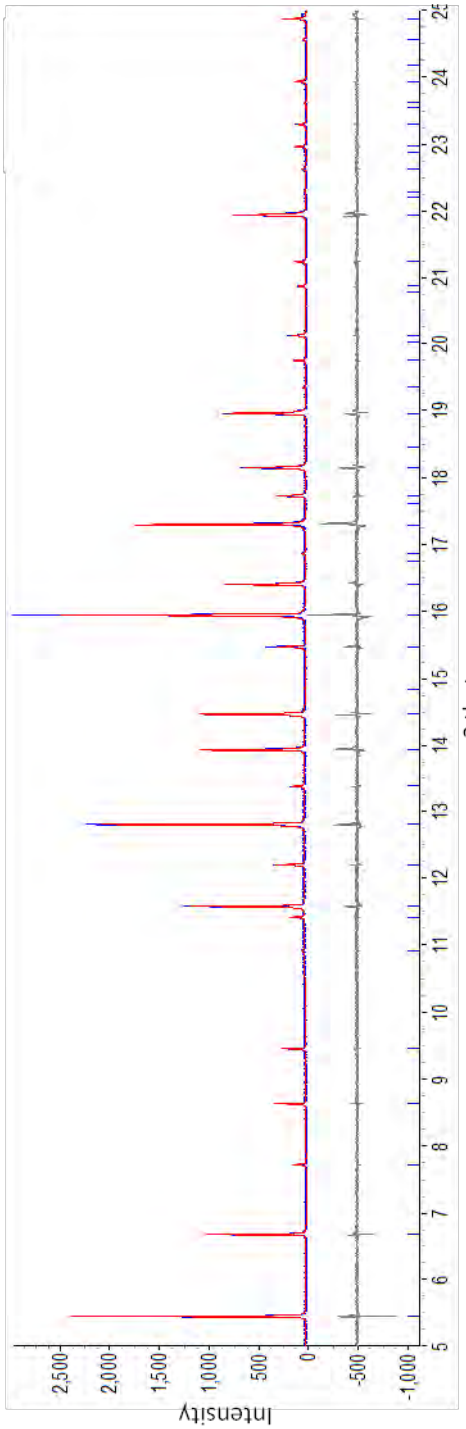

Figure 3.39 *- Rietveld refinement plot of hydrated K-A at 300 K.*

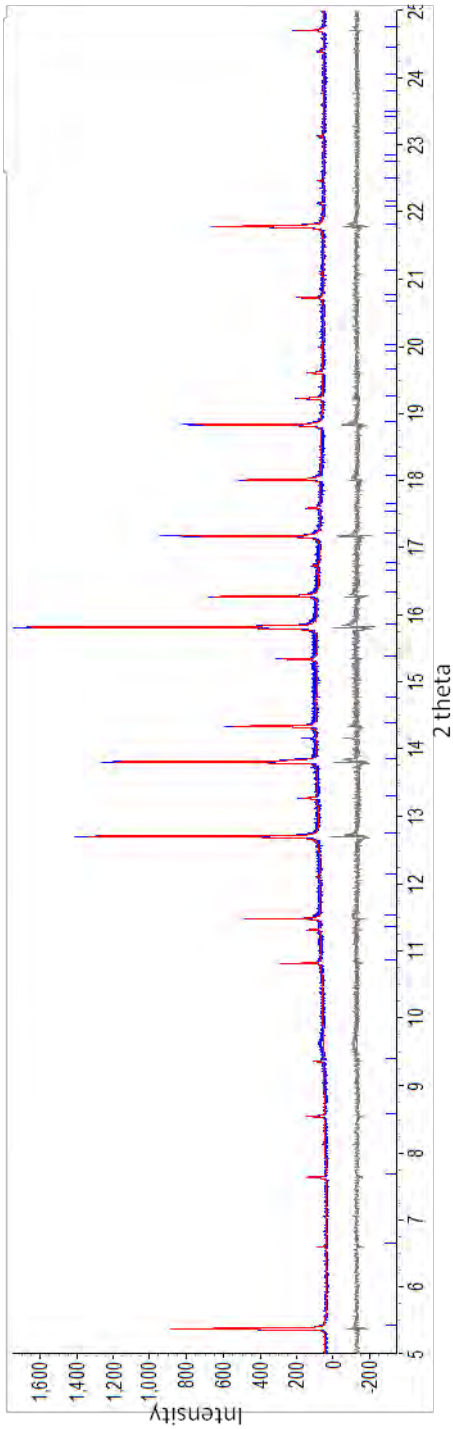

Figure 3.40 *- Rietveld refinement plot of hydrated* $Rb_{0.79}Na_{0.21}$*-A at 300 K.*

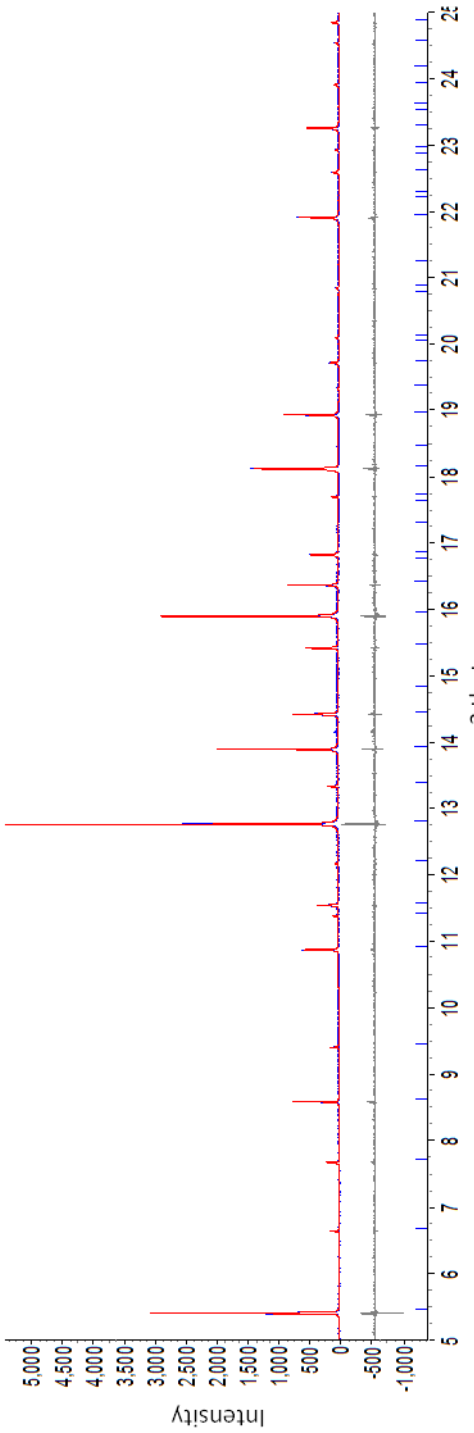

Figure 3.41 *- Rietveld refinement plot of hydrated* $Cs_{0.58}Na_{0.42}$*-A at 300 K.*

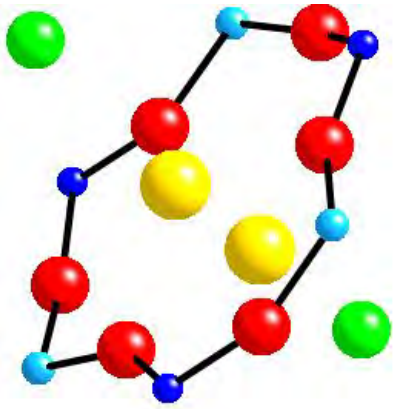

Figure 3.42 *– Diagram illustrating water molecules coordinating to cations either side of the 6-ring (dark blue = Si, light blue = Al, red = O (zeolite), yellow = M^+ and green = O (water).*

In contrast to Ag-A, larger unit cell volumes were observed upon hydration for all of the alkali-metal-exchanged zeolites. Two common cation positions were identified in the hydrated systems: the 6-ring and 8-ring. In the majority of the hydrated systems, cations in the 6-ring site were not found to occupy the centre of the ring but were located either side in the α-cage or β-cage. Similarly to hydrated Ag-A, this delocalisation over the site may have been caused by the coordination of the cations to water molecules either side of the 6-ring (figure 3.42). Li^+ cations were found to occupy the centre of the 6-ring site but were refined to have a relatively low occupancy. Poor scattering of the Li^+ cations meant it was extremely difficult to identify the small cations amongst the many disordered water molecules using powder XRD data. In contrast to the literature,[53-55] cations in the 8-ring position were not shifted into the α-cage in the hydrated alkali-metal-exchanged systems, but remained in the plane of the 8-ring as observed in the dehydrated systems. Larger cations were located near the centre of the 8-ring and smaller cations were located further away. Cations in the 4-ring position were not identified. TGA and mass spectroscopy analysis showed that each 12 Å cell contained ~20 water molecules in all of the hydrated systems (table 3.25). This was similar to the reported values determined through single crystal XRD.[51, 53, 55]

Table 3.25 *– Calculated water content from TGA for all of the hydrated alkali-metal-exchanged zeolite A systems at 300 K.*

Hydrated System	Water molecules	
	/ **unit cell**	/ **12^3 Å^3**
Li-A	155.2	19.4
Na-A	158.4	19.8
K-A	161.6	20.2
$Rb_{0.79}Na_{0.21}$-A	136.8	17.1
$Cs_{0.58}Na_{0.42}$-A	152.8	19.1

Table 3.26 *- Calculated Si–O–Al bond angles for all of the dehydrated alkali metal exchanged zeolite A systems at 300 K [error at 1σ level].*

Hydrated System	T–O(1)–T	T–O(2)–T	T–O(3)–T
Li-A	162.9(4)	128.7(5)	133.5(3)
Na-A	147.2(3)	157.9(5)	154.6(3)
K-A	123.0(4)	152.1(6)	155.9(3)
$Rb_{0.79}Na_{0.21}$-A	135.2(5)	152.1(6)	154.5(5)
$Cs_{0.58}Na_{0.42}$-A	143.7(5)	158.2(7)	145.5(4)

Table 3.26 shows the calculated Si–O–Al bond angles for the hydrated zeolite A systems at 300 K. Similarly to the dehydrated system, a large contraction in the 8-ring diameter was observed as the size of the cations was increased, which was mirrored by the contraction in the Si–O(1)–Al bond angle. Significant expansion of the 6-ring was also observed when larger cations than Li^+ were introduced, however, the diameter of the 6-ring remained roughly the same in Na- and K-A. As shown in table 3.26, the Si–O(2)–Al and Si–O(3)–Al bond angles of these systems were comparable. This similarity in 6-ring diameter may have been caused by both Na^+ and K^+ cations being positioned either side of the ring in the hydrated systems due to their coordination to water.

Significant distortions in the TO_4 tetrahedra were also observed in hydrated alkali-metal-exchanged systems, similar to those observed in hydrated Ag-A. With the exception of Na-A, large contractions away from the ideal tetrahedra were observed in all the O(1)–T-O(2) bond angles whereas smaller expansions were observed in O(2)–T–O(3) bond angles. These distortions in the tetrahedra again may have been caused by the high concentration of water molecules in the structure, which in turn had an effect on the position of the cations and the zeolite framework.

3.3.2.3 Thermal Expansion Studies of Hydrated Ag-A

Variable temperature powder synchrotron XRD studies (λ = 0.825035 Å) were used to determine the thermal expansion behaviour of hydrated Ag-A from 100–300 K. XRD patterns were collected at 20 K intervals and Rietveld analysis was performed at each interval to monitor any thermally induced structural changes. As shown in figure 3.43, much more complicated thermal expansion behaviour was observed in hydrated Ag-A when compared to the dehydrated system. PTE was observed from 260–300 K with a $\overline{\alpha_v}_{(100–300\ K)}$ value of 18.7 x 10^{-6} K^{-1}. NTE was observed from 220–260 K with a $\overline{\alpha_v}_{(100\text{-}300\ K)}$ value of – 21.1 x 10^{-6} K^{-1}. Below 220 K a small thermal hysteresis was observed with a $\overline{\alpha_v}_{(100–300\ K)}$ value of 40 x 10^{-6} K^{-1}. Despite these dramatic changes in unit cell volume relatively little change in the powder XRD patterns was observed over this temperature range (figure 3.44). This was also reflected in the calculated Si–O–Al and O–T–O angles as shown in figures 3.45, 3.46 and table 3.27.

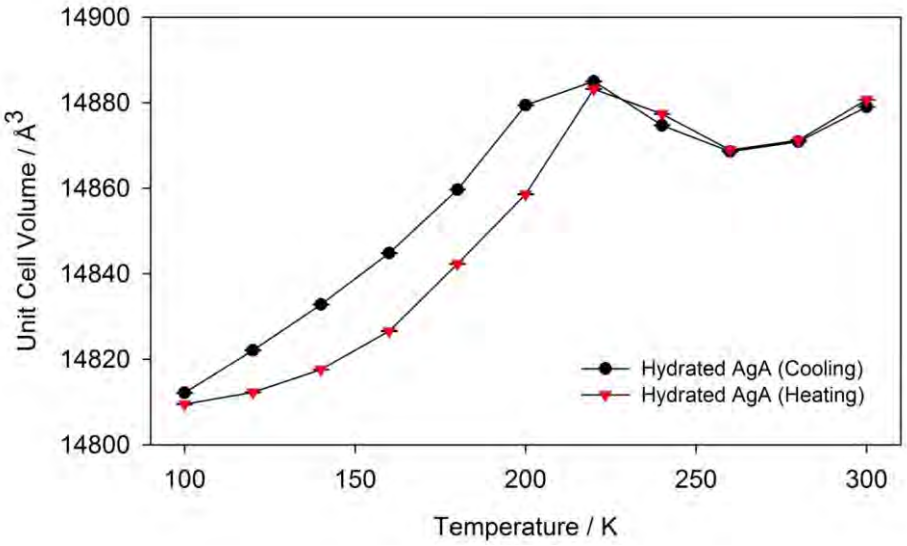

Figure 3.43 *- Calculated unit cell volumes of hydrated Ag-A from 100–300 K [errors at 3σ level].*

No structural mechanism has been determined behind the overall PTE behaviour observed in hydrated Ag-A. One possible hypothesis is that the high content of water molecules in the zeolite pores prevented the TO_4 tetrahedra from rotating upon heating thus shutting down the NTE mechanism. Thermal expansion of the unit cell may then have proceeded due to normal convention however significant changes in the calculated bond were not shown within error.

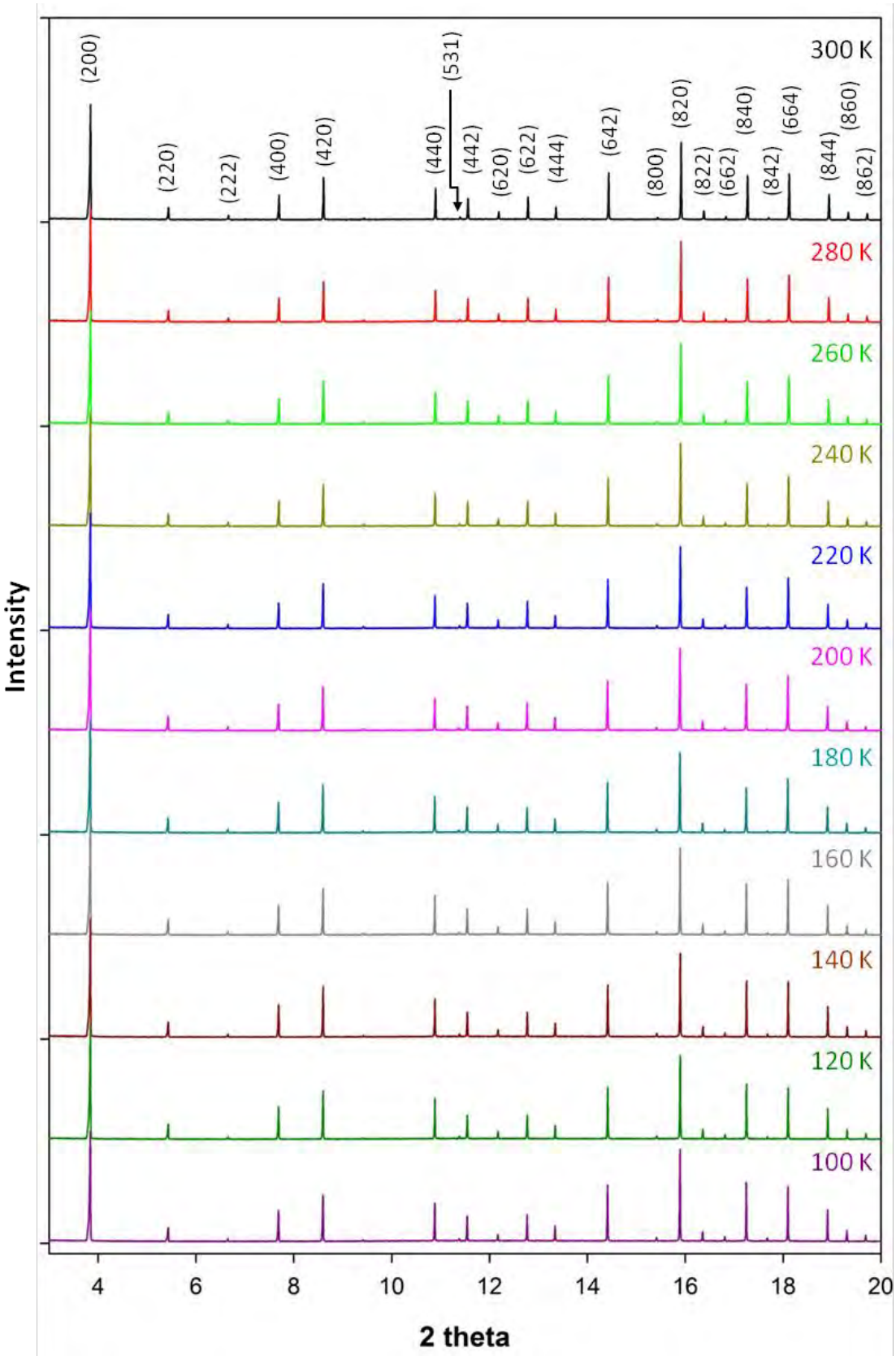

Figure 3.44 *– Powder synchrotron XRD patterns of hydrated Ag-A from 100–300 K.*

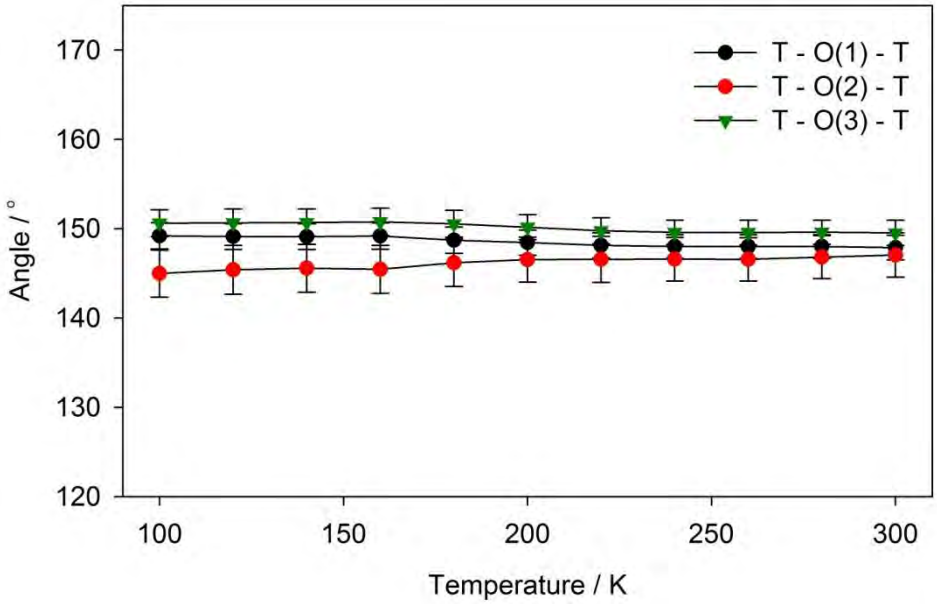

Figure 3.45 – *Calculated Si–O–Al bond angles for hydrated Ag-A from 100–300 K [errors at 3σ level].*

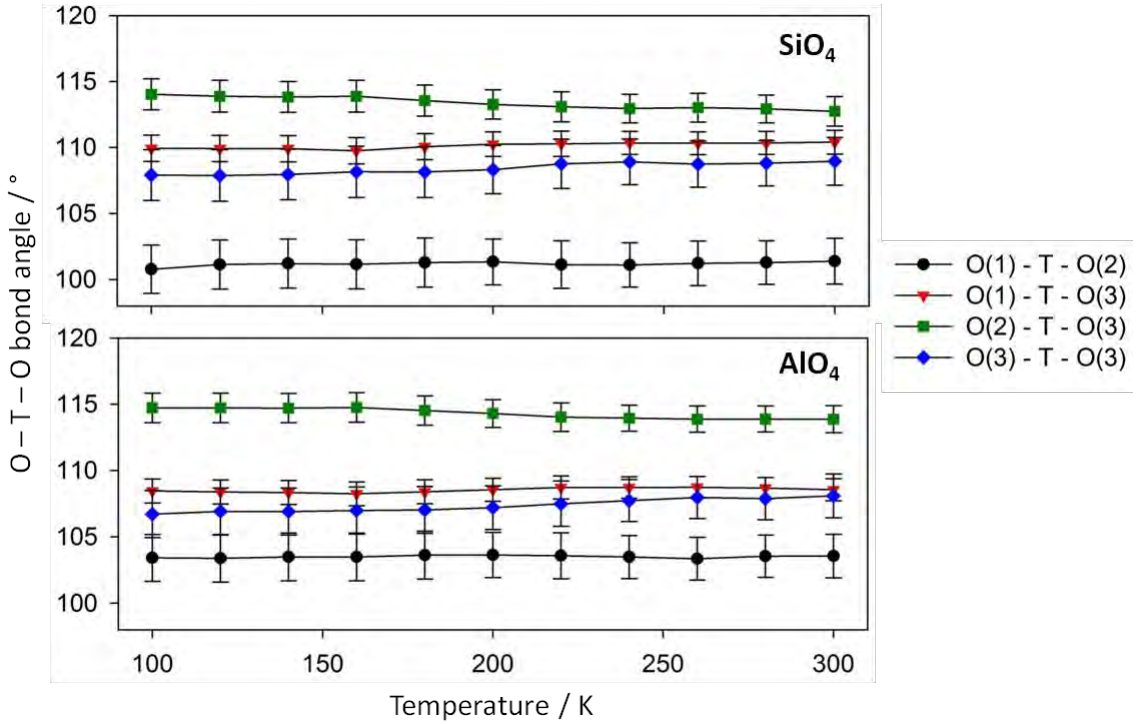

Figure 3.46 – *Calculated O–T–O bond angles for hydrated Ag-A from 100–300 K [errors at 3σ level].*

Table 3.27 *– Bond Distances (Å) and Angles (deg) in Hydrated Ag–A from 100–300 K (errors at 1σ level).*

Bond Length/Angle	Temperature										
	300K	280K	260K	240K	220K	200K	180K	160K	140K	120K	100K
Si – O1	1.57(1)	1.57(1)	1.57(1)	1.58(1)	1.57(1)	1.57(1)	1.56(1)	1.57(1)	1.56(1)	1.56(1)	1.56(1)
Si – O2	1.68(1)	1.67(1)	1.67(1)	1.68(1)	1.68(1)	1.68(1)	1.68(2)	1.68(2)	1.68(2)	1.68(2)	1.68(2)
Si – O3	1.535(7)	1.536(7)	1.539(7)	1.536(7)	1.536(8)	1.531(8)	1.529(8)	1.530(8)	1.529(8)	1.528(8)	1.526(8)
Al – O1	1.83(1)	1.82(1)	1.82(1)	1.81(1)	1.81(1)	1.81(1)	1.81(1)	1.80(1)	1.81(1)	1.81(1)	1.81(1)
Al – O2	1.73(1)	1.74(1)	1.74(1)	1.73(1)	1.73(1)	1.73(1)	1.73(1)	1.74(2)	1.74(2)	1.74(2)	1.74(1)
Al – O3	1.670(8)	1.700(7)	1.700(7)	1.705(7)	1.706(8)	1.706(8)	1.702(8)	1.700(8)	1.700(8)	1.701(8)	1.702(8)
Si – O1 – Al	147.9(5)	148.0(4)	148.0(4)	148.0(4)	148.1(5)	148.5(5)	148.7(5)	149.2(5)	149.1(5)	149.1(5)	149.2(5)
Si – O2 – Al	147.1(8)	146.8(8)	146.6(8)	146.6(8)	146.6(9)	146.5(8)	146.2(9)	145.5(9)	145.6(9)	145.4(9)	145.0(9)
Si – O3 – Al	149.6(5)	149.6(5)	149.6(5)	149.6(5)	149.8(5)	150.27(5)	150.6(5)	150.8(5)	150.7(5)	150.7(5)	150.6(5)
O1 – Si – O2	101.4(6)	101.3(6)	101.2(6)	101.1(6)	101.1(6)	101.3(6)	101.3(6)	101.2(6)	101.2(6)	101.1(6)	100.8(6)
O1 – Si – O3	110.4(3)	110.4(3)	110.3(3)	110.4(3)	110.3(3)	110.3(3)	110.1(3)	109.8(3)	109.9(3)	109.9(3)	109.9(3)
O2 – Si – O3	112.7(4)	112.9(4)	113.0(4)	113.0(4)	113.1(4)	113.3(4)	113.6(4)	113.9(4)	113.8(4)	113.9(4)	114.0(4)
O3 – Si – O3	109.0(6)	108.8(6)	108.7(6)	108.9(6)	108.8(6)	108.3(6)	108.2(6)	108.2(7)	108.0(6)	107.9(7)	107.9(6)
O1 – Al – O2	103.6(6)	103.6(5)	103.4(5)	103.5(5)	103.6(6)	103.6(6)	103.6(6)	103.5(6)	103.5(6)	103.4(6)	103.4(6)
O1 – Al – O3	108.6(3)	108.7(3)	108.7(3)	108.7(3)	108.7(3)	108.6(3)	108.4(3)	108.3(3)	108.4(3)	108.4(3)	108.5(3)
O2 – Al – O3	113.9(3)	113.9(3)	113.9(3)	114.0(3)	114.0(4)	114.3(4)	114.5(4)	114.8(4)	114.7(4)	114.7(4)	114.7(4)
O3 – Al – O3	108.1(6)	107.9(5)	108.0(5)	107.7(5)	107.5(6)	107.2(6)	107.0(6)	107.0(6)	106.9(6)	106.9(6)	106.7(6)
Lattice Parameter (Å)	24.5966(1)	24.5913(1)	24.5901(1)	24.5947(1)	24.5979(1)	24.5844(1)	24.5754(1)	24.5667(1)	24.5618(1)	24.5588(1)	24.5573(1)
Unit Cell Volume (Å)	14880.76(8)	14871.15(8)	14868.97(8)	14877.32(8)	14883.1(1)	14858.6(1)	14842.3(1)	14826.6(1)	14817.7(1)	14812.3(1)	14809.6(1)

3.3.2.4 Thermal Expansion Studies of the Hydrated Alkali-Metal-Exchanged Zeolite A Systems

Variable temperature powder synchrotron XRD studies (λ = 0.827412 Å) were used to determine the thermal expansion behaviour of all the hydrated alkali-metal-exchanged zeolite A systems from 100–300 K. XRD patterns were collected at 20 K intervals and Rietveld analysis was performed at each interval to monitor any thermally induced structural changes. Linear PTE behaviour was observed in all of the hydrated systems as detailed in table 3.28. Mean volume thermal expansion coefficients were shown to increase in value in the fully exchanged systems as the size of the cations in the pores was increased. Smaller PTE coefficients were determined for the partially exchanged $Rb_{0.79}Na_{0.21}$-A and $Cs_{0.58}Na_{0.42}$-A systems when compared to Na-A. No structural mechanism has been determined behind the PTE behaviour observed in hydrated alkali-metal-exchanged systems. As with hydrated Ag-A no significant changes in the Si–O–Al and O–T–O bond angles were determined over this temperature range that would explain the thermal expansion behaviour (appendix 2). The high content of water molecules in the zeolite pores again may have prevented the TO_4 tetrahedra from rotating upon heating thus shutting down the NTE mechanism.

Table 3.28 – *Calculated mean volume thermal expansion coefficients of the hydrated LTA systems.*

Hydrated LTA System	Mean Volume Thermal Expansion Coefficient / x 10^{-6} K^{-1}
Li–A	16.5
Na–A	18.8
K–A	32.6
$Rb_{0.79}Na_{0.21}$-A	11.9
$Cs_{0.58}Na_{0.42}$-A	14.0

3.4 Conclusion

Strong NTE behaviour was observed in the purely siliceous form of the LTA structure where the pores of the zeolite framework are vacant. As with the majority of siliceous zeolite frameworks, NTE was caused by the rotation of the rigid SiO_4 upon thermal excitation causing a decrease in the zeolite pore volume and an overall contraction of the unit cell. When cations were present into the structure, the rotation of the TO_4 tetrahedra was restricted. Depending upon the size of the monovalent cations, different levels of strain were introduced into the zeolite framework. Ideally sized cations such as Ag^+ and Na^+ were able to fit perfectly into the zeolite 6-ring and caused the least amount of strain. Cation binding caused rotation of the TO_4 tetrahedra to be restricted in dehydrated Na- and Ag-A resulting in a distortion of the tetrahedra and a weaker NTE coefficient. Cations that were not a good fit for the 6-ring (such as K^+ and Li^+) introduced a much larger strain in the zeolite framework and significantly changed the Si–O–Al bond angles. In these systems the TO_4 tetrahedra were prevented from moving upon thermal excitation resulting in a weak PTE. When both cations and water molecules were present in the zeolite framework PTE behaviour was observed. Stronger PTE coefficients were shown as the size of the zeolitic cation was increased. No structural mechanism has been determined for the PTE behaviour. It was clear that the mechanism responsible for the NTE behaviour in the LTA-zeolite was shut down when cations and water molecules were introduced. This may have been due high pore content restricting the movement of the framework tetrahedra.

3.5 References

1. J. W. Couves, R. H. Jones, S. C. Parker, P. Tschaufeser and C. R. A. Catlow, *J. Phys.: Condens. Matter*, 1993, **5**, 329-332.
2. X. Wang, J. C. Hanson, J. Szanyi and J. A. Rodriguez, *J. Phys. Chem. B*, 2004, **108**, 16613-16616.
3. P. M. Jardim, B. A. Marinkovic, A. Saavedra, L. Y. Lau, C. Baehtz and F. Rizzo, *Micropor. Mesopor. Mater.*, 2004, **76**, 23-28.
4. R. M. Reisner, Y. Lee, J. C. Hanson, G. A. Jones, J. B. Parise, D. R. Corbin, B. H. Toby, A. Freitag, J. Z. Larese and V. Kahlenberg, *Chem. Commun.*, 2000, 2221-2222.
5. Patent No: 3,375,205, 1967.
6. G. T. Kerr, *Inorg. Chem.*, 1966, **5**, 1537-1539.
7. Patent No: 3,414,752, 1967.
8. Patent No: 4,299,686, 1981.
9. A. Corma, F. Rey, J. Rius, M. J. Sabater and S. Valencia, *Nature*, 2004, **431**, 287-290.
10. N. Hedin, G. J. DeMartin, K. G. Strohmaier and S. C. Reyes, *Micro. and Meso. Mater.*, 2007, **98**, 182-188.
11. N. Hedin, G. J. DeMartin, W. J. Roth, K. G. Strohmaier and S. C. Reyes, *Micro. and Meso. Mater.*, 2008, **109**, 327-334.
12. A. Huang and J. Caro, *Chem. Commun.*, 2010, **46**, 7748-7750.
13. R. Krishna and J. M. v. Baten, *Micro. and Meso. Mater.*, 2011, **137**, 83-91.
14. E. N. Gribov, G. Sastre and A. Corma, *J. Phys. Chem. B*, 2005, **109**, 23794-23803.
15. M. A. Granato, T. J. H. Vlugt and A. E. Rodrigues, *Adsorption*, 2008, **14**, 763-770.
16. A. Garcia-Sanchez, D. Dubbeldam and S. Calero, *J. Phys. Chem. C*, 2010, **114**, 15068-15074.
17. M. Ralek, P. Jiru, O. Grubner and H. Beyer, *Czech Chem. Commun*, 1962, **27**, 142.

18. R. A. Schoonheydt, M. B. Hall and J. H. Lundsford, *Inorg. Chem.*, 1983, **22**, 3834-3839.

19. R. Seifert, A. Kunzmann and G. Calzaferri, *Angew. Chem. Int. Ed.*, 1998, **37**.

20. R. Seifert, R. Rytz and G. Calzaferri, *J. Phys. Chem. A*, 2000, **104**, 7473-7483.

21. P. H. Kasai, *J. Chem. Phys.*, 1965, **43**, 3322-3327.

22. L. Ferrerira, A. M. Fonseca, G. Botelho, C. Almeida-Aguiar and I. Neves, *Micro. and Meso. Mater.*, 2012, **160**, 126-132.

23. A. Fernandez, E. Soriano, P. Hernandez-Munoz and R. Gavara, *J. Food Science* 2010, **75**, 186-193.

24. T. Moretro, G. Hoiby-Pettersen, C. K. Halvorsen and S. Langsrud, *Food Control*, 2012, **28**, 118-121.

25. M. M. Cowen, K. Z. Abshire, S. L. Houk and S. M. Evans, *J. Ind. Microbiol. Biotechnol.*, 2003, **30**, 102-106.

26. K. Kawahara, K. Tsuruda, M. Morishita and M. Uchida, *Dent. Mater.*, 2000, **16**, 452-455.

27. R. Beer, G. Calzaferri, J. Li and B. Waldeck, *Coord. Chem. Rev.*, 1991, **111**, 193-200.

28. P. A. Jacobs and J. B. Uytterhoeven, *J. C. S. Chem. Comm.*, 1977, 128-129.

29. G. Calzaferri, *Top. Catal.*, 2010, **53**, 130-140.

30. G. Calzaferri, N. Gfeller and K. Pfanner, *J. Photoch. Photobio.*, 1995, **87**, 81-84.

31. G. Calzaferri, O. Bossart, D. Bruhwiler, S. Huber, C. Leiggener, M. K. V. Veen and A. Z. Ruiz, *Chimie*, 2006, **9**, 214-225.

32. W. Chen, Z. Wang, Z. Lin, L. Lin, K. Fang, Y. Xu, M. Su and J. Lin, *J. Appl. Phys*, 1998, **83**, 3811-3815.

33. W. Chen, A. G. Joly and J. Roark, *Phys. Rev. B*, 2002, **65**, 245404

34. K. Seff and T. Sun, *Chem. Rev.*, 1994, **94**, 857-870.

35. Y. Kim and K. Seff, *J. Am. Chem. Soc.*, 1977, **100**, 175-180.

36. Y. Kim and K. Seff, *J. Am. Chem. Soc.*, 1978, **100**, 6989-6997.

37. P. A. Jacobs, J. B. Uytterhoeven and H. K. Beyer, *J. Chem. Soc. Faraday Trans. I*, 1979, **75**, 56-64.

38. L. R. Gellens, W. J. Mortier, R. A. Schoonheydt and J. B. Uytterhoeven, *J. Phys. Chem.*, 1981, **85**, 2783-2788.

39. D. Hermerschmidt and R. Haul, *Ber. Bunsen-Ges. Phys. Chem.*, 1980, **84**, 902-907.

40. P. J. Grobet and R. A. Schoonheydt, *Surf. Sci*, 1985, **156**, 893-898.

41. B. Xu and L. Kevan, *J. Phys. Chem.*, 1992, **96**, 3647-3652.

42. H. Tsutsumi and H. Takahashi, *Bull. Chem. Soc. Jpn.*, 1972, **45**, 2332-2337.

43. J. R. Morton and K. F. Preston, *Zeolites*, 1987, **7**, 2-4.

44. D. R. Brown and L. Kevan, *J. Phys. Chem.*, 1986, **90**, 1129-1133.

45. J. Michalik and L. Kevan, *J. Am. Chem. Soc.*, 1986, **108**, 4247-4253.

46. N. Narayana and L. Kevan, *J. Chem. Phys.*, 1982, **76**, 3999-4005.

47. K. Seff and Y. Kim, *Am. Chem. Soc.*, 1978, 175-180.

48. P. A. Anderson, *Molecular Sieves*, Springer-Verlag, Berlin Heidelberg, 2002, p307-338.

49. I. S. Z. Kerr, *Kristallogr.*, 1974, **139**, 186-189.

50. Z. Jirak, V. Bosacek, S. Vratislav, H. Herden, R. Schollner, W. J. Mortier, L. Gellens and J. B. Uytterhoeven, *Zeolites*, 1983, **3**, 255-258.

51. T. B. Reed and D. W. Breck, *J. Am. Chem. Soc.*, 1956, **78**, 5972-5977.

52. J. J. Pluth and J. V. Smith, *J. Am. Chem. Soc.*, 1980, **102**, 4704-4708.

53. P. C. W. Leung, K. B. Kunz, K. Seff and I. E. Maxwell, *J. Phys. Chem.*, 1975, **79**, 2157-2162.

54. R. L. Firor and K. Seff, *J. Am. Chem. Soc.*, 1977, **99**, 1112-1117.

55. T. B. V. Jr. and K. Seff, *J. Phys. Chem.*, 1975, **79**, 2163-2167.

56. H. Robson and K. P. Lillerud, *Verified Syntheses of Zeolitic Materials*, 2nd revised edn., Elsevier, 2001.

57. H. S. Sherry and H. F. Walton, *J. Phys. Chem.*, 1967, **71**, 1457-1465.

58. A. Coelho, Topas Academic Version 4.1., 2007

59. A. Mayoral, T. Carey, P. A. Anderson, A. Lubk and I. Diaz, *Angew. Chem. Int. Ed.*, 2011, **50**, 11230-11233.

60. D. A. Woodcock, P. Lightfoot, L. A. Villaescusa, M. Díaz-Cabañas, M. A. Camblor and D. Engberg, *Chem. Mater.*, 1999, **11**, 2508-2514.

61. K. D. Hammonds, V. Heine and M. Dove, *J. Phys. Chem. B*, 1998, **102**, 1759-1767.

62. I. D. Brown, *Acta. Cryst.*, 1985, **B41**, 244-247.

63. R. T. Sanderson, *J. Am. Chem. Soc.*, 1983, **105**, 2259-2261.

64. W. Depmeier, *Acta Cryst.*, 1985, **B41**, 101-108.

Chapter 4 – Framework Modification

4.1 Introduction

This chapter will discuss the effect of varying the aluminium content on the thermal expansion behaviour of zeolites with the LTA topology. De-aluminated structures have a weaker net negative charge over the whole zeolite framework. This in turn means that fewer cations are incorporated in the zeolite pores to balance the overall charge. Only the sodium forms of various dehydrated and hydrated ZK-4 systems have been studied in this project to eliminate the influence different cations can have on the thermal expansion behaviour. As in chapter 3, data was collected in the sub-ambient temperature range of 100–300 K to avoid compositional changes from dehydration.

4.1.1 Zeolite ZK-4

Kerr and Kokotailo first reported in 1961 that ZK-4 could be prepared using the organic structure-directing ion tetramethylammonium (TMA^+).[1] TMA^+ is one of the most simple and commonly used structure-directing agents to synthesise porous structures.[2-4] The charge-balancing counter-ion TMA^+ is thought to act by limiting the number of ions and molecules that are able to fit inside the zeolite pores, especially in β-cages.[5] This in turn has an effect on the incorporation of aluminium into the zeolite framework and results in the formation of structures with higher Si/Al ratios. Several reported studies have investigated the location preference of the AlO_4 tetrahedra and cations inside ZK-4 structures.[6-11] Computational simulations have suggested that long range ordering of silicon and aluminium can only occur in ZK-4 structures with Si/Al ratios greater than 1.4.[12] These findings were supported

by Cheetham and co-workers[8] who reported that no superlattice reflections resulting from Si/Al ordering (531 peak) were present in the powder neutron diffraction patterns of ZK-4 structure with Si/Al < 1.65. Cheetham *et al*.[7-8] also reported that the cationic 8-ring site was preferentially depopulated in ZK-4 and suggested that this characteristic was responsible for the ability of sodium ZK-4, but not Na-A, to absorb large hydrocarbon chains such as hexane.

Despite the large amount of research published on de-aluminated zeolite structures, relatively few studies have investigated the effect of changing the zeolite framework content can have on their thermal expansion properties. High-temperature powder XRD studies by Bhange and co-workers reported that strong NTE behaviour was shown when iron or tin were introduced into the MFI-zeolite frameworks.[13-15] Large NTE coefficients were attributed to increased transverse thermal vibrations of framework oxygens but no structural mechanism was provided.

4.2 Synthesis

ZK-4 samples were prepared using a modified version of the method reported by Jarman *et al.*[16] Structures with different Si/Al ratios were synthesised by varying the amount of SiO_2 in the gel mixture as detailed in table 4.1. Tetramethylammonium hydroxide (TMAOH; 25 wt% with water) was stirred with colloidal silica (SiO_2; 40 wt% with water) for 30 mins. In a separate container, sodium aluminate was dissolved in an appropriate amount of water and sodium hydroxide was added if required. These two solutions were then mixed and stirred until a homogeneous white paste was formed. The resulting gel was then left to age for a number of days at room temperature before heating in a hydrothermal oven at 373 K for 24 hrs. The white solid product was separated from solution through filtration and washed with

Table 4.1 *– Gel composition for the ZK-4 samples*

Si/Al ratio	Unit Cell Formula	TMAOH / g	SiO_2 / g	$NaAlO_2$ / g	H_2O / g	NaOH / g	Ageing Time / h
2.39	$Na_{7.3}(Al_{7.3}Si_{16.7}O_{48})$	11.75	7.8	1	27.2	-	66
1.66	$Na_9(Al_9Si_{15}O_{48})$	15	5	1.03	27.2	-	48
1.33	$Na_{10.4}(Al_{10.4}Si_{13.6}O_{48})$	15	3	1.03	27.2	0.1	48

copious water. The organic template was removed by heating the samples formed at 773 K under flowing oxygen for 72 hrs. After cooling the resulting zeolites were then stirred in a 0.1 mol dm^{-3} sodium chloride solution to ensure that any H^+ cations were removed. Powder XRD was used to check the crystallinity of the ion-exchanged zeolites and XRF analysis was used to confirm their elemental composition. All ZK-4 samples discussed in this thesis were prepared by Marek Colligan at the University of Birmingham.

4.3 Results and Discussion

4.3.1 Dehydrated ZK-4 Systems

4.3.1.1 Structural Analysis of the Dehydrated ZK-4 Systems at 300 K

All crystal structures of the dehydrated ZK-4 systems were refined from powder synchrotron XRD data (λ = 0.827154 Å). Successful Rietveld analyses were performed in the cubic space group $Pm\bar{3}m$. Structural analysis was not performed in the $Fm\bar{3}c$ space group as the Si/Al ratio was greater than 1. Rietveld refinement plots and calculated atomic coordinates of all the dehydrated ZK-4 systems at 300 K are shown in figures 4.1-4.3 and tables 4.2-4.4, respectively.

Table 4.2 *– Refined atomic parameters the dehydrated ZK-4 (2.39) at 300K [errors at 1σ level].*[a]

Atom	Wyckoff position	*x*	*y*	*z*	Occupancy	B
Si(1)	24k	0	0.1855(4)	0.3699(4)	0.696	0.7(1)
Al(1)	24k	0	0.1855(4)	0.3699(4)	0.304	0.7(1)
O(1)	12h	0	0.5	0.2090(9)	1	0.9(2)
O(2)	12i	0	0.2897(6)	0.2897(6)	1	0.9(2)
O(3)	24m	0.1111(5)	0.1111(5)	0.3395(6)	1	0.9(2)
Na(1)	8g	0.2098(7)	0.2098(7)	0.2098(7)	0.75(2)	3.0(6)

[a] *$a = 12.1227(4)$ Å, space group: $Pm\bar{3}m$, $\chi^2 = 1.21$, $R_{wp} = 18.13$ %, $R_p = 15.00$ %*

Table 4.3 – *Refined atomic parameters the dehydrated ZK-4 (1.66) at 300K [errors at 1σ level].*[a]

Atom	Wyckoff position	*x*	*y*	*z*	Occupancy	B
Si(1)	24k	0	0.1841(1)	0.3702(1)	0.625	0.71(3)
Al(1)	24k	0	0.1841(1)	0.3702(1)	0.375	0.71(3)
O(1)	12h	0	0.5	0.2171(4)	1	1.44(6)
O(2)	12i	0	0.2921(2)	0.2921(2)	1	1.44(6)
O(3)	24m	0.1118(2)	0.1118(2)	0.3414(2)	1	1.44(6)
Na(1)	8g	0.2072(2)	0.2072(2)	0.2072(2)	0.895(6)	2.1(1)
Na(2)	12i	0	0.557(2)	0.557(2)	0.053(2)	2.1(1)

[a] *$a = 12.19240(7)$ Å, space group: $Pm\bar{3}m$, $\chi^2 = 1.27$, $R_{wp} = 15.64$ %, $R_p = 12.32$ %*

Table 4.4 – *Refined atomic parameters the dehydrated ZK-4 (1.33) at 300K [errors at 1σ level].*

Atom	Wyckoff position	*x*	*y*	*z*	Occupancy	B
Si(1)	24k	0	0.1851(2)	0.3700(2)	0.565	0.64(4)
Al(1)	24k	0	0.1851(2)	0.3700(2)	0.435	0.64(4)
O(1)	12h	0	0.5	0.2202(4)	1	1.37(7)
O(2)	12i	0	0.2930(3)	0.2930(3)	1	1.37(7)
O(3)	24m	0.1116(2)	0.1116(2)	0.3431(3)	1	1.37(7)
Na(1)	8g	0.2039(2)	0.2039(2)	0.2039(2)	0.902(8)	1.4(2)
Na(2)	12i	0	0.565(1)	0.565(1)	0.151(3)	1.4(2)

[a] *$a = 12.2210(1)$ Å, space group: $Pm\bar{3}m$, $\chi^2 = 1.25$, $R_{wp} = 15.73$ %, $R_p = 12.63$ %*

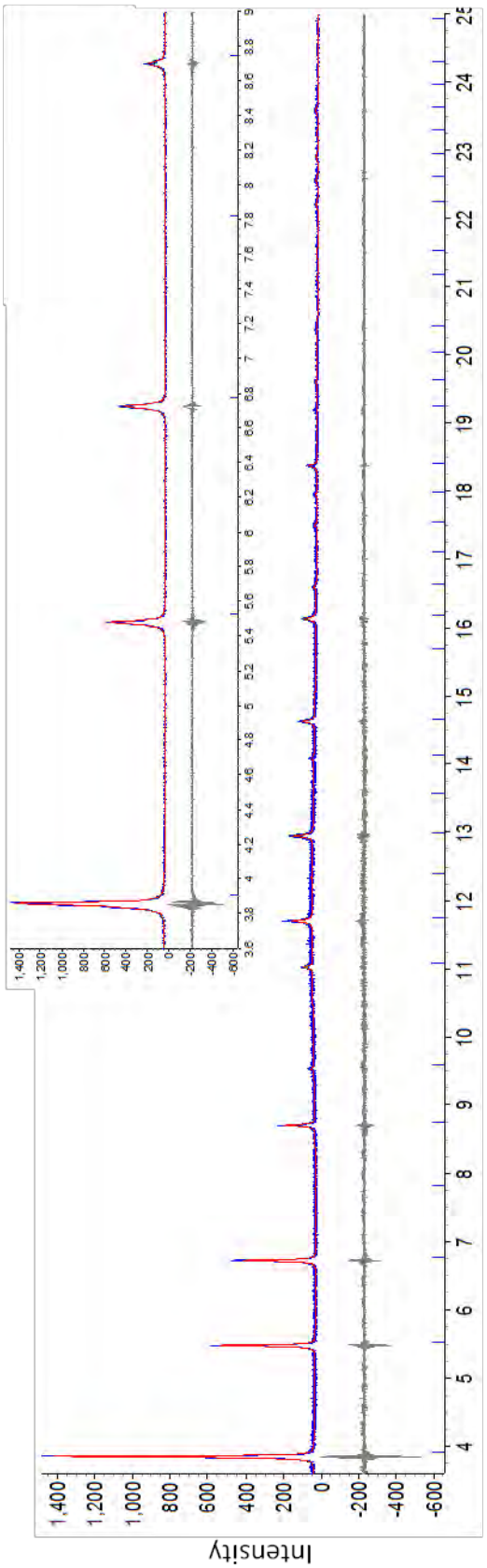

Figure4.1 *– Rietveld refinement plot of dehydrated ZK-4 (2.39) at 300 K*

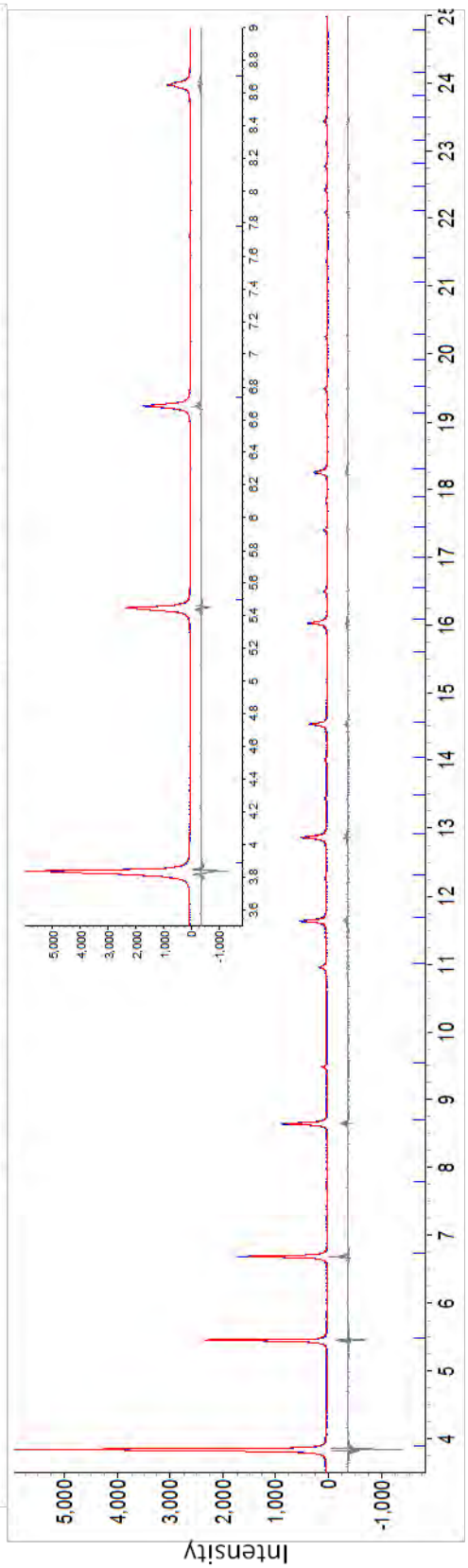

Figure4.2 *– Rietveld refinement plot of dehydrated ZK-4 (1.66) at 300 K.*

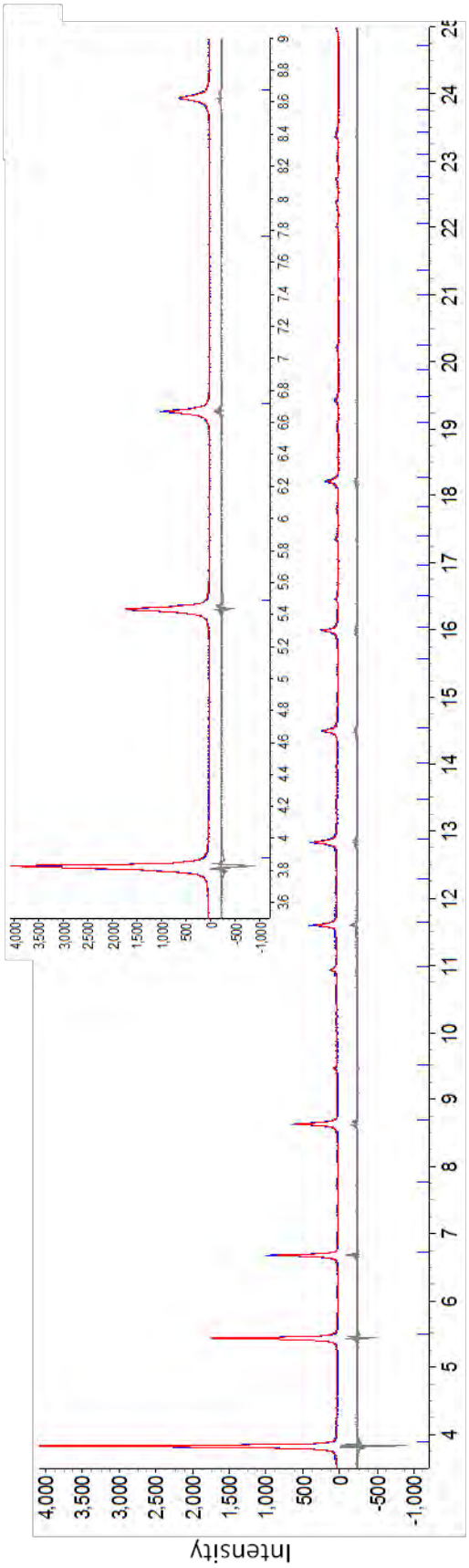

Figure4.3 – *Rietveld refinement plot of dehydrated ZK-4 (1.33) at 300 K.*

A significant increase in the cation content was observed as the amount of aluminium in the zeolite framework was increased. These cations were shown to have a preference to occupy the 6-ring position before any another other site in the LTA zeolite framework as this location offers the highest possible coordination to the framework oxygens atoms.[11] Eight 6-ring sites (8g), three 8-ring sites (12i) and twelve 4-ring sites (12j) are available per ~12 Å unit cell. In dehydrated ZK-4 (2.39), only the 6-ring sites were occupied as there were less than eight Na^+ cations per unit cell. However, in dehydrated ZK-4 (1.33) and ZK-4 (1.66) both the 6-ring and 8-ring positions were occupied as the unit cells contained more than eight Na^+ cations. No cations were identified in the 4-ring site.

Significant changes in the calculated T–O–T and O–T–O bond angles were also observed as the LTA zeolite aluminium content was increased. As shown in table 4.5, the T–O(1)–T bond angle was much larger in dehydrated ZK-4 (2.39) when compared to ITQ-29 whereas the T-O(3)–T angle was much smaller. These changes in the T–O–T bond angles were caused by the introduction of Na^+ cations into the zeolite 6-ring and their consequent coordination to the framework O(2) and O(3) atoms which resulted in the oxygen atoms being pulled towards the centre of the zeolite ring. This in turn caused a distortion in the TO_4 tetrahedra and increase in the O(1)–T–O(2) and T–O(1)–T bond angles. Considerable contractions in the T–O(1)–T and T-O(2)-T bond angles were also observed as the zeolite aluminium content was further increased. This may have been due to a higher number Na^+ cations occupying the 8-ring position in the dehydrated ZK-4 systems which caused the framework O(1) and O(2) atoms to be pulled towards the centre of the zeolite ring (figure 4.4). Fewer distortions in the TO_4 tetrahedra were observed when cations occupied both the 6-ring and 8-ring.

Table 4.5 *- Calculated bond lengths and angles for ITQ-29 and the dehydrated ZK-4 systems at 300 K [errors at 1σ level].*

LTA System	ITQ-29	ZK-4 (2.39)	ZK-4 (1.66)	ZK-4 (1.33)
T–O(1) / Å	1.609(4)	1.603(5)	1.634(2)	1.646(3)
T–O(2) / Å	1.578(4)	1.594(5)	1.625(2)	1.619(2)
T–O(3) / Å	1.589(3)	1.662(4)	1.661(1)	1.661(1)
O(2)–Na(1) / Å	-	2.889(5)	2.920(2)	2.930(2)
O(3)–Na(1) / Å	-	2.310(9)	2.321(3)	2.332(4)
T–O(1)–T / °	146.2(6)	159.5(9)	151.5(3)	149.8(4)
T–O(2)–T / °	162.6(5)	165.1(8)	161.7(3)	161.0(3)
T–O(3)–T / °	152.3(4)	146.1(6)	145.8(2)	147.6(3)
O(1)–T–O(2) / °	109.41(4)	117.3(6)	111.6(2)	110.4(3)
O(1)–T–O(3) / °	108.7(3)	108.3(4)	109.6(1)	109.3(2)
O(2)–T–O(3) / °	110.9(3)	107.2(4)	107.9(1)	109.0(2)
O(3)–T–O(3) / °	108.2(4)	108.2(6)	110.3(2)	109.9(3)
8R Diameter (T-T) / Å	8.099 Å	8.255 Å	8.239 Å	8.326 Å
6R Diameter (T-T) / Å	6.203 Å	6.342 Å	6.383 Å	6.394 Å

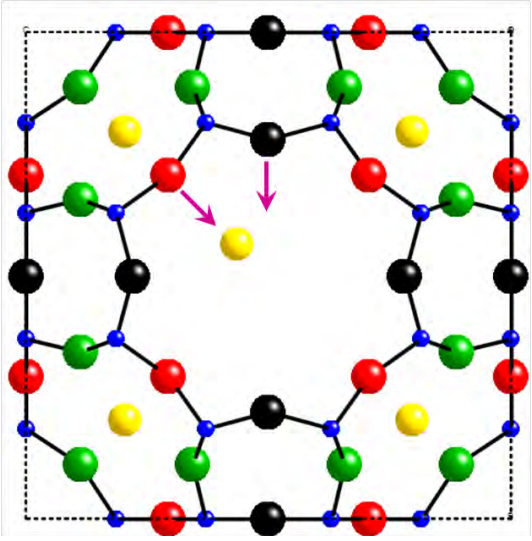

Figure 4.4 *– Diagram illustrating the movement of the framework O(1) and O(2) atoms as the Al-content is increased in dehydrated ZK-4 (blue = Si(1)/Al(1), black = O(1), red = O(2), green = O(3) and yellow = Na).*

It is worth noting that these calculated bond angles may not be true representations of the actual bond angles present in the dehydrated ZK-4 systems but in fact virtual bond angles instead. Due to the non-uniform distribution of AlO_4 tetrahedra and relatively low occupancy of the 8-ring cations in the ZK-4 systems (especially in the case of dehydrated ZK-4 (1.33)), local distortions[17] may have been present in the structure which could have lead to averaged bond angle values being calculated. Unlike the zeolite A samples where there was a uniform distribution of AlO_4 tetrahedra and cations within the zeolite, the TO_4 tetrahedra in the ZK-4 samples may have had slightly different orientations depending upon their relative proximity and coordination to the 8-ring Na^+ cations. Na(2) cations could only interact with 10.6% of the available O(1) atoms (effectively the double 4-rings) in the ZK-4 (1.33) and 5.3% of the O(2) atoms. In ZK-4 (1.66), greater interaction was observed with 30.2 % of the O(1) atoms and 15.1 % of the O(2) atoms available to interact with the Na(2) cations. Correlated movement of all eight tetrahedra that make up a double 4-ring may have also meant that a greater proportion of the structure was affected by the small number of cations that occupied the 8-ring. As a result of this local structure uncertainty, definitive conclusions on the effect increased aluminium/cation content has zeolite framework cannot be formed from powder XRD data. Despite the changes in the calculated T–O–T and O–T–O bond angles, contraction of the zeolite pores was not observed upon cation inclusion. Average T-O bond lengths were shown to increase with aluminium content which resulted in larger pore diameters and overall unit cell volumes.

Table 4.6 *– Calculated mean volume thermal expansion coefficients of the anhydrous LTA systems.*

Dehydrated LTA-Zeolite System	Mean Volume Thermal Expansion Coefficient / x 10^{-6} K^{-1}
ITQ-29	−22.1
ZK-4 (2.39)	−12.6
ZK-4 (1.66)	−8.59
ZK-4 (1.33)	−6.47
Na-A	−6.34

4.3.1.2 Thermal Expansion Studies of the Dehydrated ZK-4 Systems

Variable temperature powder synchrotron XRD studies were used to determine the thermal expansion behaviour of all the dehydrated ZK-4 systems from 100–300 K. XRD patterns were collected at 20 K intervals and Rietveld analysis was performed at each interval to monitor any thermally induced structural changes. Calculated atomic coordinates of all the dehydrated ZK-4 systems over this temperature range can be found in appendix 3. As shown in table 4.6, NTE coefficients of decreasing value were determined for the dehydrated ZK-4 systems as the aluminium content was increased. A clear trend was also observed when these values were compared to the calculated thermal expansion coefficients of ITQ-29 and dehydrated Na-A. It is worth noting that the thermal expansion coefficient calculated for dehydrated ZK-4 (2.39) was determined from data between 140-300 K. As illustrated in figure 4.5, the sample capillary leaked during data collection and was hydrated by the atmosphere. This meant that all data collected below 140 K could not be used. Several attempts were made to recollect this synchrotron data set however none were successful. Figure 4.6 illustrates how laboratory based XRD data could not be used as the errors in the calculated unit cell volumes were too large to base any firm conclusions on.

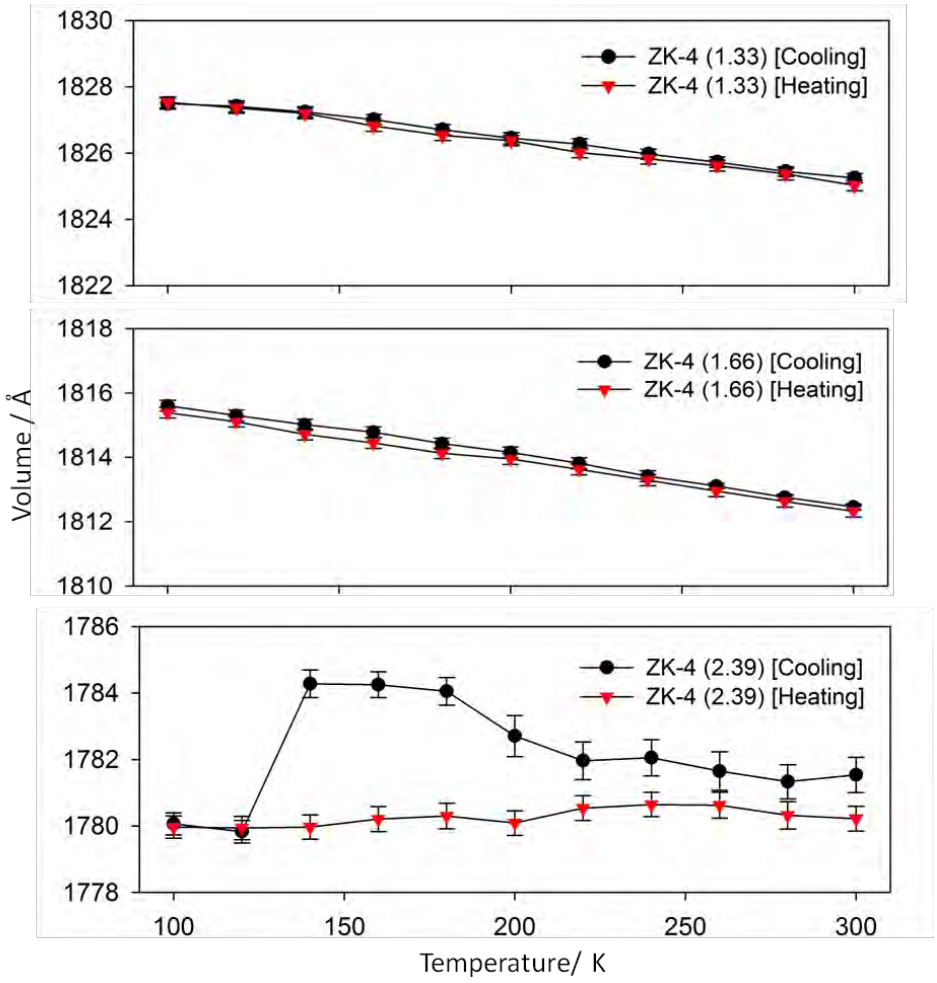

Figure 4.5 *– Calculated unit cell volumes from powder synchrotron XRD data for the dehydrated ZK-4 systems between 100–300 K [errors at 3σ level].*

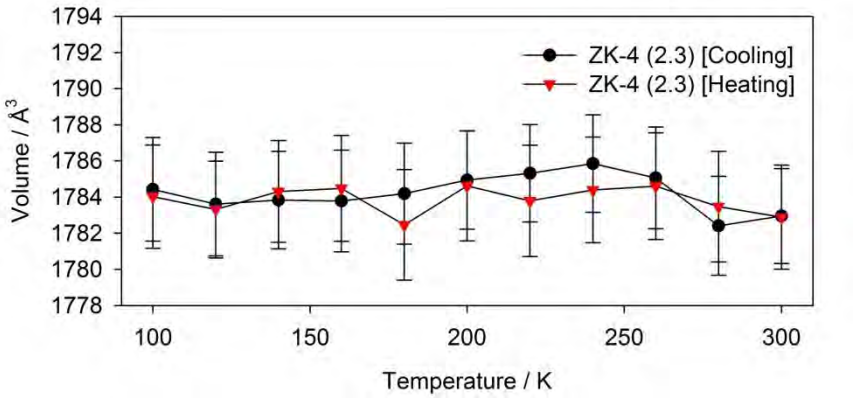

Figure 4.6 *– Calculated unit cell volumes from laboratory XRD data for dehydrated ZK-4 (2.39) between 100–300 K [errors at 3σ level].*

The calculated bond lengths and angles for all the dehydrated ZK-4 samples are detailed in tables 4.7–4.9. Unlike the previous chapter it was not possible to explain the mechanism behind the thermal contraction through examining the calculated bond angles (figure 4.7–4.9). Surprisingly no significant changes in the calculated bond angles were observed over the whole temperature range. The small increase in the O(1)–T–O(2) bond angle of dehydrated ZK-4 (2.39) on heating was not deemed significant as the observed changes were within error. As discussed earlier, these calculated values may not have been accurate representations of the actual bond angles in the dehydrated ZK-4 systems but in fact virtual bond angles instead. As a result of this any subtle changes in the framework structure that may have caused the NTE behaviour may have been masked by the calculated virtual angles.

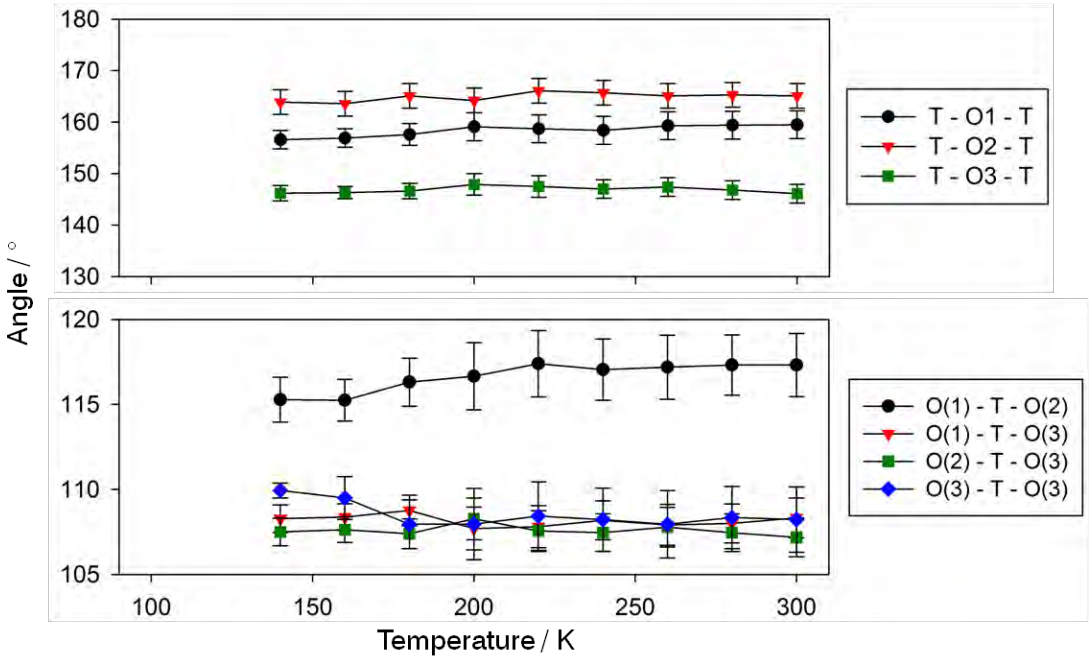

Figure 4.4 *– Calculated T–O–T and O–T–O T bond angles for dehydrated ZK-4 (2.39) from 100–300 K [errors at 3σ level].*

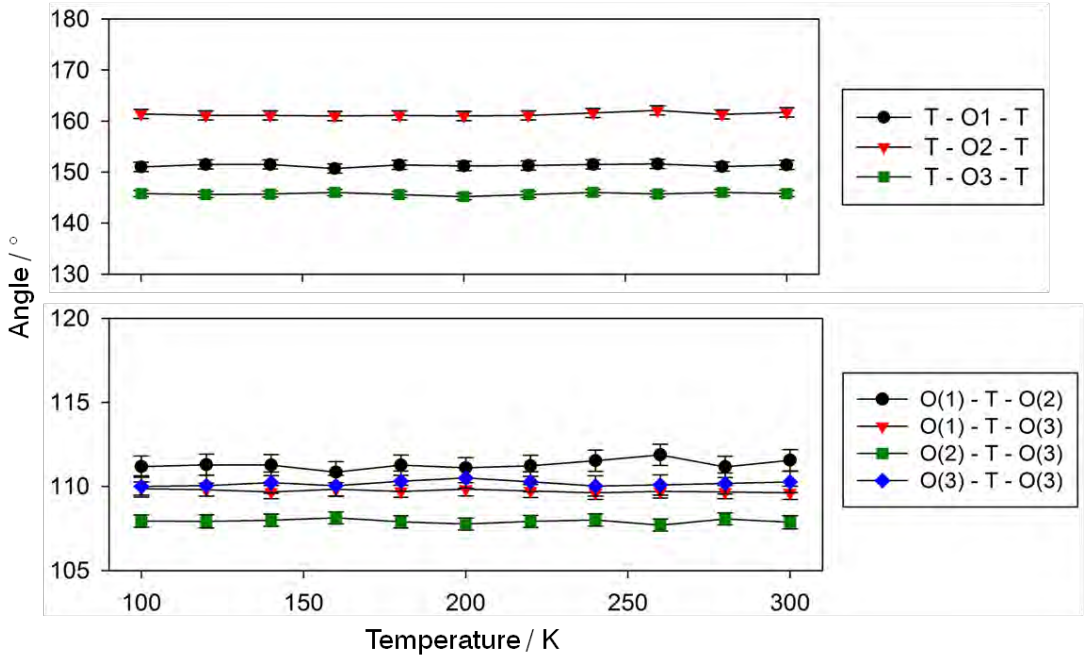

Figure 4.5 *– Calculated T–O–T and O–T–O bond angles for dehydrated ZK-4 (1.6) from 100–300 K [errors at 3σ level].*

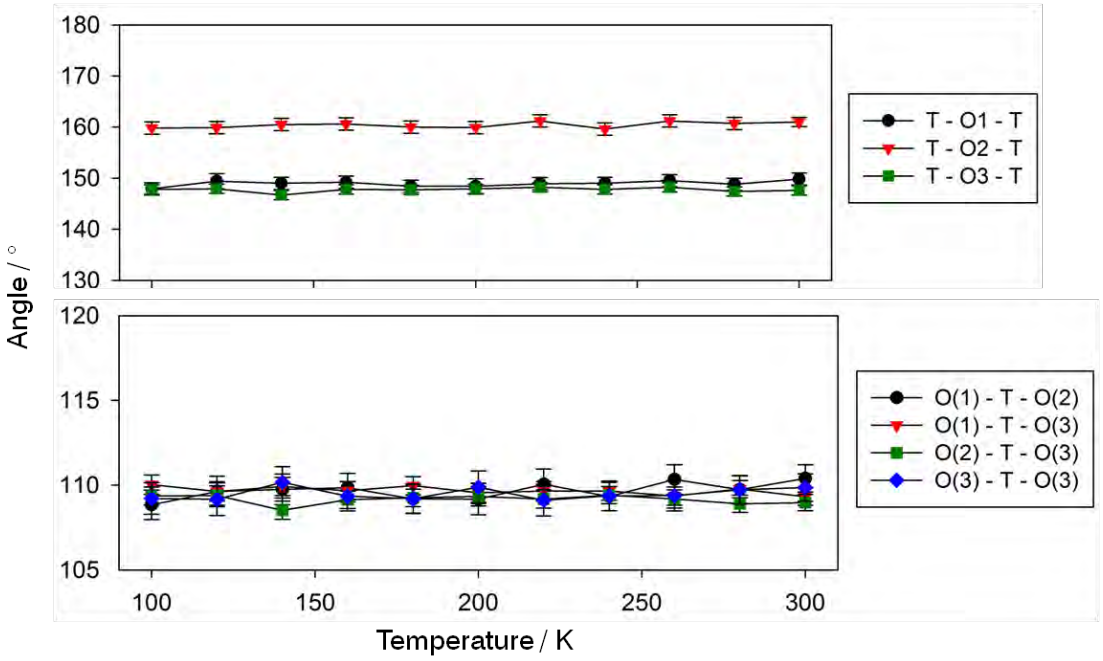

Figure 4.6 *– Calculated T–O–T and O–T–O bond angles for dehydrated ZK-4 (1.3) from 100–300 K [errors at 3σ level].*

Table 4.7 *– Bond Distances (Å) and Angles (deg) in Dehydrated ZK-4 (2.39) from 100–300 K [errors at 1σ level].*

Bond Length/Angle	Temperature										
	300K	280K	260K	240K	220K	200K	180K	160K	140K	120K	100K
Si – O1	1.603(5)	1.610(5)	1.609(6)	1.611(5)	1.618(6)	1.615(6)	1.606(4)	1.619(4)	1.617(4)	-	-
Si – O2	1.594(5)	1.589(5)	1.592(6)	1.590(5)	1.584(6)	1.591(6)	1.599(4)	1.599(4)	1.600(4)	-	-
Si – O3	1.662(4)	1.659(4)	1.655(4)	1.658(4)	1.656(4)	1.653(4)	1.659(3)	1.655(3)	1.654(3)	-	-
Si – O1 – Si	159.5(9)	159.4(8)	159.3(9)	158.4(9)	158.7(9)	159.1(9)	157.3(7)	156.9(6)	156.6(6)	-	-
Si – O2 – Si	165.1(8)	165.3(8)	165.1(8)	165.7(8)	166.1(8)	164.2(9)	165.1(6)	163.6(5)	163.9(6)	-	-
Si – O3 – Si	146.1(6)	146.8(6)	147.4(7)	147.0(6)	147.5(7)	147.9(7)	146.4(5)	146.3(4)	146.2(5)	-	-
O1 – Si – O2	117.3(6)	117.3(6)	117.2(6)	117.1(6)	117.4(7)	116.7(7)	116.3(5)	115.3(4)	115.3(4)	-	-
O1 – Si – O3	108.3(4)	108.0(4)	107.9(4)	108.2(4)	107.8(4)	107.7(4)	108.8(3)	108.4(3)	108.3(3)	-	-
O2 – Si – O3	107.2(4)	107.5(4)	107.8(4)	107.5(4)	107.6(4)	108.3(4)	107.4(3)	107.6(3)	107.5(3)	-	-
O3 – Si – O3	108.2(6)	108.4(6)	108.0(7)	108.2(6)	108.4(7)	108.0(7)	108.0(5)	109.5(4)	109.9(4)	-	-
Lattice Parameter (Å)	12.0545(2)	12.0495(2)	12.0448(2)	12.0407(2)	12.0373(3)	12.0348(2)	12.0331(3)	12.0312(3)	12.0296(3)	-	-
Unit Cell Volume (Å)	1751.64(8)	1749.46(9)	1747.44(9)	1745.64(1)	1744.2(1)	1743.1(1)	1742.4(1)	1741.5(1)	1740.8(1)	-	-

Table 4.8 *– Bond Distances (Å) and Angles (deg) in Dehydrated ZK-4 (1.66) from 100–300 K [errors at 1σ level].*

Bond Length/Angle	Temperature										
	300K	280K	260K	240K	220K	200K	180K	160K	140K	120K	100K
Si – O1	1.634(2)	1.635(2)	1.631(2)	1.632(2)	1.634(2)	1.633(2)	1.633(2)	1.637(2)	1.637(2)	1.634(2)	1.635(2)
Si – O2	1.625(2)	1.625(2)	1.624(2)	1.625(2)	1.627(2)	1.629(2)	1.628(2)	1.627(2)	1.624(2)	1.627(2)	1.627(2)
Si – O3	1.661(1)	1.661(1)	1.663(1)	1.661(1)	1.661(1)	1.663(1)	1.662(1)	1.661(1)	1.663(1)	1.663(1)	1.661(1)
Si – O1 – Si	151.5(3)	151.1(3)	151.6(3)	151.5(3)	151.3(3)	151.2(3)	151.4(3)	150.7(3)	151.5(3)	151.5(3)	151.0(3)
Si – O2 – Si	161.7(3)	161.3(3)	162.1(3)	161.6(3)	161.1(3)	161.0(3)	161.1(3)	161.0(3)	161.1(3)	161.1(3)	161.4(3)
Si – O3 – Si	145.8(2)	146.0(2)	145.7(2)	146.0(2)	145.6(2)	145.2(2)	145.6(2)	146.0(2)	145.7(2)	145.6(2)	145.8(2)
O1 – Si – O2	111.6(2)	111.2(2)	111.9(2)	111.5(2)	111.2(2)	111.1(2)	111.3(2)	110.9(2)	111.3(2)	111.3(2)	111.2(2)
O1 – Si – O3	109.6(1)	109.7(1)	109.7(1)	109.6(1)	109.7(1)	109.8(1)	109.7(1)	109.8(1)	109.7(1)	109.8(1)	109.9(1)
O2 – Si – O3	107.9(1)	108.1(1)	107.7(1)	108.0(1)	107.9(1)	107.8(1)	107.9(1)	108.1(1)	108.0(1)	107.9(1)	107.9(1)
O3 – Si – O3	110.3(2)	110.2(2)	110.1(2)	110.0(2)	110.3(2)	110.5(2)	110.3(2)	110.0(2)	110.2(2)	110.1(2)	110.0(2)
Lattice Parameter (Å)	12.19240(7)	12.19307(7)	12.19386(7)	12.1945(1)	12.1954(1)	12.1962(1)	12.1968(1)	12.1976(1)	12.1981(1)	12.1988(1)	12.1995(1)
Unit Cell Volume (Å)	1812.46(3)	1812.76(3)	1813.11(3)	1813.41(6)	1813.81(6)	1814.15(6)	1814.43(6)	1814.78(6)	1815.01(6)	1815.30(6)	1815.60(6)

Table 4.9 *– Bond Distances (Å) and Angles (deg) in Dehydrated ZK-4 (1.3) from 100–300 K [errors at 1σ level].*

Bond Length/Angle	Temperature										
	300K	280K	260K	240K	220K	200K	180K	160K	140K	120K	100K
Si – O1	1.646(3)	1.645(3)	1.647(3)	1.651(3)	1.646(3)	1.652(3)	1.649(3)	1.645(3)	1.645(3)	1.647(3)	1.652(3)
Si – O2	1.619(2)	1.625(3)	1.618(3)	1.619(3)	1.620(3)	1.624(3)	1.624(3)	1.623(3)	1.626(3)	1.622(3)	1.626(3)
Si – O3	1.666(2)	1.666(2)	1.666(2)	1.668(2)	1.666(2)	1.664(2)	1.666(2)	1.667(2)	1.670(2)	1.668(2)	1.665(2)
Si – O1 – Si	149.8(4)	148.8(4)	149.5(4)	149.0(4)	148.9(4)	148.4(5)	148.4(4)	149.2(4)	148.9(4)	149.4(5)	147.9(4)
Si – O2 – Si	161.0(3)	160.7(4)	161.2(4)	159.6(4)	161.2(4)	159.9(4)	160.0(4)	160.6(4)	160.6(4)	159.9(4)	159.8(4)
Si – O3 – Si	147.6(3)	147.4(3)	148.2(3)	147.8(3)	148.2(3)	147.9(3)	147.7(3)	147.8(3)	146.5(3)	147.9(3)	147.8(3)
O1 – Si – O2	110.4(3)	109.7(3)	110.3(3)	109.3(3)	110.1(3)	109.2(3)	109.2(3)	109.9(3)	109.8(3)	109.6(3)	108.8(3)
O1 – Si – O3	109.3(2)	109.8(2)	109.4(2)	109.7(2)	109.7(2)	109.6(2)	110.0(2)	109.7(2)	109.9(2)	109.6(2)	110.0(2)
O2 – Si – O3	109.0(2)	108.9(2)	109.2(2)	109.4(2)	109.2(2)	109.3(2)	109.3(2)	109.1(2)	108.5(2)	109.4(2)	109.4(2)
O3 – Si – O3	109.9(3)	109.9(3)	109.9(3)	109.9(3)	109.9(3)	109.9(3)	109.9(3)	109.9(3)	109.9(3)	109.9(3)	109.9(3)
Lattice Parameter (Å)	12.2210(1)	12.2215(1)	12.2221(1)	12.2226(1)	12.2233(1)	12.2237(1)	12.2243(1)	12.2249(1)	12.2255(1)	12.2258(1)	12.2260(1)
Unit Cell Volume (Å)	1825.25(5)	1825.44(5)	1825.72(5)	1825.97(5)	1826.27(5)	1826.44(6)	1826.70(5)	1827.01(5)	1827.24(5)	1827.41(6)	1827.49(5)

4.3.2 Hydrated ZK-4 Systems

TGA and mass spectrometry analysis showed that the amount of water molecules present inside the pores of the hydrated ZK-4 samples increased as the framework aluminium content was increased (table 4.10). This was to be expected as water molecules are attracted to charged zeolite frameworks. Successful Rietveld analysis was not possible for the hydrated ZK-4 systems as a variety of compositional phases were shown to be present in the samples. Figure 4.7 illustrates the peak splitting that was observed in all of the powder synchrotron XRD patterns of the hydrated systems. Peak splitting was observed in every peak and became more defined at high two theta angles. This suggested that

Table 4.10 *– Calculated unit cell parameters and water content for all of the hydrated ZK-4 systems at 300 K [errors at 1σ level].*

Hydrated ZK-4 System	Lattice Parameter / Å	Water Molecules / unit cell
ZK-4 (2.39)	12.048(3)	9.9
ZK-4 (1.66)	12.156(2)	19.5
ZK-4 (1.33)	12.226(2)	20.1

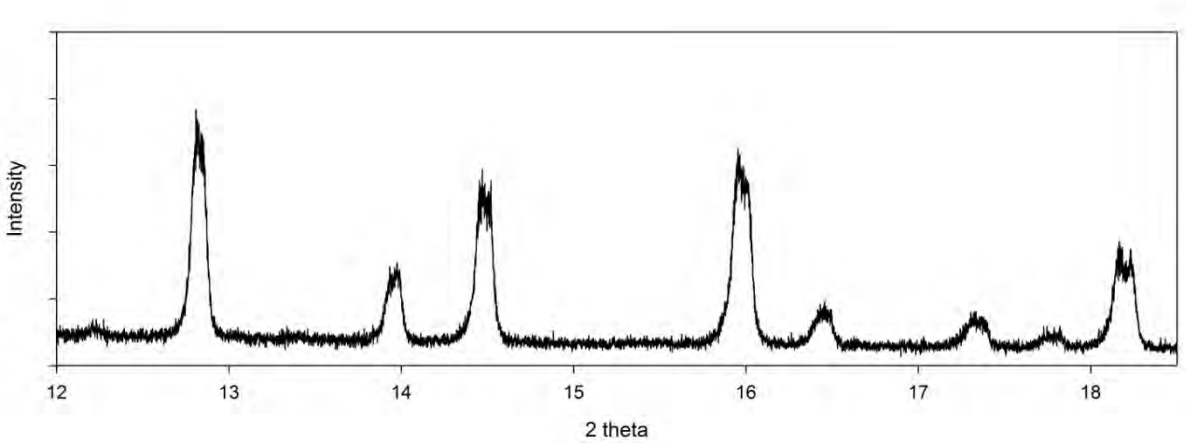

Figure 4.7 *– Powder synchrotron XRD pattern of hydrated ZK-4 (1.33) at 300 K.*

either the hydrated ZK-4 samples were not phase pure before analysis or that the samples were changing in the intense synchrotron beamline. TGA and mass spectroscopy analysis showed that only water molecules were released from the hydrated samples upon heating. This confirmed that the organic structure directing agent was no longer present in the samples and that remaining TMS^+ was not responsible for peak splitting (figure 4.8). As shown in figure 4.9, no peak splitting was observed in the powder XRD patterns recorded on the laboratory diffractometer. However, the lower resolution of this data meant that it may not have been possible to observe the peak splitting shown in the synchrotron powder XRD patterns. Through overlaying the powder synchrotron XRD patterns recorded for both dehydrated and hydrated ZK-4 (1.33) it was shown that some amount of dehydration had taken place in the hydrated samples whilst in the synchrotron beam.

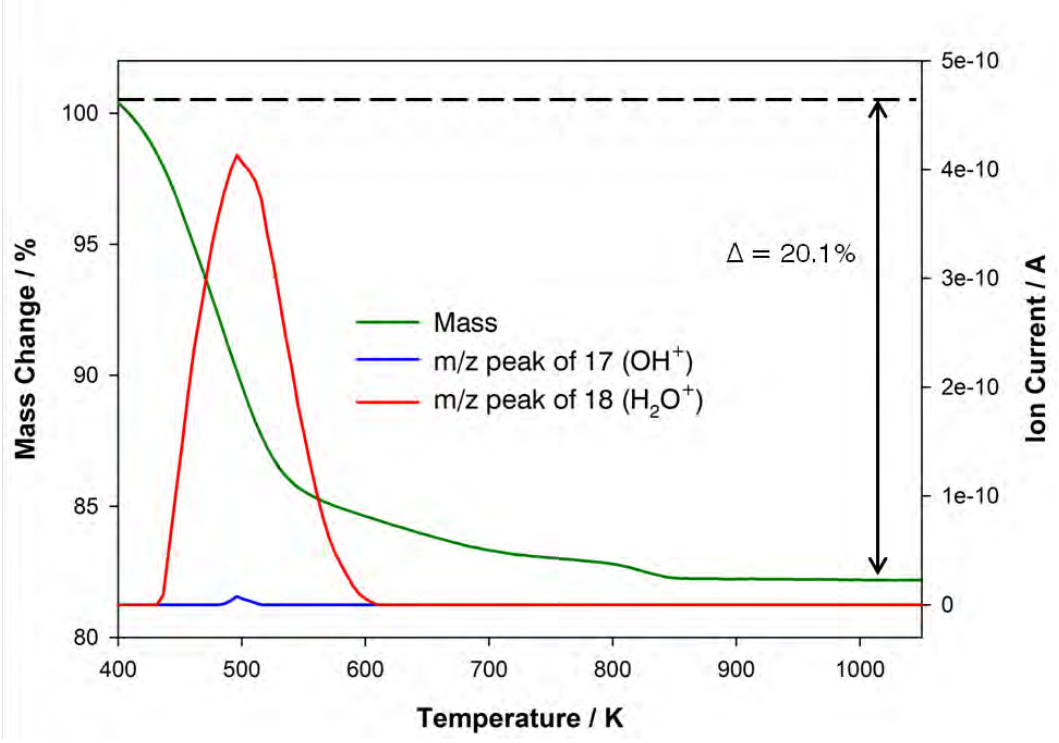

Figure 4.8 *– TGA and mass spectroscopy plot of hydrated ZK-4 (1.3) from 298–673 K.*

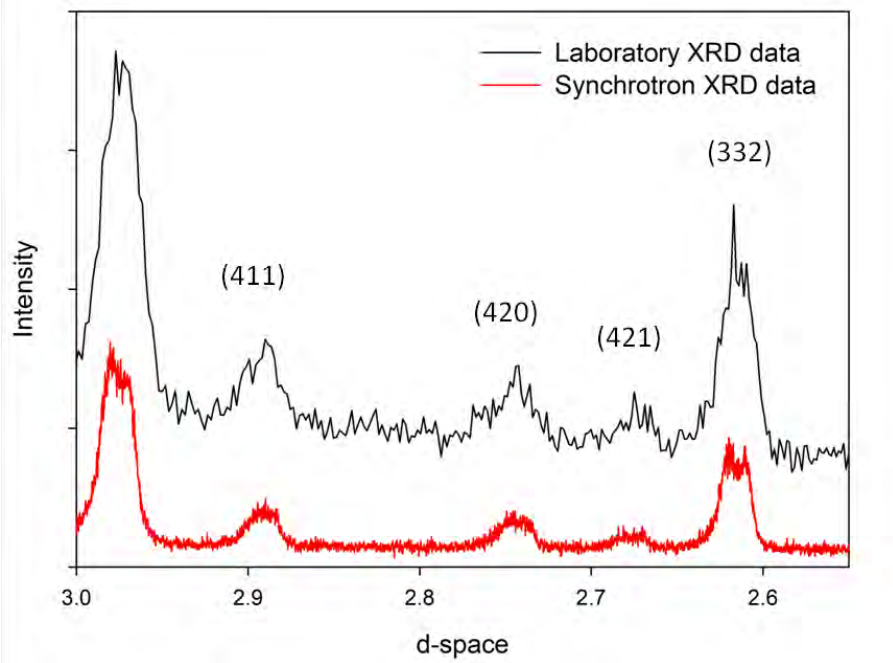

Figure 4.9 *– Comparison of the laboratory and synchrotron powder XRD patterns of hydrated ZK-4 (1.33) at 300 K.*

As shown in figure 4.10, XRD peaks from the dehydrated system perfectly overlapped with the split peaks from the hydrated system on the high angle side. This suggested that water had been quickly released from some of the sample whilst in the beam causing a contraction of the unit cell. Through performing a two phase Pawley analysis it was determined that there was a lattice parameter difference of ~0.3 Å between the hydrated and dehydrated unit cells. It is worth noting that no evidence of similar peak splitting was observed in the hydrated alkali metal exchanged zeolite A systems. The fluffy nature of the ZK-4 samples meant that the sealed capillaries were not as tightly packed when compared to the zeolite A systems. This extra space in the sealed capillaries may have allowed for water to escape from the zeolite samples and cause the split peaks. No change in the powder XRD patterns of hydrated ZK-4 (1.3) was observed after the variable temperature run (figure 4.10). This indicated that complete zeolite dehydration was not achieved

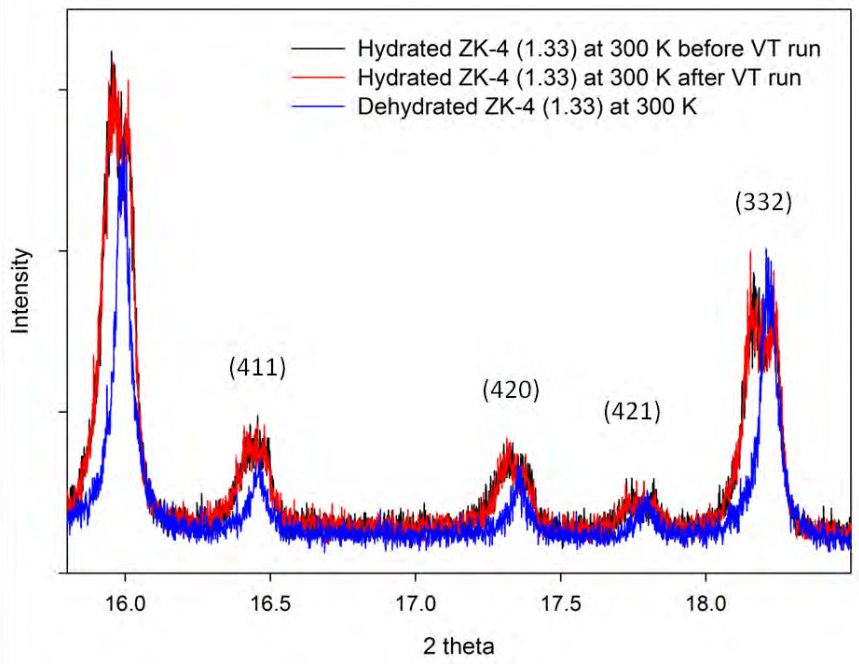

Figure 4.10 *– Powder synchrotron XRD patterns of dehydrated and hydrated ZK-4 (1.3) at 300 K*

during the data collection run and perhaps humidity equilibrium had been reached inside the sealed capillaries.

Dehydration of the samples in the beam meant that the thermal expansion behaviour of the hydrated ZK-4 systems could not be determined using variable-temperature powder synchrotron XRD data. However, through performing Pawley analysis on the variable temperature XRD data collected on the laboratory diffractometer it was shown that PTE behaviour was observed for the hydrated ZK-4 (2.39) system between 100-300 K (figure 4.11). The thermal expansion behaviour for the ZK-4 (1.6) and (1.3) systems could not be determined within error. Accurate thermal expansion coefficients and structural analysis could not be produced from this data as the errors in the calculated values were too large to base any firm conclusions on. Lattice parameters reported in table 4.11 were calculated from Pawley analysis of the laboratory XRD data.

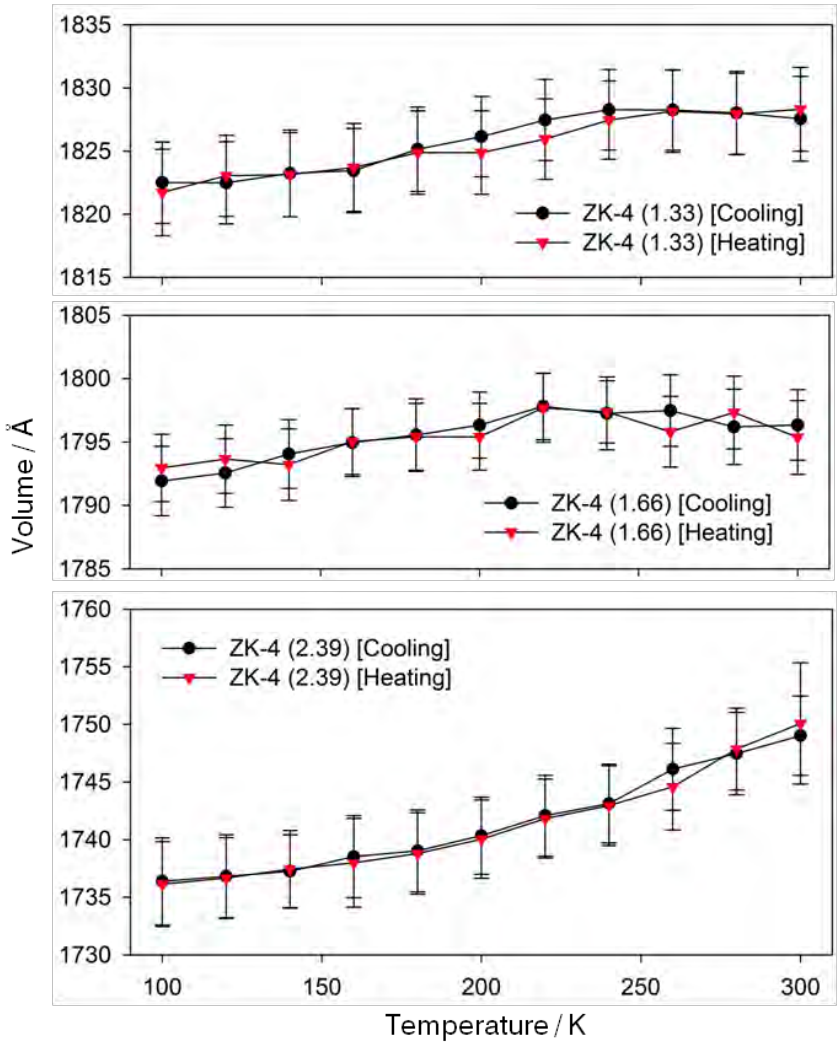

Figure 4.11 *– Calculated unit cell volumes from laboratory powder XRD data for the hydrated ZK-4 systems from 100–300 K [errors at 3σ level].*

4.4 Conclusion

NTE behaviour was observed for all the dehydrated ZK-4 systems between 100–300 K. Weaker thermal expansion coefficients were determined as the framework aluminium and consequent cation content was increased. Cations were shown to have a preference to occupy the zeolite 6-ring sites rather than any other site in the framework. This was due to cations having the highest coordination to the framework oxygen atoms when located on this site. No structural mechanism was determined for NTE behaviour; however, significant

distortions in the zeolite framework T–O–T and O–T–O bond angles were observed which were dependent on the amount of cations in the structure. One possible explanation behind the weaker thermal expansion coefficients is that the cations had an anchoring effect on the framework tetrahedra and restricted their rotation in a similar way to that described in chapter 3. Greater cation loading of the zeolite then may have restricted tetrahedra rotation further and caused weaker NTE. Structural analysis of the hydrated system was not possible due to compositional changes in the beam. From laboratory XRD data it can be shown that PTE behaviour was observed for the hydrated ZK-4 (2.39) system from 100-300 K. Accurate thermal expansion coefficients were not determined for any of the hydrated systems due to large errors in the laboratory based XRD data.

4.5 References

1. G. T. Kerr and G. T. Kolotailo, *J. Am. Chem. Soc.*, 1961, **83**, 4675-4676.
2. C. Baerlocher and R. M. Meier, *Helv. Chim. Acta.*, 1969, **7**, 188-189.
3. G. S. Zhu, S. L. Qiu, J. H. Yu, Y. Sakamoto, F. S. Xiao, R. R. Xu and O. Terasaki, 1998, **10**, 1483-1486.
4. S. Mintova, N. H. Olson, V. Valtchev and T. Bein, *Science*, 1999, **283**, 958-960.
5. T. Kodaira and T. Ikeda, 2010, J. Phys. Chem. C, 12885-12895.
6. A. Dyer and R. B. Gettins, *J. Inorg. Nucl. Chem*, 1970, **32**, 319-327.
7. A. K. Cheetham, M. M. Eddy, J. Klinowski and J. M. Thomas, *J. Chem. Soc., Chem. Commun.*, 1983, 23-25.
8. M. M. Eddy and K. Cheetham, *Zeolites*, 1985, **6**, 449-454.
9. M. T. Melchior, D. E. W. Vaughan, R. H. Jarman and A. J. Jacobson, *Nature*, 1982, **298**, 455-456.

10. J. M. Thomas, C. A. Fyfe, S. Ramdas, J. Klinowski and G. C. Gobb, *J. Phys. Chem.*, 1982, **86**, 3061-3064.

11. R. Seifert, R. Rytz and G. Calzaferri, *J. Phys. Chem. A*, 2000, **104**, 7473-7483.

12. C. P. Herrero, *J. Phys. Condens. Matter.*, 1993, **5**, 4125-4136.

13. N. N. Tušar, N. Z. Loger, I. Arčon, F. Thibault-Starzyk, A. Ristić, N. Rajić and V. Kaučič, *Chem. Mater.*, 2003, **15**, 4745-4750.

14. D. S. Bhange and V. Ramaswamy, *Micropor. and Mesopor. Mater.*, 2010, **130**, 322-326.

15. P. S. Niphadkar, D. S. Bhange, K. Selvaraj and P. N. Joshi, *Chem. Phys. Lett.*, 2012, **548**, 51-54.

16. R. H. Jarman, M. T. Melchior and D. E. W. Vaughan, *J. Am. Chem. Soc.*, 1983, **218**, 267-281.

17. K. D. Hammonds, V. Heine and M. Dove, *J. Phys. Chem. B*, 1998, **102**, 1759-1767.

Chapter 5 – Occlusion of Silver Nitrate in Silver Zeolite A

5.1 Introduction

Modification of the pore contents in LTA-zeolites has been shown to have a considerable effect on their thermal expansion properties (chapter 3). Consequently the effect of loading the zeolite pores with salt molecules was also of much interest. The process of heating a zeolite and salt whereby the salt "dissolves" into the zeolite cages is known as occlusion. One system of particular interest is formed when silver nitrate is occluded in Ag-A. Previous work has reported that a strong NTE was observed during the synthesis of this system with the formation of a superlattice structure.[1-2] No structural model or thermal expansion mechanism has yet been produced for the silver nitrate loaded Ag-A system. This chapter will focus on the structural analysis Ag-A with occluded silver nitrate and investigate the factors affecting the quantity and ordering of the salt molecules inside the pores. Thermal expansion studies of this system will be discussed in chapter 6. Further insights have been gained into the formation of the superlattice structure, especially the role intrapore water molecules play. Structure solution has also been attempted using a wide range of techniques.

5.1.1 Salt Occlusion and Structure Determination

Clarke and Steiger first reported in 1899 that salt melts could be used as a method of zeolite ion exchange.[3] Following this discovery other research groups later reported that, depending upon the framework cavity dimensions, some salts could penetrate zeolite structures and occupy the pores.[2, 4-11] Research into ion exchange through molten salt

mixtures has largely been reported on natural zeolites due their application in nuclear waste treatments and slow release fertilisers.[12-18] Publications on synthetic structures have mainly concentrated on zeolites X, Y and A.[19-23] Liquornik and co-workers[4-6] showed that cation exchange could be achieved in various nitrate-containing zeolites using molten sodium nitrate as a solvent. Full ion exchange of Na-A containing sodium nitrate was achieved when heated with silver or lithium nitrate. However, only partial exchange was found with other salts depending upon the size of the nitrate counter-ion. Petranovic and co-workers continued this work by comparing the aqueous and salt melt ion exchange properties of lithium nitrate containing Li-A and sodium nitrate containing Na-A with other alkali metal salts.[8] The aqueous exchange capacity of the salt-containing zeolites was found to be dependent on the temperature at which the salt occlusion reaction was performed. No aqueous ion exchange was observed when the occluded zeolites were formed above 600°C. However, ion exchange capacity did return when exposed to water for several days. It was therefore postulated that water must be present in the zeolite framework in order for ion exchange to occur. Nevertheless, full ion exchange of lithium nitrate containing Li-A was achieved from a salt melt with silver nitrate even after the salt occlusion reaction was performed above 600°C. Daniels and Joshi[24] later used a neutron activated isotherm experiment to show that ion exchange occurred in zeolite X well below the melting point of silver nitrate (212°C). However, salt occlusion was only observed when silver nitrate was in the molten state.

In 1958 Barrer and Meier[2] were first to report structural investigations of salts occluded in zeolites. The silver, lithium, sodium and ammonium nitrate containing forms of zeolite A were studied as well as the occlusion of NaCl by zeolite Na-X. Barrer and Meier reported that a maximum of nine silver nitrate units could be incorporated into the α-cages of zeolite

Ag-A, which resulted in the formation of a superlattice structure, where guest silver and nitrate ions were structurally ordered inside the zeolite host. No atomistic model has ever been developed for this system; however, Barrer and Meier did propose from the powder XRD pattern that the superlattice reflections were consistent with a tetragonal unit cell with the lattice constants, a' = 2a and c' = a, where a is the unit cell of zeolite Ag-A. It was suggested that the nine silver nitrate units adopted a rock-salt type configuration inside each α-cage as this arrangement was the only one that would satisfy the type of superstructure and available space inside the pores (figure 5.1). XRD studies were not carried further as the actual positions of the nitrate ions could not be located due to the presence of the strongly scattering silver cations. Superlattice reflections were best observed in the XRD pattern when the sample was cooled slowly to room temperature but were completely removed when the zeolite was excessively washed with water. Superlattice reflections were also observed for lithium nitrate in Li-A but no more structural information was given.

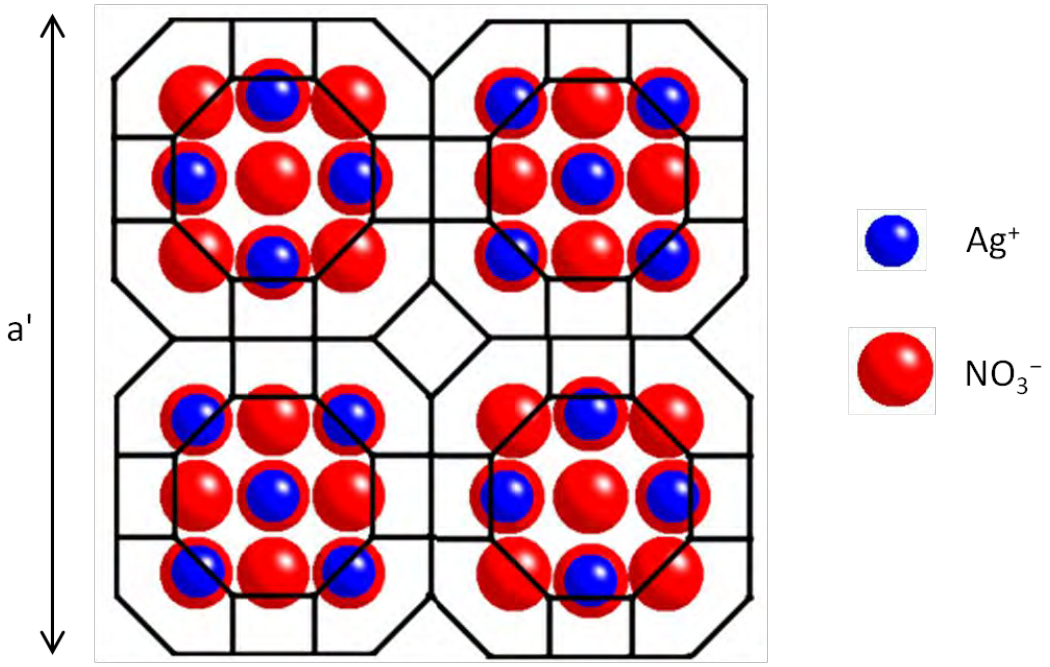

Figure 5.1 *– Diagram illustrating the rock-salt type arrangement of $AgNO_3$ inside the α-cage of zeolite Ag-A as suggested by Barrer and Meier.*[2]

Further studies by a number of research groups extended the work on salt containing zeolites by investigating the occlusion of a range of anions and cations.[7-9, 20-23, 25] Occlusion of various phosphate, sulphate, carbonate and silicate salts were found to result in the destruction of zeolite frameworks.[11] Petranovic and co-workers continued the work of Barrer and Meier by studying nitrate salt occlusion in zeolite A and determined that there were up to ten silver nitrate units per α-cage. This value was also supported in the work reported by Liquornik and Marcus,[4] although both groups did note that it was impossible to determine at what point all of the non-occluded salt had been removed through washing and none of the occluded salt. Structural analysis of the silver nitrate containing zeolite A was attempted by Petranovic *et al.*; however, it was reported that the refinement process "did not progress in a satisfactory manner."[25] This may have been due to the high degree of disorder of silver cations that was said to be present.

Successful structural analysis of sodium nitrate in Na-A was reported by two research groups.[25-26] Both studies performed the structural refinement in the cubic space group $Pm\bar{3}m$ (~12 Å unit cell), but Barrer and Villiger[26] did state that not all Bragg reflections were accounted for in the proposed unit cell, so the structure may be more complicated. Approximately ten sodium nitrate units and 6.7 water molecules were refined per unit cell. Similar Na^+ cation positions (in the 6-ring, near the 4-ring in the α-cage and at the centre of the α-cage) were identified in both of these publications. Most of the nitrate ions were found to be located on a three-fold axis inside the α-cage facing the 6-ring as illustrated in figure 5.2. These nitrates were described as being coordinated to the cations in the 4-ring and 6-ring positions. However, different positions for the remaining nitrate anions were described in the different studies. Petranovic *et al.*[25] assumed that remaining nitrate ions were located near the centre of the α-cage and in the 8-ring between two cages, whereas Barrer and

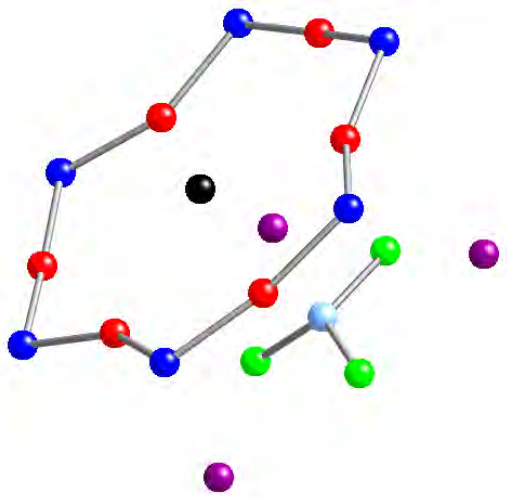

Figure 5.2 *– Diagram illustrating the proposed nitrate position on the three-fold axis near the zeolite 6-ring [dark blue = Si, red = oxygen (zeolite), black = Na^+ (6-ring), purple = Na^+ (near 4-ring), green = oxygen (nitrate) and light blue = nitrogen].*

Villiger[26] found two nitrate ions inside the β-cage on the same three-fold axis. A number of groups have investigated the occlusion of salts in zeolite β-cages.[2, 11] Due to the small diameter of the 6-ring (~2.2 Å) entry into the cage is restricted. Some relatively large species, such as halide and nitrate anions, have been shown to enter the zeolite β-cage at elevated temperature,[11] though their method of entry has caused some speculation. One proposed mechanism is through bond-breaking in the 6-ring.[27] Another method, specific to nitrate ions, is by smaller NO or NO_2 molecules entering the β-cage and then reacting with the zeolite framework.[11] A more probable mechanism for entry of large molecules is through pore breathing modes in the zeolite 6-ring caused by correlated T–O–T vibrations.[28]

IR spectroscopy was also carried out by Petranovic *et al.* in order to establish the nitrate location in the zeolite. IR bands originating from the zeolite framework (at ca. 990, 553 and 452 cm^{-1}) were slightly affected by the introduction of nitrate salt due to the coordination with the oxygen atoms. The most pronounced change was in the splitting in the double 4-

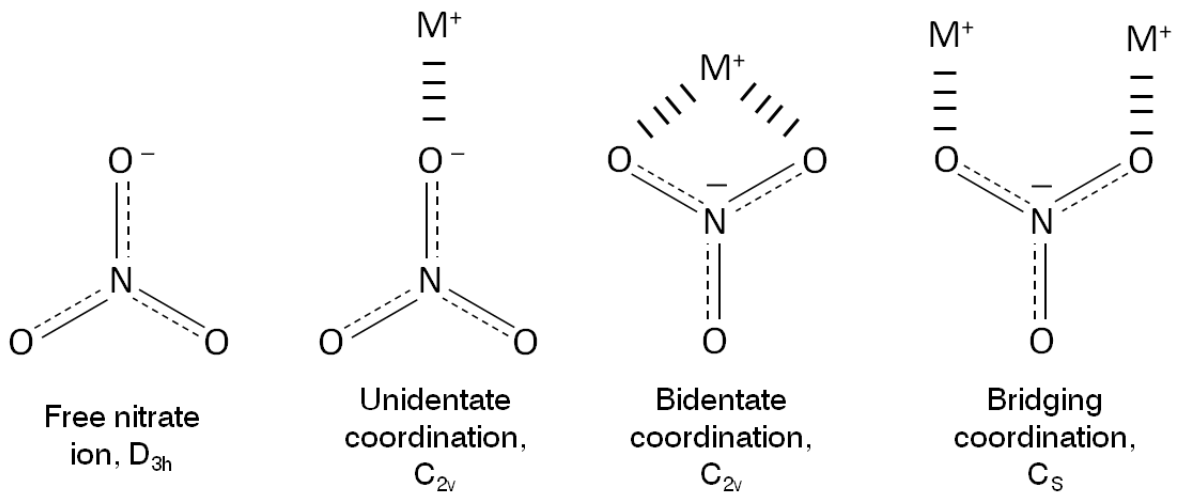

Figure 5.3 *– Diagram illustrating the different types of metal nitrate coordination.*

ring band at ca. 553 cm^{-1}. Bands characteristic of OH and water molecules were identified at wavenumbers above 2500 cm^{-1}.

Complex bands at 2440, 1750, 1450, 1300 and 1050 cm^{-1} suggested that nitrate anions were coordinated to the metal cations inside the zeolite cages. Unidentate, bidentate or bridging coordination are possible for nitrate anions resulting in a lowering of symmetry and a change in point group from the free ion (figure 5.3). Bands at 1380 and 820 cm^{-1} showed that the nitrate anions also existed as free ions within the zeolite. However, these bands may have been caused by nitrates on the surface of the zeolite. Through comparison of their IR and XRD results, Petranovic *et al.* concluded that a bridged coordination of the nitrate anions was most likely in sodium nitrate containing Na-A. Later work by other research groups attributed the broad band at ~1430 cm^{-1} to two nitrate anions in the β-cage.[29-30] This assignment was supported by Petfield and Clooney[31] who also attributed a similar band at ~1400 cm^{-1} to two nitrate ions in the β-cage of sodium nitrate containing zeolite Na-X.

Structural analysis of lithium nitrate in Li-A was also reported by Petranovic *et al*.[25] A structure similar to the sodium nitrate containing system was determined from single crystal XRD data, however, small differences in the zeolite fingerprint range (300 to 750 cm^{-1}) of the IR spectra were observed. An intense band at 1330 cm^{-1} in the IR spectrum of silver nitrate in Ag-A suggested that unidentate coordination of the nitrate anions was more pronounced in that system.

Further structural work by Viertelhaus *et al.*[1] on silver nitrate in zeolite Ag-A showed it was possible to index all but one of the powder XRD peaks in the tetragonal space group *P4/nmm* (a subgroup of $Pm\bar{3}m$) with unit cell parameters a' = 17.573(5) Å and c' = 12.48(1) Å. This proposed unit cell had only half the volume of the unit cell suggested by Barrer and Meier[2] and was related to the ~12 Å cubic unit cell ($Pm\bar{3}m$) of zeolite A as follows (figure 5.4):

$$a' = \sqrt{2}a \qquad \text{and} \qquad c' = c$$

The one remaining XRD peak (531) is caused by Si/Al ordering and can be indexed in the cubic space group $Fm\bar{3}c$. Similar unit cell symmetry reduction has been shown in lead iodide containing zeolite Na-A to the space group *P4/ncc*.[32] As the superlattice XRD peaks were much broader than the sharp zeolite peaks, Viertelhaus *et al.* suggested an incommensurate system where the $AgNO_3$ guest clusters inside the zeolite cages are arranged in a lattice that does not have the full symmetry of the host i.e. the superlattice is a different size to the zeolite host lattice. The broad peaks indicated a smaller domain size for the superlattice, consistent with the guest lattice breaking down after approximately five repeating units. The intensities of the host zeolite peaks were reported to be affected by silver nitrate ordering but remained sharp. No structural model was produced from this

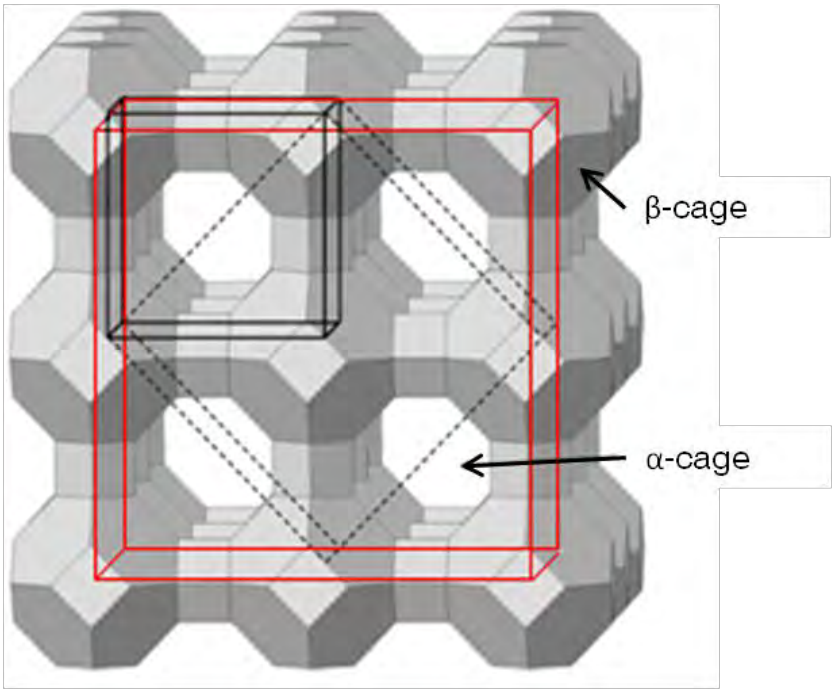

Figure 5.4 *– Structure of zeolite A illustrating the different proposed unit cells for the structure: $Pm\bar{3}m$ (black) $Fm\bar{3}c$ (red) and P4/nmm (dotted). Figure adapted from reference.*[1]

study; however, it was postulated from neutron diffraction analysis that the superlattice structure mainly involved silver cations as the nitrate anions maybe more disordered through rotation inside the zeolite cages. This deduction was made as no superlattice peaks were present in neutron diffraction data.

5.2 Synthesis

Two different methods of preparing silver nitrate containing Ag-A were used in this research. One method was done in air as described by Barrer and Meier,[2] and the other was done in rigorously anhydrous and oxygen-free conditions under high vacuum. Large single crystals were also prepared for single crystal XRD analysis.

5.2.1 Preparation under Atmospheric Conditions

Zeolite Ag-A was prepared from Na-A as described in sections 3.3.2 and 3.2.3. Silver nitrate and Ag-A were weighed out in a 5:1 weight ratio and ground together in a mortar and pestle. The mixture was then placed in an alumina crucible and heated slowly (to prevent splitting due to over-rapid release of water during zeolite dehydration) to 533 K for 8 hours, before being slowly cooled to room temperature over 12 hours. The resulting product was finely ground and washed with a small amount of cold water to remove surface silver nitrate. Samples were stored in vials covered in aluminium foil due to their photosensitivity.

5.2.2 Preparation under Anhydrous Conditions

Zeolite Ag-A was dehydrated as described in section 3.2.4 and stored in a dry glove box. Silver nitrate and dehydrated Ag-A were weighed out in a stoichiometric 9:1 molar ratio and ground together using a mortar and pestle. The resulting mixture was then placed in a quartz tube, with a Young's tap attached, and evacuated on a two-stage vacuum pump to a pressure below 5×10^{-9} bar. This evacuated tube was then sealed using a blowtorch flame and heated to 533 K for 96 hours. The mixture was then slowly cooled to 373 K over 12 hours, cooled further to 353 K over 24 hours, and finally cooled to room temperature over 12 hours. The sealed tube was then taken into a dry glove box to be prepared for analysis.

5.2.3 Single Crystal Preparation of Silver Nitrate in Zeolite Ag-A

Large single crystals of zeolite Na-A were grown by heating sodium metasilicate with sodium aluminate in the presence of triethanolamine as a stabilising agent, as described by Charnell.[33] A sodium metasilicate solution was prepared by dissolving 18.662 g of sodium metasilicate pentahydrate and 25 ml of triethanolamine in 175 ml of deionised water under

gentle heating. The sodium aluminate solution was prepared by dissolving 20 g of sodium aluminate and 25 ml of triethanolamine in 175 ml of deionised water. Both solutions were then filtered with the aid of vacuum through a 0.2 μm pore filter, mixed in a polypropylene jar and heated in a covered water bath at 80°C for 3 weeks. The resulting crystals were then washed with deionised water and dried overnight. Larger single crystals were produced when the reaction mixture was heated for 5 weeks in a seeded container.

Silver ion exchange was achieved by dissolving the prepared Na-A single crystals in a 0.1 mol dm^{-3} silver nitrate solution and gently shaking the reaction vessel for 24 hours. The resulting crystals were then washed with deionised water and dried overnight. This process was repeated twice to ensure complete ion exchange.

Silver nitrate occlusion was achieved by heating the silver-exchanged single crystals with a large excess of silver nitrate under atmospheric conditions as described in section 5.3.1. The samples were not ground during this process to ensure the zeolite single crystals remained as large as possible.

5.3 Results and Discussion

5.3.1 Superlattice Formation

Intra-pore water molecules were discovered to play a vital role in the formation of the superlattice structure in silver nitrate occluded zeolite Ag-A. As shown in figure 5.5, broad superlattice peaks were observed in the powder XRD pattern when the salt-containing zeolite was prepared under atmospheric conditions. However, when prepared under rigorously anhydrous and oxygen-free conditions the superlattice peaks were not present.

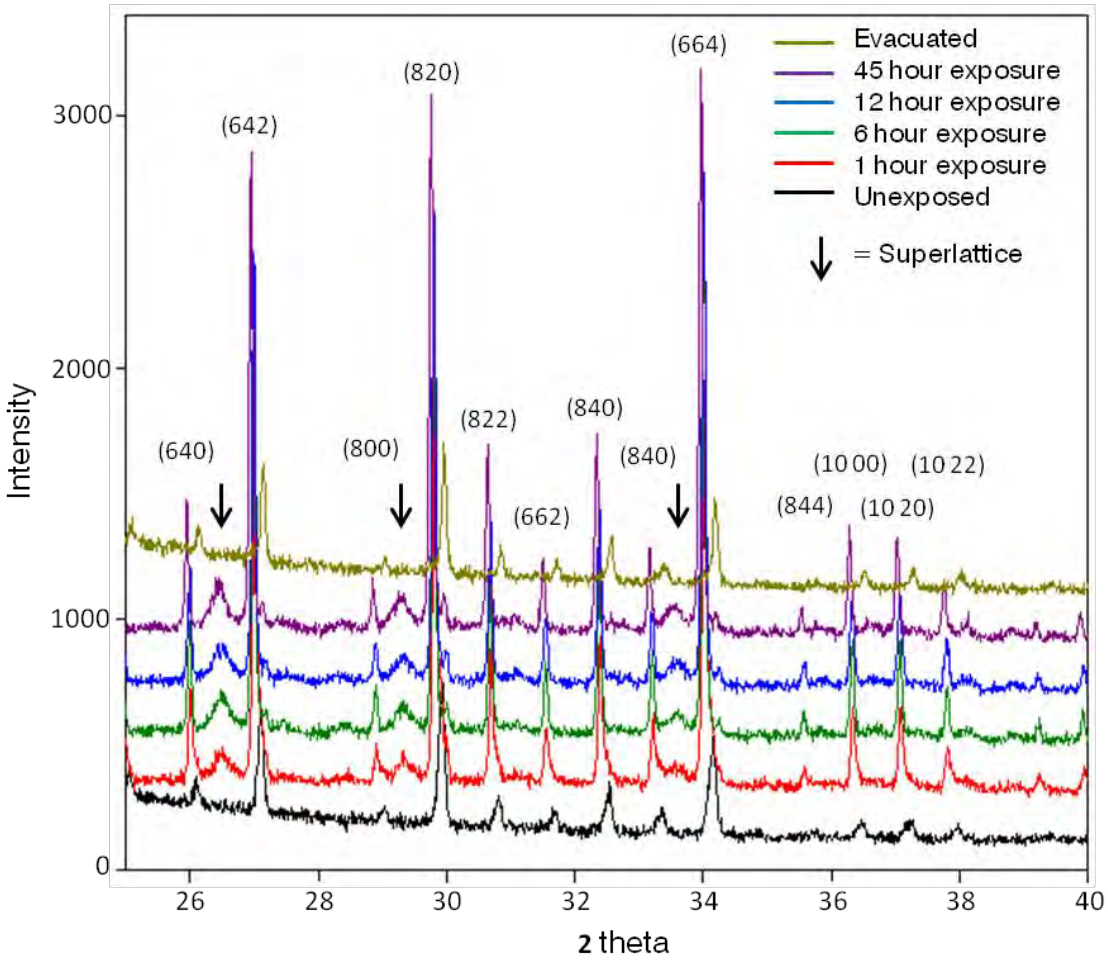

Figure 5.5 *– Powder XRD patterns of silver nitrate containing zeolite Ag-A illustrating the appearance of superlattice peaks upon exposure to the atmosphere (zeolite peaks indexed using a cubic space group $Fm\bar{3}c$, $a \approx 24.65$ Å).*

After exposing this sample to the atmosphere, broad superlattice peaks were seen to appear in the powder XRD pattern. This suggested that water molecules present in the atmosphere had been absorbed into the zeolite upon exposure and resulted in the formation of the superlattice. The superlattice formation was also shown to be reversible as the superlattice peaks were seen to disappear after the exposed sample was put under high vacuum. TGA and mass spectrometry were used in order to determine the type of molecules that were causing the superlattice structure. As shown in figure 5.6, water was released from the zeolite between 300 K and 620 K and nitric oxide molecules were released

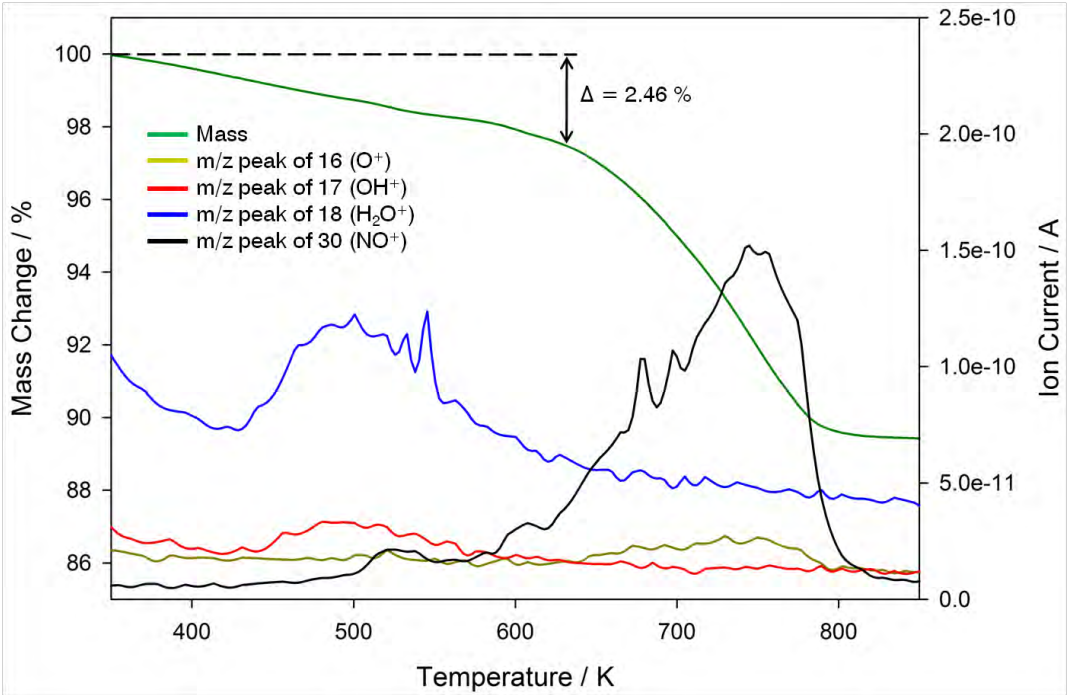

Figure 5.6 *– TGA of silver nitrate occluded zeolite Ag-A from 300–670 K.*

above 600 K. This suggested that water molecules absorbed from the atmosphere caused a structural change in the zeolite cage contents. This was confirmed by collecting powder XRD data of the salt-containing zeolite as the sample was exposed to atmospheres with different levels of humidity. As shown in figure 5.7 no superlattice peaks were observed when the sample was exposed to synthetic air (20 % oxygen/80 % nitrogen) with 0 % humidity. However, even in humidified environments as low as 5 % humidity, broad superlattice peaks were observed. From the TGA and mass spectroscopy analysis it was determined that approximately 29.6 water molecules were present per unit cell ($Ag_{96}[Si_{96}Al_{96}O_{384}].72AgNO_3.29.6H_2O$) in the zeolite.

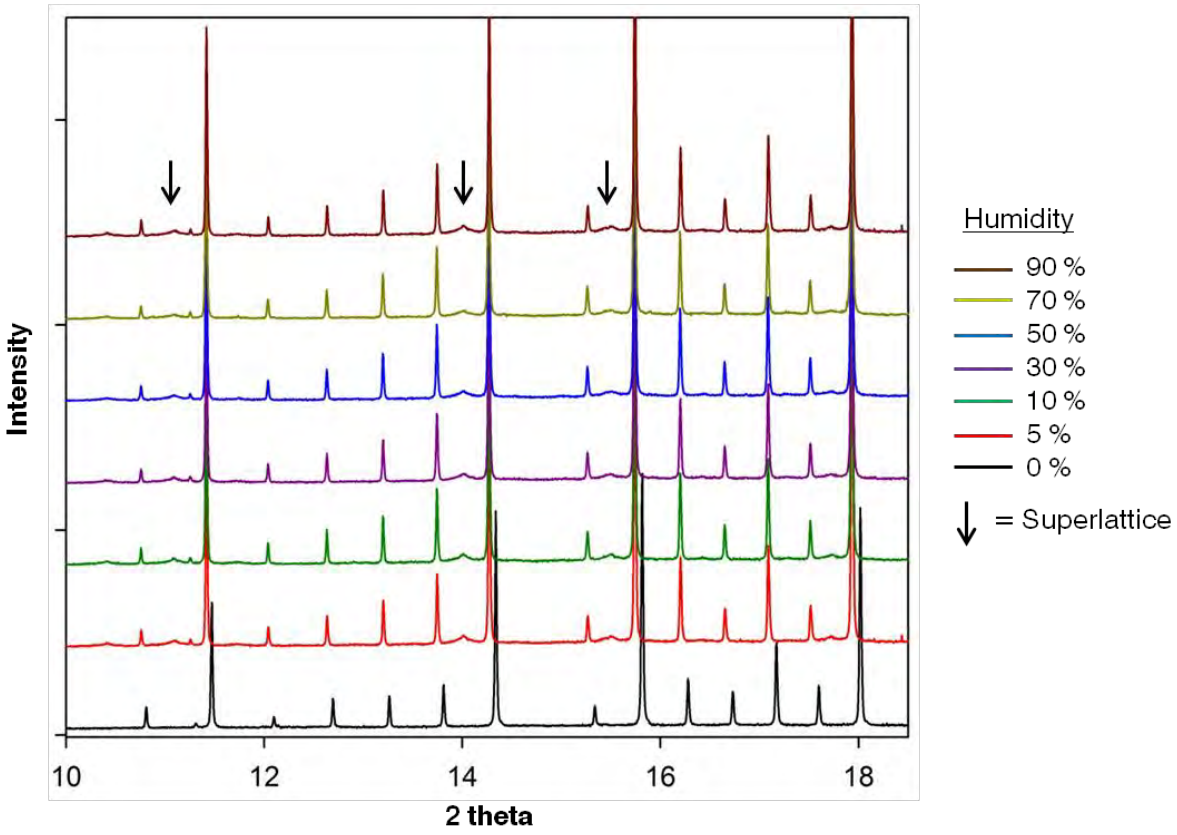

Figure 5.7 *– Powder synchrotron XRD patterns of silver nitrate containing zeolite Ag-A when exposed to a range of humidified atmospheres (data collected using humidity cell).*

Partial loading of the zeolite pores was also carried out in order to determine what effect it had on the superlattice formation. This was done by mixing dehydrated Ag-A and silver nitrate in a range of molar ratios (zeolite 1 : n $AgNO_3$, where n = 1–9) and performing a salt occlusion reaction. As shown in figure 5.8, a splitting of the peaks was observed in the powder synchrotron XRD patterns of the partially loaded samples. A shift in intensity from right to left was also shown in the split peaks as the amount of silver nitrate was increased. This peak splitting was attributed to a two phase system whereby the zeolite cages were either loaded with silver nitrate and water molecules or not. Superlattice peaks were also only observed at high loading levels of silver nitrate. Through applying the Scherrer equation (equation 5.1) to the broad superlattice peaks it can be determined that the

superlattice structure has a domain size of approximately 300 Å (~12 unit cells), much smaller than that of the average zeolite crystal size.

$$\text{Crystallite size} = \frac{B\lambda}{\beta \cos\theta} \qquad (5.1)$$

where *B* is the crystalline shape factor, λ is the X-ray wavelength, β is the line broadening at half the maximum intensity (in radians) and θ is the Bragg angle.

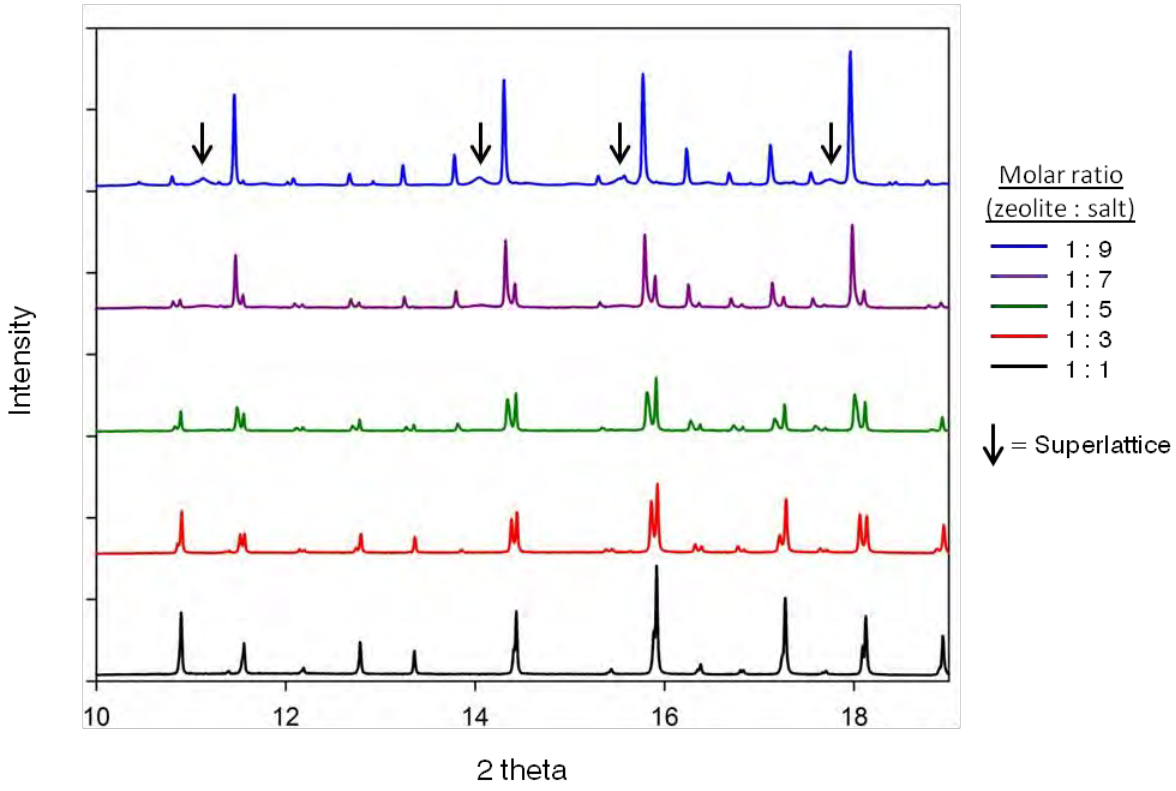

Figure 5.8 *– Powder synchrotron XRD patterns of zeolite Ag-A containing various amounts of silver nitrate.*

5.3.2 Indexing and Space Group Determination

The peak positions from powder XRD patterns of hydrated and anhydrous silver nitrate containing Ag-A ($(AgNO_3)_{72}$–AgA) were run through the indexing routine in Topas.[34] All XRD peaks in the anhydrous system were indexed in the cubic space group *Fm*$\bar{3}$*c,* which was the same as the parent zeolite Ag-A. For the hydrated system a trial and error approach was applied. Investigation of the systematic absences of the diffraction pattern indicated that a primitive unit cell was most likely with *Pn*$\bar{3}$*n, Pm*$\bar{3}$*n, Pa*$\bar{3}$*, P2*$_1$*3* or *P23* as the most probable space groups. From this small list *Pn*$\bar{3}$*n,* which is a symmetry related subgroup of *Fm*$\bar{3}$*c,* was deemed best space group. Unit cell parameters of a = 24.60590(3) Å and 24.7617(2) Å were obtained for the anhydrous and hydrated systems, respectively, through Pawley refinement.

When the symmetry related space groups are compared, *Fm*$\bar{3}$*c* has a face centred lattice with a much higher symmetry than that of the primitive *Pn*$\bar{3}$*n* lattice (table 5.1). Any atoms positioned on the special sites in *Fm*$\bar{3}$*c* will be reflected over the entire unit cell. However, atoms occupying the 16f, 12e and 2a sites in *Pn*$\bar{3}$*n* are only reflected in 2/8 of the unit cell as illustrated in figure 5.9a. Atoms positioned on the 24g, 12d and 6b sites are only reflected in the remaining 6/8 of the unit cell (figure 5.9b). This suggested that the position of the ions and molecules inside the loaded zeolite pores were no longer symmetry related in the unit cell after hydration. Therefore, water molecules had an ordering or disordering effect on the zeolite pore contents after absorption into $(AgNO_3)_{72}$–AgA, resulting in a change in unit cell symmetry.

Table 5.1 *– Special positions available in the cubic space groups* $Fm\bar{3}c$ *and* $Pn\bar{3}n$.

Fm–3c *(F 4/m* $\bar{3}$ *2/c)*	***Pn–3n*** *(P 4/n* $\bar{3}$ *2/n)*
192 i (x, y, z)	48 i (x, y, z)
96 i (0, y, z)	24 h (¼, y, y)
96 h (¼, y, y)	24 g (x, ¾, ¼)
64 g (x, x, x)	16 f (x, x, x)
48 f (x, ¼, ¼)	12 e (x, ¼, ¼)
48 e (x, 0, 0)	12 d (0, ¾, ¼)
24 d (0, ¼, ¼)	8 c (0, 0, 0)
24 c (¼, 0, 0)	6 b (¾, ¼, ¼)
8 b (0, 0, 0)	2 a (¼, ¼, ¼)
8 a (¼, ¼, ¼)	

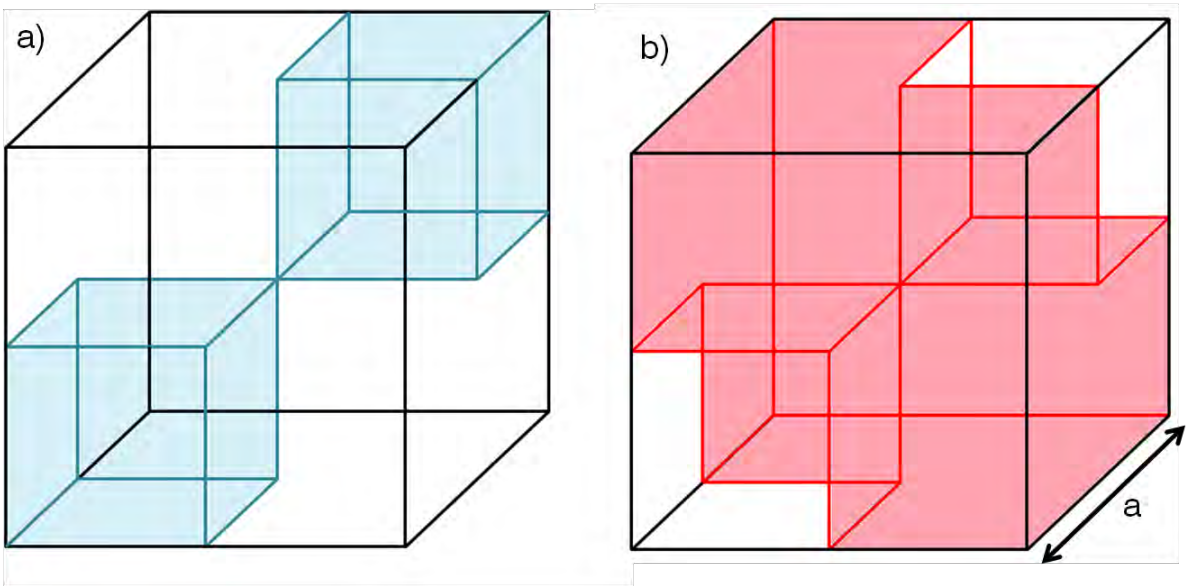

Figure 5.9 *– Diagram illustrating the symmetry relationships in the space group* $Pn\bar{3}n$ *for special positions that are located in a) 2/8 and b) 6/8 of the unit cell. Shaded areas indicate where special sites are located.*

Table 5.2 *– Refined atomic coordinates of anhydrous silver nitrate loaded Ag-A from powder synchrotron XRD data.*[a]

Atom	Wyckoff Position	x	y	z	Occupancy	B
Si(1)	96i	0	0.3127(3)	0.5909(2)	1	1.75(6)
Al(1)	96i	0	0.8137(3)	0.5899(2)	1	1.75(6)
O(1)	96i	0	0.7528(6)	0.8947(2)	1	4.9(1)
O(2)	96i	0	0.6303(5)	0.6303(5)	1	4.9(1)
O(3)	192j	0.0518(3)	0.0478(3)	0.1715(2)	1	4.9(1)
Ag(1)	64g	0.9300(2)	0.9300(2)	0.9300(2)	0.306(7)	2.89(6)
Ag(2)	64g	0.9137(4)	0.9137(4)	0.9137(4)	0.199(6)	2.89(6)
Ag(3)	64g	0.8894(1)	0.8894(1)	0.8894(1)	0.304(3)	2.89(6)
Ag(4)	192j	0.9539(5)	0.2400(8)	0.2035(5)	0.045(1)	2.89(6)
Ag(5)	48e	0.9193(3)	0	0	0.165(2)	2.89(6)
Ag(6)	192j	0.0965(2)	0.1595(3)	0.2643(2)	0.122(1)	2.89(6)
Ag(7)	96h	0.25	0.8824(1)	0.8824(1)	0.260(2)	2.89(6)

[a] *$a = 24.60590(3)$ Å, space group = $Fm\bar{3}c$, $\chi^2=2.07$, $R_{wp} = 8.74$ %, $R_p = 4.22$ %*

5.3.3 Structural Analysis of Powder Synchrotron XRD Data

5.3.3.1 Anhydrous Silver Nitrate Loaded Ag-A

Rietveld analysis of anhydrous $(AgNO_3)_{72}$–AgA was attempted in the cubic space group $Fm\bar{3}c$ using the reported structure for sodium nitrate in Na-A[25] ($Pm\bar{3}m$) as a starting point. Atomic zeolite framework coordinates were calculated for the larger unit cell and refined against the recorded powder synchrotron XRD data with the computer software Topas.[34] The positions of the ions and molecules inside the zeolite pores were analysed through difference Fourier mapping. Table 5.2 shows the refined atomic coordinates for anhydrous silver nitrate loaded Ag-A. Four different regions of electron density were identified inside the LTA framework: near the 6-ring, 8-ring, 4-ring and inside the β-cage. Three separate spots of electron density were found near the 6-ring as illustrated in figure 5.10. These were assigned to be disordered Ag^+ cation sites which were coordinated to framework O(2) and O(3) atoms and had a combined refined occupancy of 0.809. Cations on the Ag(1) and

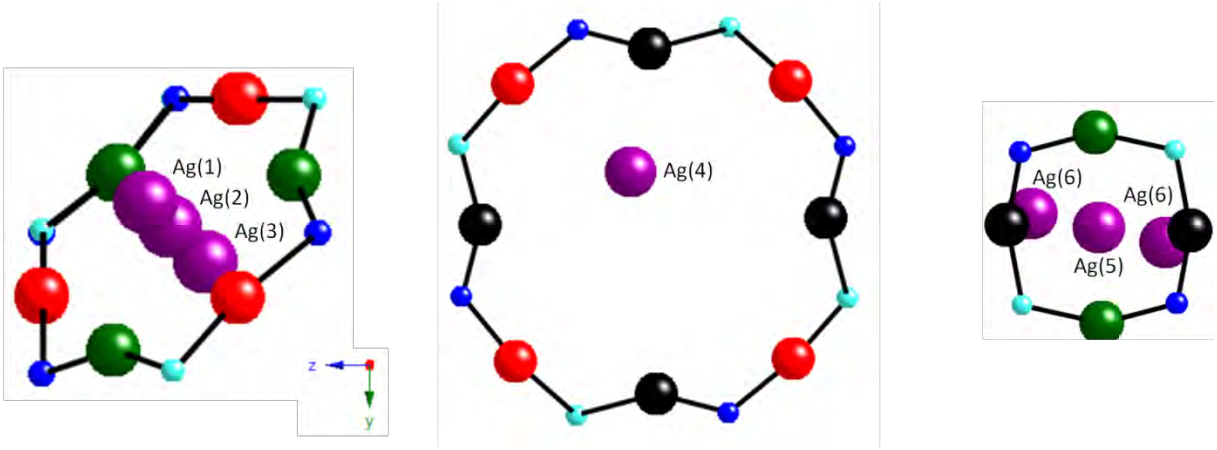

Figure 5.10 *– Diagrams illustrating the refined Ag^+ positions near the 6-ring [left], 8-ring [centre] and 4-ring [right] of anhydrous $(AgNO_3)_{72}$–AgA (dark blue = Si, light blue = Al, black = O(1), red = O(2), green = O(3) and purple = Ag).*

Ag(3) sites were slightly displaced out of the plane of the 6-ring by ~0.8 Å into the β-cage and α-cage, respectively.

Electron density near the 8-ring was also identified as Ag^+ cations which were coordinated to framework O(1) and O(2) atoms (figure 5.10). Ag(4) cations were located just off centre in the zeolite ring and were ~1 Å from the plane of the 8-ring inside the α-cage. Three separate electron density spots were identified near the 4-ring which were identified as disordered Ag^+ cation sites. Cations on the Ag(5) site were located in a centralised 4-ring position approximately 2.2 Å from the plane of the ring inside the α-cage. Cations on the Ag(6) site were located in an off centre 4-ring position with a further distance of approximately 2.6 Å from the plane of the ring. The distance between cationic sites Ag(5) and Ag(6) was 1.19 Å. This distance is similar to the N–O bond distance (1.12 Å) in a nitrate molecule, however, the possibility of nitrate anions being located in this position was quickly dismissed due to the arrangement of the electron density spots.

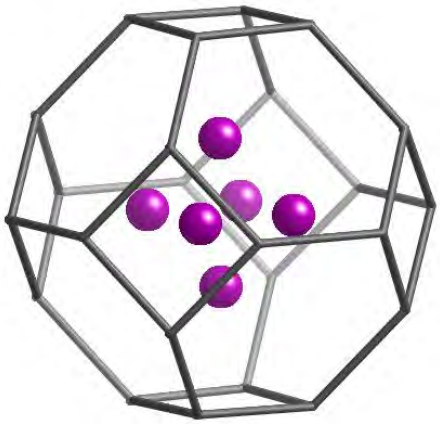

Figure 5.11 *– Octahedral silver clusters identified in the β-cages of anhydrous* $(AgNO_3)_{72}$*–AgA.*

The final area where electron density spots were identified was in the zeolite β-cage. As illustrated in figure 5.11, these spots had an octahedral geometry, which may have been residual Ag_6^0 clusters, which formed on dehydration of Ag-A, [35] and remained after the salt occlusion reaction. Another possible cause of these spots may have due to two nitrate anions located in the β-cage as described by Barrer and Villiger.[26] After measuring a distance of 2.55 Å between the spots it was determined that silver clusters in the β-cage were responsible as the distance was similar to that observed in dehydrated Ag-A (section 3.6.1.2). Planar nitrate ions have a smaller O-O distance of ~2.1 Å.

No other localised spots of electron density were identified through Fourier mapping. However as illustrated in figure 5.12, a large cloud of weak electron density remained in the α-cage which suggested that the nitrate anions and remaining Ag^+ cations were highly disordered. Figure 5.13 shows the Rietveld refinement plot of anhydrous $(AgNO_3)_{72}$–AgA using only the identified zeolite framework and silver atoms ($\chi^2 = 2.07$, $R_{wp} = 8.74$ %). Small amounts of excess non-occluded silver nitrate and silver metal were also shown to be present in the XRD pattern. Silver metal was believed to be caused by the excess silver

nitrate decomposing in the intense synchrotron X–ray beam. In an attempt to improve this Rietveld fit, nitrate ions were introduced into the refinement using the reported atomic coordinates from the sodium nitrate in Na-A system.[25] Unfortunately after applying these changes the fit was shown to be significantly worse.

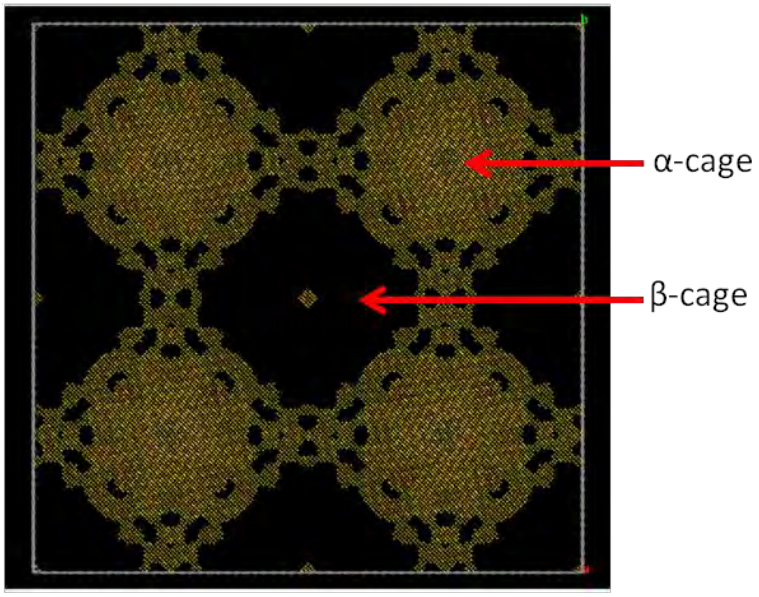

Figure 5.12 *– 3D difference Fourier map of anhydrous $(AgNO_3)_{72}$–AgA after zeolite framework and silver cations have been refined.*

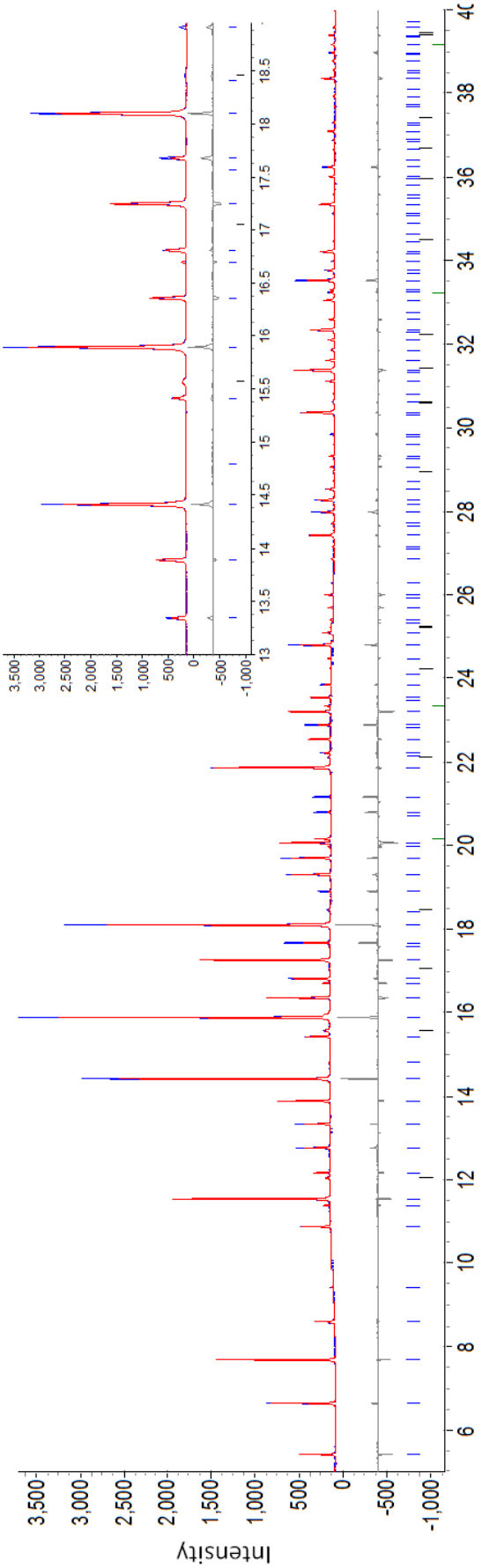

***Figure 5.13** – Rietveld refinement plot of anhydrous ($AgNO_3$)$_{72}$–AgAat 300 K.*

Table 5.3 *– Refined atomic coordinates of hydrated $(AgNO_3)_{72}$–AgA from powder synchrotron XRD data.*[a]

	Site	Wyckoff Position	x	y	z	occ	B
Zeolite Framework	Si(1)	48i	0.00(4)	0.91(6)	0.82(6)	1	2
	Si(2)	48i	0.00(3)	0.09(6)	0.82(6)	1	2
	Al(1)	48i	0.00(4)	0.41(6)	0.82(6)	1	2
	Al(2)	48i	0.00(3)	0.59(6)	0.82(6)	1	2
	O(1)	48i	0.00(1)	0.74(2)	0.89(1)	1	2
	O(2)	48i	0.99(1)	0.25(1)	0.89(1)	1	2
	O(3)	48i	0.99(1)	0.65(6)	0.65(6)	1	2
	O(4)	48i	0.991(6)	0.36(2)	0.64(2)	1	2
	O(5)	48i	0.44(1)	0.44(1)	0.32(2)	1	2
	O(6)	48i	0.56(7)	0.55(8)	0.32(2)	1	2
	O(7)	48i	0.55(1)	0.44(1)	0.68(4)	1	2
	O(8)	48i	0.44(1)	0.56(1)	0.68(5)	1	2
6R	Ag(1)	16f	0.411(5)	0.411(5)	0.411(5)	0.36(3)	2.5
	Ag(2)	16f	0.926(6)	0.926(6)	0.926(6)	0.61(3)	2.5
	Ag(3)	48i	0.391(2)	0.391(2)	0.609(2)	0.49(3)	2.5
	Ag(4)	48i	0.079(3)	0.92(1)	0.92(1)	0.57(3)	2.5
4R	Ag(5)	24h	0.25	0.113(1)	0.113(1)	0.44(6)	3
	Ag(6)	24h	0.25	0.870(1)	0.870(1)	0.41(6)	3
	Ag(7)	48i	0.75	0.116(1)	0.616(1)	0.52(3)	3
	Ag(8)	48i	0.132(1)	0.202(6)	0.303(7)	0.25(3)	3
	Ag(9)	48i	0.930(1)	0.795(1)	0.235(2)	0.59(3)	3
	Ag(10)	48i	0.910(1)	0.207(1)	0.752(3)	0.34(3)	3
	Ag(11)	48i	0.084(1)	0.838(9)	0.765(1)	0.41(3)	3

[a] *$a = 24.7617(2)$ Å, space group = $Pn\bar{3}n$, $\chi^2=3.41$, $R_{wp} = 21.44$ %, $R_p = 6.27$ %*

5.3.3.2 Hydrated Silver Nitrate Loaded Ag-A

Rietveld analysis of hydrated $(AgNO_3)_{72}$–AgA was attempted in the cubic space group *$Pn\bar{3}n$.* Atomic zeolite framework coordinates were calculated from the face-centred parent unit cell and refined against the recorded powder synchrotron XRD data with the computer software Topas.[34] Lower unit cell symmetry meant that more crystallographic sites were required when compared to the space group *$Fm\bar{3}c$*. The positions of the ions and molecules inside the zeolite pores were analysed through difference Fourier mapping. Successful structure refinement was not possible using powder synchrotron XRD data due the high

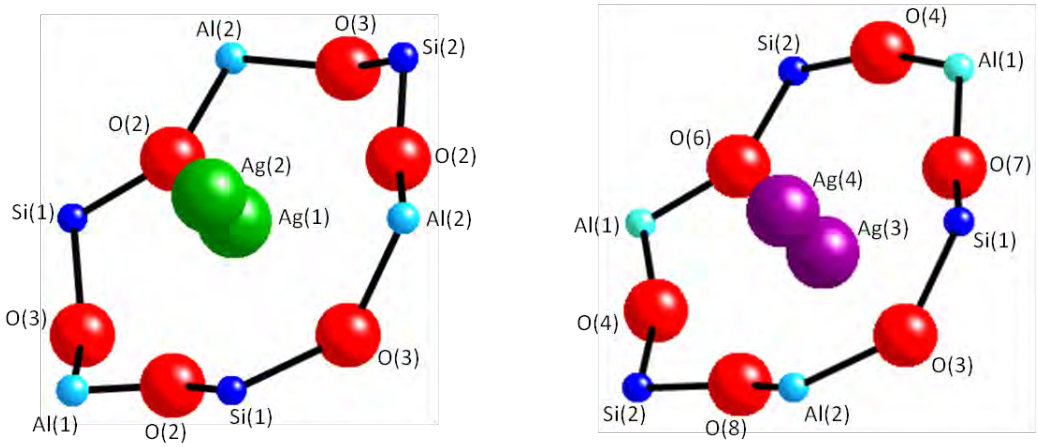

Figure 5.14 *– Diagrams illustrating the refined Ag^+ positions near the 6-ring hydrated $(AgNO_3)_{72}$–AgA*

disorder of the zeolite pore contents. Table 5.3 shows the refined atomic coordinates for the atoms that were located in the hydrated system. Areas of localised electron density were identified in two different regions of the LTA framework: near the 6-ring and 4-ring. Two separate spots of electron density were found near all of the 6-ring's as illustrated in figure 5.14. Ag(1) and Ag(2) were cationic sites located on the special position 16f. These two sites had a distance of ~0.6 Å between them and occupied only ¼ of the possible 6-ring in the unit cell. Cations occupying these sites were coordinated to framework atoms O(2) and O(3). Ag(3) and Ag(4) were cationic sites that occupied the remainder the 6-ring's in the unit cell and had a larger distance of 1.04 Å between them. Cations occupying these sites were coordinated to framework atoms O(4), O(6), O(7) and O(8).

Three separate electron density spots were identified near the 4-ring which were identified as Ag^+ cation sites. Sites Ag(5) and Ag(8) were only located near a ¼ of the 4-ring's in the unit cell whereas Ag(6), Ag(7) and Ag(9)-Ag(11) were located near the remaining 4-ring's. Cations on the Ag(5) site were located in a centralised 4-ring position approximately 2.4 Å from the plane of the ring inside the α-cage (figure 5.15). Cations on the Ag(8) site were

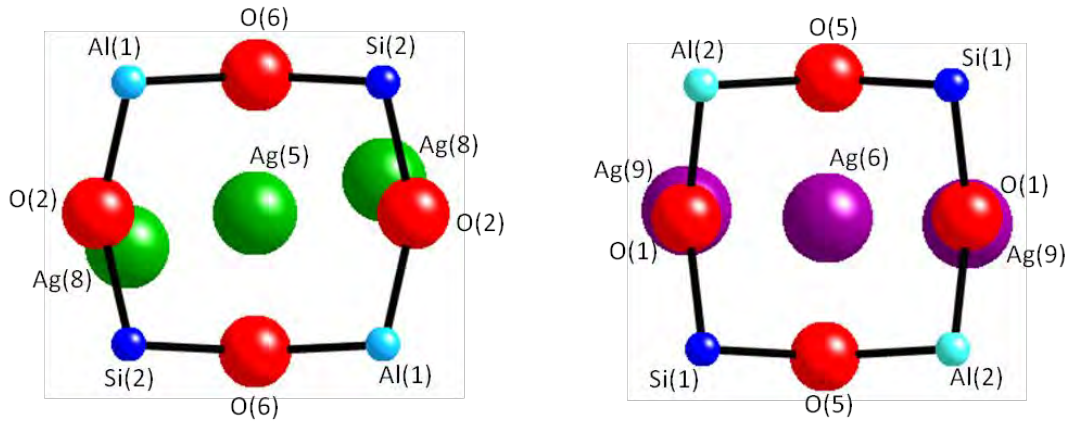

Figure 5.15 *– Diagrams illustrating the refined Ag^+ positions near the 4-ring of hydrated $(AgNO_3)_{72}$–AgA*

located in an off-centre 4-ring position either side of Ag(5) with a further distance of approximately 3.07 Å from the plane of the ring. The distance between cationic sites Ag(5) and Ag(8) was 1.19 Å. Similarly to Ag(5), the cationic sites Ag(6) and Ag(7) were also positioned in a centralised 4-ring location with a distance of approximately 2.39 Å from the plane of the ring inside the α-cage. Ag(9) was positioned either side of Ag(6) on a 48i site whereas Ag(10) and Ag(11) were either side of Ag(7). These cationic sites were similar to the respective sites in the anhydrous system. Interestingly however, intensity in the broad superlattice peaks was only observed during the refinement process when atoms occupied either the Ag(8), Ag(9), Ag(10) or Ag(11) sites in the structural model (figure 5.16). This suggested that a displacement of the 4-ring cations from a more symmetric position had occurred upon hydration, which had lead to a change in the unit cell symmetry. No further information on the positions of the nitrate anions and water molecules was gained from the powder synchrotron XRD data. Figure 5.17 shows the difference Fourier map of hydrated $(AgNO_3)_{72}$–AgA after the after the framework atoms and some of the Ag^+ cation had been refined. Successful structural refinement of hydrated $(AgNO_3)_{72}$–AgA was not achieved through analysis of the powder synchrotron XRD data.

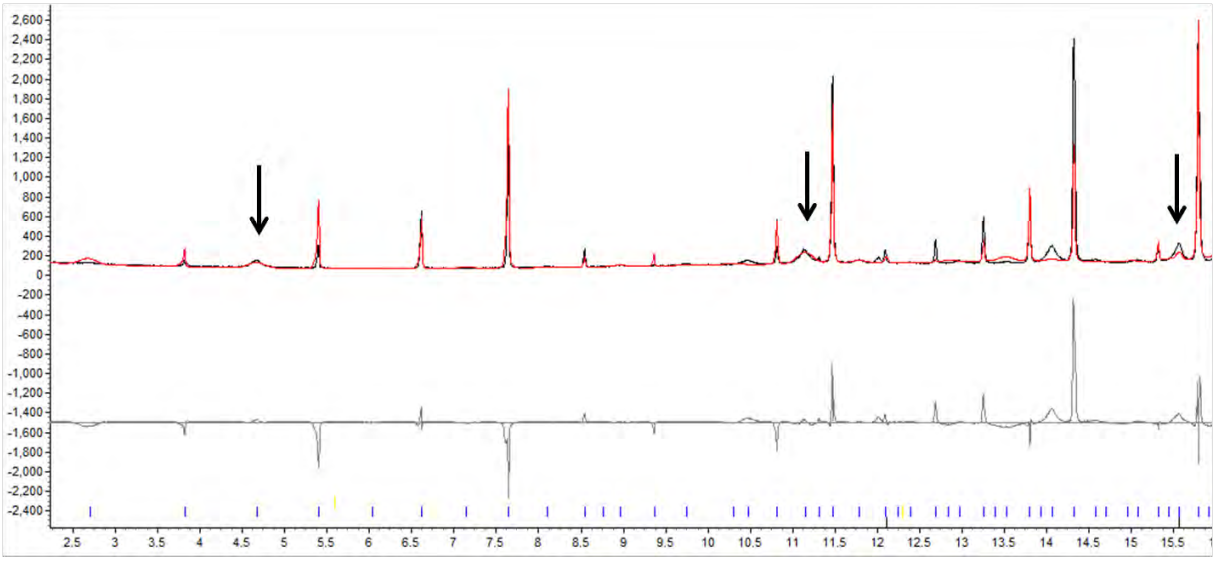

Figure 5.16 *– Diagram illustrating the Rietveld fit when atoms occupied either the Ag(8), Ag(9), Ag(10) or Ag(11) sites.*

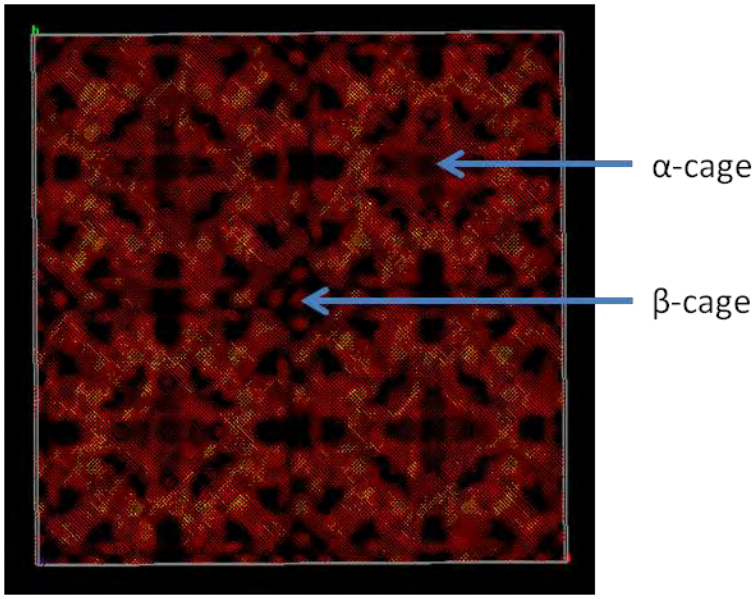

Figure 5.17 *– 3D difference Fourier map of hydrated $(AgNO_3)_{72}$–AgA after zeolite framework and silver cations have been refined.*

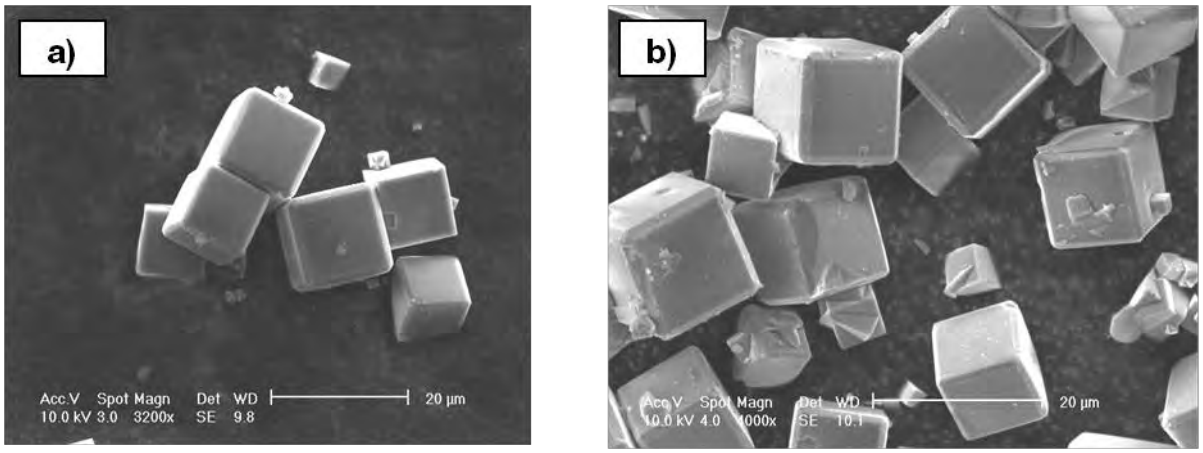

Figure 5.18 *– SEM images of a) zeolite Na-A and b) silver nitrate loaded zeolite Ag-A single crystals.*

5.3.4 Single Crystal XRD Analysis of Hydrated Silver Nitrate Loaded Ag-A

Single crystals of silver nitrate containing Ag-A were prepared in attempt to solve the superlattice structure using single crystal XRD. Figure 5.18 shows SEM images of the cube-shaped zeolite A single crystals before and after ion exchange and reaction with silver nitrate. Synchrotron single crystal XRD data were collected for the silver nitrate loaded Ag-A system as the data obtained from a laboratory diffractometer was not of high enough resolution to observe the weak superlattice reflections. Two different data collections were required at the synchrotron source to account for the large difference in the intensities of the diffraction spots. Data collected for high intensity and low intensity reflections were attenuated and combined to give the full diffraction pattern of the occluded system. All data had to be collected at 300 K as the superlattice structure was shown to disappear at low temperature as discussed in chapter 6. The cubic space groups $Pm\bar{3}n$ and $Pn\bar{3}n$ were suggested as the most likely space groups for the unit cell of the salt-containing system using the computer indexing software CrystalClear.[36] $Pm\bar{3}n$ was quickly dismissed as a possible space group as it did not allow for Si/Al ordering in the zeolite framework. $Pn\bar{3}n$ was the same space group that was suggested from analysis of the powder synchrotron

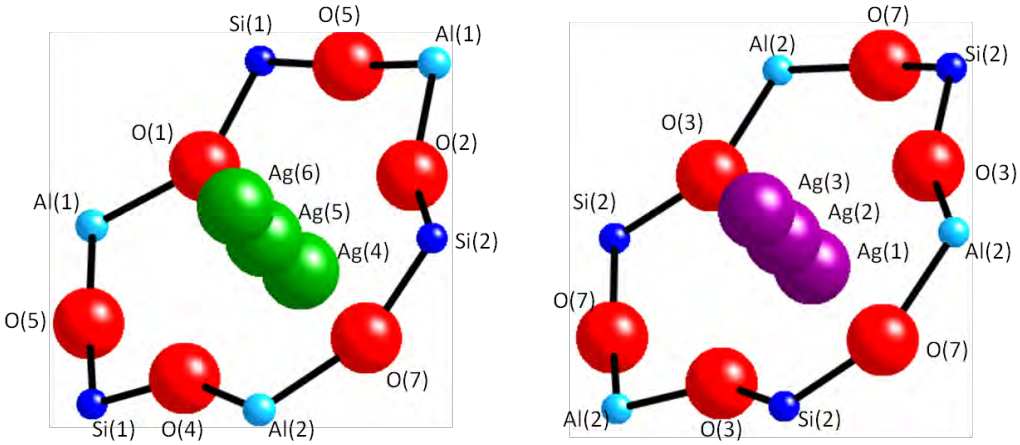

Figure 5.19 *– Diagrams illustrating the refined Ag^+ positions near the 6-ring of hydrated silver nitrate loaded Ag-A.*

XRD data and was accepted as the correct space group. A unit cell parameter of a = 24.784(1) Å was calculated from indexing the diffraction patterns. Difference Fourier mapping was used to identify the positions of the atoms within the unit cell. The strong areas of electron density and obvious coordination to one another meant that the zeolite framework atoms were quickly and easily identified. However the assignment of the ions and molecules within the zeolite pores proved much more difficult due to the high disorder in the system. Table 5.4 details the refined atomic coordinates determined from the single crystal synchrotron data. Areas of localised electron density were identified in three key regions of the LTA framework: near the 6-ring, 8-ring and 4-ring. Three separate spots of electron density were identified in a linear arrangement near all of the 6-ring sites (figure 5.19). Ag(1)–(3) were all located on a 16f special position and occupied ¼ of the 6-ring sites. However, Ag(4)–(6) were all located on a 48i special position and occupied the remainder of the 6-ring sites. Ag(2) and Ag(6) were positioned in the plane of the 6-ring and the remainder of the 6-ring Ag cations were located ~0.65 Å either side of the plane.

Table 5.4 *– Refined atomic coordinates of hydrated silver nitrate loaded Ag-A from single crystal synchrotron XRD data.*[a]

	Site	Wyckoff Position	x	y	z	occ	U_{iso}
Zeolite Framework	Si(1)	48i	0.9071(2)	0.9997(2)	0.1850(2)	1	0.02
	Si(2)	48i	0.0926(2)	0.9987(2)	0.1850(2)	1	0.02
	Al(1)	48i	0.9988(2)	0.9099(2)	0.1863(2)	1	0.02
	Al(2)	48i	0.0010(2)	0.0898(2)	0.1868(2)	1	0.02
	O(1)	48i	0.9377(4)	0.9431(4)	0.1783(5)	1	0.02
	O(2)	48i	0.0590(4)	0.9443(4)	0.1753(5)	1	0.02
	O(3)	48i	0.0584(4)	0.0530(4)	0.1694(5)	1	0.02
	O(4)	48i	0.9466(4)	0.0494(5)	0.1724(5)	1	0.02
	O(5)	48i	0.0004(5)	0.8584(5)	0.1404(5)	1	0.02
	O(6)	48i	0.0040(4)	0.8584(6)	0.2526(4)	1	0.02
	O(7)	48i	0.1466(5)	0.9985(4)	0.1483(5)	1	0.02
	O(8)	48i	0.1139(5)	0.0054(5)	0.2469(4)	1	0.02
6R	Ag(1)	16f	0.1079(2)	0.1079(2)	0.1079(2)	0.33	0.025(2)
	Ag(2)	16f	0.0923(3)	0.0923(3)	0.0923(3)	0.33	0.027(2)
	Ag(3)	16f	0.0773(4)	0.0773(4)	0.0773(4)	0.33	0.037(3)
	Ag(4)	48i	0.8856(3)	0.8856(3)	0.1091(3)	0.33	0.041(2)
	Ag(5)	48i	0.9037(2)	0.9045(2)	0.0971(2)	0.33	0.026(1)
	Ag(6)	48i	0.9208(3)	0.9214(3)	0.0824(3)	0.33	0.034(7)
8R	Ag(7)	48i	0.0007(7)	0.7848(9)	0.218(1)	0.25	0.122(8)
	Ag(8)	48i	0.2184(8)	0.0016(6)	0.2139(8)	0.25	0.101(6)
4R	Ag(9)	24h	0.1117(4)	0.1117(4)	0.25	0.5	0.097(3)
	Ag(10)	48i	0.103(1)	0.181(1)	0.2511(9)	0.25	0.17(1)
	Ag(11)	24h	0.8824(4)	0.8824(4)	0.25	0.5	0.174(8)
	Ag(12)	48i	0.1212(5)	0.8906(5)	0.2498(4)	0.25	0.090(3)
	Ag(13)	48i	0.099(1)	0.866(1)	0.2499(8)	0.13	0.094(6)

[a] *a =24.784(1) Å, space group = $Pn\bar{3}n$, R1 = 0.2914*

In contrast to the results obtained from the powder synchrotron XRD data, areas of electron density were found to occupy the zeolite 8-ring. These were attributed to Ag^+ cations in the 8-ring [Ag(7)–(8)] and were located in a similar position to that observed in dehydrated Ag-A. Differences in the electron density spots located near the zeolite 4-ring were also shown throughout the entire unit cell. In ¼ of the 4-ring sites, a row of three spots were identified (as illustrated in figure 5.20) and were attributed to disordered Ag^+ cation sites. Ag(9)

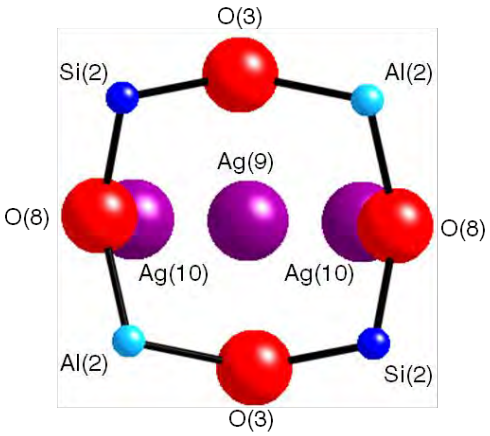

Figure 5.20 *– Diagram illustrating the refined Ag^+ positions near ¼ of the 4R sites in hydrated silver nitrate loaded Ag-A.*

cations were positioned on a 48i site located in the centre of the 4-ring approximately 2.4 Å from the plane of the ring. Ag(10) cations were located ~1.73 Å either side of Ag(9) and were approximately 3.32 Å from the plane of the 4-ring. In the remaining ¾ of the unit cell electron density was found to be much more localised around the central 4-ring position. Ag(11) and Ag(12) were located in the centre of the 4-ring approximately 2.8 Å from the plane of the ring. Ag(13) was the only non-centralised site identified near the 4-ring and had a distance of ~1.43 Å from Ag(12). This suggested that position of the 4-ring Ag^+ cations were no longer symmetry related after hydration, leading to a superlattice formation. No clear positions were identified for the nitrate anions. Despite determining the location of the all framework atoms and the majority of the Ag^+ cations, successful structural refinement was not achieved (R1 = 0.2914). This may have been due to a high degree of disorder in the remaining contents of the zeolite pores.

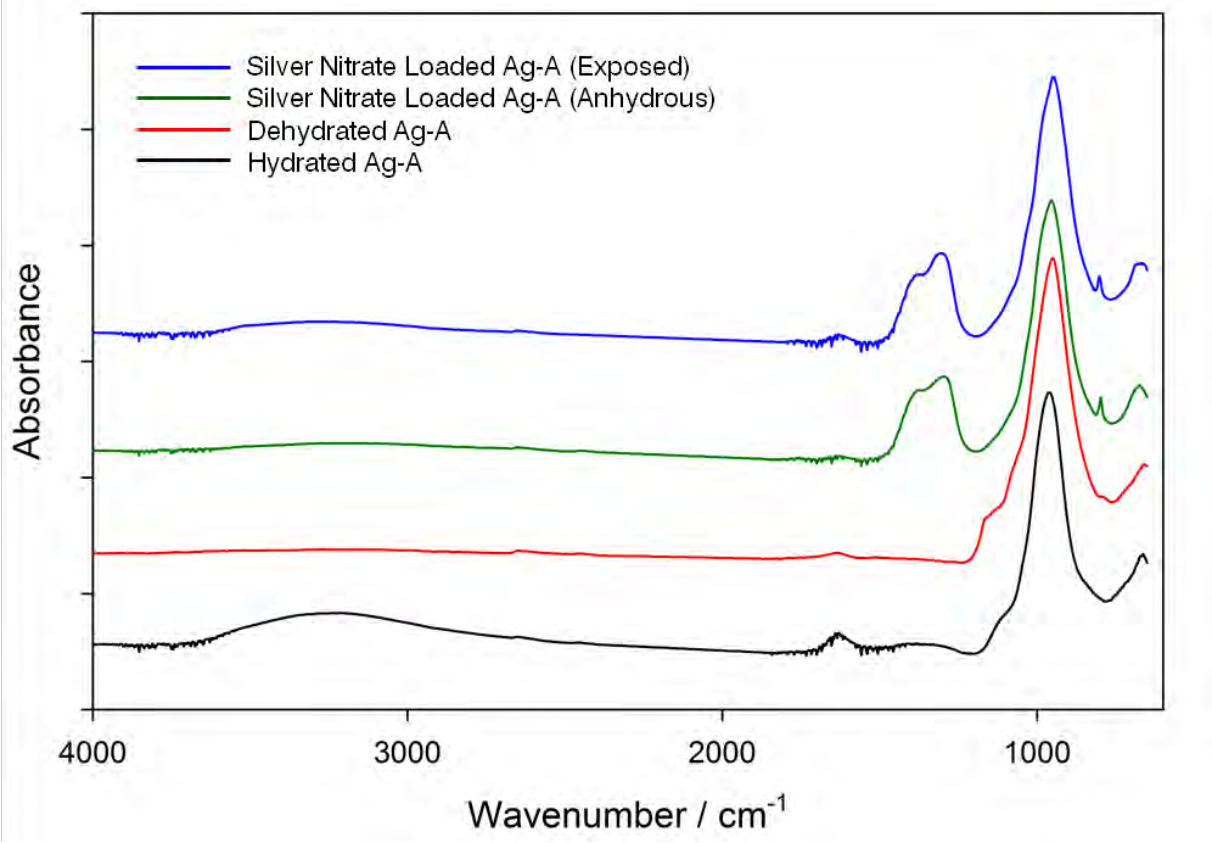

Figure 5.21 *– Infra-red spectra for the anhydrous and hydrated forms of zeolite Ag-A and* $(AgNO_3)_{72}$*–AgA.*

5.3.5 Infra-red and Raman Spectroscopy

IR and Raman spectroscopy data were collected for both the anhydrous and hydrated forms of Ag-A and $(AgNO_3)_{72}$–AgA in an attempt to gain more information on the nitrate ion coordination inside the zeolite framework. Figure 5.21 shows the IR spectra of all four systems recorded from 650–4000 cm^{-1}. Data below 650 cm^{-1} were not collected due to instrumental limitations. The strongest IR band in the region 900–1200 cm^{-1} was observed in all spectra and corresponded to T–O asymmetric stretching modes in the zeolite framework.[25, 37] The shoulder on the left side of this band (~1150 cm^{-1}) was shown to diminish when silver nitrate was introduced into the zeolite framework. A weaker band at ~660 cm^{-1} was also present in every spectrum and corresponded to T–O symmetric

stretching modes. A small shift to higher wavenumber was observed in this band in the silver nitrate loaded systems. Two weak broad bands at ~3250 cm^{-1} and 1700 cm^{-1} correspond to the stretching mode and bending mode of water molecules, respectively. These bands were only prominent in the IR spectra of hydrated Ag-A and $(AgNO_3)_{72}$–AgA after being exposed to the atmosphere. The intensity of these bands was much greater in the spectrum of hydrated Ag-A as more water molecules were present inside the zeolite pores. Nitrate bands in the region 1200–1500 cm^{-1} were observed in the spectra of the silver nitrate loaded systems. These bands were characteristic of nitrate ions that are coordinated to silver ions. However, a weaker nitrate band at ~800 cm^{-1} corresponded to anions that are uncoordinated. These results were similar to those reported by Petranovic *et al.*[25] and suggested that the nitrate anions existed as both coordinated and free ions in silver nitrate loaded Ag-A. Little difference in the IR spectra of anhydrous and hydrated $(AgNO_3)_{72}$–AgA suggested that the anion coordination was not significantly affected by the introduction of water molecules into the zeolite pores.

Figure 5.22 shows the Raman spectra of all four systems recorded from 300–3000 cm^{-1}. Significant changes in the Raman spectra were observed as the zeolite pore contents were modified. Only one weak band at ~700 cm^{-1} was observed in the spectrum of hydrated Ag-A. This band was initially reported to be caused by asymmetric T–O stretching modes in the zeolite framework.[38] However, later work attributed this band to T–O(1)–T and O(3)–T–O(3) bending modes present in the zeolite double 4-ring. No active Raman bands were observed in the spectrum of Ag-A after dehydration. A sharp asymmetric band at ~1040 cm^{-1} and a weaker band at ~600 cm^{-1} were observed in the spectrum of anhydrous silver nitrate loaded Ag-A. Both of these bands were attributed to nitrate Raman modes. Studies on molten silver nitrate[39] have suggested that the asymmetry of the band at ~1040 cm^{-1} may result

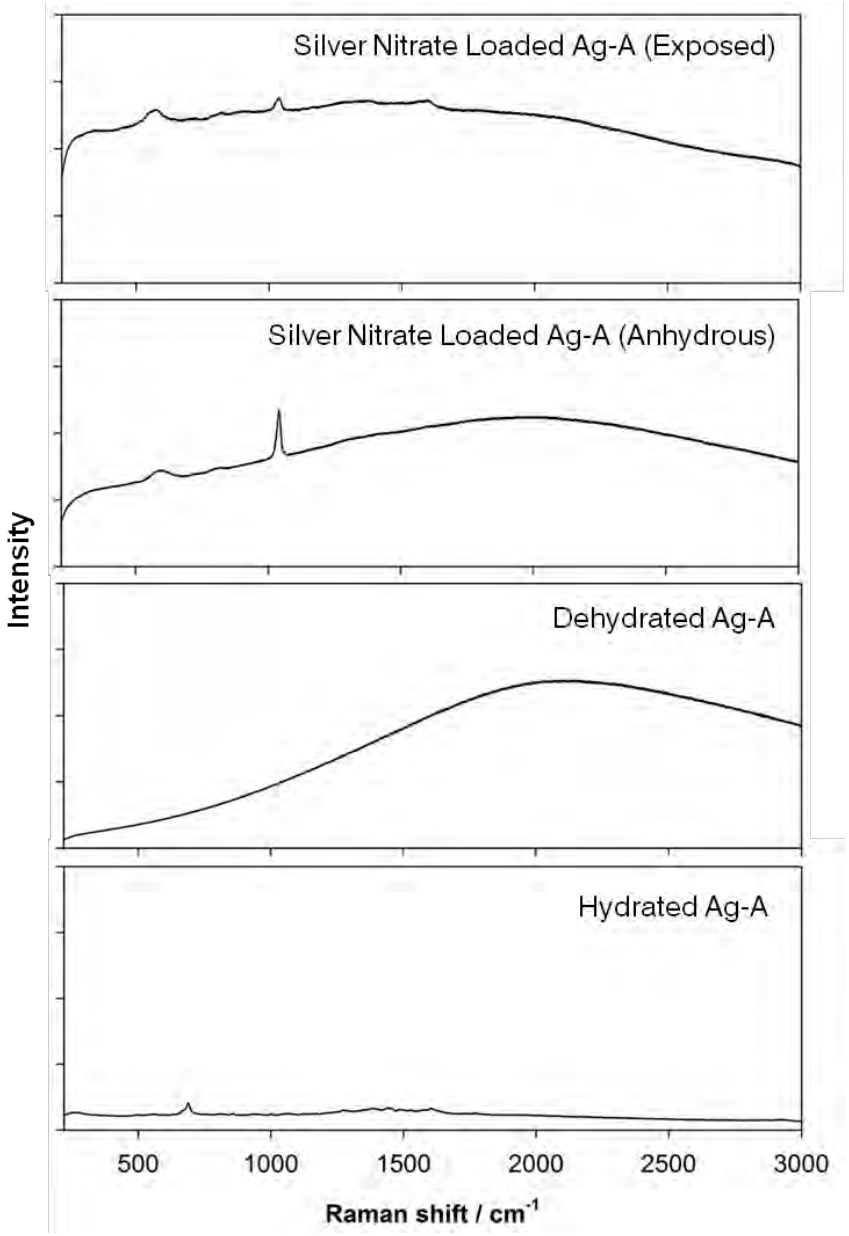

Figure 5.22 *– Raman spectra for the anhydrous and hydrated forms of zeolite Ag-A and* $(AgNO_3)_{72}$*–AgA.*

from nitrate anions existing as both coordinated and free ions (figure 5.23). A significant decrease in the intensity of this band was also observed upon exposure of the silver nitrate loaded system to the atmosphere. A similar decrease in intensity was reported in silver nitrate at elevated temperatures and was attributed to decreased association.[39]

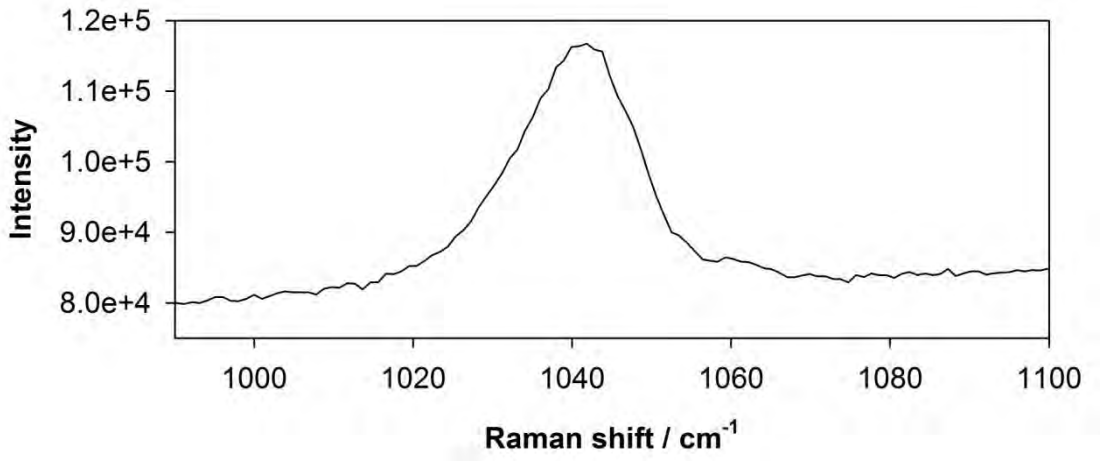

Figure 5.23 *–The asymmetric band at 1040 cm^{-1} in the Raman spectrum of anhydrous $(AgNO_3)_{72}$–AgA.*

5.4 Conclusion

Significant breakthroughs have been made with regards to understanding the anhydrous and hydrated forms of $(AgNO_3)_{72}$–AgA. Water molecules have been shown to play a key role in the superlattice formation. Approximately 29.6 water molecules were absorbed per unit cell after anhydrous synthesis and exposure to the atmosphere, leading to a unit cell symmetry change. All XRD peaks (both sharp and broad) from both powder and single crystal data of hydrated $(AgNO_3)_{72}$–AgA were indexed in the cubic space group $Pn\bar{3}n$. Difference Fourier mapping showed that the Ag^+ cations occupied three common sites in the LTA framework for both the anhydrous and hydrated forms of $(AgNO_3)_{72}$–AgA: the 6-ring, 8-ring and 4-ring. Data suggested that a displacement of the 4-ring cations from a more symmetric position had occurred upon hydration, which may have lead to a change in the unit cell symmetry from $Fm\bar{3}c$ to $Pn\bar{3}n$. No structural information on the position of the nitrate and water molecules in hydrated $(AgNO_3)_{72}$–AgA was gained from XRD data. This may have been due to the high degree of disorder in the zeolite pores and the heavy scattering nature of silver. Raman and IR spectroscopy data indicated that the nitrate

anions existed as both coordinated and free ions in anhydrous and hydrated $(AgNO_3)_{72}$–AgA.

5.5 References

1. M. Viertelhaus, A. E. Taylor, L. Kloo, I. Gameson and P. A. Anderson, *Dalton Trans.*, 2006, 2368-2373.
2. W. E. Meier and R. M. Barrer, *J. Chem. Soc.*, 1958, 299-304.
3. F. W. Clarke and G. Steiger, *Amer. J. Sci.*, 1899, **8**, 245-257.
4. M. Liquornik and Y. Marcus, *J. Phys. Chem.*, 1968, **72**, 2885-2889.
5. M. Liquornik and Y. Marcus, *J. Phys. Chem.*, 1968, **72**, 4704-4705.
6. M. Liquornik and J. J. W. Irvine, *Inorg. Chem.*, 1970, **9**, 1330-1333.
7. N. A. Petranović and M. V. Šušić, *J. Inorg. Nucl. Chem* 1969, **31**, 551-557.
8. N. A. Petranović, M. V. Šušić and D. A. Mioč, *J. Inorg. Nucl. Chem.*, 1971, **33**, 2667-2675.
9. N. A. Petranović and M. V. Šušić, *J. Inorg. Nucl. Chem*, 1975, **37**, 284-285.
10. W. A. Platek and J. A. Marinsky, *J. Phys. Chem.*, 1961, **65**, 2118-2122.
11. J. A. Rabo and P. H. Kasai, *Progress in Solid State Chemistry*, Pergamon Press, Oxford, UK, 1975.
12. M. Park and S. Komarneni, *Zeolites*, 1997, **18**, 171-175.
13. M. Park, C. L. Choi, J. S. Kim, D. H. Lee, K. S. Kim, N. H. Heo and J. Choi, *Micropor. and Mesopor. Mater.*, 2003, **62**, 1-7.
14. T. Suzuki, M. Tanaka and S. Koyama, *Progress in Nuclear Energy*, 2011, **53**, 969-973.
15. A. K. Bansiwal, S. S. Rayalu, N. K. Labhasetwar, A. A. Juwarkar and S. Devotta, *J. Agric. Food Chem.*, 2006, **54**, 4773-4779.
16. A. Dyer and M. Zubair, *Micropor. and Mesopor. Mater.*, 1997, **22**, 135-150.

17. A. R. D. Attiah, R. Blackburn, A. Dyer and C. D. Williams, 2011, **288**, 97-99.

18. O. H. Ahmed, G. Sumalatha and A. M. N. Muhamad, *Int. J. Phys. Sci.*, 2010, **5**, 2393-2401.

19. P. A. Anderson, M. J. Edmondson, P. P. Edwards, I. Gameson, P. J. Meadows, S. R. Johnson and W. Zhou, *Z. Anorg. Allg. Chem.*, 2005, **631**, 443-447.

20. A. Mayoral, Y. Sakamoto and P. A. Anderson, *Cryst. Eng. Comm.*, 2010, **12**, 3012-3018.

21. D. Lexa, L. Leibowitz and J. Kropf, *J. Nucl. Mater.*, 2000, **279**, 57-64.

22. I. Kiricsi, I. Hannus, A. Kiss and P. Fejes, *Zeolites*, 1982, **2**, 247-251.

23. S. Phongikaroon and M. F. Simpson, *AIChE Journel*, 2006, **52**, 1736-1743.

24. E. A. Daniels and H. P. Joshi, *J. Radioanal. Nucl. Chem., Letters*, 1985, **98**, 413-418.

25. N. Petranović, U. Mioč and M. Šušić, *J. Chem. Soc, Faraday Trans. 1*, 1981, **77**, 379-389.

26. R. M. Barrer and H. Villiger, *Z. Kristallogr.*, 1975, **142**, 82-98.

27. E. Garrone, N. Russo, P. Marturano, B. Onida, F. D. Renzo and M. Lasperas, *Chem. Commun.*, 1998.

28. M. Bärtsch, P.Bornhauser, G. Calzaferri and R. Imhof, *J. Phys. Chem.*, 1994, **98**, 2817-2831.

29. M. J. Edmonson, Ph. D Thesis, University of Birmingham, 2002.

30. K. R. Loos and J. F. Cole, 1973.

31. A. T. Petfield and R. P. Clooney, *Aust. J. Chem.*, 1980, **33**, 659-664.

32. N. Togashi, Y. Sakamoto, T. Ohsuna and O. Terasaki, *Mater. Sci. Eng. A*, 2001, **312**, 267-273.

33. J. F. Charnell, *J. Cryst. Growth*, 1971, 291-294.

34. A. Coelho, Topas Academic Version 4.1., 2007

35. Y. Kim and K. Seff, *J. Am. Chem. Soc.*, 1977, **100**, 175-180.

36. CrystalClear2.0, Rigaku Americas Corporation, 2006-2009

37. Y. Huang and Z. Jiang, *Micropor. Mater.*, 1997, **12**, 341-345.

38. S. M. Auerbach, K. A. Carrado and P. K. Dutta, *Handbook of Zeolite Science and Technology*, Dekker, 2003.

39. G. E. Walrafen and D. E. Irish, *J. Phys. Chem.*, 1963, **40**, 911-913.

Chapter 6 – Thermal Expansion Studies of Silver Nitrate Loaded Silver Zeolite A

6.1 Introduction

This chapter will discuss the effect that loading the pores of zeolite Ag-A with silver nitrate and water molecules had on the thermal expansion behaviour. Very few thermal studies have been reported on salt containing zeolites[1-4] and even fewer have reported their thermal expansion properties.[5-7] In 1991, Buhl[5] reported that strong PTE behaviour was observed for nitrate loaded sodalite with a mean volume thermal expansion coefficient, $\overline{\alpha_v}_{(298–920\ K)}$, of $92.9 \times 10^{-6}\ K^{-1}$. In contrast, Lexa *et al*.[6] reported that NTE expansion behaviour was observed between 460–840 K for zeolite A which had been loaded with a eutectic salt mixture (uranium trichloride + lithium chloride + potassium chloride).

Viertelhaus *et al*.[7] first reported in 2006 that a strong NTE was observed for silver nitrate containing Ag-A formed in atmospheric conditions, with a $\overline{\alpha_v}_{(298–533\ K)}$ of $-20 \times 10^{-6}\ K^{-1}$. Structural analysis of the salt loaded zeolite was reported in this study under ambient conditions, but no structural mechanism behind the NTE behaviour was produced. Superlattice peaks in the reported XRD patterns were shown to disappear at temperatures above 353 K (80°C), which was attributed to melting of the superlattice structure. However, the same superlattice peaks were shown to return when the system was cooled below this same temperature.

6.2 Synthesis

All samples were prepared as described in chapter 5.

6.3 Results and Discussion

Variable temperature powder synchrotron XRD studies were used to determine the thermal expansion behaviour of the anhydrous and hydrated forms of $(AgNO_3)_{72}$–Ag-A from 100–300 K. XRD patterns were collected at 20 K intervals and unit cell parameters were determined through Pawley refinements. Rietveld analysis of the silver nitrate loaded systems was not possible as accurate structural models were not produced due to the high disorder in the zeolite pores (chapter 5). Complex thermal expansion behaviour was observed for both the anhydrous and hydrated forms of $(AgNO_3)_{72}$–Ag-A. These will now be discussed in turn.

6.3.1 Thermal Expansion Studies of Anhydrous Silver Nitrate Loaded Ag-A

Figure 6.1 shows the calculated unit cell volumes that were determined for anhydrous silver nitrate loaded Ag-A as the sample was cycled twice between 100–300 K. Each variable temperature run took approximately 2 hours, however, due to problems with the cryostream it was not possible to collect XRD data at 100 K during the second cooling run. As shown in figure 6.1, almost no change in the unit cell volume was observed in the initial cooling run. After this stage in the experiment PTE behaviour was observed with a strong thermal hysteresis (where the rate of change in unit cell volume was different upon cooling from what it was upon heating). At no stage during the experiment did the unit cell volume return to its original value.

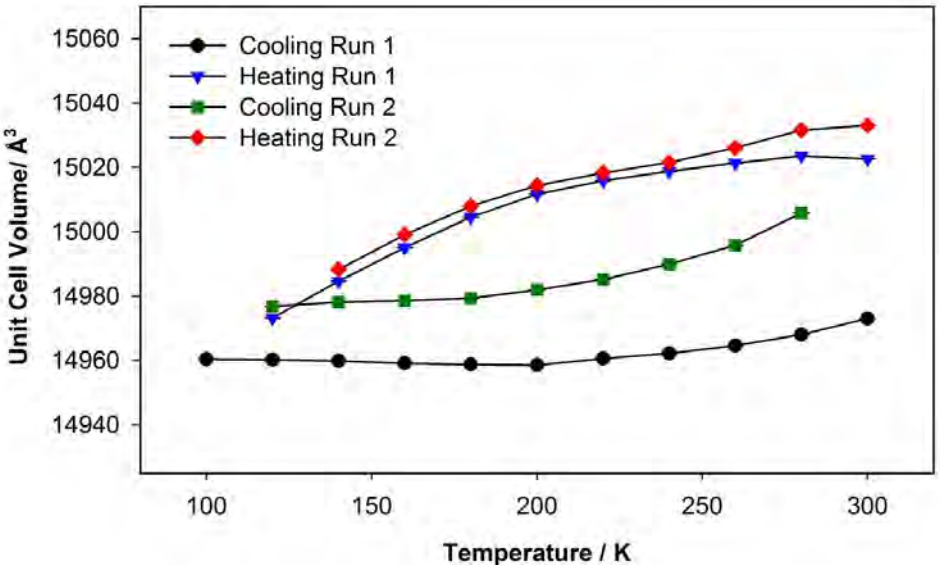

Figure 6.1 – *Calculated unit cell volumes of anhydrous $(AgNO_3)_{72}$–Ag-A cycled quickly between 100 and 300 K [errors at 3σ level, not visible on this scale].*

Significant changes in the powder synchrotron XRD patterns were also observed after the initial cooling run as illustrated in figure 6.2. The relative peak intensities of the (220) and (422) peaks were shown to increase, whereas the (420), (662) and (860) peaks all decreased. Taken together these observations initially indicated that an irreversible structural change had occurred upon cooling. However, the observation of the thermal hysteresis cycle suggested that the thermal kinetics of the salt containing system were much slower than the unoccluded zeolite Ag-A. This meant that unit cell volumes calculated after the initial 300 K value were not stable as the anhydrous $(AgNO_3)_{72}$–Ag-A sample had not had enough time to thermally equilibrate at each temperature. This was investigated further by performing a longer variable temperature experiment. As illustrated in figure 6.3, powder synchrotron XRD data was initially collected at 300 K and a unit cell parameter of a = 24.6372(1) Å was determined. This was taken to be the equilibrium unit cell parameter

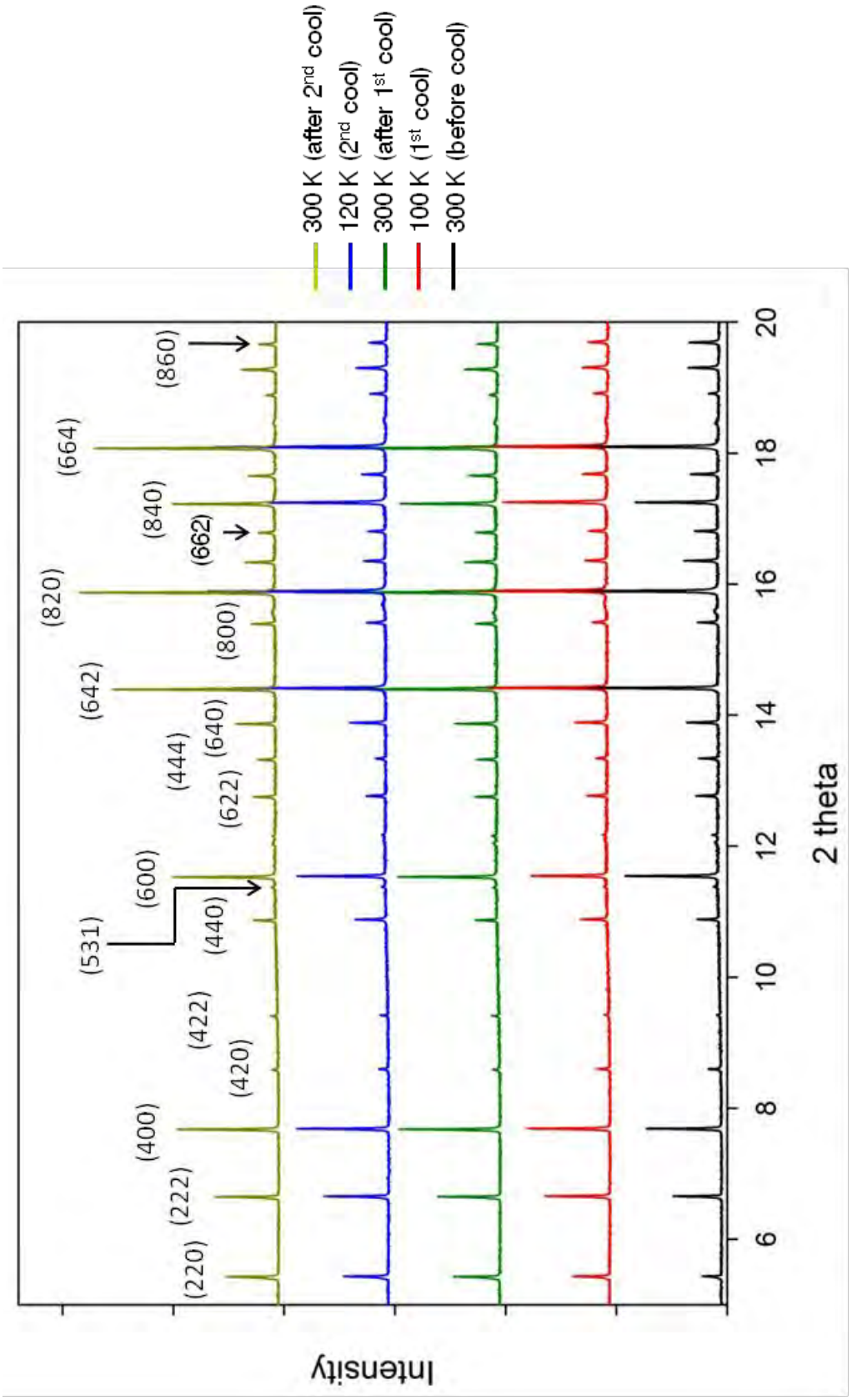

Figure 6.2 *– Variable-temperature powder synchrotron XRD patterns of anhydrous* $(AgNO_3)_{72}$*–AgA cycled quickly between 100–300 K.*

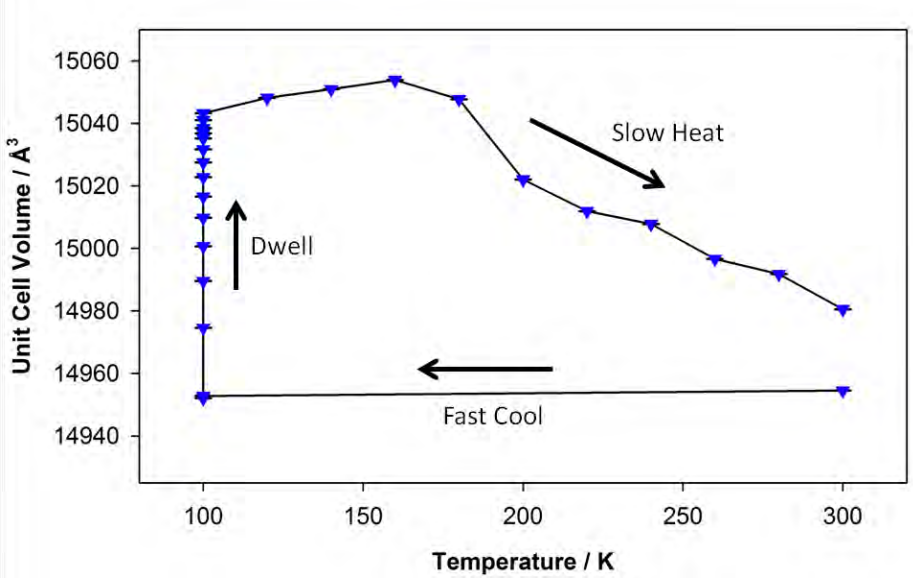

Figure 6.3 – *Calculated unit cell volumes of anhydrous $(AgNO_3)_{72}$–Ag-A cycled slowly between 100 and 300 K [errors at 3σ level, not visible on this scale].*

at 300 K. After collecting these data the sample was quickly cooled to 100 K and kept at this temperature whilst monitoring any changes in the recorded XRD patterns. As shown in figure 6.3, a large expansion in the unit cell was observed at low temperature. This was attributed to the atomic unit cell contents being allowed enough time to react to the induced temperature change and re-establish thermal equilibrium. After ~7 hours the unit cell stopped expanding and a unit cell parameter of 24.6858(1) Å was determined. This value was accepted to be the equilibrium unit cell parameter at 100 K. The sample was then heated slowly back to 300 K over a period of 20 hours to determine if the thermal expansion behaviour was reversible. However, despite this slow heating run the unit cell did not return exactly to its original volume within the time period.

Significant changes in the powder synchrotron XRD patterns were also observed during the long variable temperature experiment. As shown in figure 6.4, the relative peak intensities of

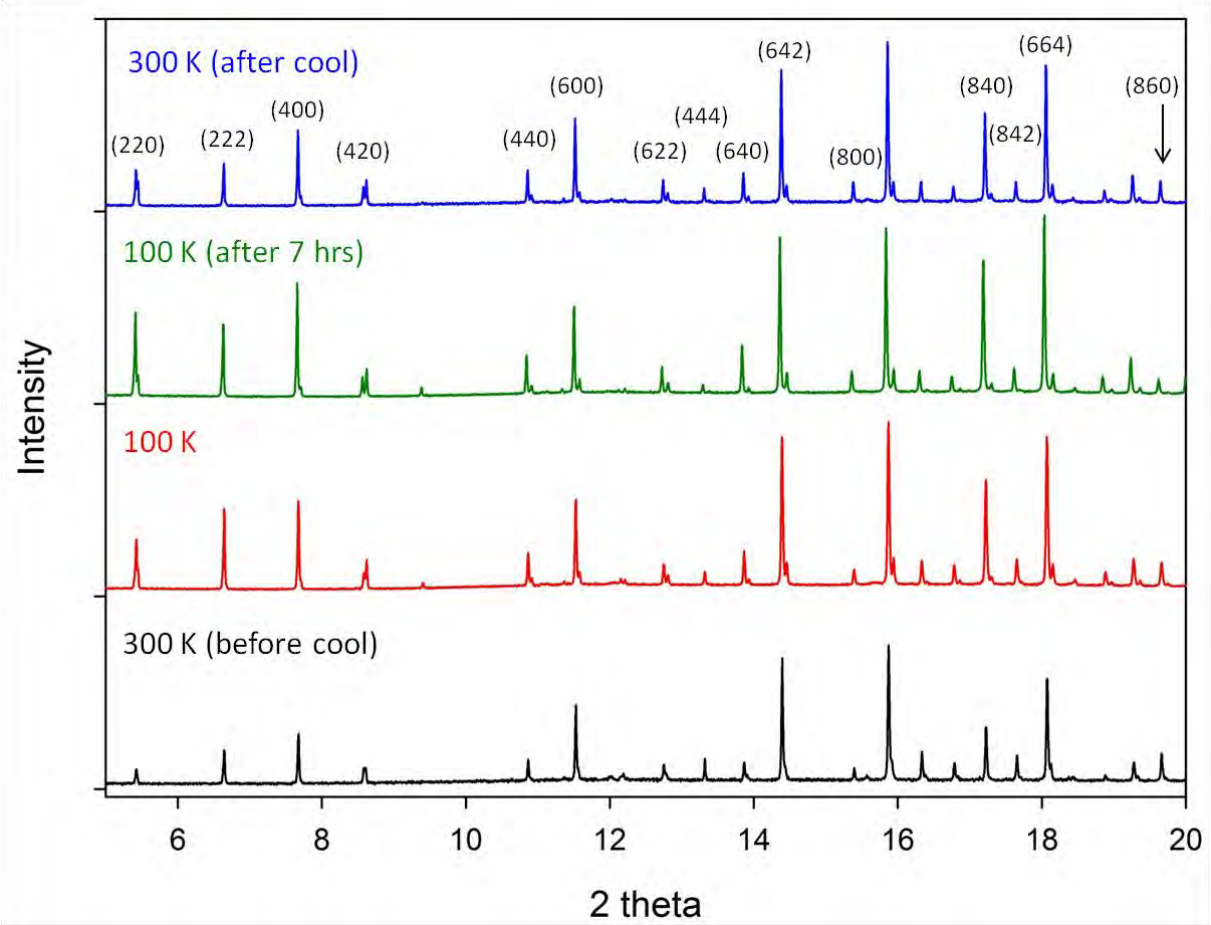

Figure 6.4 *– Variable temperature powder synchrotron XRD patterns of anhydrous $(AgNO_3)_{72}$–Ag-A cycled slowly between 100–300 K.*

the (220), (222), (400), (440), (640), (840) and (664) all increased upon cooling, whereas the (444) and (860) peaks both decreased. All of the changes in the relative peak intensities were shown to be reversed upon re-heating but they did not return exactly to those observed in the original powder XRD pattern at 300 K.

Peak splitting was also observed in all of the XRD patterns recorded in the slow variable temperature experiment, where low intensity peaks were observed at higher angle to the majority of zeolite peaks (except the (222), (422), (444), (842), (800) and (860)). This peak splitting may have been caused by a number of reasons, including a leak in the capillary or

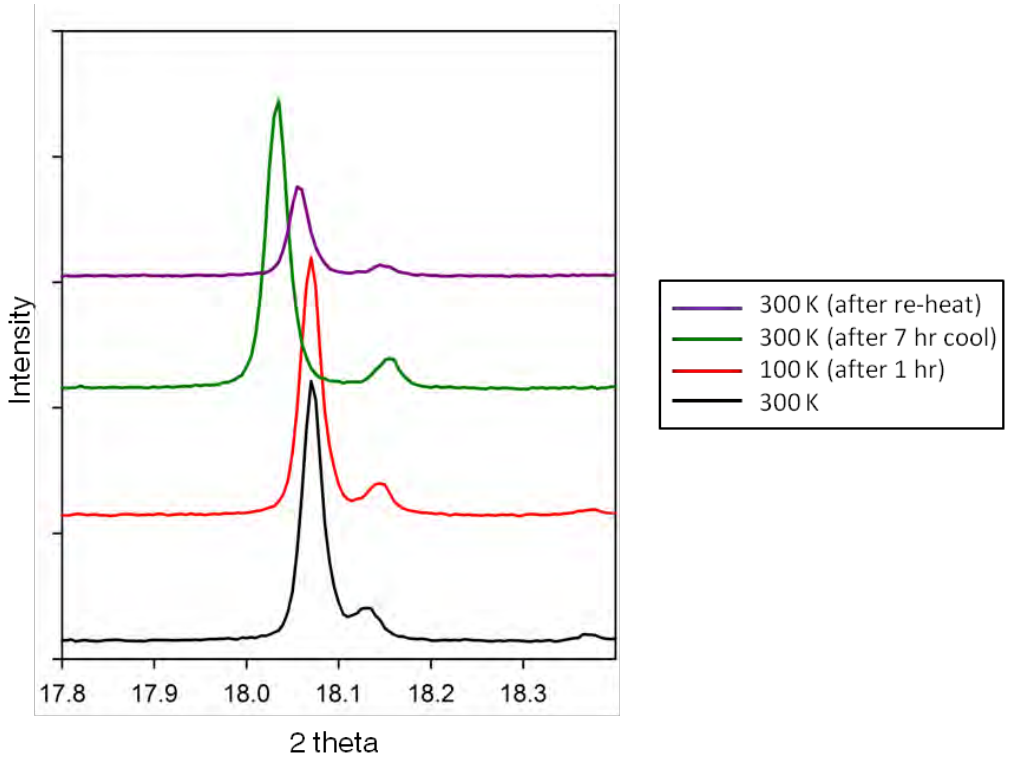

Figure 6.5 *– Peak splitting observed in the variable temperature powder synchrotron XRD patterns of anhydrous* $(AgNO_3)_{72}$*–Ag-A.*

a decomposition of the sample in the intense synchrotron beam. As peak splitting was only shown in the majority of the peaks and superlattice peaks were not observed, it was determined that the additional peaks in the XRD pattern were not caused by sample hydration. The unit cell of the hydrated salt occluded zeolite was also shown to be larger in volume than the anhydrous system (see next section); therefore the hydrated salt occluded zeolite peaks would have been at lower 2 theta positions than the anhydrous system peaks. This meant that the split peaks were more likely caused by sample decomposition. As illustrated in figure 6.5, the peak splitting was shown to become greater upon cooling as the low angle peaks shifted towards lower 2 theta and the high angle peaks shifted towards higher 2 theta. This suggested that either there were 2 different phases present in this system with opposite thermal expansion properties or a lowering of the unit cell had

occurred which had resulted in an anisotropic thermal expansion. Attempts were made to index all of the XRD peaks in a lower symmetry unit cell using TOPAS,[8] however, none were successful. Further analysis also showed that the higher angle peaks were all consistently lower in intensity by a factor ~10 when compared to the lower angle peaks. This indicated that the peak splitting was not caused by a unit cell symmetry change, as the difference in relative intensity between the split peaks would not be consistently the same. Additionally, no evidence of this peak splitting was observed in the fast variable temperature XRD patterns. Taken together these results indicated that only partial sample decomposition had occurred in the synchrotron beam during the long variable temperature experiment. Unfortunately, the origin of the additional phase has not yet been determined. All lower angle peaks with strong intensity were indexed in the cubic space group $Fm\bar{3}c$ and were attributed to the anhydrous $(AgNO_3)_{72}$–Ag-A peaks which had not decomposed in the beam.

Using only the unit cell parameters calculated at the two thermal equilibrium points during the slow variable temperature experiment, a mean volume thermal expansion coefficient, $\overline{\alpha_v}_{(100–300\ K)}$, of – 29.47 × 10^{-6} K^{-1} was determined for anhydrous $(AgNO_3)_{72}$–Ag-A. This mean thermal expansion coefficient was similar to the value reported by Viertelhaus *et al*.[7] and to the value calculated for ITQ-29. Through applying the findings from the previous chapters in this thesis, a small NTE or PTE coefficient was expected as the rigid TO_4 should in theory have had less room to rotate in the loaded zeolite pores. The structural mechanism responsible for the strong NTE behaviour in this case has not been determined.

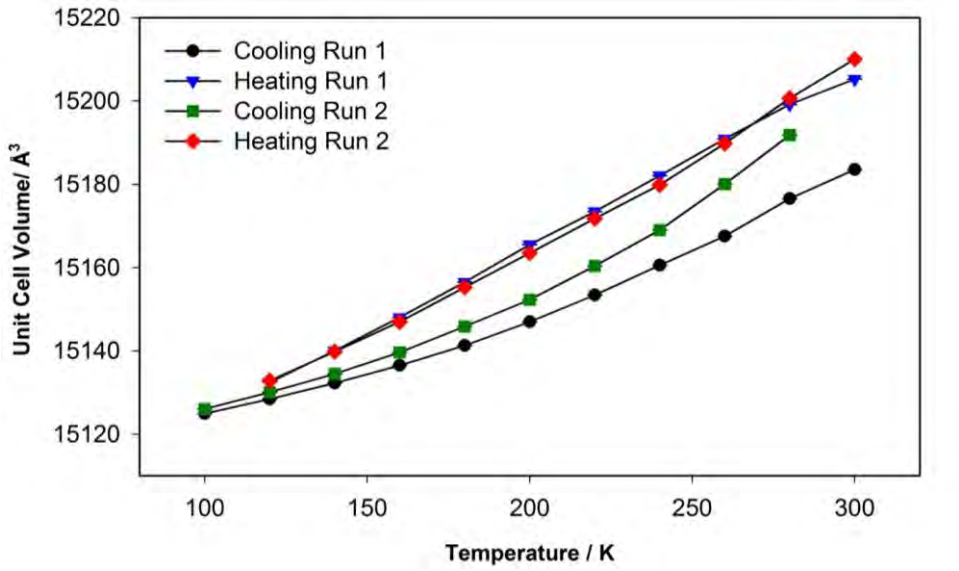

Figure 6.6 *– Calculated unit cell volumes of hydrated $(AgNO_3)_{72}$–Ag-A cycled quickly between 100 and 300 K [errors at 3σ level, not visible on this scale].*

6.3.2 Thermal Expansion Studies of Hydrated Silver Nitrate Loaded Ag-A

Anhydrous $(AgNO_3)_{72}$–Ag-A was exposed to the atmosphere and quickly cycled (over an 8 hour period) twice between 100 K and 300 K. Figure 6.6 shows the calculated unit cell volumes that were determined from the powder synchrotron XRD data collected during this variable temperature experiment. PTE behaviour was observed for the hydrated occluded system with a weak thermal hysteresis. Similarly to the anhydrous system, the unit cell volume of exposed silver nitrate loaded Ag-A did not return to its original value at any stage after the initial cooling run.

Significant changes in the powder synchrotron XRD patterns were also observed after the initial cooling run as illustrated in figure 6.7. The relative peak intensities of the (220), (422), (800) and (840) peaks were shown to increase, whereas the (420) and (862) peaks both decreased. Taken together these results suggested that, similarly to the anhydrous system, the thermal kinetics of the hydrated salt containing system were much slower when

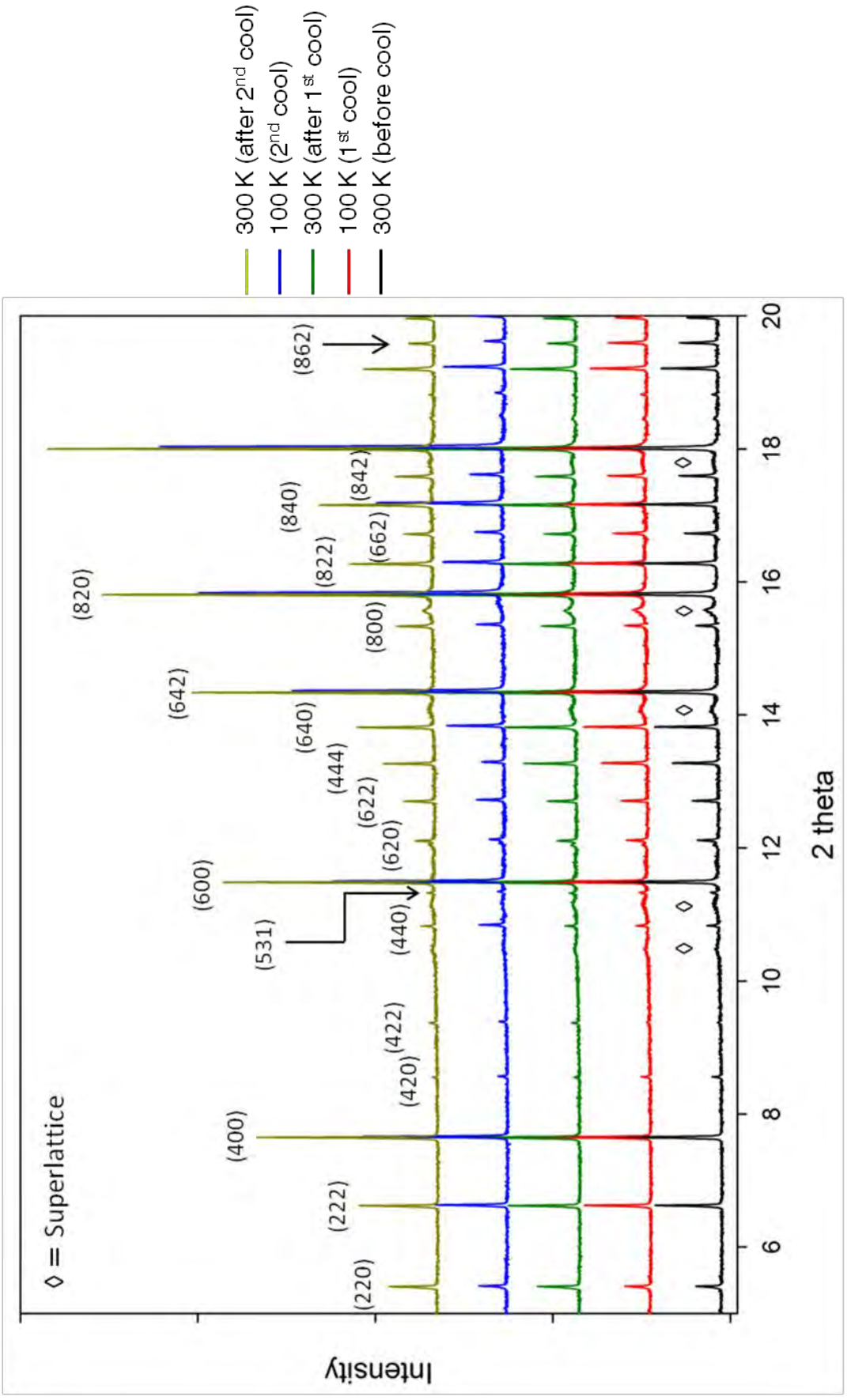

Figure 6.7 – *Variable-temperature powder synchrotron XRD patterns of hydrated $(AgNO_3)_{72}$–Ag-A cycled quickly between 100-300 K.*

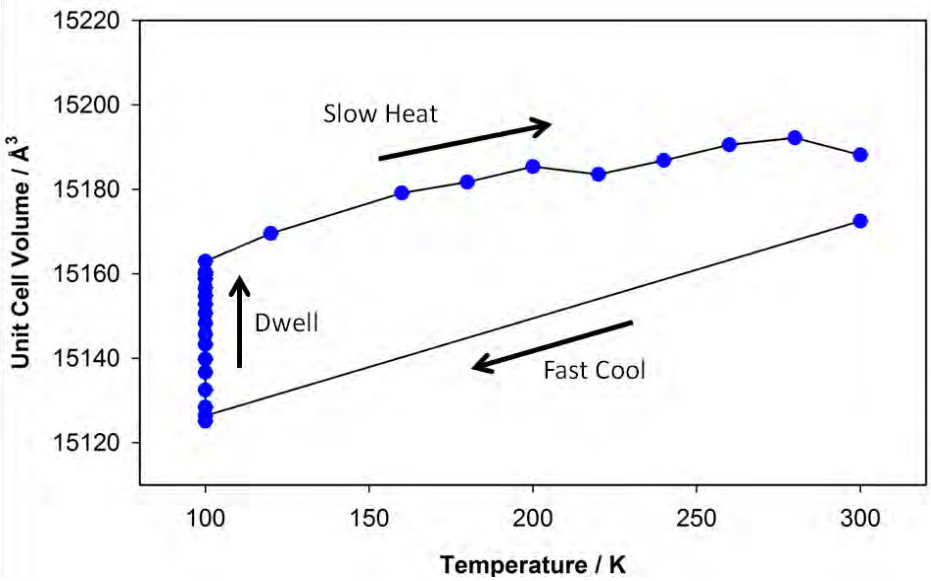

Figure 6.8 – *Calculated unit cell volumes of hydrated $(AgNO_3)_{72}$–Ag-A cycled slowly between 100 and 300 K [errors at 3σ level, not visible on this scale].*

compared to unoccluded zeolite. This was investigated further by performing a longer variable temperature experiment. As illustrated in figure 6.8, powder synchrotron XRD data were initially collected at 300 K and a unit cell parameter of a = 24.7563(2) Å was determined. This was taken to be the equilibrium unit cell parameter at 300 K. After collecting these data the sample was quickly cooled to 100 K and kept at this temperature whilst monitoring any changes in the recorded XRD patterns. As shown in figure 6.8, a large expansion in the unit cell was observed at low temperature. This was attributed to the atomic unit cell contents being allowed enough time to react to the induced temperature change and re-establish thermal equilibrium. After ~6 hours the unit cell stopped expanding and a unit cell parameter of 24.7511(9) Å was determined. This value was accepted to be the equilibrium unit cell parameter at 100 K. The sample was then heated slowly back to 300 K over a period of 12 hours to determine if the thermal expansion behaviour was reversible. However, despite this slow heating run, the unit cell did not return to its original volume within the time period. Using only the unit cell parameters calculated

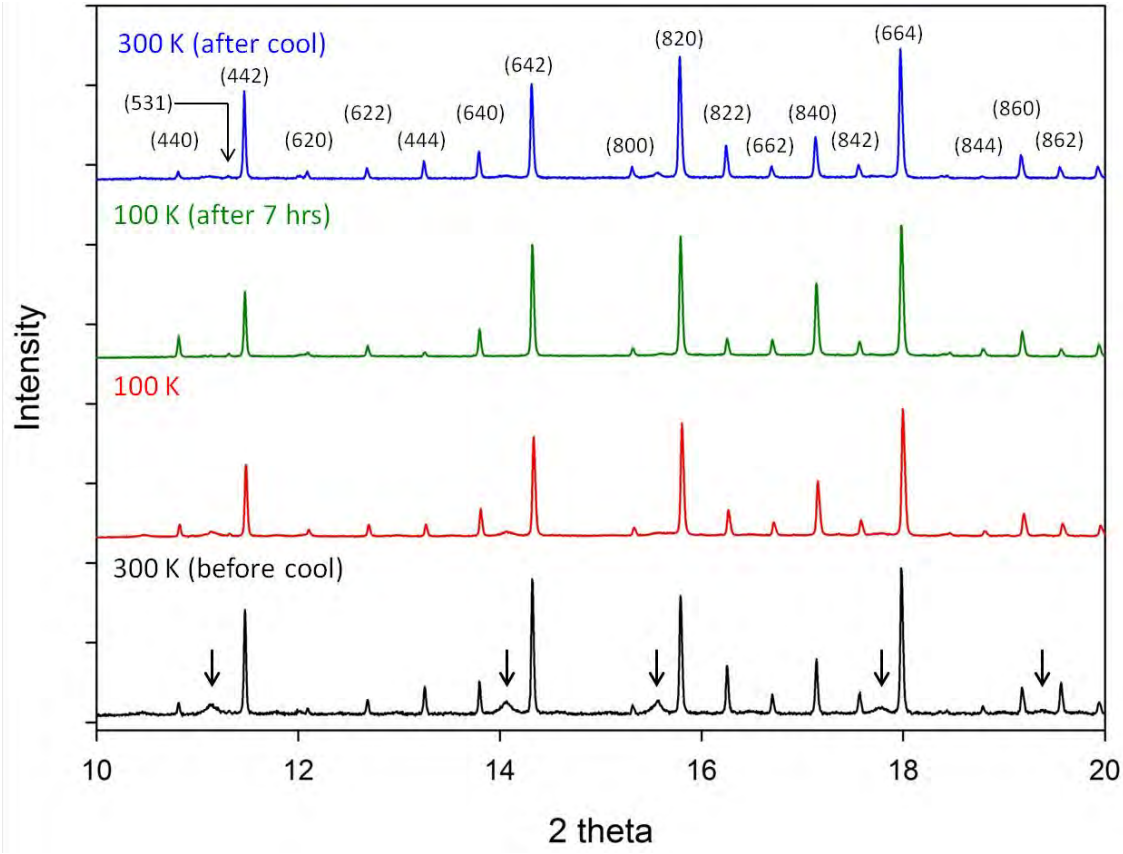

Figure 6.9 – *Variable temperature powder synchrotron XRD patterns of hydrated $(AgNO_3)_{72}$–Ag-A cycled slowly between 100 and 300 K.*

at the two thermal equilibrium points during the slow variable experiment, a mean volume thermal expansion coefficient, $\overline{\alpha_v}_{(100–300\ K)}$, of 3.15 × 10^{-6} K^{-1} was determined for hydrated $(AgNO_3)_{72}$–Ag-A. Similarly to the unoccluded zeolite A systems studied in this thesis, a shift from NTE to PTE behaviour was observed when water molecules were introduced into the zeolite pores. Unfortunately, no structural mechanism was produced for this system as an accurate structure has not yet been determined.

Significant changes in the powder synchrotron XRD patterns were also observed during the slow variable temperature experiment. As shown in figure 6.9, the relative peak intensities of the (440) and (840) peaks both increased upon cooling, whereas the (444), (642), (822) and

(862) peaks all decreased. Superlattice peaks were also shown to disappear upon cooling which suggested that significant changes in the zeolite intra-pore structure occurred at lower temperatures. As this was a sub-ambient thermal study, it can be speculated that intra-pore water molecules, which play a vital role in the formation of the superlattice, may have been affected by the below freezing temperatures, destroying the superlattice structure. No definitive evidence of superlattice re-formation was observed upon heating.

6.4 Conclusion

Dramatic differences in the thermal expansion behaviour of the anhydrous and hydrated forms of $(AgNO_3)_{72}$–Ag-A were observed between 100–300 K. Strong NTE behaviour was shown by the anhydrous system with a calculated mean thermal expansion coefficient greater than that of ITQ-29. Very weak PTE was exhibited by the hydrated system with a calculated mean thermal expansion coefficient smaller than that observed for the unoccluded hydrated systems. Extremely slow changes in the unit cell volumes were also shown during the variable temperature experiments. This was deemed to be caused by the small amount of free space remaining in the zeolite pores after salt occlusion, which in turn resulted in very slow thermally induced structural changes. Destruction of the superlattice was observed at low temperature. This may have been caused by the intrapore water molecules, which play a key role in the superlattice formation, being removed by sub-ambient temperatures.

6.5 References

1. M. Park and S. Komarneni, *Zeolites*, 1997, **18**, 171-175.
2. M. Park, S. C. Shin, C. L. Choi, D. H. Lee, W. T. Lim, S. Komarneni, M. C. Kim, J. Choi and N. H. Heo, *Micro. and Meso. Mater.*, 2001, **50**, 91-99.
3. M. Park, C. L. Choi, J. S. Kim, D. H. Lee, K. S. Kim, N. H. Heo and J. Choi, *Micropor. and Mesopor. Mater.*, 2003, **62**, 1-7.
4. N. Petranović and M. Šušić, *Thermochim. Acta*, 1979, **31**, 211-219.
5. J.-C. Buhl, *Thermochim. Acta*, 1991, **189**, 75-82.
6. D. Lexa, L. Leibowitz and J. Kropf, *J. Nucl. Mater.*, 2000, **279**, 57-64.
7. M. Viertelhaus, A. E. Taylor, L. Kloo, I. Gameson and P. A. Anderson, *Dalton Trans.*, 2006, 2368-2373.
8. A. Coelho, Topas Academic Version 4.1., 2007

Chapter 7 – Summary and Further Work

7.1 Research Summary

The thermal expansion properties of zeolites with the LTA topology have been shown to be greatly affected by chemical modification of the zeolite framework and pore contents. Similar to other reported purely siliceous zeolite structures, strong NTE behaviour was observed for ITQ-29 where the zeolite pore contents are vacant. Experimental data showed that this NTE was caused by the rotation of rigid SiO_4 tetrahedra upon thermal excitation and highlighted the importance of the Si–O(1)–Si bond angle which bridges the β-cages cages. When cations were present into the structure, various levels of strain were introduced into the zeolite framework, which lead to restricted TO_4 rotation on heating. Ideally sized cations were able fit perfectly into the zeolite 6-ring and caused the least amount of strain. Cation binding caused rotation of the TO_4 tetrahedra to be restricted in dehydrated Na- and Ag-A resulting in a distortion of the tetrahedra and a weaker NTE coefficient. Cations that were not a good fit for the 6-ring introduced a much larger strain in the zeolite framework. In these systems the TO_4 tetrahedra were prevented from moving upon thermal excitation resulting in a weak PTE.

Significantly weaker NTE behaviour was shown as the aluminium content in the zeolite framework was increased. No thermal expansion mechanism was discovered for the dehydrated ZK-4 systems, although it was postulated that the increased Na^+ cation content had a restricting factor on the TO_4 rotation; therefore weaker NTE coefficients were determined. More surprisingly, very strong NTE behaviour was observed when silver

zeolite A was occluded with silver nitrate. No structural mechanism was produced for this study due to the high degree of disorder inside the pores.

PTE behaviour was observed for all of the hydrated systems studied. However, accurate structural analysis could not be completed to increased disorder in the pores. Water molecules were determined to play a key role in the formation of a superlattice structure when silver nitrate occluded zeolite Ag-A is exposed to the atmosphere. A space group change from $Fm\bar{3}c$ to $Pn\bar{3}n$ was determined when approximately 29.6 water molecules were introduced into the unit cell upon hydration.

7.2 Further Work

This work has made a significant contribution to establishing whether it is possible to tune chemically zeolite materials to produce a desired coefficient of thermal expansion. However, further areas of research are now required in order to build on these findings. One area of research would be to produce a series of dehydrated mixed cation zeolite A systems, such as $Ag_{96-n}K_n(Al_{96}Si_{96}O_{384})$ where n ranges from 1-96, and study the thermal expansion properties using variable-temperature synchrotron XRD. As dehydrated K-A and Ag-A have been shown to exhibit PTE and NTE behaviour respectively, it may be possible to observe a shift in the thermal expansion behaviour and show a change in structural mechanism.

Another area of research would be to investigate the thermal expansion properties of zeolite A systems which have had different cations and salt molecules incorporated into the pores. One possible study could involve investigating the effect of introducing divalent cations or halogen salts into the framework of zeolite and investigating if there was any change in

thermal expansion behaviour. This area of study could also branch out into investigating other zeolite frameworks and determine if it is possible to modify their thermal expansion properties.

With regards to determining the superlattice structure of silver nitrate occluded zeolite Ag-A, a neutron diffraction experiment could provide valuable information with the aim of identifying the positions of water and nitrate molecules in hydrated $(AgNO_3)_{72}$–AgA. With the new knowledge on the vital role water molecules play in the superlattice formation, neutron and X–ray diffraction data could be compared and possibly provide the superlattice structure.